

**Fast Wave Ion Cyclotron Resonance Heating Experiments
on the Advanced Toroidal Facility**

A DISSERTATION

**Presented to
The Academic Faculty**

**by
Myeun Kwon**

**In Partial Fulfillment
of the Requirements for the Degree of**

DOCTOR OF PHILOSOPHY
in the school of Nuclear Engineering

**Georgia Institute of Technology
September 1990**

**Fast Wave Ion Cyclotron Resonance Heating Experiments
on the Advanced Toroidal Facility**

APPROVED:

C. E. Thomas, Chairman

W. M. Stacey

J. Mandrekas

A. Zangwill

R. J. Colchin

Date Approved by Chairperson

8/27/98

*This thesis is
dedicated to my parents.*

Acknowledgements

First of all, I thank God the Father for His Love and for my Lord Jesus Christ, without Him nothing what I have done has any meaning.

I would like to thank my advisor, Dr. C. E. (Tommy) Thomas, for his guidance during this work. He gave me an opportunity to work on this interesting project in a great scientific environment. He was always there even in the late night or the weekend, when I lost direction in the middle of scientific, technical, and even cultural darkness. Certainly, without him I could not have completed this work. I also wish to thank Drs. Bill Stacey, John Mandrekas, Andy Zangwill, and Dick Colchin for serving as committee members.

Since most of the work was performed on the Advanced Toroidal Facility (ATF) at the Oak Ridge National Laboratory, I am greatly indebted to the Laboratory and the members of the ATF and RF group, whose support was the most invaluable gift that I could have imagined. In particular, I wish to thank Drs. Julian Dunlap, David Swain, and Dan Hoffman for their hospitality and encouragement during my stay at ORNL.

I am grateful to Dr. Rick Goulding for his guidance during the early periods of the experiment when I had no idea how this experiment would run. He provided me the basic knowledge that an experimental RF physicist should know from Smith charts to how to do antenna conditioning. I wish to thank Dr. Tom Shepard for his guidance during the period of the RF heating experiments. He always answered my elementary questions about ICRH in a simple and imaginative way. It was a delightful experience when we spent several days and nights looking together for a solution to RF-leakage and performing extensive antenna conditioning.

Important contributions came from some of the staff members in the ATF and RF group. Dr. Dick Colchin and my fellow graduate student, Mickey Wade deserve a special thanks for providing the neutral particle analyzer (NPA) data and for enlightening discussions and valuable comments on the analysis of the data. I would like to thank Drs. Ralph Isler, Charlie Crume, Lorne Horton, Tanner Uckan, Shinji Hiroe, John Bell, Gary Bell, Bill Wing, Al England, and Dave Rasmussen for freely providing data from various diagnostics for which they were responsible, and for quick answers to my requests. These experiments were made possible by the dedicated efforts of the ATF operations group, and I am very grateful to Dr. John Glowienka and Jack Yarber, Tim Bigelow, Chuck Schaich, and Terrel Patrick. I also wish to thank Dr. Massanori Murakami for his interest in ICRH and his help in scheduling dedicated experimental time.

Data analysis has benefitted from the contributions of and discussions with many scientists in the Theory group. I am grateful to Dr. Fred Jaeger for allowing me to use his 2-D RF heating code and for spending time with me so that I might understand the algorithm and use it properly. Drs. Don Batchelor, Lou Hedrick, Nicholas Dominguez, Phil Ryan, and Mark Carter have always been willing to discuss many topics that I brought in. I especially wish to thank Dr. Mark Carter for providing his Fokker-Planck code, Dr. Ron Fowler for an ATF-orbit following code, Dr. Doug Lee for the code for calculating the ATF vacuum magnetic field, and fellow graduate student, Scott Painter for a Monte Carlo orbit code. The computing scheme and aspects were discussed with Dr. Bill Wing and Dave Giles, whose help is gratefully acknowledged.

Excellent technical support was provided by Glenn Barber and Dennis Sparks for the RF transmitter, and Chuck Schaich for vacuum techniques and leak testing. Also I wish to thank the electricians and research mechanics especially, Gene Purdy, and T. Muhammed for fabricating the probes and associated electrical and electronic

systems under the direction of Alex Gabbard and Jack Yarber.

I would like to thank several people here who had a profound effect on the direction of my study, Professors K. H. Chung and Prof. S. H. Hong in the Seoul National University, who opened my eyes to plasma physics and fusion research when I was an undergraduate and Professor Bill Stacey who continued this work when I was a graduate student. I also wish to thank Dr. G. S. Lee (presently at MIT) for fascinating discussions on physics, from which I formed a rough outline of what I was doing.

Finally, I thank my parents and parents-in-law for their love, encouragement, and support. I am especially indebted to my wife, Mee, for her love and understanding for the last six years, and for caring for our little daughter, Heidi. This work would not have been possible without her patience and undying support.

Table of Contents

Acknowledgements	ii
Table of Contents	v
List of Tables	viii
List of Figures	ix
Summary	xiv
I. INTRODUCTION	1
Background	1
Motivation	5
Outline of Thesis	6
References	9
II. INTRODUCTION TO ICRH	11
Background	12
Cold Plasma Wave Theory	16
Effect of the Boundary	25
Effect of the Thermal Motion	28
Wave Absorption	35
Wave Thermalization	40
Effect of the Helical Geometry	44
Numerical Simulation of ICRH in a Helical System	46

ICRH Experiments	52
Early Experiments	52
Tokamak Experiments	54
Recent ICRH Experiments	58
ICRH in Helical Devices	61
References	65
III.EXPERIMENTAL APPARATUS	72
The Advanced Toroidal Facility	72
The Fast Wave Antenna	76
Mechanical Design	77
Electrical Properties	78
Loading Calculations	88
RF System	91
Description of the RF Transmitter	91
RF System Operation	93
Edge Probes	95
Theoretical Considerations	96
Applications of Probe Measurements to ICRH Experiments on ATF .	110
Experimental Considerations	112
The ATF Data Acquisition System	117
ATF Data System	117
ICRH Data System	118
References	121
IV.EXPERIMENTAL OBSERVATIONS	124
Wall Conditioning and ECH Target Plasma	124
Wall conditioning in ATF	124

ECH Target Plasmas and Changes During ICRH	128
Loading Measurements	131
Spectroscopic Measurements	137
The Neutral Particle Analyzer Measurements	146
Edge Probe Measurements	157
Langmuir Probe Measurements	157
RF Probe Measurements	161
Summary	168
References	169
V. DATA ANALYSIS AND DISCUSSION	171
Simulation With a 2-D RF Heating Code	172
RF/Edge Interaction	184
Fast Ion Studies	190
Power Balance Calculations	206
References	218
VI. CONCLUSIONS	221
Summary and Conclusions	221
Prospects for Future Experiments on ATF	225
Future Work	233
References	236
APPENDIX	237
References	243

Vita

List of Tables

2.1	ATF Simulation Parameters	51
2.2	Heating Result in TFR	56
2.3	General Changes in Edge Plasmas during ICRH	59
3.1	ATF Machine Parameters	73
3.2	Antenna Model Parameters	80
3.3	Probe Location	111
3.4	ICRF Data Signals	119
4.1	ATF Parameter	129
5.1	Typical Input Parameters for Simulation	172
5.2	Input Parameters for <i>RFTRANS</i>	213
6.1	Input Parameters for Simulation	228

List of Figures

2.1	RF-Plasma Interaction	12
2.2	CMA diagram	22
2.3	Cold Plasma Dispersion Relation	23
2.4	Hot plasma dispersion relation	34
2.5	Minority ion distribution function	43
2.6	Helical Magnetic Geometry	45
2.7	Helical Symmetry	47
2.8	ATF Magnetic Geometry	48
2.9	ATF Dispersion Relation	50
2.10	Magnetic beach	53
3.1	Top View of the ATF	74
3.2	The ATF Coil Sets	75
3.3	The Fast Wave Antenna	76
3.4	Antenna Installation	78
3.5	The ATF Antenna Model	79
3.6	Modelling Results	84
3.7	Modelling Results	85
3.8	Loading vs. Capacitances	86
3.9	Power Handling Capability	87

3.10 VSWR vs Frequency	88
3.11 Offsets in Loading Measurements	90
3.12 Offset Correction	91
3.13 RF Transmitter	92
3.14 The ATF RF System	94
3.15 Circuit Model for the RF Probe	96
3.16 RF Probe	98
3.17 Sensitivity of the RF Probe	101
3.18 RF Probe Modeling	102
3.19 Langmuir Probe Operating Regime	103
3.20 I.V Characteristic Curve	108
3.21 RF Effect on the Probe Characteristics	108
3.22 Time-Averaged Characteristics	110
3.23 Probe Installation	112
3.24 Damaged Magnetic Probe	113
3.25 RF Probe Circuit	114
3.26 Langmuir Probe Circuit	115
3.27 Probe Positioning Circuit	116
3.28 ATF Data Acquisition System	118
3.29 ICRH Data Acquisition System	120
4.1 Antenna Conditioning	126
4.2 Effects of Gettering	127

4.3	ATF ICRH Evolution	128
4.4	Steady-Density Shot	130
4.5	Rising Density Shot	132
4.6	Density Drop	133
4.7	Density Dependence of Antenna Loading	134
4.8	Frequency Dependence of Loading	134
4.9	Frequency Dependence of Loading	135
4.10	Spectroscopic Signals	139
4.11	The Edge Cooling Effect	139
4.12	Radiated Power	140
4.13	RF Induced Sputtering	141
4.14	RF Heating Effectiveness	142
4.15	Fast Ion Distribution	143
4.16	CII Line Emission	144
4.17	Ion Temperature Measurement	145
4.18	Z_{eff} Change	146
4.19	Fast Ion Tail	147
4.20	Power Dependence of Fast Ion Tail	148
4.21	Minority Concentration Dependence of Tail	149
4.22	Hybrid Resonance Layer	150
4.23	Antenna Stripes	151
4.24	Minority Ion Tail vs Frequency	152
4.25	Fast Ion Tail in Shifted-in Plasma	153

4.26 NPA Scan Data	154
4.27 NPA Measured Ion Temperature	155
4.28 Fast Ion Tail	156
4.29 Langmuir Probe Signal Response	158
4.30 Edge Probe Measurement	160
4.31 Radial Profile	161
4.32 Magnetic Probe Measurements	162
4.33 Eigenmode Observation	164
4.34 Radial Profile of Frequency Spectrum	165
4.35 Frequency Spectrum	166
4.36 Frequency Spectrum	167
5.1 Dispersion Relation	173
5.2 Resonance Layers	174
5.3 Field Profile	176
5.4 $k_{ }$ Spectrum	177
5.5 Antenna Spectrum	178
5.6 Electric Field Profile	179
5.7 Loading vs Density	180
5.8 Loading vs Frequency	181
5.9 Flux Surface Averaged Absorbed Power	182
5.10 Energy Accounting	186
5.11 Radial Probe Translation	187

5.12 Phase vs. Poloidal Location of the RF Probe	188
5.13 Calculated Poloidal Eigenmodes Numbers Compared with the Experimental Data	189
5.14 Particle Loss Rate	192
5.15 Particle Confinement in ATF	195
5.16 Minimum-B Contours	196
5.17 RF Effects on Particle Orbit I	199
5.18 RF Effects on Particle Orbit II	200
5.19 RF Effects on Particle Orbit III	201
5.20 Resonance Layer	205
5.21 Loss Cone Definition	214
5.22 Fokker-Planck Calculation I	216
5.23 Fokker-Planck Calculation I	217
6.1 High Density Simulation	229
6.2 High Density Simulation	230
6.3 Fokker-Planck Calculation II	231
6.4 Fokker-Planck Calculation II	232
6.5 Antenna Spectrum for Modified Antenna	234
6.6 Illustration of Current Distribution	238

Summary

Fast wave ICRF heating experiments were performed on the low density ($\bar{n}_e \leq 0.8 \times 10^{13} \text{ cm}^{-3}$) ECH target plasma in the Advanced Toroidal Facility (ATF). Various heating regimes were investigated in the frequency ranges between 9.2 MHz and 28.8 MHz with magnetic fields of 0.95 T and 1.9 T on axis. The purposes of these experiments was to study the compatibility of ICRF with stellarator geometry and characterize RF-induced effects. No bulk heating was observed in any of the low density experiments.

Loading measurements were performed as a function of the frequency, the plasma density, the gap between the plasma and the current strap, and the RF power. In the hydrogen minority regime, large suprathermal ion tails were observed by the neutral particle analyzer (NPA). Data from spectroscopy and the edge RF and Langmuir probes was used to characterize the RF-induced effects on the low density ATF plasma.

A 2-D RF heating code and a Fokker-Planck code *RFTRANS* were used to simulate these low-density experiments. The simulations were in good agreement with the experimental observations. An analysis was carried out to compare with the edge probe measurements and for the confinement of the RF-generated fast ions. A power balance analysis was performed using *RFTRANS* with simple ATF plasma and RF heating models.

The simulations showed that no bulk heating was observed because the antenna design had been optimized for higher densities, so that the ICRH modes excited were dominated by edge modes. This led to strong RF/edge interaction, poor penetration to the plasma center, and heating of minority ions on unconfined orbits.

Finally, a prediction of performance for future high-power, higher-density experiments in ATF demonstrated good performance in terms of bulk heating and fast-ion confinement. It was also demonstrated that minor modifications to the existing antenna could lead to excitation of centrally penetrating modes at lower densities, so that ICRH bulk heating at lower densities might also be possible.

CHAPTER I

INTRODUCTION

Background

Toroidal devices are the most advanced option for achieving a demonstration of scientific and engineering feasibility of controlled thermonuclear fusion.

In order to achieve the desired goal of net energy yield from a controlled fusion reaction, the plasma must be heated to a sufficient temperature and the confinement time (defined as the rate at which energy escapes from the plasma) must be large enough. In a tokamak plasma, the ohmically-induced current is normally used for providing both a poloidal component of the magnetic field, which is a necessary component for a stable equilibrium, and for plasma heating. However, it is known that ohmic heating can not provide enough power¹. In a high temperature plasma, the conductivity of the plasma increases and the efficiency of ohmic heating consequently decreases with increasing temperature. Also the maximum toroidal current in a tokamak is limited by the onset of MHD instabilities. Therefore, various forms of auxiliary heating have been pursued to obtain ignition temperatures without degradation of plasma confinement. In currentless devices such as the Advanced Toroidal

¹However, there has been a design study for a purely ohmically ignited reactor called IGNITEX [1].

Facility (ATF) or Heliotron-E stellarators, auxiliary heating is necessary to increase plasma parameters to achieve the designed operational state, which is not provided by the plasma initiation method — electron cyclotron heating (ECH) for the ATF and the Heliotron-E devices. To maintain an advantage over the tokamak configuration (i.e., steady-state operation) a long-pulse (not necessarily a steady-state) heating system is desirable for stellarators.

The use of electromagnetic waves at the ion cyclotron frequency is attractive because the physics has been relatively well explored theoretically, it has shown good heating results in several preliminary experiments, and shows great promise to satisfy the technical demands for future high power heating systems. The ions in a confined magnetic field precess around the field line (the cyclotron motion) at their cyclotron frequencies. The basic idea is to heat these ions by exciting electric fields in the plasma which are circularly polarized in the same sense as the ion motion, and with proper phase and frequency.

In the late 1950s, ion cyclotron resonance heating (ICRH) was first proposed as a plasma heating scheme. The slow wave (ion cyclotron wave) and “magnetic beach” concept [2] was proposed. In cold plasma theory two electromagnetic wave branches exist which propagate in the ion cyclotron range of frequency: the so-called slow and fast wave branches. The slow wave propagates at frequencies below the ion cyclotron frequency along the magnetic field line and has a resonance at the ion cyclotron frequency. Another characteristic of this branch is that the electric field of the slow wave is completely left circularly polarized in the same sense as the ion and at the ion cyclotron frequency. In the first attempt to use this branch, slow waves were launched in a region of higher magnetic field where the excitation frequency was less than the ion cyclotron frequency. Then the wave propagated into a “magnetic beach” region where the magnetic field decreased to the point where the ion cyclotron frequency was close to the wave frequency. Wave energy was absorbed

by the plasma through cyclotron damping. This scheme was also used in Heliotron-E ICRH experiments [3] and showed good results. However accessibility was limited to low density plasma regions.

When tokamak geometry appeared as a promising option, the magnetic field line configuration of tokamaks required wave propagation across the field lines. In the 1970s the other propagating branch, the fast wave, was actively examined in tokamak geometry, even though the polarization of its electric field is not in the same sense as the ion motion. That is, fundamental cyclotron heating is not effective for the fast wave branch. Several other heating schemes were proposed [4,5,6,7,8,9], e.g. second harmonic heating, minority heating, and ion-ion hybrid heating. Cyclotron damping allowed by relaxed polarization requirements due to thermal effects was supposed to be the dominant process for dissipation of the wave energy.

In the middle of the 1970s as hot plasma effects were actively studied, it was found that including thermal effects introduces the so-called mode conversion process [10,11,12], in which the wave energy of the fast wave is converted to an electrostatic thermal wave (ion Bernstein wave) which is heavily damped via electron Landau damping. In the sense that mode conversion is closely related to the existence of a minority species and it is very difficult to obtain plasmas with a single ion species, mode conversion is always present in ICRH experiments. Generally speaking, hot plasma effects have to be understood very precisely to find effective heating regimes for ICRH.

In the 1980s, high power (≥ 1 MW) ICRH experiments were started in major tokamaks [13,14,15] (e.g., TFR600, PLT, JFT-2M, etc.) and showed good bulk ion heating results in various heating regimes. However confinement degradation due to ICRH caused great concern over whether it would be possible to achieve ignition. The so-called H-mode (high confinement regime) operation found in divertor tokamaks with neutral beam injection (NBI) provided a way to overcome this problem.

In 1986, the ASDEX team [16] reported promising results: H-mode operation with ICRH alone was achieved. Moreover, in 1989 the JET team [17] achieved $Q_{D-D} \simeq 0.8$ (effective ratio of fusion power out to fusion power in, if DT fuel were used) mainly with ICRH heating.

Although the scientific feasibility of ICRH was first tested in the stellarator geometry, after introduction of the tokamak concept, the study in stellarators was limited to a few small machines. ICRH experiments with the stellarator geometry were also limited to low power levels and were without variety. Plasma initiation by ICRF and also heating experiments were performed in the USSR and the United States in the 1970s and the early 1980s. In the mid-1980s, several new stellarators were built around the world and extensive ICRH experiments were begun in new machines such as Heliotron-E in Japan. These experiments showed good heating results, comparable to results from similar-sized tokamaks.

However, at the present time there are still many unexplained phenomena in ICRH experiments and limited agreement with theory. In several small tokamaks, bulk ion heating failed and anomalous loading was observed [18]. Strong radiation emission and uncertainty about RF/edge interaction have also been concerns. Nonlinear phenomena such as parametric coupling and ponderomotive effects are expected to play an important role in coupling [19,20]. In stellarators, RF-induced fast ion confinement has not been clearly addressed. Also whether the techniques used in tokamaks (such as fast-wave heating) are relevant to the exotic magnetic geometry of stellarators has not been fully examined.

At the present time[21], high power ICRH experiments are being done or will be performed on other tokamaks such as JET, TFTR, JT-60, D-IIID, Tore Supra, C-Mod and on helical devices such as ATF, Heliotron-E, CHS and the future Large Helical Device (LHD). Even the Compact Ignition Tokamak (CIT) and the International Thermonuclear Experimental Reactor (ITER) are being designed with ICRH

as the only auxiliary heating system.

Motivation

ICRH has been chosen as one of the major heating systems or plasma initiation techniques for stellarators since the 1950s. However, there are still many things which are not understood.

The fast-wave branch must be tested in stellarators because the slow wave is not effective in high density plasmas and the antenna for the slow wave would have to be located on the high-field side, which causes technical difficulties. The Heliotron-E stellarator used both wave branches in ICRH experiments with a high-field side launch. The ATF experiments presented further on in this document were unique in this regard because the antenna was located on the low-field side and only the fast wave branch was used.

The antenna used on ATF, a Resonant Double Loop (RDL), was unique compared to other antennas used in stellarators, even though it was tested and widely accepted in such tokamaks as DIII-D, Tore Supra and TFTR. It must be determined whether the techniques used for tokamaks are relevant to the exotic magnetic geometry and edge conditions of stellarators.

The ATF was fully-equipped with state-of-the-art diagnostics and auxiliary systems. Hence ATF provided a unique opportunity to characterize RF-induced effects with excellent diagnostics.

Heating efficiency was found to be as good as that in tokamaks and excellent bulk heating was demonstrated in Heliotron-E. Theoretical calculations also provided fairly good agreement with the experimental results for this device. However, some important issues have not been addressed in stellarators: RF-generated fast ion con-

finement (i.e., minority heating schemes), RF/edge interactions, and effects of the complex magnetic boundary (last closed flux surface and divertor stripe).

The present study was performed with modest RF power (~ 200 kW) in a relatively low density ($\bar{n}_e \leq 0.8 \times 10^{13} \text{ cm}^{-3}$) regime. This work provides a useful database for future high-power ICRH operation. The most important issues considered in this study were, therefore, the compatibility of ICRH with the ATF magnetic configuration, characterization of RF-induced effects, fast ion confinement, and RF power balance.

This work was the first step toward future high-power experiments in high-density ATF plasmas with a full range of diagnostics. The main emphasis of the dissertation was on careful analysis of experimental data, improving numerical modeling by careful comparison to the analyzed data, and predicting the performance of future high-power experiments in high-density ATF plasmas.

Outline of Thesis

The material presented following this chapter and its order are as follows. ICRH physics is reviewed in Chapter II. The cold plasma wave theory, wave absorption, and thermalization are presented. The thermal effects of a plasma on wave propagation and absorption are studied by means of the hot plasma dielectric tensor. Some effects of the helical geometry on the ICRH physics are studied. An example of numerical calculations is presented. This is followed by a survey of ICRH experiments from the beginning in the B-65 stellarator at Princeton to the high power ICRH experiment on JET in Europe. Changes in the heating scheme are traced and the overall results are compared between different schemes. Recent experiments on Heliotron-E are described in detail because it showed succesful heating results for the

first time in a stellarator geometry.

Chapter III describes the experimental apparatus starting with a brief introduction to the ATF and its diagnostics. The design features of the RDL-type fast-wave antenna and the RF transmitter are outlined, and the operation of the whole RF system is described. Details of the RF and Langmuir probes, which were specially designed for this study are presented along with their features, electronics and calibration results. A description of the ATF data acquisition system and the data flow is also provided.

Experimental data are presented in Chapter IV. The plasma loading was examined as a function of the frequency, the plasma density, gap between the last closed flux surface (LCFS) and the current strap, and the RF power. Data measured by spectrometers during the RF was used to study some RF-induced effects. The neutral particle analyzer (NPA) was used extensively in these experiments. It was used for the study of RF-induced fast ions and associated topics. The three RF probes and a Langmuir probe were used for investigating changes in the edge plasma² conditions during the RF.

In Chapter V, analysis with numerical tools and analysis and discussion of the experimental data are provided. The important issues mentioned previously are revisited for evaluation of the initial ICRH experiments on ATF. A 2-D RF heating code was used for simulation of the low density ICRH experiments. The changes in the edge plasma conditions were analyzed from the spectroscopic data and edge probe measurements. The directly edge-deposited RF energy was calculated from Langmuir probe measurements. A study of fast ions generated by the RF was performed by

²Throughout this thesis, the term "edge plasma" refers to the region between the last closed flux surface (LCFS) and the wall and the term "plasma edge" refers to the outer region of the confined plasma column

analyzing the NPA data along with investigations of the time scales of various fast ion loss channels, the loss cone in ATF plasmas, and effects of the RF on the various particle orbits. A simple RF power balance analysis was performed using a Fokker-Planck analysis code, *RFTRANS* with a simple ATF plasma model.

A summary of and conclusions drawn from the experiments are given in Chapter VI. In addition predictions for future high-power, high-density ICRH experiments are presented. These predictions were made using the 2-D RF heating code and *RFTRANS* Fokker-Planck code, which successfully simulated the low-density experiments in ATF. Finally, some suggestions for future work are presented.

In the Appendix, a derivation of the Fourier representation of the antenna spectrum (including side-wall image currents) which was used in the 2-D RF heating code is presented.

REFERENCES

- [1] Rosenbluth, M. N., Weldon, W. F., and Woodson, H. H., "Basic Design Report of the Fusion Ignition Experiment (IGNITEX)," Report, Center for Fusion Engineering, The University of Texas at Austin, 1987.
- [2] Stix, T. H. et al., in Proc. of 2nd Inter. Conf. on the Peaceful Uses of Atomic Energy, Vol. 31, 282 (U.N., Geneva, 1958).
- [3] Mutoh, T., et al., "ICRF Heating of Currentless Plasma in Heliotron-E", Proc. of the 11th International Conf. on Plasma Physics and Controlled Nuclear Fusion Research, Kyoto, IAEA-CN-47/D-III-2, 1986.
- [4] Adam, J., et al., EUR-CEA-FC-579, 29 (1971).
- [5] Klima, R., *Nucl. Fusion* **11**, 357 (1971).
- [6] Lashmore-Davies, C. N., et al., *Phys. Fluids* **15**, 1616 (1972).
- [7] Canobbio, E., *Nucl. Fusion* **12**, 561 (1972).
- [8] Brambilla, M., et al., *Nucl. Fusion* **12**, 199 (1972).
- [9] Weynants, R. R., *Phys. Rev. Lett.* **33**, 78 (1974).
- [10] Stix, T. H., *Phys. Rev. Lett.* **15**, 878 (1965).
- [11] Swanson, D. G., et al., *Phys. Rev. Lett.* **35**, 517 (1975).
- [12] Perkins, F. W., *Nucl. Fusion* **17**, 1197 (1977).
- [13] Hosea, J., et al., PPPL-2117, PPPL, Princeton University (1984).

- [14] Equipe TFR, IAEA-CN-41/I-2 (9th Conf. Proc. on Plasma Physics and Controlled Nuclear Fusion Research, Baltimore, 1982).
- [15] JFT-2 Group, IAEA-CN-44/F-1-3 (10th Conf. Proc. on Plasma Physics and Controlled Nuclear Fusion Research, London, 1984).
- [16] Steinmetz, K., et al., *Phys. Rev. Lett.* **58**, 124 (1987).
- [17] The JET team announced that they achieved $Q_{D-D} \sim 0.8$ in the late 1989 with RF+NBI+pellet. Refer the JET papers reported to the 1989 American Physical Society meeting. (*Bull. Am. Phys. Soc.* **34**, 1989)
- [18] Taylor, R. J., et al., Heating in Toroidal Plasmas(Proc. 2nd joint Grenoble-Varenna International Symposium, Villa Olmo, Italy) Vol. 1, 509 (1980).
- [19] Myra, J. R., et al., *Phys. Rev. Lett.* **53**, 914 (1984).
- [20] Skiff, F., et al., *Phys. Fluids* **27**, 105 (1984).
- [21] The new results from the large machines and the design study for the future machine are found in the recent proceedings of the European Physical Society meeting, IAEA meeting and *Bull. Am. Phys. Soc.* **34** for the American Physical Society meeting.

CHAPTER II

INTRODUCTION TO ICRH

The expression "Ion Cyclotron Resonance Heating (ICRH)" reflects the physical concepts of this process. First of all, "ion heating" implies the consequence of this process and "cyclotron resonance" describes the mechanism behind this physical process. It also contains the term "cyclotron", which implies that the cyclotron motion of a particle in a magnetic field is involved. If another descriptive term "Ion-Cyclotron-Range-of-Frequency (ICRF) Wave Heating" is used, it is immediately obvious that this process involves wave-plasma interaction and energy transfer between the two. Therefore to understand this physical process, the behavior of the wave (electrostatic or electromagnetic) in the plasma medium (with strong magnetic field for fusion plasmas) should be understood.

Since there exist many types of wave-plasma interactions in a plasma, reviewing all of plasma wave physics would require a tremendous effort and is not justified in a report of RF experiments using one or two branches out of all the available wave modes. Thus a simple model giving general characteristics applicable to any kind of plasma-wave interaction is described and emphasis is given to a specific wave mode used in the experiments described in this thesis - the ICRF fast wave.

In the first section, some basic characteristics of the interaction between a plasma and an electrostatic or electromagnetic wave are discussed, then the subsequent sections are dedicated to detailed explanation of a simple model. Some important re-

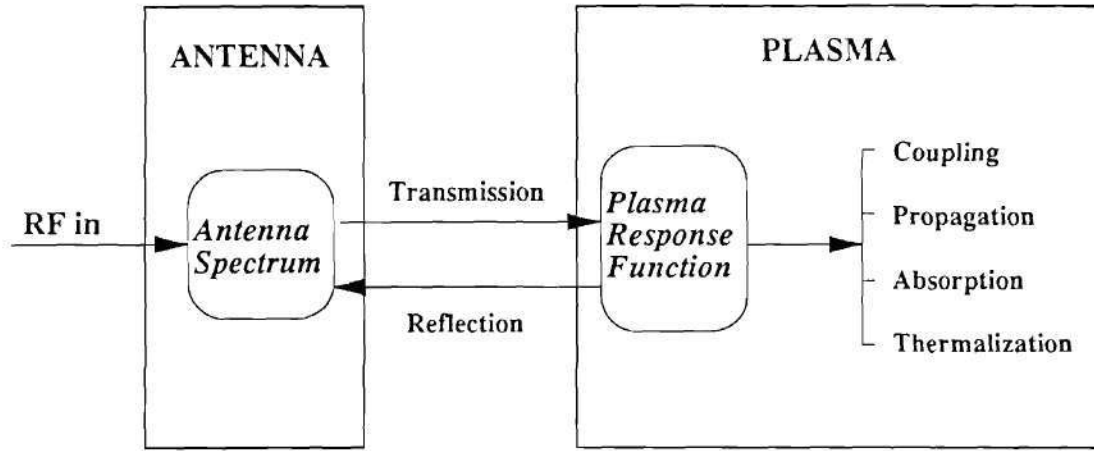


Figure 2.1: Diagram of the Effect of ICRH on the Confined Plasma System

laxations of the constraints of the model are attempted.

In the final section a survey of other ICRH experiments is given to illustrate how theoretical predictions were proven in experiments and how these experimental results affected the understanding and developments of ICRH physics.

Background

Even though there are many channels of plasma-wave interactions and varieties of wave modes, a few specific branches are emphasized for fusion applications. The major branches are the wave modes used for heating and current drive. Since the topic of this thesis is RF heating, most other wave-plasma interactions are less emphasized or omitted. Figure 2.1 shows a simple diagram of RF wave heating on a confined plasma system. A wave generated from an external source is transmitted to the

proper type of launcher, and the transmitted wave energy is transferred to the plasma medium via coupling, propagation, and absorption processes. Assuming a closed system including the launcher and plasma, the external energy flux transmitted into the plasma is conserved. The launcher and the medium are connected by the antenna spectrum and plasma response function to the externally excited wave, which affects the launcher spectrum. Therefore, this closed system should be considered in a self-consistent manner, and those two connection links (launcher spectrum, plasma response function) should be accurately known to understand the dynamics of the system.

The Maxwell equations for a macroscopic medium are the starting point.

$$\nabla \times \vec{E} = -\frac{\partial \vec{B}}{\partial t}, \quad (2.1)$$

$$\nabla \times \vec{H} = \vec{J} + \frac{\partial \vec{D}}{\partial t}, \quad (2.2)$$

$$\nabla \cdot \vec{B} = 0, \quad (2.3)$$

$$\nabla \cdot \vec{D} = \rho. \quad (2.4)$$

where \vec{E} is the electric field intensity, \vec{D} is the electric displacement vector defined as $\vec{D} = \epsilon \vec{E}$, \vec{B} is the magnetic induction and \vec{H} is the magnetic intensity related to \vec{B} as $\vec{B} = \mu \vec{H}$. Here ϵ and μ are scalar dielectric permittivity and the magnetic permeability, respectively. Also \vec{J} is the current density and ρ is the electrical charge density, which are related by the continuity equation as

$$\nabla \cdot \vec{J} + \frac{\partial \rho}{\partial t} = 0. \quad (2.5)$$

Throughout this work, SI units are used and all variables in the above equations are functions of space and time.

Since Eqs.(2.1) through (2.5) are described macroscopically, the medium should be well understood. If the medium is *conductive* like a plasma, conductivity σ is

defined as

$$\vec{J} = \sigma \vec{E}. \quad (2.6)$$

If the medium is *isotropic*, all the quantities which describe the physical properties of the medium such as ϵ , μ and σ are scalar quantities. But in an anisotropic medium, they are all tensor quantities denoted as ϵ , μ and σ , respectively. If the medium is *dielectric*,

$$\vec{D} = \epsilon_0 \vec{E} + \vec{P} \quad (2.7)$$

is defined where \vec{P} is the electric polarization:

$$\vec{P} = \epsilon_0 \chi \cdot \vec{E}, \quad (2.8)$$

where χ is the susceptibility of the medium. Therefore

$$\epsilon = \epsilon_0 (\mathbf{I} + \chi), \quad (2.9)$$

where \mathbf{I} is the unit tensor. Another important characteristic of a medium is *dispersion*. This means that the dielectric property which determines the response of the medium to the wave fields are a function of frequency. In other words, the response to the wave depends on the time variation of the fields. This is a consequence of temporally non-local connection between \vec{D} and \vec{E} [1,2], represented by

$$\vec{D}(\vec{x}, t) = \vec{E}(\vec{x}, t) + \int_{-\infty}^{\infty} G(\tau) \vec{E}(\vec{x}, t - \tau) d\tau, \quad (2.10)$$

where

$$G(\tau) = \frac{1}{2\pi} \int_{-\infty}^{\infty} [\epsilon(\omega) - 1] e^{-i\omega\tau} d\omega. \quad (2.11)$$

The plasma medium is conductive and dielectric as well. This property is related to the current which can be incorporated into the dielectric permittivity. From Eq.(2.2),

$$\vec{D} = \epsilon_0 \vec{E} - \frac{\vec{J}}{i\omega} = (\epsilon_0 - \frac{\sigma}{i\omega}) \vec{E}, \quad (2.12)$$

where the effective dielectric permittivity is defined as

$$\epsilon = \epsilon_0 - \frac{\sigma}{i\omega}. \quad (2.13)$$

A similar expression can be obtained for an anisotropic plasma medium in which the effective dielectric permittivity is a tensor. Therefore, in a plasma medium, the dispersion relation for a certain wave mode can be obtained by using this dielectric property (permittivity) of a plasma. This can be done by considering the plasma current as a displacement current and incorporating it into the effective dielectric tensor.

Since RF heating is considered a supplemental source for plasma heating, it must work very well when the primary source, ohmic heating, loses its efficiency in highly conductive plasma conditions. In this case, the E_{\parallel} -mode which propagates parallel to the magnetic field line is shorted out due to electron mobility along the magnetic field line. Thus in a highly conductive plasma the E_{\perp} -mode should be used for efficient wave propagation. For this reason, in ICRH the E_{\perp} -mode is used while the E_{\parallel} -mode is shorted out by a Faraday shield. Since the E_{\parallel} -mode does not penetrate into the plasma if it is not fully screened out, edge heating close to the Faraday shield might occur. This topic is being actively studied in a series of workshops [3]. The E_{\perp} -mode (electric field transverse to the magnetic field line) can be either an electrostatic mode ($\vec{E} \times \vec{k} = 0$) or an electromagnetic mode ($\vec{E} \times \vec{k} \neq 0$). Both modes are used for ICRH experiments.

The *thermal motion* of a plasma also affects RF wave heating. This gives more variety to the RF heating physics because it changes the plasma response function in a rather complicated way. One example is the Doppler broadening of the resonance layer given as

$$\omega - k_{\parallel}v_{\parallel} - n\Omega_i = 0, \quad (2.14)$$

where the ion cyclotron frequency is

$$\Omega_i = \frac{z_i e B}{m_i}. \quad (2.15)$$

This well-known expression describes some important wave damping mechanisms. If $n = 0$, Landau damping and transit-time damping are expected, and $n = 1$ is the condition for fundamental cyclotron damping with $|E_+|$ not equal to zero (even in a homogeneous medium) due to the extra term, $k_{\parallel} v_{\parallel}$. For $n \geq 2$, higher harmonic damping could occur. The details of these effects will be discussed in subsequent sections.

Inhomogeneities of the medium also play a significant role. Mode conversion is a good example. As the plasma propagates through density, temperature, or magnetic field gradients, it can hit resonances or cutoffs, where mode conversion often occurs. Finite boundaries lead to the appearance of discrete eigenmodes. An elementary treatment will be presented in later sections.

Cold Plasma Wave Theory

In this section the physics behind wave propagation and absorption will be approached by examining a simple model which provides surprisingly valuable insight into the theory. This is the cold plasma model in which the “cold” means that the electrons and ions have *no thermal velocities except as they are induced to move by the electric and magnetic fields of the wave*. The plasma medium is assumed infinite and homogeneous. In later sections, these limitations are discussed. A slab geometry is used in which the unperturbed magnetic field is in the z -direction and the wave only propagates in the $x - z$ plane; therefore $k_y = 0$.

To obtain the cold plasma dielectric tensor, \mathbf{K} , the plasma current must be calculated. If the two-fluid equations are used for the electronic and ionic components

of the plasma, then

$$\frac{d\vec{v}_k}{dt} = \frac{q_k}{m_k} \left\{ \vec{E} + \vec{v}_k \times \vec{B}_0 \right\}, \quad (2.16)$$

where \vec{B}_0 is the DC magnetic field and,

$$\frac{d}{dt} = \frac{\partial}{\partial t} + (\vec{v}_k \cdot \nabla). \quad (2.17)$$

The electric field strength \vec{E} and magnetic field strength \vec{B} of the wave are determined from Maxwell equations,

$$\begin{aligned} \nabla \times \vec{E} &= -\frac{\partial \vec{B}}{\partial t}, \\ \nabla \times \vec{B} &= \mu_0 \left(\epsilon_0 \frac{\partial \vec{E}}{\partial t} + \vec{J} \right), \end{aligned} \quad (2.18)$$

and \vec{J} can be represented by

$$\vec{J} = \sum_k q_k n_k \vec{v}_k. \quad (2.19)$$

Assuming that in the equilibrium state $n_e = n_i = n_0$, $\vec{v}_{k,0} = \vec{E}_0 = 0$, then Eq.(2.16) can be linearized,

$$\frac{\partial \vec{v}_{k,1}}{\partial t} = \frac{q_k}{m_k} \left\{ \vec{E}_1 + \vec{v}_{k,1} \times \vec{B}_0 \right\}. \quad (2.20)$$

Also assuming first order perturbations in a homogeneous plasma, and that all variable terms are proportional to $\exp \{i(\vec{k} \cdot \vec{r} - \omega t)\}$ (the plane wave monochromatic solution), then the fields can be expressed as:

$$\begin{aligned} \vec{E} &= |\vec{E}_1| \exp [i(\vec{k} \cdot \vec{r} - \omega t)], \\ \vec{B} &= \vec{B}_0 + |\vec{B}_1| \exp [i(\vec{k} \cdot \vec{r} - \omega t)], \\ \vec{v} &= |\vec{v}_1| \exp [i(\vec{k} \cdot \vec{r} - \omega t)], \end{aligned} \quad (2.21)$$

where the subscript 0 indicates an unperturbed quantity and 1 indicates an RF induced perturbed quantity. The *plane* means that the wave fronts (contours of constant phase) form a plane perpendicular to the direction of wave propagation, \vec{k} , and the *monochromatic* means that the field is a single frequency sinusoidal function of

the time. Therefore in a homogeneous plane wave the surfaces of constant amplitude are planes perpendicular to the direction of wave propagation. Then from Eq. (2.20)

$$-i\omega\vec{v}_{k,1} = \frac{q_k}{m_k} \left\{ \vec{E}_1 + \vec{v}_{k,1} \times \vec{B}_0 \right\}. \quad (2.22)$$

The velocity components of the particles of the k -th kind are obtained:

$$\begin{aligned} v_{k,x} &= \frac{q_k(i\omega E_x - \Omega_k E_k)}{m_k(\omega^2 - \Omega_k^2)}, \\ v_{k,y} &= \frac{q_k(i\omega E_y + \Omega_k E_x)}{m_k(\omega^2 - \Omega_k^2)}, \\ v_{k,z} &= \frac{iE_z\Omega_k}{\omega B_0}. \end{aligned} \quad (2.23)$$

By combining \vec{J} and the plasma displacement current such that

$$\vec{J} - i\omega\epsilon_0\vec{E} \simeq -i\omega\epsilon_0\mathbf{K} \cdot \vec{E},$$

the expression of the dielectric tensor can be obtained as

$$\mathbf{K} = \begin{pmatrix} K_{\perp} & -iK_{\times} & 0 \\ iK_{\times} & K_{\perp} & 0 \\ 0 & 0 & K_{\parallel} \end{pmatrix}, \quad (2.24)$$

where

$$K_{\perp} = S = 1 - \sum_k \frac{\omega_{p,k}^2}{\omega^2 - \Omega_k^2}, \quad (2.25)$$

$$K_{\times} = D = \sum_k \frac{\omega_{p,k}^2 \Omega_k}{\omega(\omega^2 - \Omega_k^2)}, \quad (2.26)$$

$$K_{\parallel} = P = 1 - \sum_k \frac{\omega_{p,k}^2}{\omega^2}, \quad (2.27)$$

$$R = S + D = 1 - \sum_k \frac{\omega_{p,k}^2}{\omega(\omega + \Omega_k)}, \quad (2.28)$$

$$L = S - D = 1 - \sum_k \frac{\omega_{p,k}^2}{\omega(\omega - \Omega_k)}, \quad (2.29)$$

where S, D, P, R and L are the well-known Stix notations, namely Sum, Difference, Plasma, Right and Left, respectively, and the plasma frequency of the particle of the k -th kind is

$$\omega_{p,k}^2 = \frac{n_k q_k^2}{m_k \epsilon_0}. \quad (2.30)$$

Therefore the cold plasma wave equation obtained from Eq. (2.1) through Eq. (2.5) becomes

$$\nabla \times \nabla \times \vec{E} = k_0^2 \mathbf{K} \cdot \vec{E}, \quad (2.31)$$

where

$$k_0^2 = \frac{\omega^2}{c^2}, \quad (2.32)$$

resulting in

$$\vec{n} \times \vec{n} \times \vec{E} + \mathbf{K} \cdot \vec{E} = 0, \quad (2.33)$$

where the index of refraction is defined as

$$\vec{n} = \frac{\vec{k}c}{\omega}. \quad (2.34)$$

Here, for $n^2 > 0$, the wave is propagating but for $n^2 < 0$, the wave is evanescent.

In the given geometry in which $\vec{B} = |B|\hat{z}$ and $k_y = 0$, the matrix form of Eq.(2.33) is

$$\begin{pmatrix} k_0^2 K_{\perp} - k_z^2 & k_0^2 K_{\times} & k_x k_z \\ -k_0^2 K_{\times} & k_0^2 K_{\perp} - k_x^2 - k_z^2 & 0 \\ k_x k_z & 0 & k_0^2 K_{\parallel} - k_x^2 \end{pmatrix} \begin{pmatrix} E_x \\ E_y \\ E_z \end{pmatrix} = 0. \quad (2.35)$$

Requiring that the determinant of the 3×3 matrix be zero for non-trivial solutions leads to the famous algebraic equation:

$$Ak_{\perp}^4 + Bk_{\perp}^2 + C = 0, \quad (2.36)$$

where

$$A = K_{\perp}, \quad (2.37)$$

$$B = k_z^2(K_{\perp} + K_{\parallel}) - k_0^2(K_{\perp}^2 + K_x^2 + K_{\parallel}K_{\perp}), \quad (2.38)$$

$$C = K_{\parallel}[(k_z^2 - k_0^2K_{\perp}) + k_0^4K_x^2]. \quad (2.39)$$

The dispersion relation can be obtained for an arbitrary angle θ between \vec{k} and \vec{B}_0 as,

$$\tan^2 \theta = -\frac{P(n^2 - R)(n^2 - L)}{(Sn^2 - RL)(n^2 - P)}. \quad (2.40)$$

For $\theta = 0$ ($k_{\perp} = 0$), the R -mode with $n^2 = R$ is a wave with right-hand circular polarization and the L -mode with $n^2 = L$ is a wave with left-hand circular polarization. For $\theta = \pi/2$ ($k_{\parallel} = 0$) the O -mode with $n^2 = P$ is an ordinary mode and X -mode with $n^2 = \frac{RL}{S}$ is an extraordinary mode. Here left-hand means the sense of the cyclotron motion of a positively charged particle. The dispersion relation for the O -mode is independent of the magnetic field and particles do not experience any effect of the magnetic field (this is also the dispersion relation for an unmagnetized plasma) while the X -mode has a rather complicated dispersion relation. These four modes are described in the CMA (Clemmow-Mullaly-Allis) diagram, which tabulates different solutions and their behavior at various angles and frequencies. The full description of this useful chart can be found in various textbooks [4,5,6]. A description of the specific modes used in ICRH experiments is given here.

The specific modes (which are the main subject of this chapter) for ICRH experiments have frequencies determined by the primary damping mechanism. For ion heating, an ion cyclotron frequency or a higher harmonic is usually used. Since the CMA diagram was tabulated only for cold plasma wave modes, hot plasma modes like the Bernstein wave are not included. The ion cyclotron wave (shear Alfvén wave) and the magnetosonic wave (compressional Alfvén wave) are two typical cold plasma modes, both of which were expected to be damped at Ω_i until the polarization was

examined. In early ICRH experiments using a “magnetic beach” geometry, ion cyclotron waves were launched from the high magnetic field side of the torus, parallel to the magnetic field. But in the CMA diagram as shown in Fig. 2.2, in region 13 near $L = \infty$, it was difficult to tell whether the slow wave mode propagates because of the condition originally used for deriving this mode, $\omega \ll \Omega_i$. In 1957, however, Stix [7] found that this mode could propagate at frequencies slightly less than Ω_i for the slow wave mode (L mode) in region 13. Recalling that the slow wave mode is left-handed polarized, the slow wave could be launched from the high-field side, which is region 13 in the vicinity of $L \rightarrow \infty$. The fast mode can propagate either in region 11 or 13, which would correspond to a low-field-side launch and a high-field-side launch, respectively.

In the ion cyclotron frequency region, $\omega \ll \Omega_e, \omega_{pe}$, the dispersion relations for the two propagating waves at finite n_{\parallel} can be calculated from Eq.(2.36) as [83],

$$\begin{aligned} n_{\perp 1}^2 &\simeq \frac{(K_{\perp} - n_{\parallel}^2)^2 + K_{\times}^2}{K_{\perp} - n_{\parallel}^2} \quad (\text{fast}), \\ n_{\perp 2}^2 &\simeq \frac{K_{\parallel}}{K_{\perp}} (K_{\perp} - n_{\parallel}^2) \quad (\text{slow}). \end{aligned} \quad (2.41)$$

In this frequency range the ordering of the components of \mathbf{K} becomes

$$K_{\perp} \sim K_{\times} = O\left(\frac{m_e}{m_i}\right) K_{\parallel}, \quad (2.42)$$

which implies that by expanding Eq.(2.35) in $\frac{m_e}{m_i}$, $E_{\parallel} = O\left(\frac{m_e}{m_i}\right) E_{\perp}$ since the electrons are very mobile and free to move along \vec{B}_0 . Sometimes $E_{\parallel} = 0$ is assumed which is called the “zero electron mass” assumption.

Figure 2.3 shows propagating and evanescent regions for both branches. Cutoffs ($n_{\perp} \rightarrow 0$) for the fast wave occur at $n_{\parallel}^2 = K_{\perp} \pm |K_{\times}|$, and fast wave is propagating between these cutoffs. This cutoff condition can be expressed as a density condition,

$$N_{cutoff} = 5.2 \times 10^{10} \frac{A\Omega_i}{z^2\omega} \left(1 + \frac{\Omega_i}{\omega}\right) k_{\parallel}^2 (m^{-1}) (cm^{-3}), \quad (2.43)$$

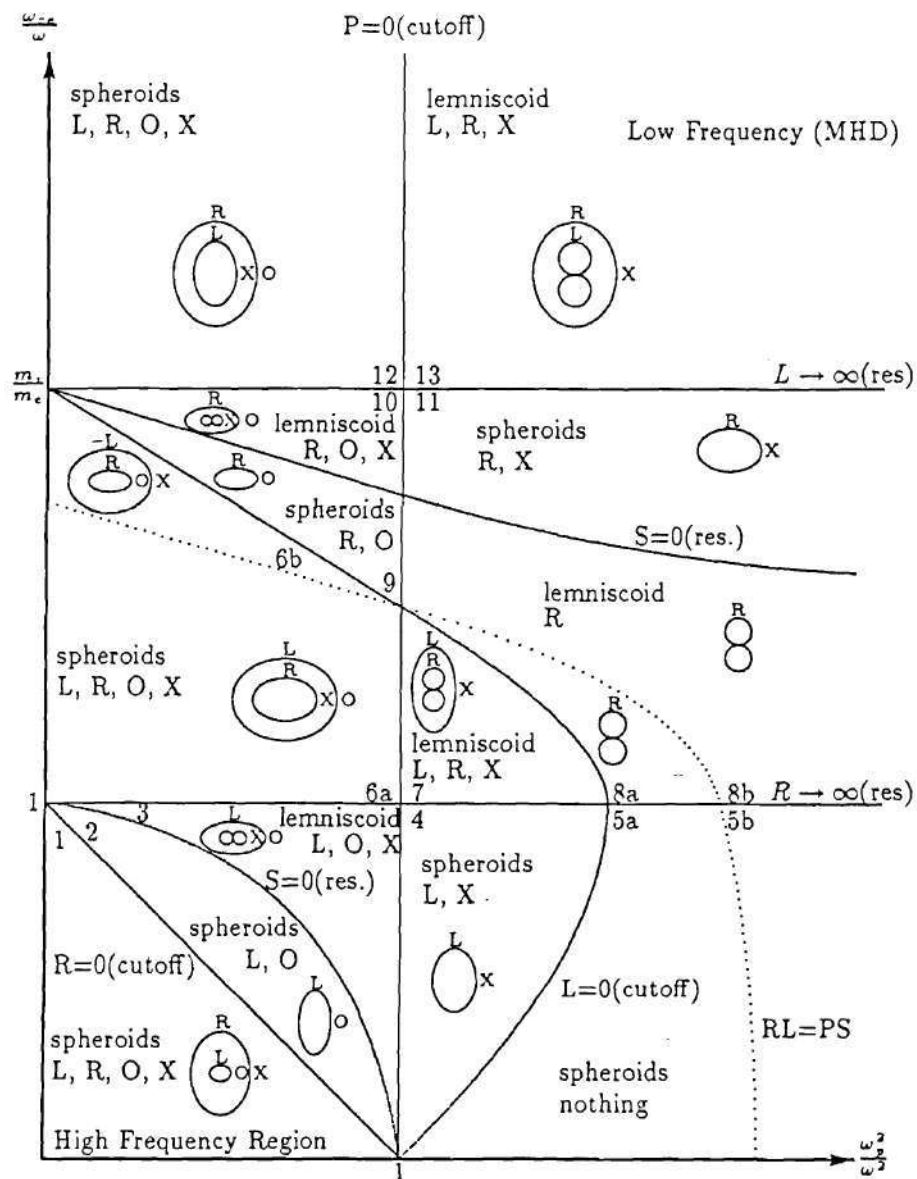


Figure 2.2: CMA Diagram for Single Species Plasma [6]

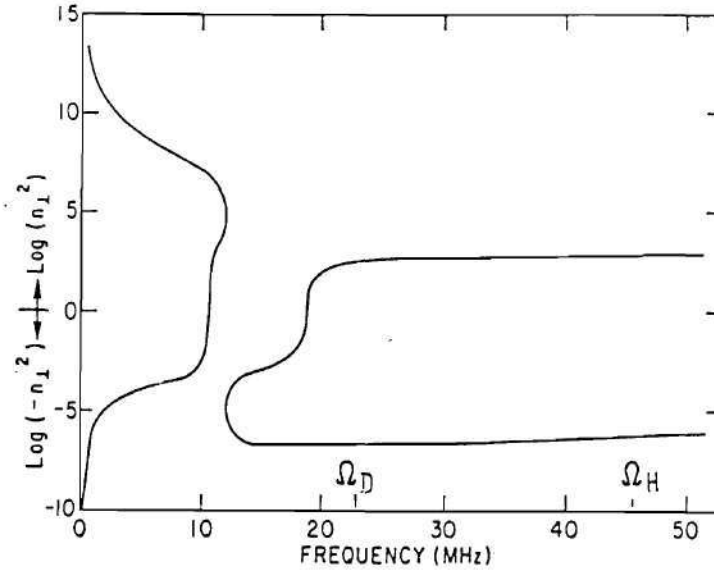


Figure 2.3: Frequency Dependence of the Cold Plasma Dispersion Relation Roots Near The Ion Cyclotron Resonance in a Pure Deuterium Plasma with $n_e(0) = 3 \times 10^{13} \text{ cm}^{-3}$, $k_{\parallel} = 10 \text{ m}^{-1}$ [83]

where A is the atomic number and z is the charge state of the ion.

In toroidal devices, the gradient along the magnetic field is considerably weaker than those across the field owing to the fact that

$$\nabla p = \vec{J} \times \vec{B} \quad (2.44)$$

holds across the transverse plasma cross section. A consequence of this situation and Snell's law, the principle of refraction, is that the wave number along the field line, k_{\parallel} , is approximately constant along the path of wave propagation while the perpendicular wave number, k_{\perp} , varies in accordance with the dispersion relation.

For the case where a minority ion species exists in the plasma, because of the contribution to the components of the dielectric tensor from each ion species there is another resonance condition, the ion-ion hybrid resonance [8,9,10,11,30] at

$$\omega^2 = \Omega_1 \Omega_2 \frac{\eta_1 \Omega_2 + \eta_2 \Omega_1}{\eta_1 \Omega_1 + \eta_2 \Omega_2}, \quad (2.45)$$

where

$$\eta_j = \frac{n_j}{\sum_{j=1,2} n_j}.$$

It was recognized that the presence of a dilute ion species changes the electric field polarization around the resonance layer (not at the resonance layer in the cold plasma wave theory) and enhances the left polarized field, thereby increasing ion heating efficiency. This can be enhanced by thermal effects such as Doppler broadening. Due to the shift of the resonance layer by $k_{\parallel} v_{\parallel}$, the resonance layer appears near the hybrid resonance layer, where the left-hand circularly polarized field is finite.

The components of \mathbf{K} have singularities at $\omega = \Omega_i$. This means that the present model is not valid in the region near the resonance layer. To avoid this singularity, collisionality or thermal motion must be included. This singularity is why the cold plasma model does not provide cyclotron damping at a fundamental resonance layer in

terms of polarization - no left-handed polarized field is permitted. By calculating the dispersion relation and polarization for different plasma conditions [12] some insight into the cold plasma wave theory in the case of the ion-ion hybrid resonance and the second harmonic resonance regime can be obtained. Even in the case where a certain amount of a minority ion species exists, the left-hand polarized field strength is zero at the fundamental resonance layer. However, at the second harmonic resonance layer, both the polarization and k_{\perp} are greatly enhanced.

Another thing that the cold plasma model does not show is the existence of a thermal ion Bernstein wave. In the hot plasma wave theory, this mode appears as a consequence of the thermal motion of the plasma particles.

Effect of the Boundary

The importance of the boundary effect depends on the strength of the damping. In the weak damping regime, power is not absorbed in a single pass making the boundary effect important. But in the strong damping case, in which the wave is absorbed in a narrow region, the wave fields do not reach the boundary. For this case the plasma can be treated as an infinite medium. The principal result of including boundary effects is a discrete \vec{k} spectrum instead of the continuous spectrum of an infinite plasma. This occurs in low density, weak damping experiments, which usually produce discrete eigenmodes.

The boundary conditions for a conducting wall are regularity at $r \rightarrow 0$ and the fact that the tangential electric field, \vec{E}_t must vanish at the wall. The application of this boundary condition is strongly affected by the type of plasma-vacuum interface (sharp boundary) or plasma-edge interface (diffuse boundary). Wave propagation also depends on the edge model, though the actual edge conditions are often unknown.

In the sharp boundary model, a surface wave may propagate in the vacuum region between the plasma and the wall with large E_z value. In the diffuse boundary model, a surface wave would be suppressed by the finite edge density.

Eigenmodes have been studied by many authors [13,14]. As an example, the wave field equations are derived in the weak damping limit for a cylindrical plasma with a uniform magnetic field in the z direction. The curl equations in Eqs. (2.1) and (2.2) can be rewritten in component form using the dielectric tensor, Eq. (2.24), and with the wave fields represented as

$$\vec{E} = \vec{E}(r)e^{i(k_z z + m\theta - \omega t)}. \quad (2.46)$$

They become:

$$\begin{aligned} \frac{im}{r} E_z - ik_z E_\theta &= i\omega B_r, \\ ik_z E_r - \frac{d}{dr} E_z &= i\omega B_\theta, \\ \frac{1}{r} \frac{d}{dr} (r E_\theta) - \frac{im}{r} E_r &= i\omega B_z, \\ \frac{im}{r} B_z - ik_z B_\theta &= -\frac{i\omega}{c^2} (K_\times E_r - iK_\times E_\theta), \\ ik_z B_r - \frac{d}{dr} B_z &= -\frac{i\omega}{c^2} (iK_\times E_r + K_\perp E_\theta), \\ \frac{1}{r} \frac{d}{dr} (r B_\theta) - \frac{im}{r} B_r &= -\frac{i\omega}{c^2} K_\parallel E_z, \end{aligned} \quad (2.47)$$

where m is azimuthal mode number. This set of equations can be reduced to two second order coupled equations for the transverse component in E_z and B_z . Following Swanson [6],

$$\alpha \nabla_\perp^2 E_z + \beta \nabla_\perp^2 B_z - i\omega B_z = 0, \quad (2.48)$$

$$\alpha \nabla_\perp^2 B_z + \gamma \nabla_\perp^2 E_z + \frac{iK_\parallel}{\omega} E_z = 0, \quad (2.49)$$

where

$$\nabla_\perp = \nabla - \hat{e}_z \frac{\partial}{\partial z}, \quad (2.50)$$

$$\alpha = \frac{c^2}{\omega^2} \frac{k_z K_X}{\kappa^2 - K_X^2}, \quad (2.51)$$

$$\beta = \frac{c^2}{\omega^2} \frac{i\omega\kappa}{\kappa^2 - K_X^2}, \quad (2.52)$$

$$\gamma = -\frac{c^2}{\omega^2} \frac{k_z^2 K_X}{\omega(\kappa^2 + K_X^2)}, \quad (2.53)$$

$$\kappa = \frac{c^2}{\omega^2} k_z^2 - K_\perp. \quad (2.54)$$

These two coupled equations lead to a fourth order equation in either E_z or B_z as

$$(\nabla_\perp^2 + k_{\perp 1}^2)(\nabla_\perp^2 + k_{\perp 2}^2)E_z = 0, \quad (2.55)$$

or

$$(\nabla_\perp^2 + k_{\perp 1}^2)(\nabla_\perp^2 + k_{\perp 2}^2)B_z = 0, \quad (2.56)$$

where $k_{\perp 1}^2$ and $k_{\perp 2}^2$ are the two solutions of the quadratic equation:

$$(\alpha^2 - \beta\gamma)k_\perp^4 - \left(i\omega\gamma - \frac{\omega^2}{c^2} \frac{i\beta K_\parallel}{\omega}\right)k_\perp^2 - \frac{\omega^2}{c^2} K_\parallel = 0. \quad (2.57)$$

From this quadratic equation in k_\perp , the dispersion relation for a cold, uniform and bounded plasma is obtained as

$$(\kappa^2 - K_\times^2 + \frac{\kappa k_\perp^2}{k_0^2})K_\parallel + (\frac{k_\perp}{k_0})^2[K_\perp(\kappa + \frac{k_\perp^2}{k_0^2}) + K_\times^2] = 0, \quad (2.58)$$

where $k_0 = \omega/c$.

At $\omega \simeq \Omega_i$, assuming that $|\frac{k_\perp^2}{k_0^2 K_\parallel}| \ll 1$ and using the ordering in Eq.(2.42), Eq.(2.58) simplifies to

$$k_z^2 \rightarrow \frac{1}{2} \left(\frac{\omega^2}{V_A^2} - k_\perp^2 \right), \quad (2.59)$$

for the fast wave where V_A is the Alfvén speed defined as

$$V_A \equiv \sqrt{\frac{B_0^2}{\mu_0 \rho_m}}, \quad (2.60)$$

and $\rho_m \simeq n_i m_i$ is the mass density of the plasma.

For the weak damping limit with a plasma, the tokamak may be treated as a dielectrically loaded cavity and eigenmodes exist at the frequencies of interest for densities high enough to allow the wave to be launched. The azimuthal mode number is included explicitly in the expression of the wave field while radial and toroidal wave number can be determined by assumptions or other constraints. Usually in a toroidal system, if shear is neglected, the parallel wave number is represented as $k_z = \frac{n}{R}$ and the radial wave number is $k_r = \frac{N}{a}$ where n and N are the parallel and radial mode numbers, and R and a are the major and minor radii, respectively. Therefore for a certain poloidal mode, m , with a given plasma density, the excited eigenmode set (n, m, N) can be obtained along with the wave fields.

In the numerical work [14,15] it was observed that modes with lower m -numbers and small n tend to have the shortest radial wavelength and strongest central focusing effects, while large m -numbers correspond to modes with fields nearer the plasma surface and would not be expected to be as desirable for central power deposition. As given in Eq.(2.41), the dependence of the radial wave number on density and magnetic field indicates that a density threshold exists for each mode, below which it cannot propagate. In a typical large tokamak with a dense and hot plasma, an multitude of eigenmodes almost approaches a continuum and strong damping processes preclude the formation of toroidal eigenmodes. However, radial eigenmodes have been observed in a hot, dense plasma due to the existence of a reflection layer inside the plasma [16].

Effect of the Thermal Motion

In order to properly model the wave-plasma interaction around the resonance layer, which includes both cyclotron damping and mode conversion, it is necessary to include thermal effects. In this section the hot plasma dielectric tensor is obtained

by first deriving the plasma current taking thermal motion into account, and then performing a finite-Larmor-orbit expansion.

The formal derivation of the hot plasma dielectric tensor requires complicated mathematical notations which will distract from the physics content. Therefore only the important steps and mathematical methods of derivation will be described in this section. Several texts [4,6,17] were referenced in obtaining the hot plasma dielectric tensor. The technique used for this derivation is called the method of characteristics and the idea is to find the perturbation of the distribution function due to the wave by integrating along the unperturbed orbits. This orbit is described by

$$\vec{R}(t) = \vec{R}[\vec{x}(t), \vec{v}(t), t], \quad (2.61)$$

where $\vec{x}(t)$, $\vec{v}(t)$ describe the unperturbed particle orbit. The collisionless Boltzman equation along this trajectory is

$$\begin{aligned} \frac{df}{dt}|_{\vec{R}} &= \frac{\partial f}{\partial t} + \frac{\partial f}{\partial \vec{x}} \cdot \frac{d\vec{x}}{dt} + \frac{\partial f}{\partial \vec{v}} \cdot \frac{d\vec{v}}{dt} \\ &= \frac{\partial f}{\partial t} + \vec{v} \cdot \frac{\partial f}{\partial \vec{x}} + \frac{q}{m} \vec{v} \times \vec{B}_0 \cdot \frac{\partial f}{\partial \vec{v}} = 0. \end{aligned} \quad (2.62)$$

Assuming first order perturbation for perturbing quantities as was done previously, then the zero-order equation is

$$\frac{df_0}{dt}|_{\vec{R}} = \frac{q}{m} \vec{v} \times \vec{B}_0 \cdot \frac{\partial f_0}{\partial \vec{v}} = 0, \quad (2.63)$$

and the first order equation is

$$\frac{df_1}{dt}|_{\vec{R}} = -\frac{q}{m} (\vec{E}_1 + \vec{v} \times \vec{B}_1) \cdot \frac{\partial f_0}{\partial \vec{v}}. \quad (2.64)$$

Therefore the equation integrated along \vec{R} is

$$\frac{df}{dt}|_{\vec{R}} = \frac{df_0}{dt}|_{\vec{R}} + \frac{df_1}{dt}|_{\vec{R}} = -\frac{q}{m} (\vec{E}_1 + \vec{v} \times \vec{B}_1) \cdot \frac{\partial f_0}{\partial \vec{v}}. \quad (2.65)$$

The integration along \vec{R} yields

$$f(\vec{x}, \vec{v}, t) = -\frac{q}{m} \int_{t_0}^t [\vec{E}_1(\vec{x}', t') + \vec{v}' \times \vec{B}_1(\vec{x}', t')] \cdot \frac{\partial f_0(\vec{v}')}{\partial \vec{v}'} dt' + f(\vec{x}, \vec{v}, t_0). \quad (2.66)$$

Here if $t_0 \rightarrow -\infty$, the initial value at this infinitely remote past time will be neglected since ω should have a positive imaginary part from the Vlasov analysis. Hence the initial point is chosen to be $t' = -\infty$ and the last term in Eq.(2.66) is neglected. In order to integrate Eq.(2.66), the expression of the characteristic trajectory should be obtained and substituted into the integral. In Cartesian coordinates, the trajectory that reaches $\vec{x}' = \vec{x}$ when $t' = t$ is governed by the equation of motion

$$\frac{d\vec{v}'}{dt} = \vec{v} \times \vec{\Omega}. \quad (2.67)$$

The solution for a spatially homogenous plasma using cylindrical coordinates is:

$$v_x = v_{\perp} \cos \phi, \quad (2.68)$$

$$v_y = v_{\perp} \sin \phi, \quad (2.69)$$

$$k_x = k_{\perp} \cos \psi, \quad (2.70)$$

$$k_y = k_{\perp} \sin \psi, \quad (2.71)$$

and the relation $v_{\perp}^2 = v_x^2 + v_y^2$, becomes

$$v'_x = v_{\perp} \cos(\phi + \epsilon\Omega\tau), \quad (2.72)$$

$$v'_y = v_{\perp} \sin(\phi + \epsilon\Omega\tau), \quad (2.73)$$

$$v'_z = v_z, \quad (2.74)$$

and

$$x' = x - \frac{\epsilon v_{\perp}}{\Omega} (\sin(\phi + \epsilon\Omega\tau) + \sin \phi), \quad (2.75)$$

$$y' = y + \frac{\epsilon v_{\perp}}{\Omega} (\cos(\phi + \epsilon\Omega\tau) - \cos \phi), \quad (2.76)$$

$$z' = z - v_z \tau, \quad (2.77)$$

where $\epsilon = q/|q|$ and $\tau = t - t'$. Then the phase factor becomes

$$\begin{aligned} i(\vec{k} \cdot \vec{x}' - \omega t') &= i\vec{k} \cdot \vec{x} - \omega t \\ &\quad - ib[\sin(\phi - \psi + \epsilon\Omega\tau) - \sin(\phi - \psi)] + ia\tau \end{aligned} \quad (2.78)$$

where $a = (\omega - k_z v_z)$, $b = \epsilon k_\perp v_\perp / \Omega$. It is important to note that since v_\perp and v_z are constants of the motion, then $f_0(v'_\perp, v'_z) = f_0(v_\perp, v_z)$. By defining

$$\frac{\partial f_0}{\partial v_\perp} \equiv f_{0\perp}, \quad (2.79)$$

$$\frac{\partial f_0}{\partial v_z} \equiv f_{0z}, \quad (2.80)$$

and calculating

$$\frac{\partial f_0}{\partial v_x} = \frac{\partial f_0}{\partial v_\perp} \frac{\partial v_\perp}{\partial v_x} = \frac{v_x}{v_\perp} f_{0\perp}, \quad (2.81)$$

$$\frac{\partial f_0}{\partial v_y} = \frac{\partial f_0}{\partial v_\perp} \frac{\partial v_\perp}{\partial v_y} = \frac{v_y}{v_\perp} f_{0\perp}, \quad (2.82)$$

the remaining factor of the integral can be written as

$$\begin{aligned} & \left(\vec{E} + \frac{(\vec{E} \cdot \vec{v}') \vec{k} - \vec{E}(\vec{v}' \cdot \vec{k})}{\omega} \right) \cdot \frac{\partial f_0(\vec{v}')}{\partial \vec{v}'} \\ &= (v_\perp \cos(\phi + \epsilon \Omega \tau) \left[\frac{E_x f_{0\perp}}{v_\perp} + \frac{E_x k_z - E_z k_\perp \cos \psi}{\omega} \left(f_{0z} - \frac{v_z}{v_\perp} f_{0\perp} \right) \right] \\ &+ (v_\perp \sin(\phi + \epsilon \Omega \tau) \left[\frac{E_y f_{0\perp}}{v_\perp} + \frac{E_y k_z - E_z k_\perp \sin \psi}{\omega} \left(f_{0z} - \frac{v_z}{v_\perp} f_{0\perp} \right) \right] \\ &+ E_z f_{0z}. \end{aligned} \quad (2.83)$$

With Eq.(2.78), Eq.(2.83) and using the Bessel identity

$$e^{i\lambda \sin \theta} = \sum_{l=-\infty}^{\infty} J_l(\lambda) e^{il\theta}, \quad (2.84)$$

and

$$J_{l+1}(\lambda) + J_{l-1}(\lambda) = \frac{2l}{\lambda} J_l(\lambda), \quad (2.85)$$

$$J_{l+1}(\lambda) - J_{l-1}(\lambda) = -2J'_l(\lambda). \quad (2.86)$$

The result of the integration of Eq.(2.66) over τ is

$$f(\vec{k}, \vec{v}, \omega) = -\frac{iq}{m} \sum_{l=-\infty}^{\infty} \sum_{p=-\infty}^{\infty} \frac{J_l(b) e^{i(l-p)(\phi-\psi)}}{\omega - p\epsilon\Omega - k_z v_z}$$

$$\begin{aligned}
& \times \left\{ \frac{pJ_p(b)}{b} \left[f_{0\perp} + \frac{k_z}{\omega} (v_\perp f_{0z} - v_z f_{0\perp}) \right] (E_x \cos \psi + E_y \sin \psi) \right. \\
& + iJ'_p(b) \left[f_{0\perp} + \frac{k_z}{\omega} (v_\perp f_{0z} - v_z f_{0\perp}) \right] (-E_x \sin \psi + E_y \cos \psi) \\
& \left. + J_p(b) \left[f_{0z} - \frac{p\epsilon\Omega}{\omega} \left(f_{0z} - \frac{v_z}{v_\perp} f_{0\perp} \right) \right] E_z \right\}. \quad (2.87)
\end{aligned}$$

The expression for the current density is represented as

$$\vec{J} = \int_0^{2\pi} d\phi \int_0^\infty v_\perp dv_\perp \int_{-\infty}^\infty dv_z \vec{v} f(v_\perp, v_z), \quad (2.88)$$

and the hot plasma dielectric tensor is defined by

$$\mathbf{K} \cdot \vec{E} \equiv \vec{E} + \frac{i}{\omega\epsilon_0} \vec{J}. \quad (2.89)$$

For an isotropic Maxwellian distribution

$$f_0(v_\perp, v_z) = \frac{1}{\pi^{3/2} v_{th}^3} e^{-v^2/v_{th}^2}, \quad (2.90)$$

the final form of the Dielectric tensor, \mathbf{K} is

$$\mathbf{K} = \begin{pmatrix} K_1 + \sin^2 \psi K_0 & K_2 - \cos \psi \sin \psi K_0 & \cos \psi K_4 + \sin \psi K_5 \\ -K_2 - \cos \psi \sin \psi K_0 & K_1 + \cos^2 \psi K_0 & \sin \psi K_4 - \cos \psi K_5 \\ \cos \psi K_4 - \sin \psi K_5 & \sin \psi K_4 + \cos \psi K_5 & K_3 \end{pmatrix}, \quad (2.91)$$

where

$$K_0 = 2 \sum_j \frac{\omega_{pj}^2 e^{-\lambda_j}}{\omega k_z v_j} \sum_{n=-\infty}^\infty \lambda_j (I_n - I'_n) Z(\zeta_{nj}), \quad (2.92)$$

$$K_1 = 1 + \sum_j \frac{\omega_{pj}^2 e^{-\lambda_j}}{\omega k_z v_j} \sum_{n=-\infty}^\infty \frac{n^2 I_n}{\lambda_j} Z(\zeta_{nj}), \quad (2.93)$$

$$K_2 = i \sum_j \frac{\epsilon_j \omega_{pj}^2 e^{-\lambda_j}}{\omega k_z v_j} \sum_{n=-\infty}^\infty n (I_n - I'_n) Z(\zeta_{nj}), \quad (2.94)$$

$$K_3 = 1 - \sum_j \frac{\omega_{pj}^2 e^{-\lambda_j}}{\omega k_z v_j} \sum_{n=-\infty}^\infty I_n \zeta_{nj} Z'(\zeta_{nj}), \quad (2.95)$$

$$K_4 = \sum_j \frac{k_\perp \omega_{pj}^2 e^{-\lambda_j}}{2\omega k_z \Omega_j} \sum_{n=-\infty}^\infty \frac{n I_n}{\lambda_j} Z'(\zeta_{nj}), \quad (2.96)$$

$$K_5 = i \sum_j \frac{k_\perp \epsilon_j \omega_{pj}^2 e^{-\lambda_j}}{2\omega k_z \Omega_j} \sum_{n=-\infty}^\infty (I_n - I'_n) Z'(\zeta_{nj}), \quad (2.97)$$

where $\lambda = \frac{1}{2}k_{\perp}^2\rho_L^2$, $\rho_L = v_{th}/\Omega$ is the Larmor radius and $Z(\zeta_{nj})$ is the plasma distribution function defined as

$$Z(\zeta) \equiv \frac{1}{\sqrt{\pi}} \int_{-\infty}^{\infty} \frac{e^{-z^2}}{z - \zeta} dz, \quad (2.98)$$

and the argument ζ_{nj} is $\frac{\omega + n\Omega_j}{k_z v_{th}}$.

In obtaining Eq.(2.92) through Eq.(2.97), one uses another Bessel identity

$$e^{\lambda \cos \Omega \tau} = \sum_{n=-\infty}^{\infty} I_n(\lambda) e^{in\Omega \tau}, \quad (2.99)$$

where I_n is the modified Bessel function of the first kind.

The final step in this section is to perform a finite-Larmor-orbit expansion. The physics of this phenomena¹ is that for any finite k_{\perp} there exists a non-vanishing contribution of the wave field to the particle orbits. Since for small $k_{\perp}\rho_L$, however, the interaction is weak, the dielectric tensor elements can be expanded in $\lambda_j = \frac{1}{2}k_{\perp}^2\rho_{Lj}^2$. If only the first order terms are considered, the resulting components are

$$K_0 = \sum_j \frac{\omega_{pj}^2}{\omega k_z v_j} [\lambda Z(\zeta_0)]_j, \quad (2.100)$$

$$K_1 = 1 + \sum_j \frac{\omega_{pj}^2}{2\omega k_z v_j} \{ [Z(\zeta_{-1}) + Z(\zeta_1)](1 - \lambda) + \lambda [Z(\zeta_{-2}) + Z(\zeta_2)] \}_j, \quad (2.101)$$

$$K_2 = i \sum_j \frac{\epsilon_j \omega_{pj}^2}{2\omega k_z v_j} \{ [Z(\zeta_{-1}) - Z(\zeta_1)](1 - 2\lambda) + \lambda [Z(\zeta_{-2}) - Z(\zeta_2)] \}_j, \quad (2.102)$$

$$K_3 = 1 - \sum_j \frac{\omega_{pj}^2}{\omega k_z v_j} \{ \zeta_0 Z'(\zeta_0)(1 - \lambda) + \frac{\lambda}{2} [\zeta_{-1} Z'(\zeta_{-1}) + \zeta_1 Z'(\zeta_1)] \}_j, \quad (2.103)$$

$$K_4 = \sum_j \frac{\omega_{pj}^2 \sqrt{\lambda_j}}{2\sqrt{2}\omega k_z v_j} [Z'(\zeta_1) - Z'(\zeta_{-1})]_j, \quad (2.104)$$

$$K_5 = i \sum_j \frac{\sqrt{\lambda_j} \epsilon_j \omega_{pj}^2}{2\sqrt{2}\omega k_z v_j} \{ Z'(\zeta_0) - \frac{1}{2} [Z'(\zeta_1) + Z'(\zeta_{-1})] \}_j. \quad (2.105)$$

¹A simple illustration of this phenomena can be found in Swanson's *Plasma Waves* published by Academic Press, New York, 1989

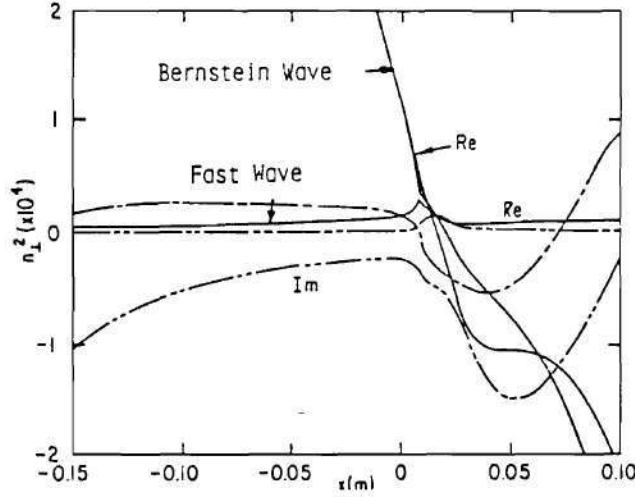


Figure 2.4: WKB dispersion relation for a hot deuteron plasma with a small component of hydrogen. Conversion to an ion Bernstein wave occurs near the cold plasma two-ion hybrid resonance [83].

It is now easy to identify the contributions from $n = 0$ (Landau damping), $n = 1$ (fundamental cyclotron damping) and $n = 2$ (second harmonic damping), clearly indicated by ζ_n . The cold plasma dielectric tensor is obtained by setting v_{th} equal to zero. In addition the ion Bernstein wave is now seen in the hot plasma dispersion relation as k_z goes to zero (electrostatic limit) as shown in Fig. 2.4. There is a possibility of mode conversion from the fast wave to the ion Bernstein wave and this greatly diversifies wave physics in the hot plasma regime. In the next section, an elementary description of the effect of the plasma inhomogeneity is presented.

Wave Absorption

A propagating wave can be absorbed in a plasma by several damping mechanisms. For ICRF heating, the basic damping mechanism is cyclotron damping. Physically, in order to interact significantly with the ion motion to produce ion heating, the wave polarization must contain a component which rotates in the sense of the ions (i.e. left-hand polarization) as mentioned before. This is exactly the case for the slow wave mode, which leads to strong absorption at the cyclotron resonance. In the case of the fast wave mode, the left-hand polarized part is almost perfectly screened out as $\omega \rightarrow \Omega_i$. However, in initial experiments in the mid-70s, it turned out that even for fast wave heating, the results were better than the theoretical expectation. In this section possible damping mechanisms and the effect of minority species and thermal effects on the wave absorption are considered.

Collisional and collisionless processes are possible for the wave damping mechanisms. Collisional damping is essentially that of ohmic heating, and becomes less effective as the temperature is increased. According to Paoloni, [15] the ohmic power loss due to collisions is just

$$P_{\text{collision}} = \int_V \frac{1}{2\eta_{\parallel}} |E_z|^2 dV, \quad (2.106)$$

where $\eta_{\parallel} = 5.2 \times 10^{-5} \frac{Z \ln \Lambda}{T^{3/2}(\text{eV})} \Omega\text{-m}$ is the parallel (to the magnetic field) Spitzer resistivity and the integration is over the volume of the tokamak. As previously mentioned, in a highly ionized plasma electron mobility increases which shorts out the parallel electric field. This significantly reduces the effectiveness of collisional damping significantly.

Collisionless damping is more complicated because the thermal motion of the particles (the hot plasma dielectric tensor) must be considered. As an introduction to how particles absorb the wave energy, single particle cyclotron damping [18] is going to be discussed. Particles that feel the wave E -field at their cyclotron frequency

absorb the wave energy. The well-known condition for such single particle resonance is $\omega - k_{\parallel}v_{\parallel} = \Omega_i$. In toroidal geometry, ions moving along the B lines which twist around the magnetic axis can pass through the resonant surface twice at each complete revolution. On each passage through resonance the ions receive a perpendicular (to \vec{B}) kick, mv_{\perp} , which is calculated from the equations of motion:

$$\dot{v}_x - \Omega(t)v_y = \frac{q}{m}E_x \cos \omega t, \quad (2.107)$$

$$\dot{v}_y + \Omega(t)v_x = -\frac{q}{m}E_y \sin \omega t. \quad (2.108)$$

Let $E_{\pm} \equiv \frac{1}{2}(E_x \pm E_y)$, $u \equiv v_x + iv_y$. Expanding the instantaneous cyclotron frequency Ω_i around the resonance,

$$\Omega_i(t) = \omega + (t + t_0) \frac{\partial \Omega_i}{\partial t} + \dots \quad (2.109)$$

The two real variable equations can then be written as a single equation in the complex variable u ,

$$\frac{du}{dt} + i\Omega(t)u = \frac{q}{m} [E_+ e^{-i\omega t} + E_- e^{i\omega t}]. \quad (2.110)$$

Here by neglecting the non-resonant term (E_-) (non-resonant due to the right-hand polarization) and integrating for $t \ll t_0$, the average change in energy per transit of the resonant surface can be computed as

$$\begin{aligned} \Delta \epsilon &= \frac{m}{2} \langle u(t)u(t)^* - u(-\infty)u(-\infty)^* \rangle, \\ &= \frac{m}{2} \left| \frac{q}{m} E_+ \right|^2 \left| \frac{2\pi}{\Omega'} \right|, \end{aligned} \quad (2.111)$$

where Ω' can be expressed by

$$\Omega' = v_{\parallel} \frac{\partial \Omega}{\partial s} \quad (2.112)$$

and $\frac{\partial}{\partial s}$ is the derivative along the field line. Particles turning near the resonance ($v_{\parallel \text{res}} \rightarrow 0$) will exhibit a singular behavior. So it will be necessary to keep more terms for these particles and their behavior can be described by what is known as the

Airy function correction in which the total absorbed energy can be written in terms of Airy functions. It was found that this higher order correction was only important for a very small number of particles [19] and in most cases the Stix formula, Eq.(2.111), was acceptable. In Eq.(2.111), it should be noted that energy gain is proportional to the left handed polarized electric field.

The second harmonic case can also be analyzed in the same way. The resulting change in energy per transit is

$$\Delta\epsilon = -\pi \frac{qv_{\perp}^2}{4\Omega_0} \frac{|\nabla E_+|^2}{|\Omega'|^{1/2}}. \quad (2.113)$$

Note that the energy gain in the second harmonic is proportional to $|\nabla E_+|$. The Larmor radius must be a non-negligible fraction of a wavelength for this case. In this case

$$v_{\parallel res} \simeq \frac{\omega - \Omega_0}{k_{\parallel}}, \quad (2.114)$$

which is not zero at the second harmonic. The polarization at the second harmonic resonance layer is not fully right-handed as seen even in cold plasma theory [12].

Landau damping and transit time magnetic pumping (TTMP) [18] both involve energy absorption by particles moving along \vec{B} with the phase velocity of the wave, i.e. particles for which $\omega - k_{\parallel}v_{\parallel} = 0$. The only difference is that in Landau damping, the force on the particle due to the wave is $q\vec{E}$ while in TTMP the acting force is $-\mu\nabla B$ as in the equation of motion

$$m \frac{dv_z}{dt} = qE_0 \cos(kz - \omega t), \quad (2.115)$$

$$m \frac{dv_z}{dt} = -\mu \frac{\partial B_z}{\partial z}. \quad (2.116)$$

In Stix[18], they were expressed as

$$\left\langle \frac{d}{dt} \frac{mv^2}{2} \right\rangle_{z_0, v_0}^L = -\frac{\pi q^2 E^2}{2m|k|} \left(\frac{\omega}{k} \right) \left(\frac{\partial f(v_0)}{\partial v_0} \right)_{v_0=\omega/k}, \quad (2.117)$$

$$\left\langle \frac{d}{dt} \frac{mv^2}{2} \right\rangle_{z_0, v_0}^{TTMP} = -\frac{\pi \mu_0^2 |k|}{2m} |B_z|^2 \left(\frac{\omega}{k} \right) \left(\frac{\partial f(v_0)}{\partial v_0} \right)_{v_0 = \omega/k} \quad (2.118)$$

Since wave absorption implies a collisionless, resonance process, in the rest of this section the processes involved in resonance absorption are considered. The resonance layer here is limited to the two-ion hybrid resonance layer. The first analysis of this process came from Budden [20]. He used a second order differential equation to describe wave phenomena near this cutoff-resonance pair². The Budden equation is

$$zy'' + \left(z + \frac{2\eta}{\pi}\right)y = 0 \quad (2.119)$$

where $\eta = \pi \lambda^2 a/2$ for $a > 0$. This equation has a pole at $z = 0$ (resonance) and a cutoff at $z = -a$. He showed that the transmission of energy was given by $T^2 = e^{-2\eta}$ for incidence from either side — incidence from the right where resonance was met first or incidence from the left where cutoff was met first. There was no reflection for the incidence from the right but $R^2 = (1 - T^2)^2$ from the left. It should be noted that the energy was not conserved as indicated by $T^2 + R^2 < 1$. This is caused by the lower order differential equation (second order here) which did not say where the depleted energy goes.

A higher order equation to describe this physical phenomena is

$$y^{iv} + \lambda^2(zy'' + \beta y) = 0 \quad (2.120)$$

as Wasow [21] used, but this equation describes only a resonance. An extension of this equation was studied by Stix [22] where he used the term “mode conversion” for the conversion of the slow wave to a warm plasma wave. Although this equation was a more generalized version of the Budden equation and suitable for studying the

²The two-ion hybrid resonance layer is always accompanied by a cutoff layer.

coupling between different modes, it did not include tunneling through the cutoff region. The fourth-order mode conversion-tunneling equation is

$$y^{iv} + \lambda^2 z y'' + (\lambda^2 z + \gamma)y = 0 \quad (2.121)$$

which was derived by Swanson [23] for the normal incidence case ($k_{\parallel} = k_y = 0$). This equation was studied by many authors [24,25,26,27] with various mathematical methods including the method of matched asymptotic expansion [24,26], the method of Laplace [24,25], and the variational method [27]. They obtained the coefficients for reflection, mode conversion and tunneling (transmission) of wave energy near the hybrid resonance layer. The important difference from Budden's result is that the wave energy is conserved, and the depleted energy in Budden's solution is mode converted to the ion Bernstein wave (IBW).

A further extension of this equation included absorption [28,29], which was written as

$$y^{iv} + \lambda^2 z y'' + (\lambda^2 z + \gamma)y = g(y, z), \quad (2.122)$$

where $g(y, z)$ represents the absorption term. The results of this calculations indicated that strong absorption suppressed the mode converted wave and reduced transmission.

Extensive numerical analysis was done by Colestock and Kashuba [30] by directly integrating the mode conversion equation for the Princeton Large Torus (PLT)³. Summarizing their work, only a very small fraction of the incident power was mode converted for low-field incidence, but minority ion damping was strong for this case. From the high-field side, a significant fraction of the incident power was converted into the backward ($v_{\text{phase}} v_{\text{group}} < 0$) Bernstein wave and was subsequently lost to

³Since their observations were for a specific experiment (PLT) the details are not true for general cases, but their general trends are.

electrons through Landau damping. At sufficiently high temperatures where cyclotron damping is enhanced due to the Doppler shifted resonance layer, the low and high-field incidence cases should approach each other as damping overcomes mode conversion. At very low k_z values, absorption decreases while from the low-field side, the reflection coefficient increases significantly.

Overall, mode conversion can be expected to play a role over a broad range of parameters, especially if low parallel wave numbers are excited where the absorption term is weak due to weak Doppler shift of the fundamental resonance layer. While these calculations may account for the overall characters of the power flow and wave damping, further refinements to include rotational transform [11,31,32,33] as well as improvements to the basic concept of RF conductivity in a plasma are likely to be required before wave absorption can be completely understood.

Wave Thermalization

The last step of the physical process of ion cyclotron resonance heating (ICRH) is the thermalization of wave energy inside the plasma. As mentioned before, the ions streaming along the field lines receive a vertical kick in energy as they pass through the resonance zone proportional to the length of time they stay at resonance. Except for a few singular orbits, most particles do not spend much time at resonance. As such, most ions receive a periodic kick in energy with plenty of time between resonance layer transits to randomize their phase with respect to the wave. The quasi-linear velocity-space diffusion [34] can be applied in this case due to the fact that this theory is developed for waves of any oscillation branch propagating at an arbitrary angle to a uniform magnetic field in a spatially uniform plasma. Stix [18] first analyzed this problem thoroughly and he obtained the velocity diffusion operator due to the

resonant interaction as

$$\begin{aligned} \frac{\partial f_{rf}(\vec{v})}{\partial t} &= \frac{\pi z^2 e^2}{8m^2 |k_{\parallel}|} |E_+|^2 \sum_n \frac{1}{v_{\perp}} \frac{\partial}{\partial v_{\perp}} \left| J_{n-1} \left(\frac{k_{\perp} v_{\perp}}{\Omega_i} \right) \right|^2 \\ &\times \delta \left[v_{\parallel} - \frac{\omega - n\Omega_i}{k_{\parallel}} \right] \frac{1}{v_{\perp}} \frac{\partial f(\vec{v})}{\partial v_{\perp}}, \end{aligned} \quad (2.123)$$

when $f(\vec{v})$ is the particle distribution function summed over the cyclotron harmonics. To obtain the expression for $f(\vec{v})$, he considered the Fokker-Planck equation in spherical velocity coordinates and dropping angular dependence:

$$\frac{\partial f(\vec{v})}{\partial t} = C(f) + \frac{\partial f_{rf}(\vec{v})}{\partial t}, \quad (2.124)$$

where

$$\begin{aligned} C(f) &= -\frac{1}{v^2} \frac{\partial}{\partial v} [v^2 (\langle \Delta v_{\parallel} \rangle + \frac{1}{2v} \langle (\Delta v_{\perp})^2 \rangle) f] \\ &= \frac{1}{2v^2} \frac{\partial^2}{\partial v^2} (v^2 \langle (\Delta v_{\parallel})^2 \rangle f) \\ &= \frac{1}{4v^2} \frac{\partial}{\partial \mu} (1 - \mu^2) \frac{\partial}{\partial \mu} (\langle (\Delta v_{\perp})^2 \rangle f). \end{aligned}$$

Here $\mu = \frac{v_{\parallel}}{v}$ and the Coulomb coefficients $\langle \Delta v_{\parallel} \rangle$, $\langle (\Delta v_{\parallel})^2 \rangle$ and $\langle (\Delta v_{\perp})^2 \rangle$ have been determined for test particles diffusing in an isotropic Maxwellian plasma of ions and electrons. Integrating Eq.(2.124) in the steady-state, he obtained an expression for $f(\vec{v})$

$$f(\vec{v}) = f(0) \exp \left[- \int_0^v dv \frac{-2\alpha v^2 + \frac{\partial}{\partial v} (\beta v^2)}{\beta v^2 + 2K v^2} \right], \quad (2.125)$$

where

$$\begin{aligned} \alpha &= \langle \Delta v_{\parallel} \rangle + \frac{1}{2v} \langle (\Delta v_{\perp})^2 \rangle, \\ \beta &= \langle (\Delta v_{\parallel})^2 \rangle, \end{aligned}$$

and

$$K = \frac{3}{2} n m_i \text{Re}(\vec{E} \cdot \vec{J}^*).$$

To discuss the behavior of $f(\vec{v})$ in Eq.(2.125), he defined an effective (ion) temperature at each value of $E = mv^2/2$,

$$\begin{aligned} [kT_{eff}]^{-1} &\equiv - \left[\frac{d(\ln f)}{dE} \right], \\ &= \frac{1}{kT_e(1+\xi)} \left[1 + \frac{R_j(T_e - T_j + \xi T_e)}{T_j(1 + R_j + \xi)} \frac{1}{1 + (E/E_j)^{3/2}} \right], \end{aligned} \quad (2.126)$$

where

$$\xi \equiv \frac{m\langle p \rangle (4\pi\epsilon_0)^2 \left(\frac{2kT_e}{m_e} \right)^{1/2}}{8\sqrt{\pi} n_e n z^2 q^4 \ln \Lambda}, \quad (2.127)$$

$$R_j \equiv \frac{n_j z_j^2 l_j}{n_e l_e}, \quad (2.128)$$

$$l_j \equiv \left(\frac{m_j}{2kT_j} \right)^{1/2}, \quad (2.129)$$

$$E \equiv \frac{mv^2}{2}, \quad (2.130)$$

$$E_j \equiv \frac{mkT_j}{m_j} \left[\frac{1 + R_j + \xi}{2\epsilon(1 + \xi)} \right]^{2/3}, \quad (2.131)$$

$$\epsilon \equiv \frac{2}{3\sqrt{\pi}}, \quad (2.132)$$

where $\langle p \rangle$ is the wave heating power per unit volume and $\ln \Lambda$ is Coulomb logarithm. The subscript "j" in m, n and z indicates parameters for the background ion and parameters without subscript represent the resonant ion, which is experiencing the cyclotron resonance energy absorption. Figure 2.5 and Eq.(2.127) show that the energy of the resonant ion distribution increases with power but inversely to the background density, resonant ion density, and charge. Figure 2.5 shows that for appropriate conditions the resonant ion species diffuses in velocity space preferentially at high energies acquiring a high energy tail due to the decreasing velocity dependence of Coulomb collisions in Eq.(2.127). The power absorption parameter $\langle p \rangle$ is somewhat ambiguous unless a dynamic interface with the RF power absorption calculation is available. Another missing characteristic is the effect of the distribution anisotropy. A bounce-averaged diffusion operator has been calculated [35,19] in which the trapped

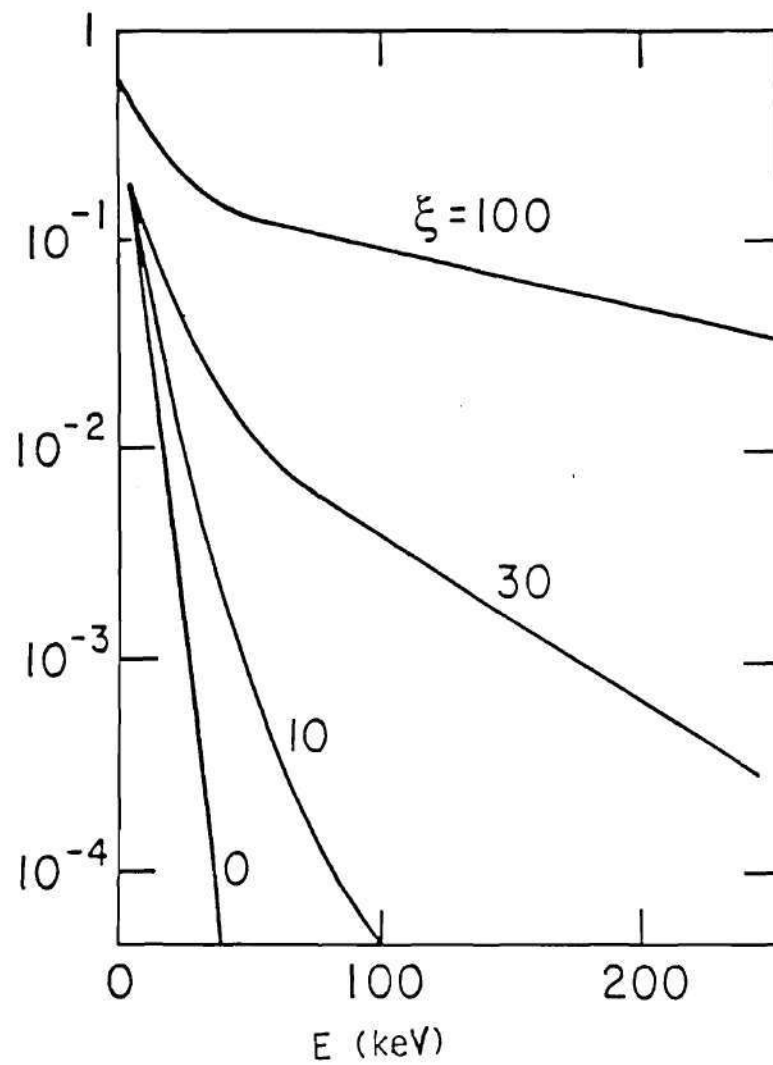


Figure 2.5: Minority ion distribution function for various values of the RF power density parameter, ξ . an energetic, non-Maxwellian distribution develops as a result of RF-induced velocity diffusion [18].

particle effect is considered by adding a drift term to the Fokker-Planck equation of the form

$$\frac{\partial f(\vec{v})}{\partial t} + \left(v_{\parallel} \frac{\partial}{\partial l} + \vec{v}_d \cdot \nabla \right) f(\vec{v}) = C(f) + \frac{\partial f_{rf}(\vec{v})}{\partial t}, \quad (2.133)$$

where l is the length along the bounce orbit and f is assumed to have been averaged over a gyro-orbit. A Monte-Carlo method for studying locally enhanced spatial diffusion indicates that enhanced fast ion diffusion from the resonance zone may occur. With simple plasma and RF models a non-bounce-averaged analysis was performed for the ATF RF power calculation in Chapter V.

Effect of the Helical Geometry

The most striking differences in a helical magnetic geometry compared to tokamak geometry are 3-dimensional characteristics such as the saddle point and helically twisting mod-B contours. Thus the inhomogeneity of the field along the ion path, toroidal asymmetry, and complex boundary which can be ignored or simplified in tokamak geometry become important.

Figure 2.6 shows a typical ATF magnetic geometry⁴. Since the mod-B contours have a saddle point (which in real space, is slightly off from the magnetic axis), there always exists a pair of resonance layers inside and outside or above and below (depending on the toroidal angle ϕ) the equatorial plane. Also note that the radial gradient of the mod-B contour is small near the saddle point.

Usually, for ICRH experiments in this geometry, the RF frequency is determined so that the resonance layer is placed on axis. For the minority heating regime, the location of the hybrid resonance layer depends on the minority concentration. The RF

⁴The author is grateful to D. K. Lee for providing this figure.

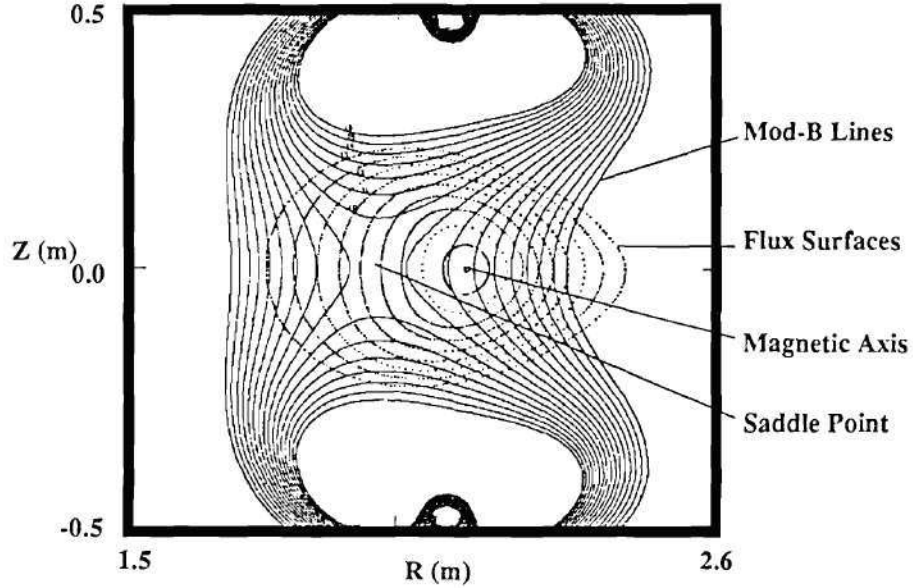


Figure 2.6: Typical magnetic geometry of the ATF Torsatron at $\phi = 15^\circ$

energy absorption would be different for each concentration. Numerical calculations were performed for several cases and are presented in Chapter V.

Since the resonance layer rotates helically, at certain antenna locations the resonance layer could be quite close to the antenna. This becomes a concern, especially when the edge evanescent layer is thick, so that RF power is likely to be deposited in the edge region. In ATF, most of the large $k_{||}$ modes have thick evanescent regions in low density target plasma, typically $\bar{n}_e \leq 0.8 \times 10^{13} \text{ cm}^{-3}$. For this case in a narrow band about $k_{||} = 0$, antenna could be efficient as happened for W VII-A (see the last section in this chapter).

After the L-2 stellarator [36] showed significant ion heating in the fast wave fundamental resonance heating regime (which was thought to be an ineffective regime due to poor polarization), a series of theoretical works [37,38] showed that helical magnetic geometry with its large inhomogeneity along the ion path could enhance the cyclotron absorption at the fundamental resonance layer.

Including the inhomogeneity of the magnetic field, the expression for the power absorbed by a particle was given as,

$$P = \frac{\omega_{pi}^2}{32\pi} \sum_{s=1}^{2l} \frac{|E_+(\theta_s)|^2}{\left| \frac{d\Omega_i}{d\theta} \right|_{\theta_s}}, \quad (2.134)$$

where l is the number of helical coils, and θ_s is the resonant angle where $\omega = \Omega_i$. Substituting $l = 1$ into this equation, Eq.(2.111) can be recovered, which was derived for tokamaks by Stix. To illustrate how much the magnetic inhomogeneity affects the RF power absorption, the coefficient of absorption enhancement κ was calculated, which becomes

$$\kappa \sim \frac{\omega_b}{(k_{||}v_i)^2} \left| \left(\frac{d\Omega_i}{d\theta} \right)_{\theta_s} \right|, \quad (2.135)$$

where ω_b is bounce frequency, usually denoted by $\frac{m}{R}v_i$ in a stellarator and $\frac{1}{qR}v_i$ in a tokamak. Here, m is the number of magnetic field periods around the torus for a stellarator and q is the quality factor for a tokamak. For $\kappa \gg 1$, the following condition should be satisfied.

$$1 \ll \eta = \frac{\Omega_i}{\omega_b} \ll \chi^2 = \left(\frac{\Omega_i}{k_{||}v_i} \right)^2. \quad (2.136)$$

In this calculation κ for a stellarator is larger than for a tokamak by a factor of mq .

There is also another theory [31] concerning cyclotron enhancement in helical geometry, in which the authors examine the effects of long wavelength modes (small $k_{||}$ or even $k_{||} = 0$ modes) which is supposed to be ineffective due to the negligible Doppler effect on resonance shift.

Numerical Simulation of ICRH in a Helical System

Here, a full wave RF heating code which calculates global RF wave fields in a helically symmetric, straight stellarator is described[39]. A modification which

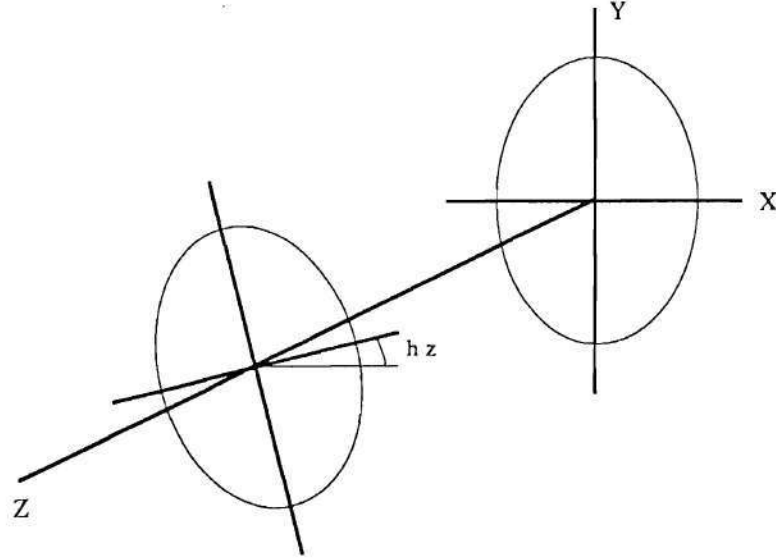


Figure 2.7: The Helically Symmetric Coordinate System

reflects the effect of the side wall image current on the antenna spectrum was made to this code[42]. The basic algorithm and ATF plasma model are discussed. Detailed modeling results for the initial ICRH experiments on ATF are discussed in Chapter V.

In a helically symmetric system as shown in Fig. 2.7, cylindrical coordinates are transformed to helical coordinates where $\phi = \theta - hz$ and h is helical pitch defined by $h = \frac{2\pi m}{R}$. Defining the scalar flux function $\psi(r, \theta)$ and $\xi(r, \theta)$ in a stellarator as,

$$\psi(r, \theta) = B_0 \frac{hr^2}{2} - r \sum_l \epsilon_l I_l'(lhr) \cos(l\phi), \quad (2.137)$$

$$\xi(r, \theta) = B_0 = \text{constant}, \quad (2.138)$$

where I_l is the modified Bessel function of order l and l is the number of helical windings. For $l = 2$ machines such as ATF, the $l = 2$ term is dominant in the \sum_l term and $\epsilon_2 = 2B_0 h a_c K_2'(2ha_c)$ where a_c is the coil radius. Then the magnetic field can be described as a function of ψ and ξ as

$$B_r^0 = \frac{1}{r} \frac{\partial \psi}{\partial \phi}, \quad (2.139)$$

$$B_\theta^0 = \frac{-\frac{\partial \psi}{\partial r} + hr\xi}{1 + h^2 r^2}, \quad (2.140)$$

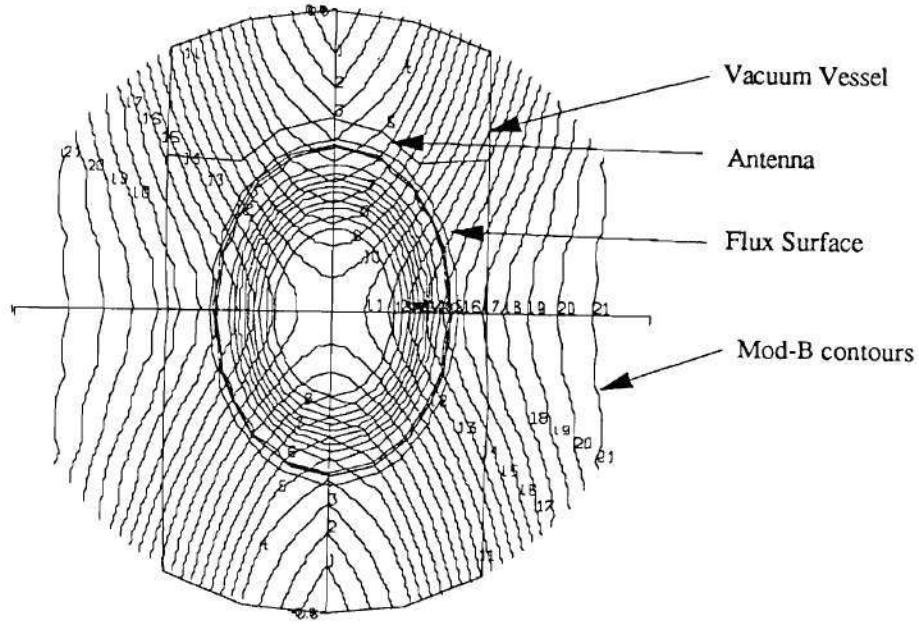


Figure 2.8: ATF Magnetic Geometry Simulated by a 2-D RF Heating Code

$$B_z^0 = \frac{hr(\frac{\partial \psi}{\partial r}) + \xi}{1 + h^2 r^2}. \quad (2.141)$$

This expression models the ATF ($l = 2, m = 12$) magnetic field structure as shown in Fig. 2.8.

The cyclotron resonance layers consist of a pair of hyperbolas. If minority ions exist, hybrid resonance layers and cut-off layers for the slow wave appear as two pairs of hyperbolas and the lower-hybrid cut-off layer as an ellipse near the plasma edge. Choosing the unit vectors in the orthogonormal coordinate system as

$$\hat{\delta}_1 = \frac{\nabla \psi}{|\nabla \psi|}, \quad (2.142)$$

$$\hat{\delta}_2 = \hat{b} \times \hat{\delta}_1, \quad (2.143)$$

$$\hat{\delta}_3 = \hat{b}, \quad (2.144)$$

where $\hat{b} = \vec{B}_0/|B_0|$, then the wave equation in helical coordinates,

$$-\nabla \times \nabla \times \vec{E} + k_0^2 \mathbf{K} \cdot \vec{E} = -i\omega\mu_0 \vec{J}_{ext}, \quad (2.145)$$

can be obtained as in Ref. [39].

In this code, warm plasma effects are included in \mathbf{K} according to the scheme of Ref. [40]. This is the so-called “reduced-order” scheme in which the ion Bernstein mode is discarded so that the order of the whole equation is reduced from fourth order to second order. It should be noted that the effect of the IBW on the energy balance exists in the kinetic flux term. \mathbf{K} is expanded to second order in the Larmor radius,

$$\mathbf{K} = \epsilon^{(0)} + ik_{\perp}\epsilon^{(1)} - k_{\perp}^2\epsilon^{(2)}, \quad (2.146)$$

where $\epsilon^{(0)}$ is the cold plasma dielectric tensor which can be expressed as

$$\epsilon^{(0)} = \mathbf{I} + \frac{i}{\epsilon_0\omega} \sum_s \sigma_s^{(0)}, \quad (2.147)$$

and $\epsilon^{(1)}$ and $\epsilon^{(2)}$ are the first and second-order finite Larmor radius corrections which can be expressed as

$$\epsilon^{(1,2)} = \frac{i}{\epsilon_0\omega} \sum_s \sigma_s^{(1,2)}, \quad (2.148)$$

and the exact form of the warm plasma conductivity tensor, σ , is given in Ref. [41]. In this code it is assumed that $E_{\parallel} = 0$ (zero electron mass). Figure 2.9 shows the warm plasma dispersion relation in ATF, calculated using the parameters in Table 2.1. In this figure, the RF frequency was reduced to show the hybrid resonance along the same chord as the fundamental minority resonance layer. Double resonance layers and cut-off layer are shown on both sides of the saddle point along with hybrid resonance and cut-off pairs for the ion Bernstein wave roots.

For the recessed box type antenna used for the ATF fast wave antenna, the image currents flow in both side walls with π phase difference from the strap current. To include the effect of this current, a modification was made to the code which includes a multistrap configuration. The detailed equations and analysis are given in Appendix A and in Ref. [42].

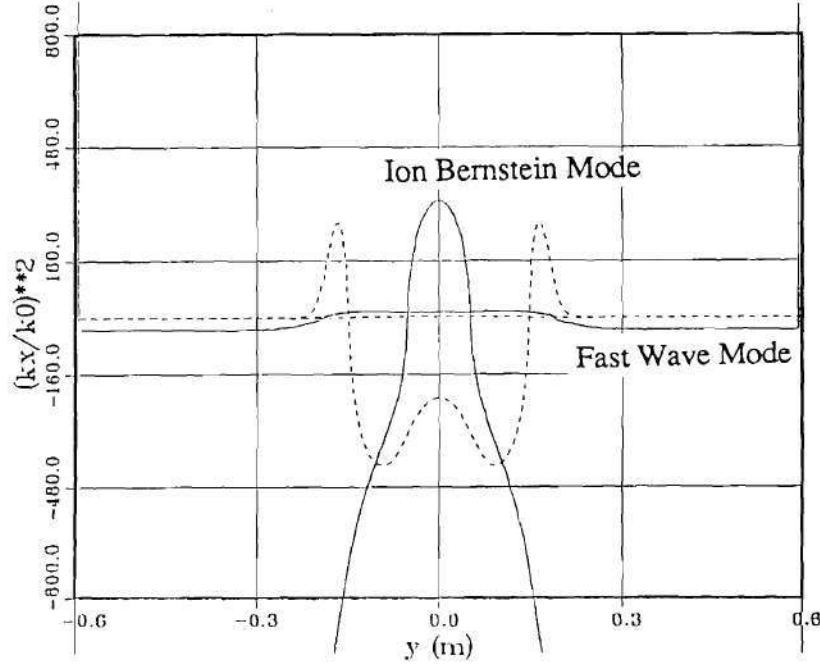


Figure 2.9: Warm Plasma Dispersion Relation in ATF Using Parameters from Table 2.1

The power absorption calculation is performed using the Poynting theorem:

$$\nabla \cdot \left\{ \frac{1}{2\mu_0} \text{Re}(\vec{E}^* \times \vec{B}) \right\} + \frac{1}{2} \text{Re} \left\{ \vec{E}^* \cdot \sum_s \vec{J}_s \right\} = -\frac{1}{2} \text{Re} \left\{ \vec{E}^* \cdot \vec{J}_{ext} \right\}, \quad (2.149)$$

where \vec{J}_s is the plasma current and \vec{J}_{ext} is the antenna current. The first term in the LHS is the Poynting flux, \vec{S}_p , the second term is the sum of the power dissipated to the plasma, $\sum_s P_s$, and the divergence of the kinetic flux of the wave, $\nabla \cdot \vec{Q}$, carried by particle's thermal motion. The mode conversion process is included in the kinetic flux term. Then Eq.(2.149) can be rewritten as

$$\nabla \cdot (\vec{S}_p + \vec{Q}) + \sum_s P_s = -\frac{1}{2} \text{Re} \left\{ \vec{E}^* \cdot \vec{J}_{ext} \right\}. \quad (2.150)$$

When the local energy deposition rate is expressed as

$$\dot{W} = \frac{1}{2} \text{Re}(\vec{E}^* \cdot \vec{J}_s), \quad (2.151)$$

Table 2.1: ATF Parameters for Simulation of D(H) Regime

Major radius	m	2.1
Minor radius	m	0.3
Magnetic field on axis	T	0.95
Central electron density	m^{-3}	3×10^{19}
Electron temperature at axis	keV	1
Ion temperature at axis	keV	0.2
Antenna Current	A	300
ICRF wave freq.	MHz	13.0

it automatically includes the $\nabla \cdot \vec{Q}$ term, which is the kinetic flux. Without an accurate definition of \vec{Q} , it is impossible to calculate the power partitioning. In this version of the code, no resolution of the absorbed power to the various plasma species was attempted.

The total loading impedance is calculated as

$$R(\omega) = \frac{2P_{tot}}{|I|^2} = \frac{4\pi}{|I|^2} \text{Re} \sum_{k_z} P_{abs}(k_z, \omega), \quad (2.152)$$

where $P_{abs}(k_z, \omega) = \int r dr \int d\theta \dot{W}(r, \theta)$.

In this code the 3-D power absorption by summing contributions from all k_z values. The helical geometry results in an asymmetric power absorption for $k_z = 0$, and the image currents suppressed the low- k_z modes. More detailed simulation of the ATF ICRH experiments was performed and is presented in Chapter V.

ICRH Experiments

Since ICRH experiments were first performed in the late 1950s, many experiments have been attempted with different schemes, powers, and goals on various devices. In this chapter, these experiments and their results are surveyed and summarized.

Early Experiments

Most of the early ICRH experiments were performed in Princeton on the B-65, B-66, and Model-C stellarators. In 1957, Stix [7] demonstrated the existence of the natural mode of oscillation of a plasma at a frequency just below the ion cyclotron frequency, and the first ICRH coupling experiment was performed on the B-65 race track stellarator in 1958 [43,44]. It is worthwhile to look at this first experiment.

The device was in the shape of a race track in which toroidal magnetic fields up to 20 kG could be produced. It was also equipped with a divertor and with helical windings to give a rotational transform to the confining magnetic field. A large transformer was used to induce an ohmic current.

The experimental procedure was as follows. After the initial ohmic heating phase, the resonance heating was turned on for 2 ms. The inductance of the heating coil was made resonant with capacitors, and measurements were made of the input voltage, the input current, and the phase angle.

Although the major ion species was deuterium, it was clear that there was a hydrogen minority in this plasma because of the double loading observed. There was a double peak in the deuterium resonance region. The second peak was interpreted as the generation of an ion cyclotron wave. This correlated with the D_β and $CIII$ line spectrum curves very well. But the neutron counting rate was sharply peaked at

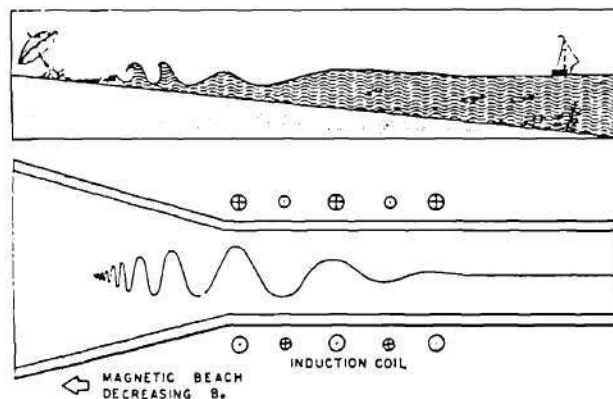


Figure 2.10: A "magnetic beach" analogy [44]

the deuterium resonance. It seems probable that these neutrons came from deuterons which were in the low density regions outside of the main discharge column and which were accelerated to high velocities by the cyclotron resonance process. The main result of this first ICRH experiment was that both the neutrons and the generation of ion cyclotron waves indicated that some of the transverse electric field penetrated into the plasma.

The wave mode used in this RF experiment was the ion cyclotron wave (slow wave) in the "magnetic beach" configuration. The term "beach" comes from the analogy with ocean waves which are moving in toward the shore and, because the water is getting shallower and shallower, the wavelength becomes shorter and shorter as shown in Fig. 2.10. Finally, in the shallow water the waves are unable to propagate and the wave energy is transformed into heat. The mode used (the slow wave) is left-hand circularly polarized in the same sense as the ion motion and gives good ion heating under the experimental conditions of devices during this period.

There were several other important effects observed which affected later experi-

ments. First, wave energy was absorbed at the cyclotron frequency of each ion species if two or more ion species existed in the plasma [43]. This phenomena contributed to uniform heating. Second, in later experiments [45] harmonic ion cyclotron wave propagation and absorption were observed and attributed to electron Landau damping of the small but finite parallel electric field associated with the slow wave branch. Third, the fast wave mode was observed propagating for frequencies just above the ion cyclotron frequency under certain experimental conditions [45]. Fourth, strong electrostatic loading of the antenna occurred which led to poor core heating and apparent surface power deposition. Finally, very energetic ions were observed and it was found that this limited the RF power which could be applied because of high radiation and neutron emission [46,47]. Fast wave characteristics and appropriate experimental condition for this wave were studied and also hot plasma effects and other damping mechanisms like transit-time magnetic pumping (TTMP) were actively studied in the late 1960's.

Tokamak Experiments

The tokamak concept was introduced [48] to the western world and actively studied in the late 1960s, and several small tokamaks were built in the early 1970s. Its different magnetic field configuration made it difficult to apply the slow wave scheme to the tokamak. Another branch, the fast wave, has the apparent disadvantage that the electric field is right-hand circularly polarized in the same direction as the electron motion and gives poor ion heating at the ion cyclotron resonance. However, in 1971, Adam and Samain [49] first reported a second harmonic heating scheme in which the poor ion heating capability of the fast wave would be enhanced at the second and higher harmonics due to thermal effects.

Another important observation was that the fast wave cavity resonance and toroidal eigenmodes exist. These were first observed in the TM-1-Vch [51] and TO-1

[52] in 1971. Cavity eigenmodes are global modes, which provide rather uniform power deposition around the torus. This eigenmode generation enhances antenna loading, so more power can be transferred to the plasma. Unfortunately, for a fixed plasma density and magnetic field, there exists an enormous set of eigenmodes and as Stix [13] pointed out, simultaneous excitation of multiple eigenmodes is undesirable because it leads to a very strong field in the local vicinity of the antenna which may cause very deleterious edge heating. Eigenmode studies were strongly pursued during the 1970s [53,54,55].

In 1974, Adam [53] tried to prove his second harmonic heating scheme and examine eigenmode characteristics in the ST tokamak. To investigate cavity modes, 22 RF probes were placed around the machine. It was found that toroidal eigenmodes depend on density variation. Plasma heating was attempted with $P_{rf} \sim 70KW$ at the fundamental and second harmonic ion cyclotron frequency.

The main results of this pioneering tokamak ICRH experiment were that second harmonic heating was more efficient than fundamental cyclotron heating and in both cases a high energy ion tail was formed. Their eigenmode study proved that eigenmodes led to large peaks in the loading just as the theory predicted. The ion temperature almost doubled in second harmonic heating but saturated due to loss of confinement of the high energy ion tail. This heating scheme was tested in other machines throughout the 70s and 80s, but the confinement of high energy ions was a major problem.

In 1976, TFR experiment [55,56,57] showed that the damping rate was stronger than predicted by theory. They found a large increase in the diamagnetic signal which had to be attributed to the presence of a minority of H in the D plasma and to damping effects associated with the presence of the $\omega = \Omega_H$ layer. They proposed that the existence of another singular layer (later it was identified as the ion-ion hybrid resonance) might play a significant role in this case. Thereafter, this hybrid

Table 2.2: Result in TFR600 for the Effect of η on Heating Features [59]
Heating Power and Thermal Energy for High η Plasma, without and with RF

		Without RF	With RF
Ohmic power	kW	420	335
RF power	kW	-	440
Electron thermal energy	kJ	6.3	7.8
Ion thermal energy	kJ	5.4	7.3
$(dW/dt)_0$	$\text{W}\cdot\text{cm}^{-3}$	-	1.4

Heating Power and Thermal Energy for Low η Plasma, without and with RF

		Without RF	With RF
Ohmic power	kW	411	510
RF power	kW	-	420
Electron thermal energy	kJ	6.6	7.3
Ion thermal energy	kJ	5.4	7.1
$(dW/dt)_0$	$\text{W}\cdot\text{cm}^{-3}$	-	1.0

resonance concept accompanied with mode conversion theory was actively examined both theoretically and experimentally.

In the minority heating regime, η , the minority concentration is a very important parameter and its effect on heating needed to be determined. The TFR600 experiment [59] in 1980 was dedicated to this subject. The results are listed in Table 2.2. Their observations were that at $\eta = 20\%$, (they called this regime the mode conversion regime because mode conversion is dominant in this case), power coupling to the plasma was linear with launched power and never saturated. Both the ion and electron temperature increased, while at $\eta \sim 2 \sim 3\%$, (they called this regime the minority regime because minority resonance heating is dominant in this case), ion heating was observed but electron heating was less efficient than that of the first

case and an unconfined high energy ion tail was produced. All subsequent TFR experiments [79,60] were performed in the mode conversion regime.

The principal conclusions in TFR Experiments were that 60% of the RF power was delivered to the plasma, 20% was lost in the antenna and transmission line, and the other 20% was lost in various mechanisms occurring near the wall (which induced an impurity generation problem). Another problem was the degradation of the energy confinement by metal impurities. In this heating regime, as expected from the theory, the main fraction of the RF power transmitted from the high field side of the torus was absorbed by electrons, leading to a fast initial heating rate of that component. In experiments with a metallic limiter, where an important fraction of the power absorbed in the center of the plasma was radiated by high Z impurities, the large heating rate of ions observed was attributed to collisional equipartition with metallic ions accelerated at their second harmonic cyclotron frequency.

While TFR experiments were performed in the mode conversion regime, PLT investigated the minority regime. First the effect of different ion species on loading was examined in a 1980 experiment [61]. They found that in the H minority regime, the proton and deuterium distributions were Maxwellian and significant electron heating was observed, while in the ^3He minority regime, the efficiency of deuterium heating was increased and there was no significant electron heating. Thus they used ^3He as the minority species for their high power minority heating experiments between 1982 and 1985 [62,63,78,64].

An impressive ion temperature increase was observed and large sawteeth in the electron temperature profile were presented. Since the ion temperature rise was very large, the PLT group hypothesized that other processes than pure cyclotron damping by the minority component played a role in the absorption mechanism in these ^3He minority heating experiments. They also made several important observations about energy loss processes: 1) Even when a metallic limiter was used, power radiation

due to the high Z impurities did not increase dramatically as observed in the TFR experiments. 2) High energy ion formation were attributed to banana trapped ions and in the ^3He minority regime the tail energy was much reduced compared to the H minority regime. 3) Electron density during RF heating was appreciably increased leading to charge exchange loss.

ICRH experiments in PLT demonstrated the efficiency of the minority heating regime, and proved that the 1980 TFR result was machine dependent: high-energy ion confinement in PLT was believed to be better than that in TFR.

Impurity production and other edge phenomena during ICRH have become concerns for efficient RF heating [65,66,67,68,69,70]. The wave spectrum launched from the antenna was believed to affect coupling, and in 1983 antenna phasing experiments were begun to examine the effect of the wave spectrum on heating, coupling and edge conditions. Impurity reduction by optimizing the antenna phasing was first observed in the JFT-2M tokamak [80]. They proved that the reduction in impurity emissions and radiation loss were closely correlated with the amount of power radiated from the antennas with a parallel wave number near $k_{\parallel} = 0$. They thought that coaxial modes propagating in the vacuum region between the plasma and vessel wall might be increasing the impurity production during ICRH. This experiment was tried in several other tokamaks and gave similar results [70,72].

General characteristics of plasma-material interaction (PMI) during ICRH are listed in Table 2.3.

Recent ICRH Experiments

Two major problems which still remain to be solved for ICRH are confinement degradation during RF heating and strong edge/RF interaction. These may be considered as a single problem because the strong edge/RF interaction is presumed to

Table 2.3: General Changes in Edge Plasmas during ICRH

Line averaged density	Up
Total radiation	Up (mostly C and O)
Edge density	Up
Scrape-off-layer (SOL) length	Up
Edge electron temperature	Up
Dependence of edge effects on antenna phase	yes
Particle acceleration in edge region	yes

be the major reason for confinement degradation. Some possible mechanisms for edge heating/ionization [73] are coupling to inaccessible modes (e.g., coaxial mode or electrostatic mode), near-field particle acceleration (e.g., resonant interaction or strong field effect), nonlinear collective effects (e.g., parametric decay or ponderomotive effect), and physical sputtering, arcing, or evaporation. In the ASDEX ICRH experiments [74], improved RF launching conditions were found when the wall was carbonized and ICRH was combined with NBI. Also a clear anticorrelation between impurity production and wave absorption was observed, with inefficient absorption leading to increased impurity production. The JET experiment [75] on impurity production also revealed that carbonization reduced impurity production.

Extensive studies of plasma edge conditions during ICRH were performed in JET with Langmuir probes. In these experiments [76,77] the following observations were made: The electron temperature in the edge region increased during ICRH, particle fluxes increased as a result of ICRH, the source of increased particle fluxes was in the edge rather than in the core plasma, plasma-sheath rectification took place, and the edge temperature rise was probably a result of direct heating of the edge by the RF. Very active study of this subject is still going on both theoretically and experimentally.

The discovery of a high-confinement regime, the so-called H-mode, which combines the virtues of good global and central confinement even with auxiliary heating was of paramount importance for fusion research. In 1986, the ASDEX team [81] investigated the H-mode in ICRH plasmas with and without additional NBI. For the first time, the H-mode was realized with ICRH alone using H minority in a deuterium plasma. With ICRH, usually the impurity situation is unfavorable for transition into the H-mode. The ICRH-induced impurity release reduces the energy flux from the center to the plasma periphery because of increased central iron radiation. Strong recycling and an enhanced low-Z impurity level may additionally cool the plasma boundary thus hampering the H-mode transition which appears to be strongly linked to high edge electron temperature. This deleterious influence of metal impurity radiation has been overcome either by increasing the power flow through additional NBI heating or by carbonizing the torus walls. Typical characteristics of the H-mode transition are density increases and the presence of the high frequency edge localized mode (ELM). It should be noted that ICRH-induced ion tails perpendicular to the toroidal field have shown no significant negative influence on global confinement.

The JET experiment is representative of the current status of ICRH heating experiments. JET has eight antennas in operation. Each antenna can launch up to 4 MW and has a quadrupole conductor and an actively cooled Faraday shield. The shield blades are tilted to line up with the equilibrium magnetic field, thereby shorting out the parallel electric field. The effect of antenna phasing on edge conditions was investigated. This experiment was performed with three antennas with various poloidal antenna current configurations. The quadrupole configuration gave the most favorable results for coupling and edge/RF interaction.

In JET, it is difficult to couple large amounts of RF energy when the plasma current is low. The plasma disrupts at $P_{rf} = 1$ MW. Combining NBI with ICRH produced favorable heating results in JET. The NBI increased the antenna loading.

There exists an interesting regime called “Monster sawtooth”, in which the internal relaxations (sawteeth) stop and the plasma is remarkably free from MHD activity for about one second. The central electron temperature more than doubles and a peak temperature of 7.4 KeV has been obtained with 10 MW of additional power. They also combined ICRH with pellet injection which again gave improved confinement. Finally, in 1989, the JET team [82] achieved $Q_{D-D} \sim 0.8$ with 16 MW ICRH + NBI and pellet injection. Many improvements in heating came from experiments with pellet injection and Be-limiter experiments. At present ICRH experiments have just begun in other large tokamaks such as TFTR, JT-60, and DIII-D with higher power and more complicated antenna systems.

The Compact Ignition Tokamak(CIT) is designed to have a high power ICRH system without an NBI system. A waveguide launcher is also being developed and tested.

The next decade will be dedicated to testing high power RF heating on reactor-sized devices. Optimized antenna phasing and favorable wall conditioning will be used to avoid deleterious impurity and radiation problems in attempts to realize D-T ignition.

ICRH in Helical Devices

Even though ICRH experiments were first performed in helical devices (the B-65 stellarator, the Model-C stellarator), few helical devices were operated after the tokamak concept was introduced in the late 1960s. The series of Uragan torsatrons and the L-2 stellarator in USSR, the series of Heliotrons in Japan, and the series of Wendelstein stellarators in Germany were important ones. There were also several small devices in England, the United States, and Australia.

In the 1980s, the study of helical devices was revisited in search of a steady-state

operational concept. Several medium-size machines were constructed and operated. The Heliotron-E, WVII-AS and ATF were designed, and built in this period.

ICRH experiments were conducted on stellarators in the USSR and Japan both for heating and plasma production. In the Uragan-3 torsatron[84], ICRF was used for plasma initiation and provided $n_e \sim 2 - 4 \times 10^{12} \text{ cm}^{-3}$, $T_i \sim 1 \text{ keV}$ and $T_e \sim 300 \text{ eV}$ plasma for $\sim 50 \text{ msec}$ with 400 kW RF power. ICRF heating was tested on this machine and previous machines in this series and anomalously fast ion heating and loss phenomena were observed. It was thought that this was due to non-linear coupling of RF power and was correlated with the existence of the parametric decay instability.

In the L-2 stellarator[85], ICRH was used on ohmic plasmas at the fundamental cyclotron resonance frequency. Although this was an unusual scenario, they observed good ion heating with this scheme. Based on this result, they theorized the enhancement of the cyclotron damping in the helical geometry described in the previous section. In the H-minority regime, they obtained a marginal increase in ion temperature of 30 to 50 eV, high toroidal damping and low loading impedance (less than 0.2Ω) with 100 to 150 kW rf power. No significant radiation nor impurity influx was observed.

In Wendelstein VII-A[86], two types of antenna were used: a narrow loop antenna and a broad antenna. Due to large increases of the radiation loss, ICRH heating efficiency was very low. In the minority regime with the broad antenna, some increase in the stored energy was observed. They suffered with very low loading, less than 0.1Ω of plasma loading compared to the 0.3Ω of vacuum loading, resulting in large ohmic loss to the antenna structure and transmission line. However, it is interesting to note that the broad antenna worked better than the conventional loop antenna, due to the fact that it launched a narrow band of the $k_{||}$ spectrum. Most of these results were in good agreement with full-wave numerical calculations.

The most successful ICRH experiments were done in Heliotron-E[87,88]. Since its size and plasma parameters are comparable to the ATF, the results of this machine is presented in some detail. They used a complicated high-field-side-launch antenna. A coupling study was done in the predecessor, Heliotron-DR, with different antenna types and configurations. The two main configurations were the low-field-side launch and the high-field-side launch. Loading was better with high-field-side launch and it showed a strong magnetic field dependence, such that loading was peaked for a magnetic configuration with the resonance layer located on axis. With low-field-side launch, peak loading always occurred for higher field with the resonance layer slightly outside the magnetic axis. The high-field-side-launch configuration was chosen for Heliotron-E and yielded good loading results, although part of antenna structure was damaged by direct contact with the plasma. The initial ICRH results were promising. Substantial bulk ion and electron heating were obtained, but a significant increase in radiation was a concern for long pulse operations. In the second stage, they upgraded the RF power source and antenna to deliver up to 1.5 MW to the plasma. They also attempted ion Bernstein wave heating (IBWH) and slow wave (ion cyclotron wave) heating, which showed good heating results. With 700 kW of RF power, they observed a 400 eV increase in the ion temperature. Very good correlation with minority concentration was observed, which demonstrated that higher RF power absorption by the minority ions occurred when the hybrid resonance layer was on axis. Radiated power and impurity influx still increased with time and suppressed any electron temperature increase. The ion heating efficiency was found to be around $1\text{-}2\text{ eV}\cdot 10^{19}\text{m}^{-3}/\text{kW}$ which is comparable to similar sized tokamaks. Numerical simulation was well matched with the experiment.

The ATF ICRH experiments should provide useful data on the other configuration — low-field-side launch with movable antenna. Loading impedances, the effect of minority concentration, frequency, and ion confinement are important issues to

be pursued and addressed. In the work described in this thesis, those issues were pursued and the experimental observations were analyzed via numerical simulations. These are the main contents of Chapters IV and V.

REFERENCES

- [1] Jackson, J. D., *Classical Electrodynamics*, (John Wiley & Sons, New York, 1975) chapter 7.
- [2] Landau, L. D., Lifshitz, E. M. and Pitaevskii, L. P., *Electrodynamics of Continuous Media*, (Pergamon Press, Oxford, 1984) chapter 9.
- [3] See reference [8] in Chapter III.
- [4] Stix, T., H., *The Theory of Plasma Waves*, (McGraw-Hill, New York, 1962) chapter 2.
- [5] Chen, F. F., *Introduction to Plasma Physics and Controlled Fusion*, (Plenum Press, New York, 1984) chapter 4.
- [6] Swanson, D. G., *Plasma Waves*, (Academic Press, San Diego, 1989) chapter 2.
- [7] Stix, T. H. et al., *Phys. Rev.* **106**, 1146 (1957).
- [8] Swanson, D. G. et al., *Phys. Rev. Lett.* **35**, 517 (1975).
- [9] Jaquinot, J. et al., *Phys. Rev. Lett.* **39**, 88 (1977).
- [10] Takahashi, H., in *Proc. of 3rd Inter. Congress on Waves and Instabilities in Plasma*, Palaiseau, France, 1977.
- [11] Perkins, F. W., *Nucl. Fusion* **17**, 1197 (1977).
- [12] Shepard, T. D., "Fast Wave Ion Cyclotron Resonance Heating Experiments on the Alcator C Tokamak," Ph.D Thesis, MIT, 1988.

- [13] Stix, T. H., in Proc. of Third Symp. on Plasma Heating in Toroidal Devices, Varenna, Italy (1976).
- [14] Thompson, H. R., "Second Harmonic Ion Cyclotron Resonance Heating by the Fast Magnetosonic Wave on the PLT Tokamak," Ph.D thesis, Princeton University, 1984.
- [15] Paoloni, F. J., MATT-1119, PPPL, Princeton University (1975).
- [16] Pochelon, A., et al., *Bull. Am. Phys. Soc.* **32**, 1838 (1987).
- [17] Ichimaru, S., Basic Principles of Plasma Physics: A Statistical Approach, (The Benjamin/Cummings Publishing Company, 1973) chapter 3.
- [18] Stix, T. H., *Nucl. Fusion* **15**, 737 (1975).
- [19] Hammet, G. W., "Fast Ion Studies of Ion Cyclotron Heating in the PLT Tokamak," Ph.D Thesis, Princeton University, 1986.
- [20] Budden, K. G., Radio Waves in the Ionosphere, (Cambridge University Press, Cambridge, 1961).
- [21] Wasow, W., *Ann. Math.* **52**, 350 (1950).
- [22] Stix, T. H., *Phys. Rev. Lett.* **15**, 878 (1965).
- [23] Swanson, D. G., "Mode Conversion and Tunneling at the Two-Ion Hybrid Resonance," *Phys. Rev. Lett.* **36**, 316 (1976).
- [24] Ngan, Y. C. and Swanson, D. G., "Mode Conversion and Tunneling in an Inhomogeneous Plasma," *Phys. Fluids* **20** 1920 (1977).
- [25] Faulconer, D. W., *Phys. Lett.* **75A**, 355 (1980).

- [26] Erokhin, N. S. and Moiseev, S. S., Review of Plasma Physics, Leontovich, M. A. eds., (Consultants Bureau, New York, 1979), Vol. 7, 181.
- [27] Antonsen, T. M. and Manheimer, W. M., *Phys. Fluids* **21**, 2295 (1978).
- [28] Swanson, D. G., "Cyclotron Harmonic Absorption via the Green's Function for the Mode Conversion-Tunneling Equation," *Phys. Fluids* **21**, 926 (1978).
- [29] Swanson, D. G., "The Effects of Localized Absorption on the Mode Conversion Process in the RF Heating of Plasmas," *Nucl. Fusion* **20**, 949 (1980).
- [30] Colestock, P. L. and Kashuba, R. J., "The Theory of Mode Conversion and Wave Damping Near the Ion Cyclotron Frequency," *Nucl. Fusion* **23**, 763 (1983).
- [31] Grekov, D. L., Carter, M. D. and Pyatak, A. I., "Cyclotron Absorption of Fast Magnetosonic Waves by Trapped Ions in Tokamak," *Sov. J. Plasma Phys.* **15**, 661 (1989).
- [32] Cattanei, G. and Croci, R., *Nucl. Fusion* **17**, 239 (1977).
- [33] Kaladze, T. D., Pyatak, A. I. and Stepanov, K. N., *Sov. J. Plasma Phys.* **7**, 539 (1981).
- [34] Kennel, C. F. and Engelman, F., "Velocity Space Diffusion from Weak Plasma Turbulence in a Magnetic Field," *Phys. Fluids* **9**, 2377 (1966).
- [35] Kerbel, D. G. and McCoy, M. G., *Phys. Fluids* **28**, 3629 (1985).
- [36] Batyuk, V. A. et al., Proceedings of the 11th European Conf. on Controlled Fusion and Plasma Physics, Aachen, 1983.
- [37] Kovrizhnykh, L. M. and Moroz, P. E., *Sov. Phys. Tech. Phys.* **29**, 384 (1984).
- [38] Kovrizhnykh, L. M. and Moroz, P. E., *Sov. Phys. JETP* **60**, 946 (1984).

- [39] Jaeger, E. F., Weitzner, H. and Batchelor, D. B., "ICRF Heating in a Straight, Helically Symmetric Stellarator," Report ORNL/TM-10223, 1987.
- [40] Smithe, D., et al., "An Algorithm for the Calculation of Three-Dimensional ICRF Fields in Tokamak Geometry," *Nucl. Fusion* **27**, 1319 (1987).
- [41] Jaeger, E. F., Weitzner, H. and Batchelor, D. B., "Exact and Approximate Solutions to the Finite Temperature Wave Equation in a One-Dimensional Perpendicularly Stratified Plasma," *Nucl. Fusion* **28**, 53 (1988).
- [42] Kwon, M., et al., "Simulation of ICRH on ATF," *Bull. Am. Phys. Soc.* **33**, 2016 (1988).
- [43] Stix, T. H., et al., *Phys. Fluids* **1**, 446 (1958).
- [44] Stix, T. H., et al., in Proc. of 2nd Inter. Conf. on the Peaceful Uses of Atomic Energy, Vol. 31, 282 (U.N., Geneva, 1958).
- [45] Kristiansen, M., et al., *Phys. Fluids* **10**, 596 (1967).
- [46] Hooks, W. M., et al., *Phys. Fluids* **8**, 1146 (1965).
- [47] Rothman, M. A., et al., *Phys. Fluids* **12**, 2211 (1969).
- [48] Artsimovich, L. A., *Nucl. Fusion* **12**, 215 (1972).
- [49] Adam, J. et al., EUR-CEA-FC-579, 29 (1971).
- [50] Klima, R., *Nucl. Fusion* **11**, 357 (1971).
- [51] Vdovin, V. L., et al., *JETP Lett.* **14**, 149 (1971).
- [52] Ivanov, N. V., et al., *JETP Lett.* **14**, 138 (1971).

- [53] Adam, J., et al., IAEA-CN-33/A3-2 (5th Conf. Proc. on Plasma Physics and Controlled Nuclear Fusion Research, Tokyo, 1974).
- [54] Hosea, J., Proc. of Third Symp. on Plasma Heating in Toroidal Devices, Varenna, Italy (1976).
- [55] Equipe TFR, in Proc. of Third Symp. on Plasma Heating in Toroidal Devices, Varenna, Italy (1976).
- [56] TFR Group, in Proc. of Third Symp. on Plasma Heating in Toroidal Devices, Varenna, Italy (1976).
- [57] TFR Group, in Theoretical and Experimental Aspects of Heating of Toroidal Plasmas (Proc. 3rd International Meeting, Grenoble, France, (1976).
- [58] Adam, J., et al., in Proc. of 4th European Conf. on Cont. Fusion and Plasma Physics, Rome (1970).
- [59] Equipe TFR, IAEA-CN-38/D-3 (8th Conf. Proc. on Plasma Physics and Controlled Nuclear Fusion Research, Brussels, 1980).
- [60] Equipe TFR, Heating in Toroidal Plasmas(Proc. 3rd joint Varenna-Grenoble International Symposium, Grenoble, France) Vol.1, 225 (1982).
- [61] Hosea, J., et al., IAEA-CN-38/D-5-1 (8th Conf. Proc. on Plasma Physics and Controlled Nuclear Fusion Research, Brussels, 1980).
- [62] Whang, D. Q., et al., IAEA-CN-41/I-1 (9th Conf. Proc. on Plasma Physics and Controlled Nuclear Fusion Research, Baltimore, 1982).
- [63] Kaita, R., et al., PPPL-1993, PPPL, Princeton University (1983).
- [64] Mazzucato, E., et al., PPPL-2208, PPPL, Princeton University (1985).

- [65] Whang, D. Q., et al., *J. Vac. Sci. Technol.* **20**, 1273 (1982).
- [66] Cohen, S. A., et al., *J. Nucl. Matt.* **128-129**, 280 (1984).
- [67] Ogawa, H., et al., *J. Nucl. Matt.* **128-129**, 298 (1984).
- [68] Noda, N., et al., *J. Nucl. Matt.* **128-129**, 304 (1984).
- [69] De Chambrier, A., et al., *J. Nucl. Matt.* **128-129**, 310 (1984).
- [70] Colestock, P. L., et al., *J. Vac. Sci. Technol.* **A3**, 1211 (1985).
- [71] JFT-2 Group, IAEA-CN-44/F-1-3 (10th Conf. Proc. on Plasma Physics and Controlled Nuclear Fusion Research, London, 1984).
- [72] Tamai, H., et al., *Nucl. Fusion* **26**, 365 (1986).
- [73] Colestock, P. L., ICRH/Edge Workshop, Oak Ridge, 1987.
- [74] Fussmann, G., et al., *J. Nucl. Matt.* **145-147**, 96 (1987).
- [75] Stangeby, P. C., *J. Nucl. Matt.* **145-147**, 105 (1987).
- [76] Erents, S. K., et al., *J. Nucl. Matt.* **145-147**, 231 (1987).
- [77] Bures, M., et al., JET-P(87)18, JET Joint Undertaking (1987).
- [78] Hosea, J., et al., PPPL-2117, PPPL, Princeton University (1984).
- [79] Equipe TFR, IAEA-CN-41/I-2 (9th Conf. Proc. on Plasma Physics and Controlled Nuclear Fusion Research, Baltimore, 1982).
- [80] JFT-2 Group, IAEA-CN-44/F-1-3 (10th Conf. Proc. on Plasma Physics and Controlled Nuclear Fusion Research, London, 1984).
- [81] Steinmetz, K., et al., *Phys. Rev. Lett.* **58**, 124 (1987).

- [82] JET team announced that they got $Q_{D-D} \sim 0.8$ at the late 1989 with RF+NBI+pellet. See JET posters in *Bull. Am. Phys. Soc* **34**, 1989.
- [83] Colestock, P. L., Course and Workshop on Applications of RF waves to Tokamak Plasmas, Varenna, Italy (1985).
- [84] Bacaev, V. V., et al., IAEA-CN-44/D-I-3 (10th Conf. Proc. on Plasma Physics and Controlled Nuclear Fusion Research, London, 1982).
- [85] Batyuk, V. A., et al., in Proc. of 11th European Conf. on Cont. Fusion and Plasma Physics, Aachen (1983).
- [86] Cattanei, C., et al., IPP Report 2/290, Max-Planck-Institut für Plasmaphysik (1987).
- [87] Mutho, T., et al., *Nucl. Fusion* **24**, 1003 (1984).
- [88] Mutho, T., et al., IAEA-CN-47/D-I-1 (11th Conf. Proc. on Plasma Physics and Controlled Nuclear Fusion Research, Kyoto, 1986).

CHAPTER III

EXPERIMENTAL APPARATUS

In this chapter, the Advanced Toroidal Facility (ATF) and its operating parameters will be presented with brief description of the available diagnostics for ICRH studies. The antenna and RF systems are also described. More lengthy explanation will be given for the Langmuir probe and RF probes, which were specially fabricated for this study. Finally the ATF data acquisition system will be outlined.

The Advanced Toroidal Facility

The ATF is a torsatron type stellarator with $l = 2$ and $m = 12$, which means that there are two sets of helical field coils with 12 field-periods. Several references[1, 2,3,4,5] have been published reporting the features of ATF and some initial results of operations. Here, some of the essential features and goals of ATF are described along with physical machine parameters. Table 3.1 shows the major physical dimensions of ATF and the parameters of its magnetic configuration.

A currentless plasma was generated by two, 53 GHz, 200 kW gyrotrons¹. Most of the current-driven instabilities can be avoided in this scheme. Three pairs

¹Some amount of current still exist.

Table 3.1: Parameters of ATF Vacuum Vessel and Magnetic Configuration

Major Radius	m	2.1
Average Plasma Radius	m	0.3
Average HF Coil Radius	m	0.46
Plasma Volume	m ³	3.7
Magnetic Field on Axis	T	0.95 or 1.9
Number of HF Coils		2
Number of Toroidal Periods		12
Plasma Aspect Ratio		7
Edge Rotational Transform		0.95
Central Rotational Transform		0.35

of vertical-field (VF) coils provide the opportunity to study various magnetic configurations for optimization. This feature is closely related to the potential of high- β operation with an optimized magnetic configuration and to operation in the second stability regime. Initial results on this issue were encouraging[5,6].

A top view of the ATF showing the locations of the major diagnostics is shown in Fig. 3.1. The fast wave antenna was located at the TN-5 port. Two RF probes and a Langmuir probe were located at the same port. Another RF probe was placed on Bottom-4 port. The scannable neutral particle analyzer (NPA) was at the TN-1 port and measured the minority ion tail and ion distribution. Spectrometers were at the adjacent port, TN-23, and consisted of a grazing incidence spectrometer, a vacuum Czerny-Turner spectrometer and a visible spectrometer. Two pumped limiters were located at Top-14 and Bottom-16 and the ECE system at Top-6. The Thomson scattering system was located at Top and Bottom-8 and TN-9 ports and a 2 mm interferometer was located at TN-21. Two ECH inputs came from Top-10 and

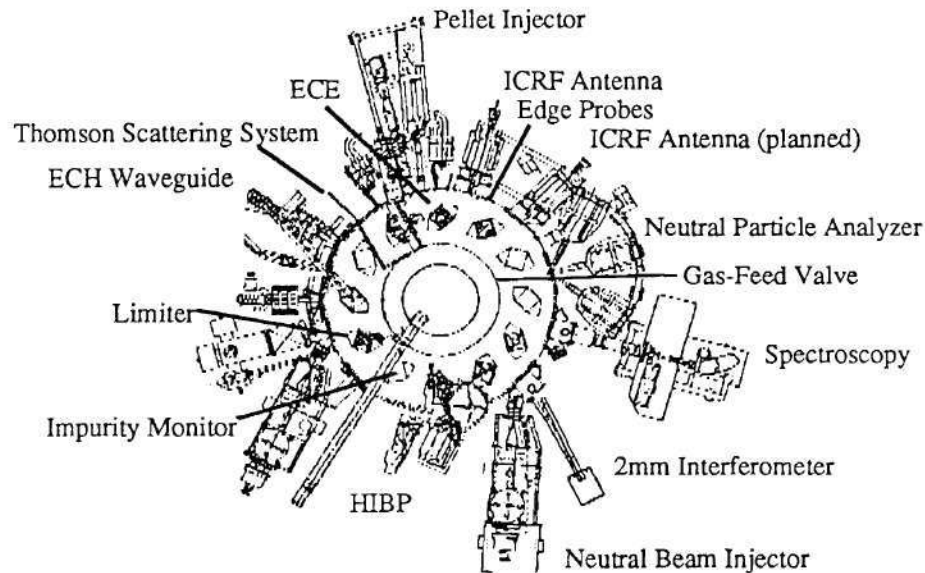


Figure 3.1: Top View of the ATF with Diagnostics

12 ports and two gas-puff valves were located in IN-1 and IN-17.

The optimized helical field coil configuration ($l = 2, m = 12$) gives a moderate rotational transform ($\iota/2\pi|_{r=0} = 0.35, \iota/2\pi|_{r=a} = 0.95$), shear (~ 3), and aspect ratio ($R/\bar{a} \simeq 7$). This configuration was optimized for high- β operation in the second stability regime which is one of the original goals of the ATF project.

Figure 3.2 shows the ATF magnetic coil sets consisting of two sets of helical coils, and three pairs of poloidal field coils referred to as inner, outer, and mid-vertical field coils. With these coil sets, wide variations from the standard magnetic configuration can be obtained which provides for great flexibility in the study of various magnetic configurations.

The $|B|$ contours are rather complicated because of the two sets of helical windings as shown in Fig. 2.6.

The $|B|$ contours are important to ICRH experiments because they determine

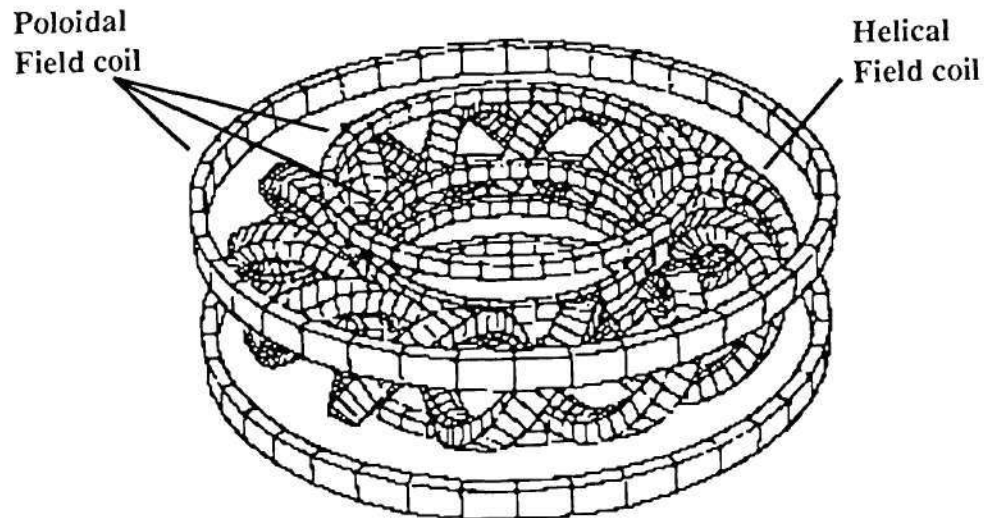


Figure 3.2: The ATF Coil Sets

the location of wave resonance layers². The profound difference from tokamaks is that the $|B|$ contours are quadrupolar and twisted. This makes the wave-particle interaction a three dimensional problem and difficult to simulate when compared with calculations for tokamak geometry.

The ATF has run with magnetic fields of 0.95 T and 1.9 T at the magnetic axis. In both cases, the $|B|$ contours are very similar.

²In a real situation, the actual location of the resonance layer also depends on particle velocities, the wave propagation angle, and the minority concentration.

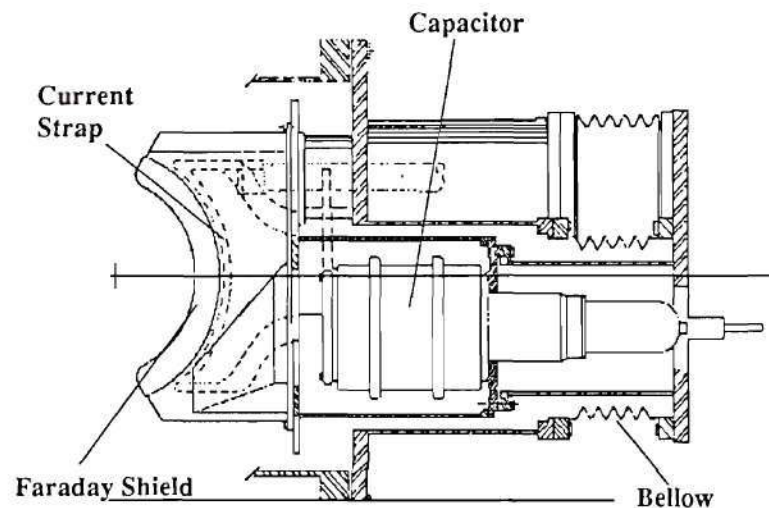


Figure 3.3: The ATF Fast Wave ICRH Antenna

The Fast Wave Antenna

The ATF ICRF antenna is a resonant double loop (RDL) type antenna which has two grounded capacitors. The ATF antenna³ is shown in Fig. 3.3. Compared to other types of antennas such as a single loop antenna, the RDL configuration has advantageous electrical properties. Since the RDL antenna is matched at the feed point, it results in low voltages and currents in the feedline. The antenna is tunable over a wide frequency range, too. For the ATF antenna, this range extends from several MHz to mid-thirty MHz. In addition to these advantages, there were no external tuning loops or tuning elements, which simplified the system and significantly reduced the overall cost. But there were mechanical disadvantages to be overcome

³The author is grateful to R. H. Goulding, F. W. Baity, T. D. Shepard and D. J. Hoffman for providing data about antenna measurements and for enlightening discussions about antenna modeling.

such as vacuum-side complexity and no access to the tuning capacitors while the system is under vacuum.

Mechanical Design

The ATF fast-wave antenna was designed to launch the fast wave at power levels up to 1 MW, to be radially movable with a range of 15 cm, and to have no external cooling system for short pulse operations.

The current strap was made from copper and most of the other structures were fabricated from stainless steel except the Faraday shield tubes, which were made from Inconel 600 and brazed to graphite tile. The current strap was 10.8 cm wide and 43.3 cm in total length. The total poloidal width was 122 degrees in angle with a radius of 20.3 cm. Two legs which stretched from either end of the strap were connected to the capacitor housing. The RF power was fed to the top end of the strap by a 50 Ω , transmission line with copper-inner-conductor, stainless-steel-outer-conductor, which was connected to a 50 Ω vacuum feedthrough located about 2 m from the antenna. Figure 3.4 is a side view of the antenna in which a cross section of the ATF vacuum vessel, relative antenna location, bellows system and vacuum feedthrough are shown. The current strap was tilted by 10 degrees to the vertical alignment to optimize the polarization of the launched wave by minimizing $E_{||}$ components. The minimum distance between the current strap and the back plane was about 12.3 cm and the distance of each side wall from the center was 10.5 cm.

There were 45 Faraday shield tubes arranged in two tiers. The front rods were 0.95 cm in diameter, copper plated Inconel tubes with front half sections brazed to graphite. The rear rods were 1.27 cm in diameter, fabricated from stainless steel with rear half sections which were thick copper plated. These elements were welded to the stainless-steel Faraday-shield frame, which also consisted of a side wall and strap housing. The inside of the Faraday shield frame was copper plated. Graphite

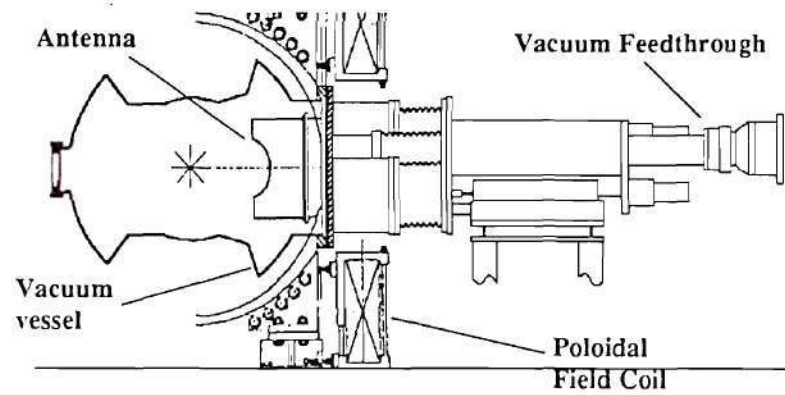


Figure 3.4: Diagram of the ATF Antenna System Installation

bumper tiles were also provided to protect the welds and the side walls.

The radial translation of the antenna was provided by an electric motor. Rotation was changed to translation by a ball screw and thrust bearing unit. A bellows was provided between the port cover section and the moving carriage section.

Electrical Properties

The electrical behavior of the antenna was modeled in two different ways[7]. The simple model is a lumped-element model, as shown in Fig. 3.5.(a). To take the finite wavelength effect into account, a distributed model was also considered as shown in Fig. 3.5.(b).

In a lumped-element model, an electrical circuit is represented by a few properly chosen lumped coupling elements, in which the distributed effects of the electric or magnetic fields are neglected.

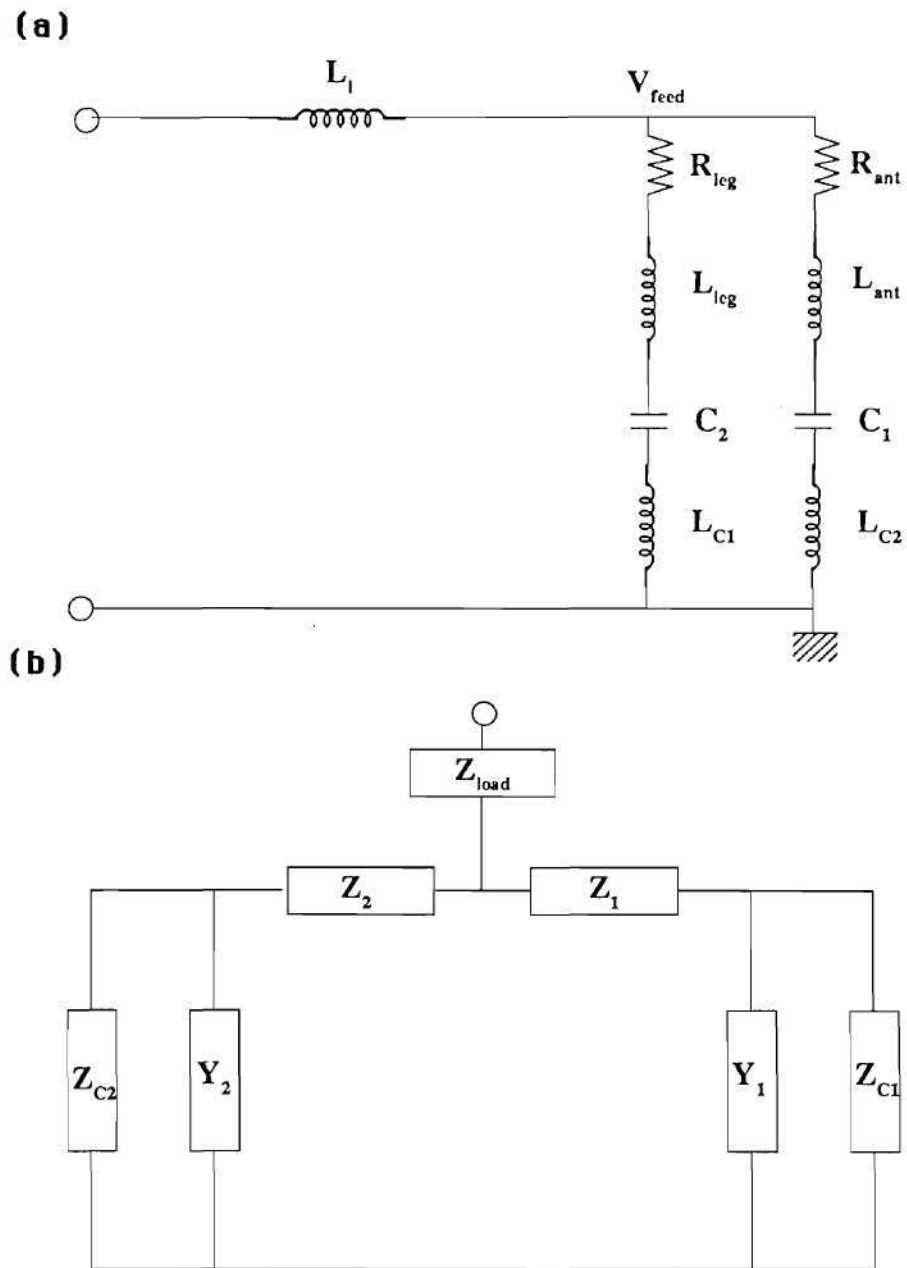


Figure 3.5: The Electrical Circuit Model of the ATF Antenna (a) Lumped-Element Model (b) Transmission Line Model

Table 3.2: Parameters for Lumped Elements in the Antenna Modelling Calculation for $C_1=1413$ pF, $C_2=1620$ pF, and $f=9.3$ MHz

L_l	nH	30
L_{ant}	nH	47
L_{leg}	nH	75
L_{C1}	nH	68.9
L_{C2}	nH	72.1
R_{ant}	Ω	0.23

The capacitors used for the ATF antenna were the Jennings CWV2-1600, which have a capacitance range of 112 to 1620 pF, a peak working voltage rating of 24 kV, and a maximum operating current which depends on frequency, but is ≈ 650 A in the ATF ICRH operational regime for which the limitation is due to bellows heating. The calculations took into account the series inductance of the capacitor, which scales roughly linearly with capacitance from 47.7 nH at 112 pF to 72.1 nH at 1620 pF.

The plasma loading was assumed to be evenly distributed along the current strap in the distributed model and to be a resistance in the lumped-element model. Table 3.2 shows the parameters used in the following calculations.

In Fig. 3.5, L_l denoted lead inductance, while the lead resistance was neglected. V_f represented the voltage at the feed point and the series inductances of the capacitor, L_{C1} and L_{C2} were included.

There are two loops with loop currents I_1 , and I_2 . The governing equations for this circuit are

$$V_f = I_1 Z_1,$$

$$= I_1 \{ R_{\text{ant}} + R_{\text{plasma}} + j[\omega(L_{\text{ant}} + L_{C1} + L_{\text{plasma}}) - \frac{1}{\omega C1}] \}, \quad (3.1)$$

$$\begin{aligned} V_f &= I_2 Z_2, \\ &= I_2 \{ R_{\text{leg}} + j[\omega(L_{\text{leg}} + L_{C2}) - \frac{1}{\omega C2}] \}. \end{aligned} \quad (3.2)$$

V_f is determined from $V_f = \sqrt{P Z_A}$, where P is the power input to the antenna and Z_A is the impedance looking into the antenna at the feed point, which is denoted as

$$Z_A = \frac{Z_1 Z_2}{Z_1 + Z_2}. \quad (3.3)$$

Now, the current at each loop is obtained by

$$\begin{aligned} I_1 &= \frac{V_f}{Z_1}, \\ &= \sqrt{\frac{P Z_2}{Z_1(Z_1 + Z_2)}}, \end{aligned} \quad (3.4)$$

$$\begin{aligned} I_2 &= \frac{V_f}{Z_2}, \\ &= \sqrt{\frac{P Z_1}{Z_2(Z_1 + Z_2)}}. \end{aligned} \quad (3.5)$$

To match the antenna input impedance to the transmission line, which is assumed to be 50Ω ,

$$Z_{\text{in}} = Z_A + j\omega L_l = 50\Omega. \quad (3.6)$$

Therefore,

$$\begin{aligned} \text{Re}(Z_{\text{in}}) &= 50\Omega, \\ \text{Im}(Z_{\text{in}}) &= 0. \end{aligned} \quad (3.7)$$

Equation (3.7) is a system of two nonlinear, algebraic equations for the two unknown capacitances, $C1$ and $C2$. A "root-finder" routine was used to obtain the capacitances at the matching condition given an initial guess.

When the frequency is high and/or the dimension of the system is large enough, the distributed effects become important. In Fig. 3.5.(b), it was assumed that the plasma loading was evenly distributed along the current strap.

For a lossy-transmission line[7],

$$\gamma_1 = \sqrt{Z_1 Y_1}, \quad (3.8)$$

$$\gamma_2 = \sqrt{Z_2 Y_2}, \quad (3.9)$$

where,

$$Z_1 = R_{\text{ant}} + R_{\text{plasma}} + j\omega(L_{\text{ant}} + L_{\text{plasma}}), \quad (3.10)$$

$$Y_1 = j\omega C_{\text{ant}}, \quad (3.11)$$

$$Z_2 = R_{\text{leg}} + j\omega L_{\text{leg}}, \quad (3.12)$$

$$Y_2 = j\omega C_{\text{leg}}. \quad (3.13)$$

Here γ is the propagation constant, and all parameters have units per length.

Then, the characteristic impedances can be denoted by

$$Z_{0\text{ant}} = \sqrt{\frac{Z_1}{Y_1}}, \quad (3.14)$$

$$Z_{0\text{leg}} = \sqrt{\frac{Z_2}{Y_2}}, \quad (3.15)$$

and the input impedance at $z = -l$ is denoted by

$$Z_i = Z_0 \left[\frac{Z_L \cosh \gamma l + Z_0 \sinh \gamma l}{Z_0 \cosh \gamma l + Z_L \sinh \gamma l} \right]. \quad (3.16)$$

Replacing Z_L with Z_{C1} and Z_{C2} , where

$$Z_{C1} = j \left(\omega L_{C1} - \frac{1}{\omega C1} \right), \quad (3.17)$$

$$Z_{C2} = j \left(\omega L_{C2} - \frac{1}{\omega C2} \right), \quad (3.18)$$

then Z_i for each leg can be calculated.

Since the first leg consists of the current strap and a leg,

$$Z_{i1} = Z_{i\text{strap}} + Z_{i\text{leg1}}, \quad (3.19)$$

where,

$$Z_{i_{leg1}} = Z_{0leg} \left[\frac{Z_{C1} \cosh \gamma_2 l_{leg} + Z_{0leg} \sinh \gamma_2 l_{leg}}{Z_{0leg} \cosh \gamma_2 l_{leg} + Z_{C1} \sinh \gamma_2 l_{leg}} \right], \quad (3.20)$$

$$Z_{i_{strap}} = Z_{0ant} \left[\frac{Z_{i_{leg1}} \cosh \gamma_1 l_{strap} + Z_{0ant} \sinh \gamma_1 l_{strap}}{Z_{0ant} \cosh \gamma_1 l_{strap} + Z_{i_{leg1}} \sinh \gamma_1 l_{strap}} \right]. \quad (3.21)$$

Since the second leg consists of a leg only,

$$Z_{i2} = Z_{i_{leg2}} = Z_{0leg} \left[\frac{Z_{C2} \cosh \gamma_2 l_{leg} + Z_{0leg} \sinh \gamma_2 l_{leg}}{Z_{0leg} \cosh \gamma_2 l_{leg} + Z_{C2} \sinh \gamma_2 l_{leg}} \right]. \quad (3.22)$$

Finally, the input impedance can be expressed as

$$Z_A = \frac{Z_{i1} Z_{i2}}{Z_{i1} + Z_{i2}} + Z_{lead}. \quad (3.23)$$

Using the "root-finder" routine, the values of $C1$ and $C2$ can be determined at the matching condition.

Unlike the lumped-element model, the voltage and current can be obtained anywhere along the line in this model. Generally, they are represented as

$$V(z) = V_i \cosh \gamma z - I_i Z_0 \sinh \gamma z, \quad (3.24)$$

$$I(z) = I_i \cosh \gamma z - \frac{V_i}{Z_0} \sinh \gamma z, \quad (3.25)$$

where the subscript i denotes an input quantity and Z_0 is the characteristic impedance of the line.

The tuning range and power handling capability were examined using the above two models. Figure 3.6 shows the matching capacitances as a function of frequencies for the two capacitors in a lumped-element model as compared with the distributed model without plasma loading, $R_{plasma} = L_{plasma} = 0$. Figure 3.7 shows the same case with plasma loading (1Ω). As the plasma loading increases, the capacitance of the capacitor 1, the current-strap-side, increases, while the capacitance of the capacitor 2 decreases as shown in Fig. 3.8.

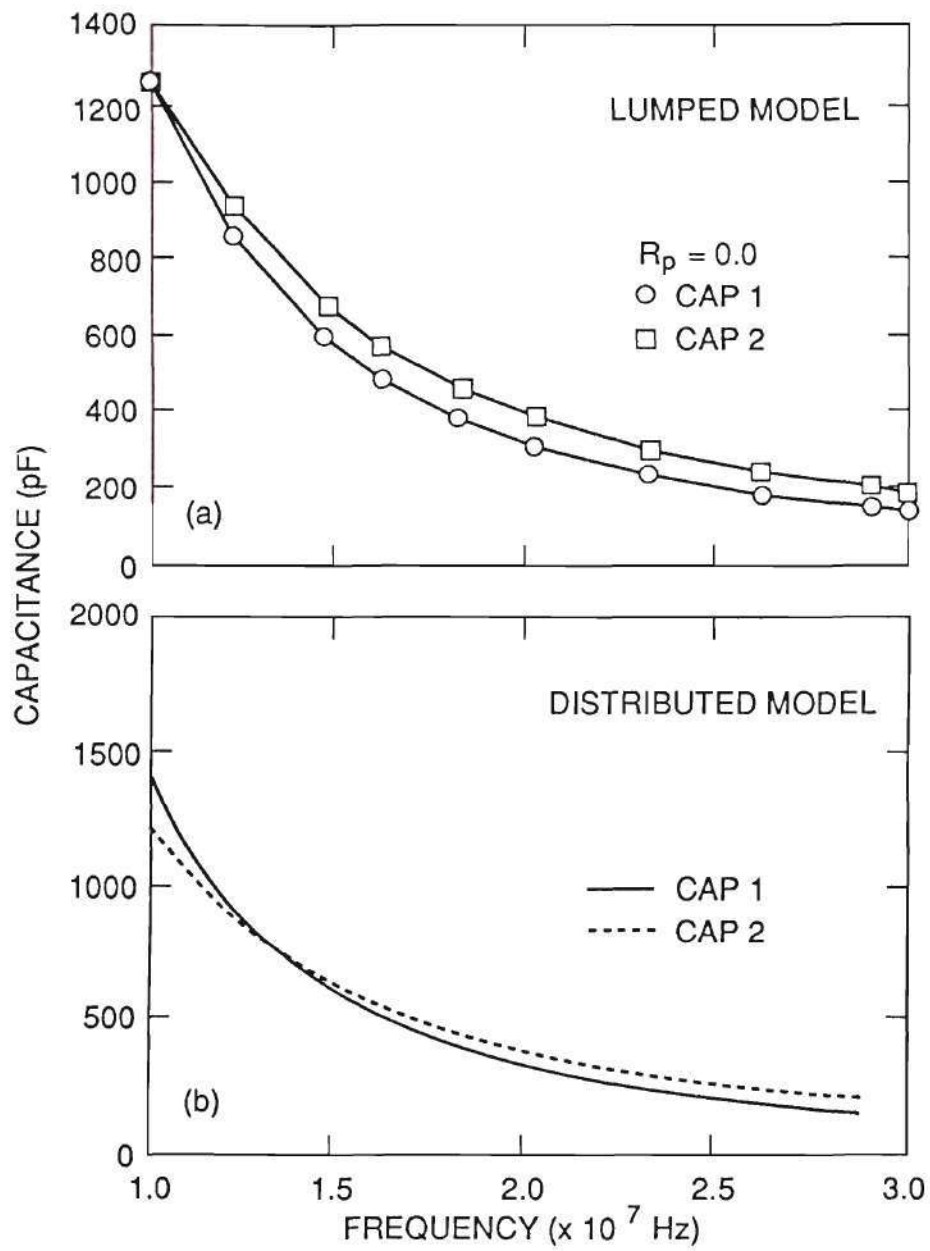


Figure 3.6: The Matching Capacitances for Two Capacitors with No Plasma Loading

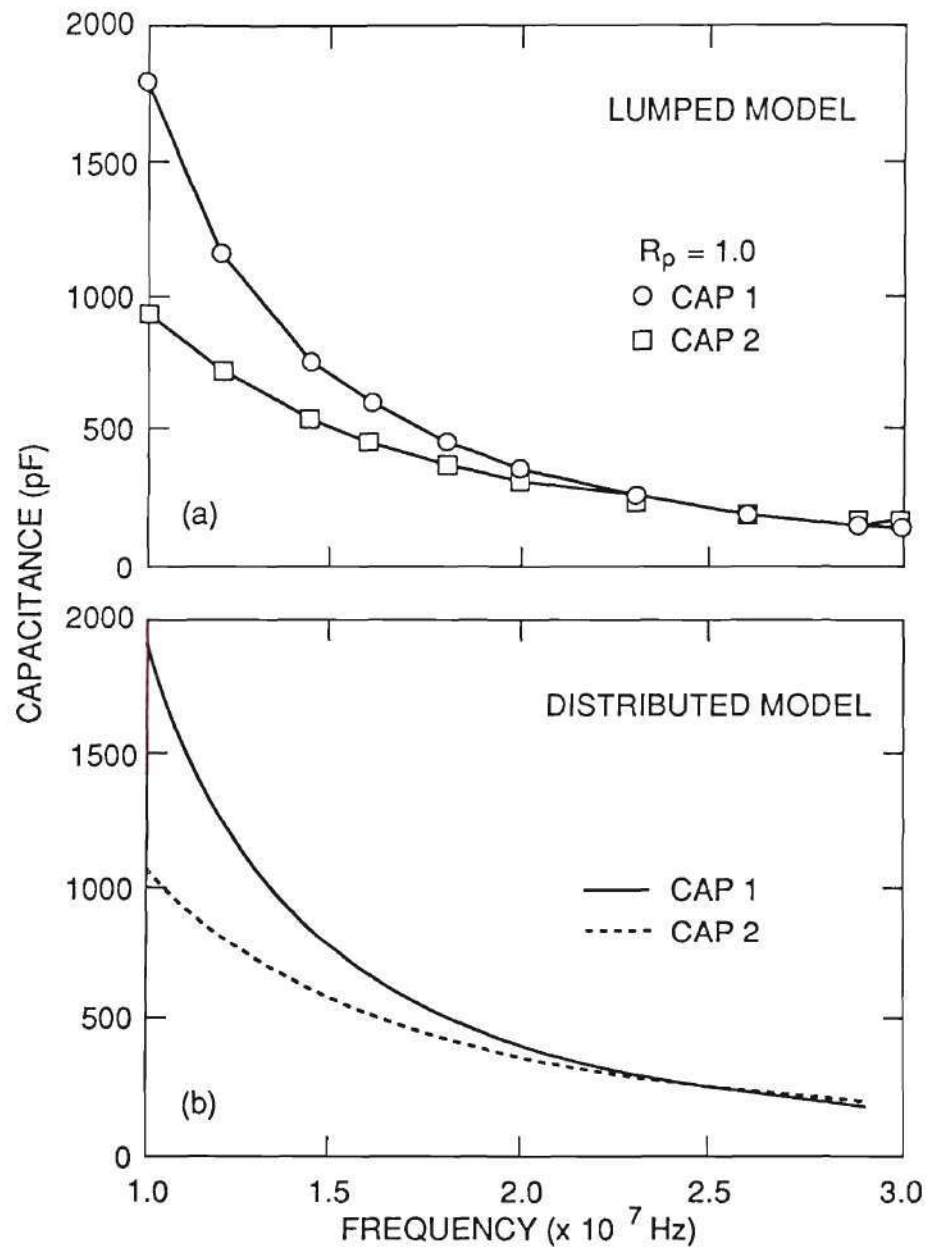


Figure 3.7: The Matching Capacitances for Two Capacitors with 1 Ohm of Plasma Loading

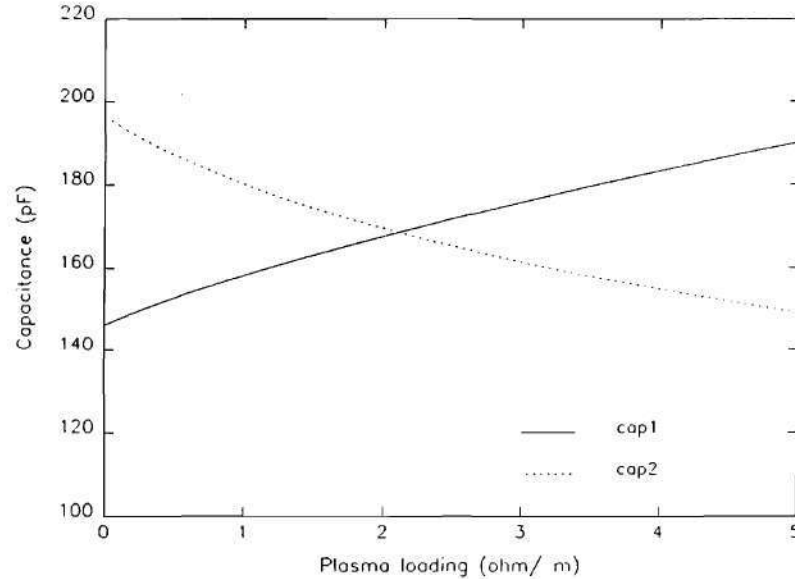


Figure 3.8: The Matching Capacitances for the Two Capacitors as a Function of Loading

The power handling capability of the RDL type antenna is limited by the voltage and current at the capacitor position, where the voltage is maximum. Since the lumped-element model did not predict voltage and current along the line, the distributed model was used to see how the voltage and current distribution changes as the loading changes. Figure 3.9 shows the results which are expected. The higher the loading, the better the power handling capability of the antenna from an electrical point of view. The ATF antenna can launch $\approx 60\text{-}80$ kW of power in vacuum⁴ ($R_{\text{plasma}} = 0$). To launch 300 kW of power into the plasma, at least $\approx 1\Omega$ loading was needed as shown in Fig. 3.9.(c). Since the loading increases linearly with density, ATF target plasmas produced by ECH cannot provide enough loading for future high-power experiments, due to the ECH density cutoff.

The distributed model was used to determine the sensitivity of the VSWR,

⁴During antenna conditioning, 100 kW power was usually used with a pulsed mode. The current limitation (650 A) at the capacitor position was calculated for cw operation.

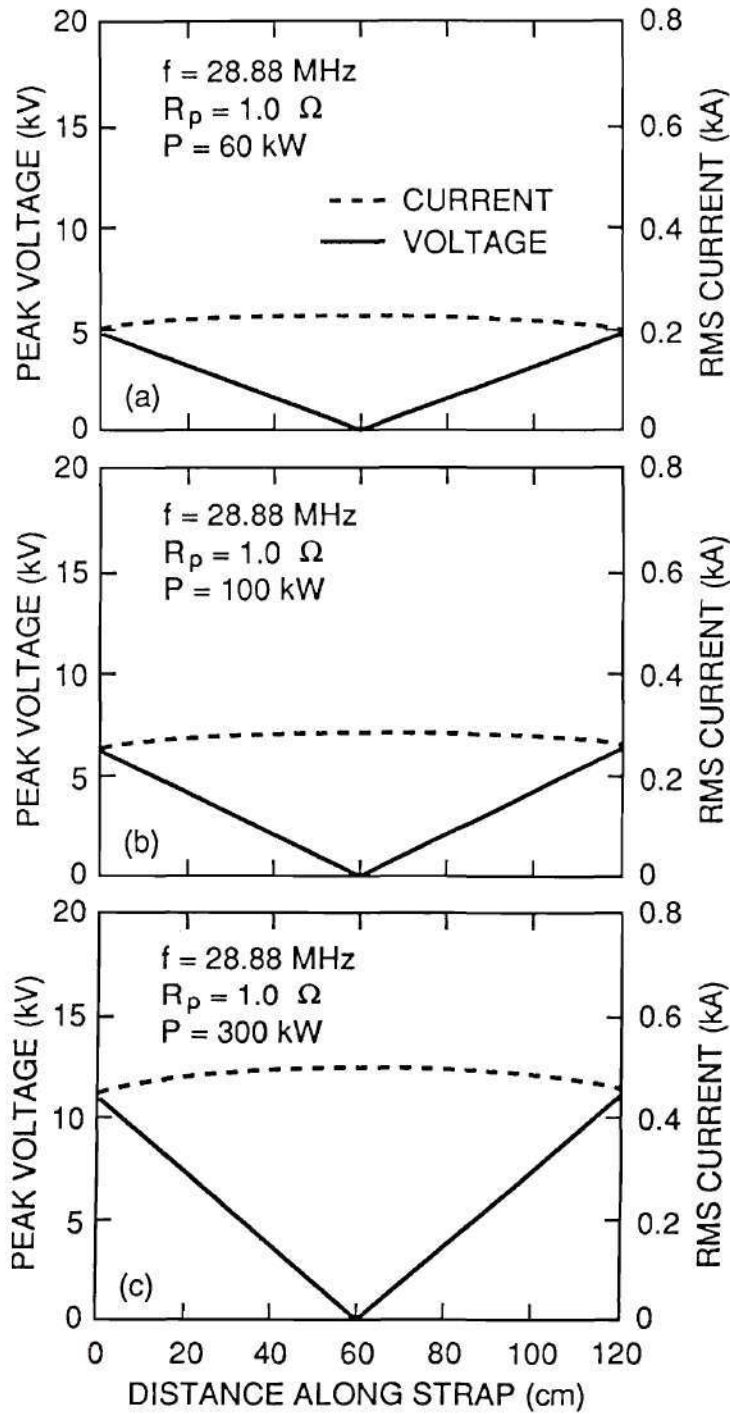


Figure 3.9: Changes in Voltage and Current Distribution Along the Transmission Line for (a) $P=60 \text{ kW}$, (b) $P=100 \text{ kW}$ and (c) $P=300 \text{ kW}$

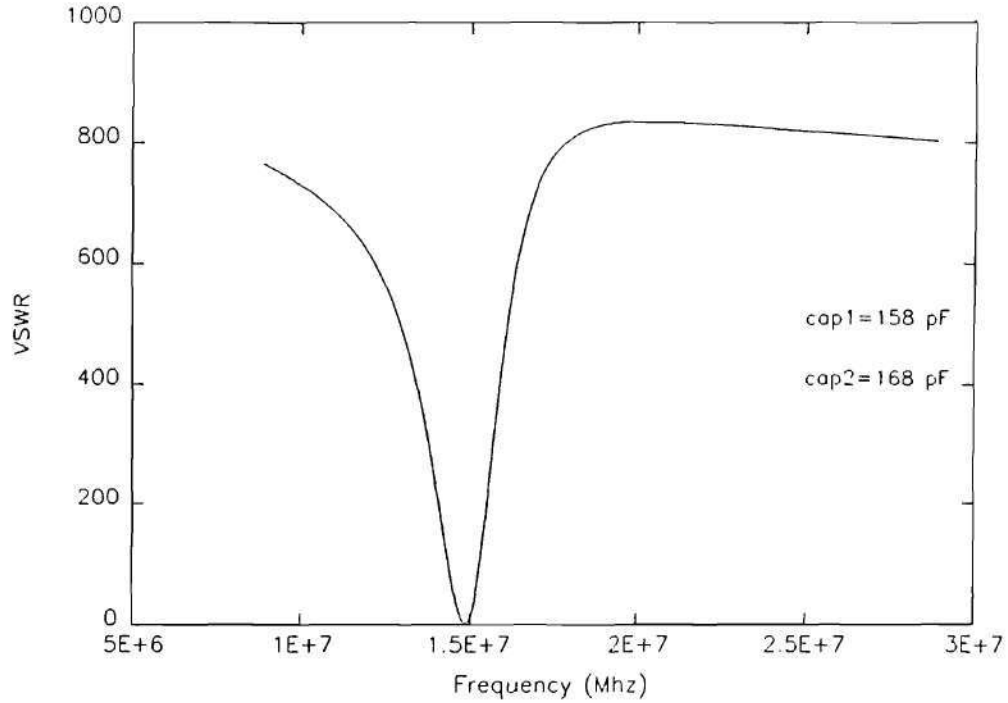


Figure 3.10: Sensitivity of the VSWR to Frequency at Fixed Capacitances

defined as

$$\text{VSWR} \equiv \frac{V_{\max}}{V_{\min}} = \frac{1 + |\rho|}{1 - |\rho|}, \quad (3.26)$$

where ρ is the reflection coefficient, to the loading and the frequency at a fixed position of the capacitors. As shown in Fig. 3.10, the VSWR is sensitive to the frequency. If the VSWR is to be lower than 2, the ATF antenna has a very narrow band of frequency for a reasonable matching condition.

Loading Calculations

In experiments, for loading calculation the forward and reflected power were measured with directional couplers placed at the generator-side of the dc-break, were measured. In the lumped-element model, the impedance was calculated at the feed point as a function of the plasma loading. From the coupler, the transmission line model was used to calculate the impedance at the feed point from the measured value of the reflection coefficient. By matching these two values at the feed point, the real

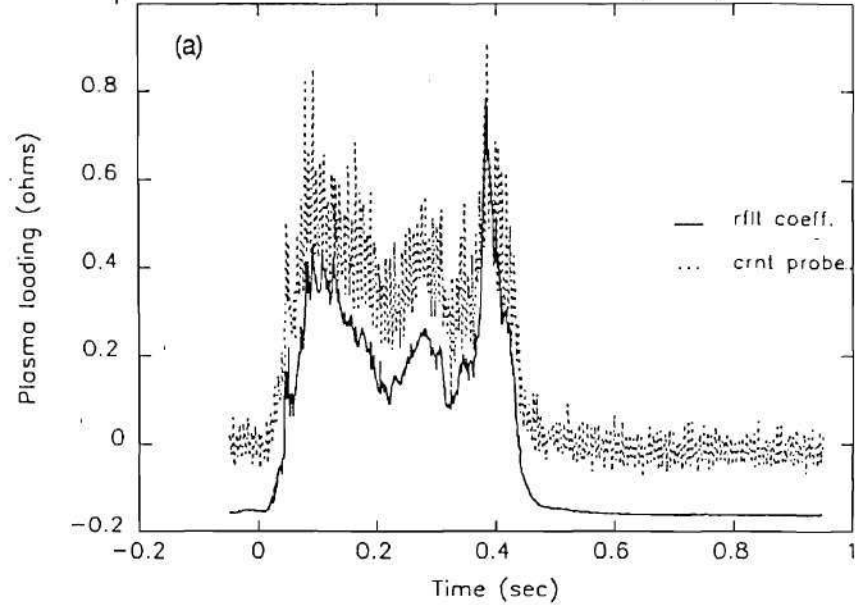
and imaginary parts of the plasma loading were obtained. In this case it was assumed that the plasma loading affected only the parameters of the current strap, and not those of the legs. This is the simplest way to determine the plasma loading from the experimental data because the loading is represented explicitly as a function of the measured reflection coefficient.

In the distributed model, the loading is expressed implicitly as a function of the measured reflection coefficient in nonlinear, algebraic equations. When using "root-finder" to solve it, however, it turned out to be very sensitive to the initial value and it was not possible to follow rapidly fluctuating experimental values.

Another concern in determination of the plasma loading is calibration. For ATF, the current monitor placed near the current strap was also used to measure the antenna current. The loading calculated from this signal was similar to the loading calculated by a lumped-element model, but there was an "offset" between those two values as shown in Fig. 3.11. In Fig. 3.11(a), the offset looks like a linear offset due to miscalibration. But in Fig. 3.11(b), the offset only occurred in the higher-VSWR region. Two things that might have caused this problem would be inaccurate calibration of the measuring system and using incorrect antenna parameters such as electrical length, intrinsic resistance, inductance and physical dimensions.

Changing the electrical length of the transmission line reduced the offset but also reduced the loading and changed the shape. The offset was also dependent on the intrinsic resistance and inductance of the current strap and legs. Varying these parameters only reduced the offset, but did not change the shape of the signal. However varying these parameters changed the measured loading quite substantially. A combination of adjustments turned out to be best. Figure 3.11(b) shows a "non-linear" offset between the two signals as mentioned above. Figure 3.12 shows the result of the same shot after modifying the electrical length of the transmission line from 3.771 m to 3.4 m and the intrinsic resistance of the antenna from $.23 \Omega$ to $.18$

Comparison of loading between two signals(shot= 4784)



Comparison of loading between two signals(shot= 4575)

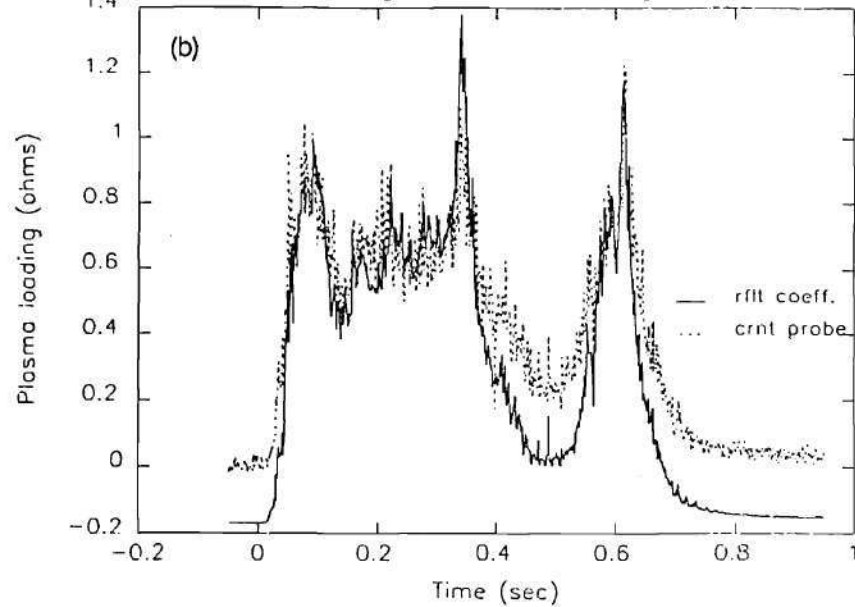


Figure 3.11: Two Kinds of Offset in Loading Measurements Calculated from Reflection Coefficient and Current Probe Signal. (a) Linear Type (b) Non-Linear Type.

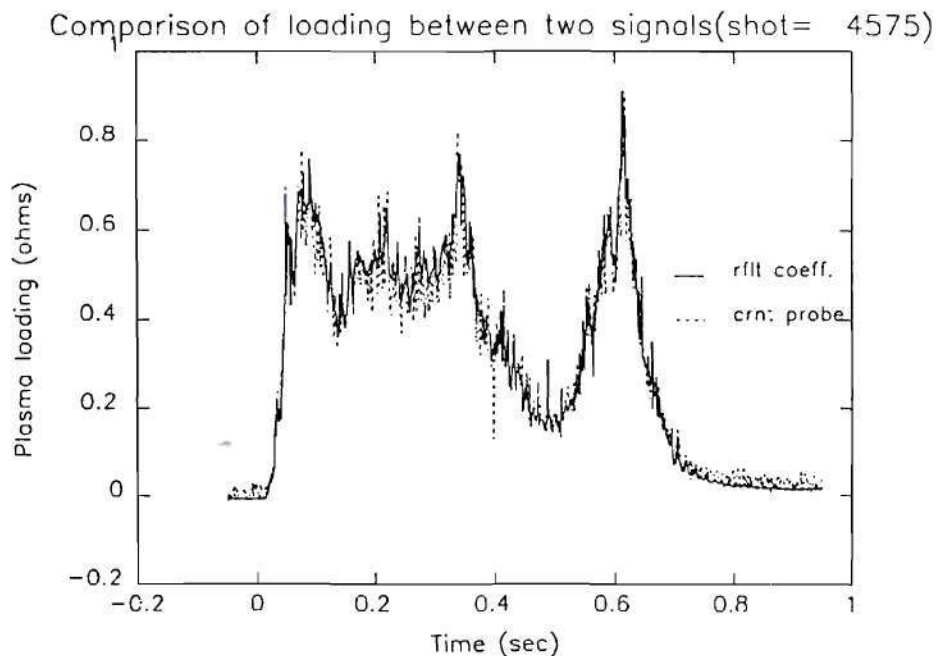


Figure 3.12: Corrected Loading Data from Two Signals with Modified Electrical Constants

Ω. The offset disappeared everywhere.

RF System

Description of the RF Transmitter

For ATF ICRH experiments, two transmitters were used. One provided 100 kW of RF power in the 5 - 30 MHz range, while the other provided 200 kW in the 5 - 19 MHz range. Except for the output power levels, the transmitters are fairly similar.

Each transmitter (AN/FRT-86) consists of an exciter (modulator-synthesizer), a series of RF power amplifiers and a water, vapor, and forced air cooler. The exciter determined the output frequency, produced the modulation process, and furnished

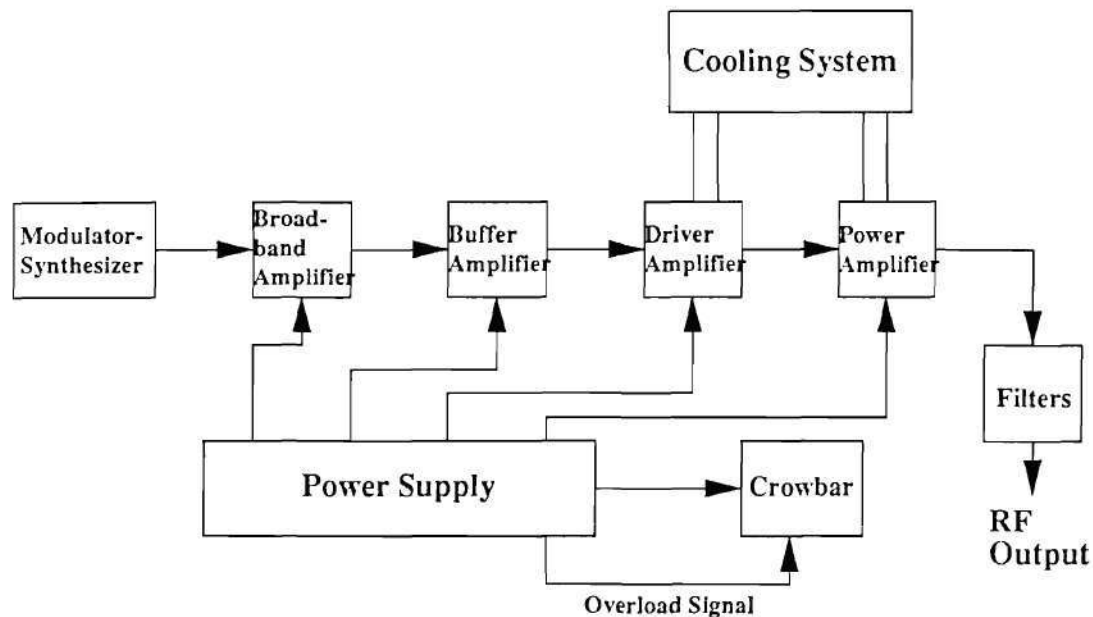


Figure 3.13: Block Diagram of the RF Transmitter, AN/FRT-86

up to 250 mW of signal to the power amplifier. Then power amplifier provides 200 kW average RF power to a $50\ \Omega$ load. Figure 3.13 shows the overall block diagram of the transmitter.

The series of amplifiers consists of two 4CX350A broadband amplifiers operated with a nominal load of $200\ \Omega$ and two 4CX350A buffer amplifiers in parallel as the first tuned stage with a nominal load impedance of $200\ \Omega$. A 4CW2500A driver amplifier feeds the final power amplifier tube, a 4CV250.000A.

The output tank circuit consists of a conventional $\pi - L$ network which transformed the resonant plate impedance of the tube (500Ω) to the desired $50\ \Omega$ output. A tunable harmonic filter was provided to suppress harmonics at least 80 dB below the carrier power. This filter is followed by a fixed tuned VHF filter with a cut-off around 36 MHz. Note that harmonic generation of the output could also be controlled by setting a proper load Q for the output tank circuit. The driver tube and power tube require forced cooling even at low duty cycle due to the large, continuous

filament power being dissipated. The vapor phase cooling was used to cool the anode of the power amplifier tube and the water cooling was used on the driver tube, filament of the power tube, coils, filters and capacitors.

Equipment protection was provided by a crowbar for the final power amplifier tube. The crowbar consists of an ignitron tube as a fast timing switch in series with a non-inductive damping resistor connected across the output of the high voltage supply. This crowbar circuit could be initiated by short circuits on the supply line or arcs within the tube, resulting in fast discharge of the plate power supply for the power amplifier tube. Other protection circuits were also furnished to protect equipment and personnel.

RF System Operation

The ATF RF system is outlined in Fig. 3.14. A Hewlett-Packard network analyzer (HP8753A) was used to generate a continuous RF signal with the desired frequency and the waveform envelope was provided by a Wavetek waveform generator (Model 175). These signals were fed to a mixer to modulate the cw signal with the waveform envelope and then delivered to the transmitter input terminal. There were two directional couplers at the location of the transmitter output to detect forward and reflected signal. The reflected signal was also fed back to the mixer/arc detector module to initiate the transmitter protection circuit when the reflected power exceeded a pre-set level.

Since there were two transmitters to feed the antenna, a coaxial switch was installed to maintain a proper configuration — always one transmitter to a dummy load and the other one to the antenna. A power combiner to combine the output of both transmitters and provide 300 kW output power was designed and fabricated but was not installed for these experiments. A long transmission line linked between the transmitter and antenna. Two directional couplers at the antenna side measured

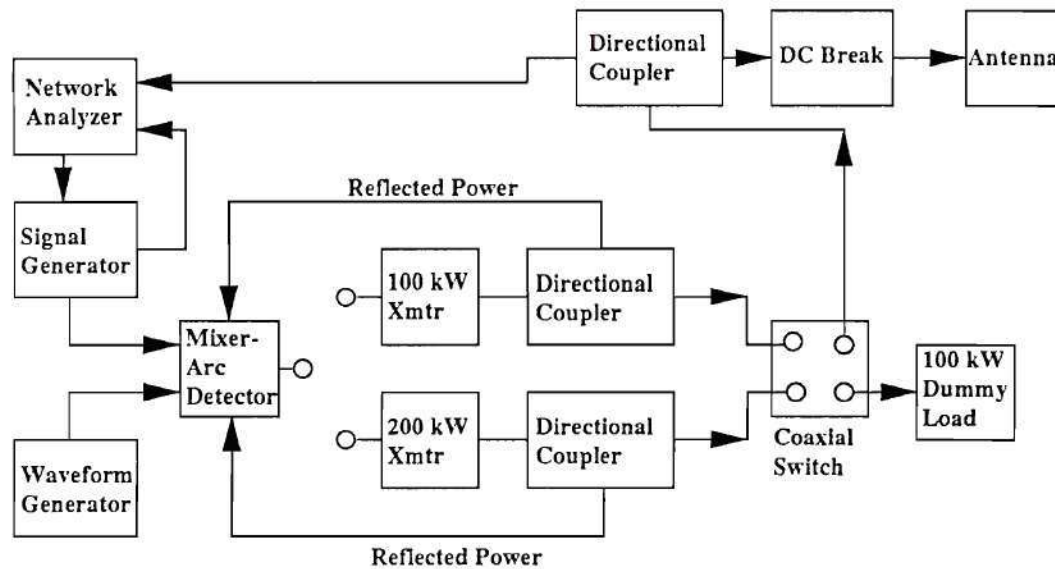


Figure 3.14: Diagram of the ATF ICRH System

forward and reflected power for use in antenna tuning and loading calculations.

The transmitter had an internal interlock string to assure a safe operational state before high RF power was generated. The ATF also had an interlock string including the antenna and ATF logic, which had to be satisfied before any RF power operation. If both of these internal and external interlock strings were satisfied, the system was ready for RF operation by applying an RF drive signal to the transmitter.

Edge Probes

A double-tip Langmuir probe and three magnetic (RF) probes⁵ were installed on ATF around the ICRH antenna. The main purpose of the probe measurements was to monitor the antenna near-field patterns and the plasma edge conditions during ICRF wave heating.

The RF/edge coupling is a complicated, multi-coupled process which has not yet been well addressed. Theoretical efforts[8] have suggested several possible mechanisms driving this process. Some of them are the effect of E_{\parallel} component of the antenna fields which should be eliminated by a Faraday shield, non-linear coupling (ponderomotive force) in front of the Faraday shield due to the ripple of the electric fields, direct edge heating, sheath effect of the Faraday shield or other antenna structures, and surface waves, etc.. Experimental approaches[8,9,10] to understand these phenomena must be carefully designed and performed.

By measuring the edge RF field patterns during ICRH and monitoring the changes in the edge plasma, especially electron density, temperature and floating potential, these data can be correlated with global plasma behavior such as heating, impurity generation, radiated power, and particle transport.

In addition to this, limited fluctuation measurements can be performed with these probes in the edge region during ICRH. These measurements can indicate the presence of nonlinear phenomena such as RF sheath formation or the parametric decay instability, and possibly effects related to the fluctuation-induced transport (anomalous transport).

⁵The author is grateful to R. H. Goulding for guidance in the probe design and analysis and to Gene Purdy and T. Muhammed for fabricating the probes.

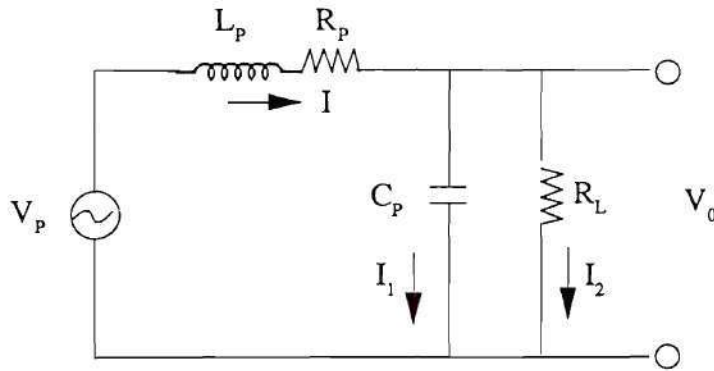


Figure 3.15: Electrical Circuit Model for the Magnetic Probe

Here both Langmuir and magnetic probe theory, probe design, and experimental set-up are presented and the experimental results will be described in subsequent chapters.

Theoretical Considerations

Magnetic (RF) Probe Magnetic probe measurements exploit the simple principle that a changing magnetic field in a closed loop can induce a current. By taking a simple model[11,12,13,14], one can simulate these measurements. Figure 3.15 shows the equivalent circuit model used in several previous works. Here, L_p represents the self-inductance of the coil, R_p is the resistance of the coil (which is frequency-dependent due to the skin-depth effect), C_p is an effective capacitance representing the stray capacitance of the coil and its lead, and R_L is the load resistance. V_p is the EMF generated by the external magnetic fields. It is proportional to the number of turns N , to the coil area A , and to the time rate of change of flux linking the coil.

Thus V_p is written as

$$V_p = NA \frac{dB}{dt}. \quad (3.27)$$

In RF experiments, usually $\frac{dB}{dt}$ is written as ωB where ω is the angular frequency of the launched wave, and where B and V_p vary as $e^{i\omega t}$. To obtain V_0 , one can manipulate the following equations:

$$\begin{aligned} I &= I_1 + I_2, \\ R_L I_2 &= -\frac{i}{\omega C} I_1, \\ V_p &= (i\omega L_p + R_p)I + \left(\frac{R_L}{1 + i\omega C_p R_L}\right)I. \end{aligned} \quad (3.28)$$

Then

$$\begin{aligned} V_0 &= I \frac{R_L}{1 + i\omega C_p R_L}, \\ &= \frac{V_p}{i\omega L_p + R_p + \frac{R_L}{1 + i\omega C_p R_L}} \frac{R_L}{1 + i\omega C_p R_L}, \\ &= \frac{V_p}{(1 - \omega^2 C_p L_p + \frac{R_p}{R_L}) + i(\omega C_p R_p + \frac{\omega L_p}{R_L})}, \\ &= \frac{V_p e^{i\theta}}{[(1 - \omega^2 C_p L_p + \frac{R_p}{R_L})^2 + (\omega C_p R_p + \frac{\omega L_p}{R_L})^2]^{\frac{1}{2}}}, \end{aligned} \quad (3.29)$$

where,

$$\theta = \tan^{-1} \left[\frac{\omega R_p C_p + \frac{\omega L_p}{R_L}}{1 - \omega^2 C_p L_p + \frac{R_p}{R_L}} \right].$$

Neglecting C_p and R_p , Eq.(3.29) can be rewritten as

$$V_0 = \frac{V_p e^{i\theta}}{[1 + (\frac{\omega L_p}{R_L})^2]^{\frac{1}{2}}}, \quad (3.30)$$

where,

$$\theta = \tan^{-1} \left(\frac{\omega L_p}{R_L} \right).$$

Defining the sensitivity of the probe as

$$S = \frac{V_0}{B}, \quad (3.31)$$

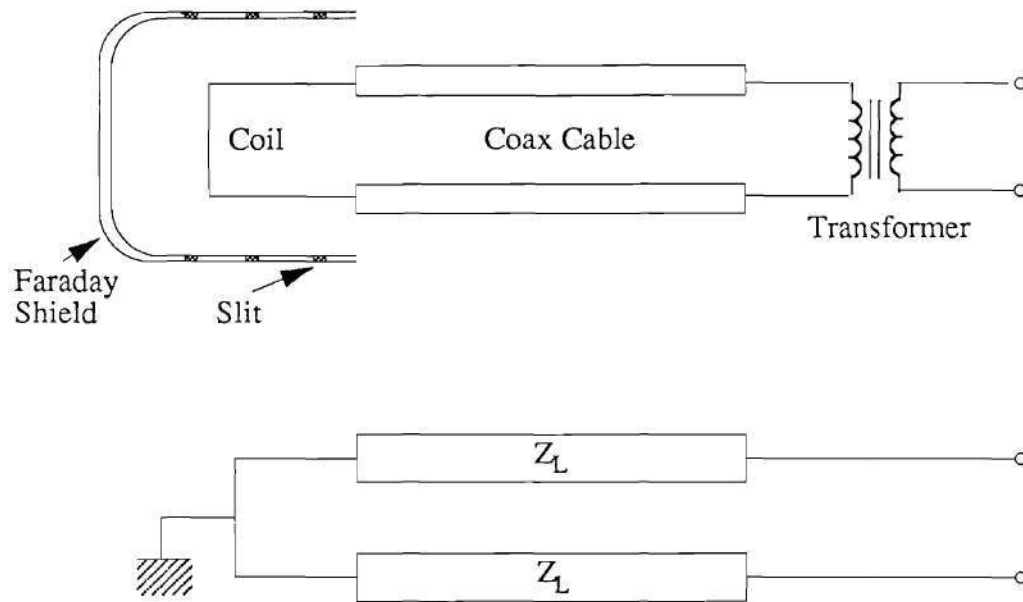


Figure 3.16: The ATF RF Probe and Equivalent Circuit Diagram

it becomes a function of N . The frequency response of the probe can be represented by the time constant, $\tau = \frac{L_p}{R_L}$, which is also a function of N . Here, L_p is equal to $N^2 L_0$ where L_0 is the inductance of one turn. Usually, in RF experiments where high frequency response is necessary, a one turn coil is used.

The RF probes used in this experiments were designed in a different way. Figure 3.16 illustrates one of the magnetic probes and its equivalent circuit. A larger coil area was used for better signal output and two coax cables ran through to an RF transformer. A transmission line model⁶ was used for this probe as shown in Fig. 3.16. A virtual ground exists at the middle of the coil, so the system can be divided into two identical circuits. By doing a simple impedance calculation with a lossy-transmission line model[7], one can obtain

$$V_0 = 2I \cdot Z_L,$$

⁶This model was suggested by R. H. Goulding.

$$\begin{aligned}
&= 2 \frac{V_p}{Z_i} \cdot Z_L, \\
&= 2V_p Z_L \left[Z_0 \frac{Z_L \cos \beta l + i Z_0 \sin \beta l}{Z_0 \cos \beta l + i Z_L \sin \beta l} \right]^{-1}, \tag{3.32}
\end{aligned}$$

where,

$$\beta = \frac{2\pi}{\lambda},$$

where λ is the wavelength.

It should be mentioned that the magnetic probe picks up some amount of electrostatic signal from capacitive coupling between the probe and plasma, as well as the desired electromagnetic signal. To compensate for this effect, a Faraday shield is usually used. Another method is to place a second coil, wound in the opposite direction, next to the first loop. If it is assumed that these two coils pick up same amount of electrostatic signal, this signal is easily cancelled by connecting the center conductors to opposite ends of a transformer. The former method was applied for the ATF RF probe and was incorporated with a shield for protection from particle bombardments.

Before fabricating the magnetic probe, a prototype magnetic probe (without a Faraday shield) was made to test the signal level compared to the usual single turn loop probe and the signal attenuation between two orthogonal loops. It turned out that the signal level was very sensitive to grounding and circuit shielding used to suppress external signals.

To compare signal levels between the prototype probe and the small single turn probe, the expected output power from each probe was calculated. The ratio of the output power from both of these probes was represented by

$$\frac{P_{\text{prototype}}}{P_{\text{smallprobe}}} = \left(\frac{V_{\text{prototype}}}{V_{\text{smallprobe}}} \right)^2 = \left(\frac{\phi_{\text{prototype}}}{\phi_{\text{smallprobe}}} \right)^2. \tag{3.33}$$

With the given dimensions of each probe, this gave 37.5 dB. Assuming that only half the flux in the prototype was present due to the presence of the metallic center piece,

then

$$\frac{P_{\text{prototype}}}{P_{\text{smallprobe}}} = \left(\frac{\phi_{\text{prototype}}/2}{\phi_{\text{smallprobe}}} \right)^2, \quad (3.34)$$

and this gave 31.5 dB, which was close to the measured value, 30 dB. The measurements showed a linear signal level with respect to the size of the loop.

The prototype probe showed good signal polarization between the two orthogonal positions. The measured phase differences as the coil was turned 180 degrees appeared as almost 180 degrees. It was not possible to measure how much signal would be attenuated due to graphite shield with this prototype probe because it had no Faraday shield.

After fabricating the actual probes, they were tested to examine the frequency response, sensitivity and how much the Faraday shield attenuated the signal. A Helmholtz coil with radius of 8.3 cm was used for absolute calibration of the probe by measuring sensitivity, defined as in Eq.(3.31). This coil produced a magnetic field of 0.108I Gauss at the center where I was the current flowing through the coil. Since the coil had a resonance around 40 to 60 MHz and the total electrical length reached a quarter wave length around 80 to 100 MHz, the data was difficult to interpret in these regions. Only the results in the 1 to 30 MHz region are shown, which covers up to the second harmonic resonance frequency of the hydrogen plasma at 0.95 T in ATF. Figure 3.17 shows the data from the absolute calibration of the three probes and the previously tested prototype probe and single loop probe.

The single loop probe can be easily modeled by the equivalent circuit model given in Eq.(3.28). But our probe could not be matched by this model. The result of the transmission line model given by Eq.(3.32) showed a good match with the experimental data in most of the frequency range of interest. From comparisons in signal level between the prototype probe and one of the actual probes, it was revealed that the Faraday shield reduced the signal level by almost 60%. This seemed reasonable because the effective area was reduced $\sim 60\%$ by the Faraday shields. One

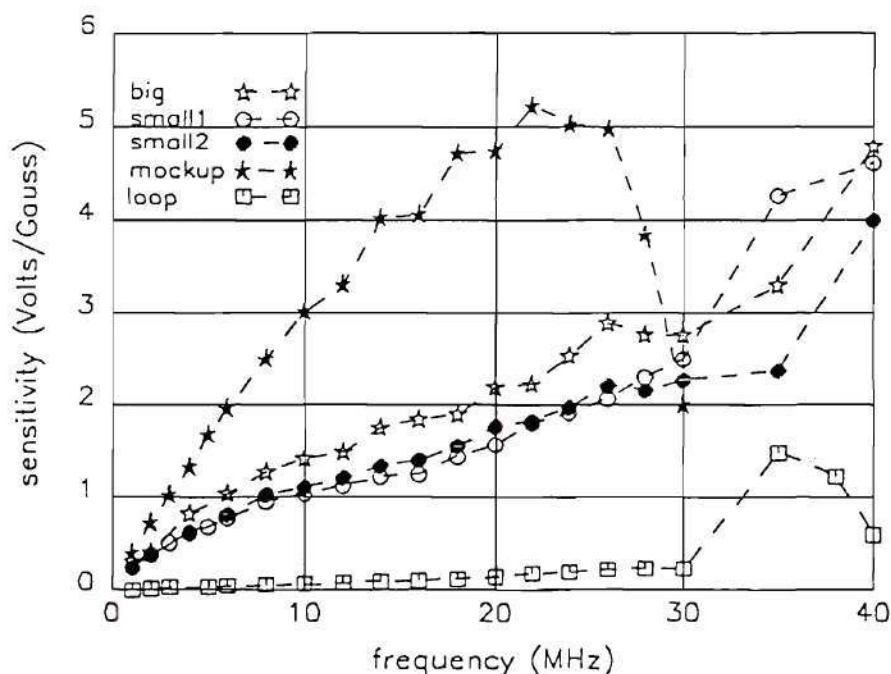


Figure 3.17: Results of the Absolute Calibration Plotted as Sensitivity vs. Frequency

of these probes was tested with the TFTR prototype antenna, at higher frequencies. In this case, the Faraday shield degraded the signal by about 5 to 10 dB. Figure 3.18 shows the comparison between the transmission model and test results measured using the Helmholtz coil from 1 to 30 MHz and the TFTR prototype antenna from 30 to 80 MHz. This figure shows the effectiveness of a transmission line model for predicting the frequency response of the ATF magnetic probes.

From all these data, well-modeled, reliable magnetic probe measurements were expected, with linear frequency response up to 30 MHz, two orthogonal loops and a good S/N ratio even though they were covered by a large area of graphite Faraday shields.

Langmuir Probe Langmuir probe measurements are made by biasing a metal probe to a voltage (V) with respect to some large conductor in contact with the plasma (single probe), or with respect to another probe (double probe) and measur-

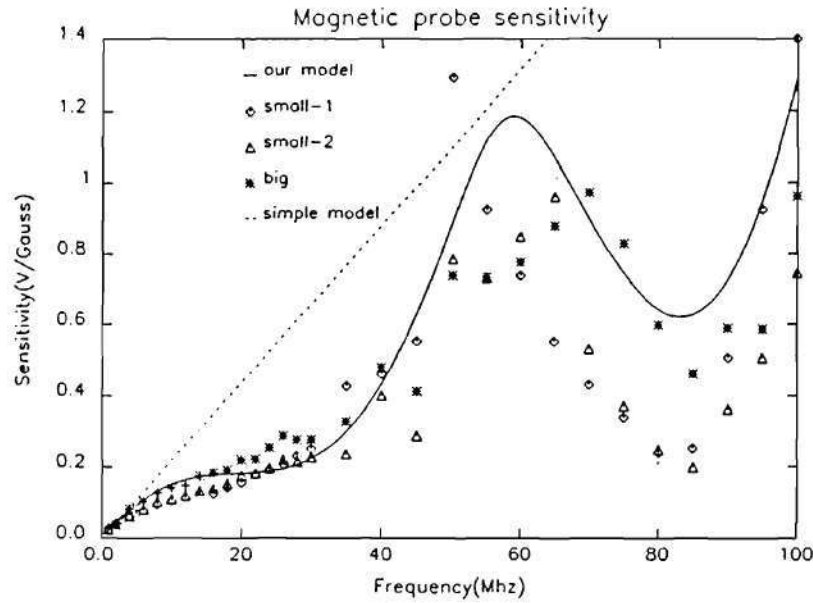


Figure 3.18: The Comparison Between the Transmission Line Model for the RF Probe and the Test Data Measured by the Helmholtz Coil and Prototype Antenna

ing the current flow (I) to the probe.

The heat flux to the probe should be minimized to avoid damage. Since the electron current to the probe is much larger than the ion current and because of other reasons listed below, the single probe method operating in the ion saturation regime was chosen for the ATF Langmuir probe. Even though the floating double probe method has advantages in this regard in normal condition, the system can not fully float in a high frequency RF environment because of the large stray capacitance between the power supply and ground[15]. Also double probe temperature measurements concern only the fast electron-tail, not those in the body of the distribution[16]. Another reason for using the single probe method in ATF experiments was that under the given conditions, in which two probe tips were used, one could measure the density, temperature, and potential simultaneously.

It is generally accepted that there are three parameters which determine the

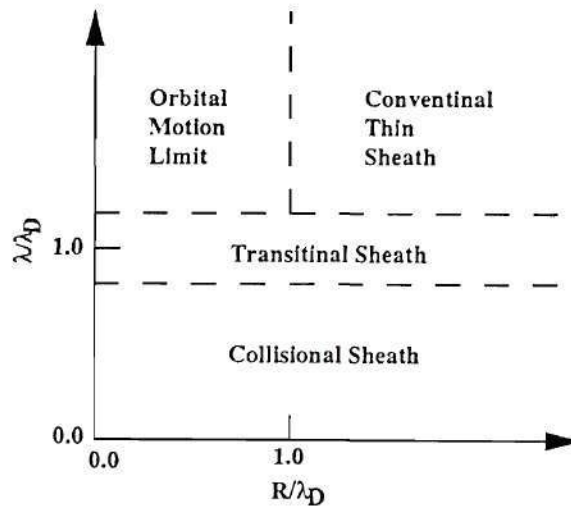


Figure 3.19: Langmuir Probe Operating Regime[17]

various operating regimes of a Langmuir probe[17]. These are λ_D/R , λ/R , and λ/λ_D where λ_D is the Debye sheath thickness, λ is the particle mean-free-path and R is the radius of the Langmuir probe. The operating regime can be divided first into two domains, depending on the magnitude of λ/R , which is called Knudsen number K_n . There is a classical Langmuir probe domain where $K_n \gg 1$ and a continuum electrostatic probe domain where $K_n \ll 1$. In each domain, one can identify several different operating regimes depending on the magnitudes of λ/λ_D and R/λ_D . If $R/\lambda_D \gg 1$, it is called a thin sheath regime, whereas if $R/\lambda_D \ll 1$, it is called a orbital-motion-limit regime. If $\lambda/\lambda_D \gg 1$, it is called a collisionless regime, whereas if $\lambda/\lambda_D \ll 1$, it is called a collisional regime. Therefore, if $\lambda_D \gg \lambda \gg R$, the probe is in a collisional thick sheath regime. Figure 3.20 shows this two-dimensional representation of the various operating regimes.

The importance of classifying the operating regimes is that the governing equations to describe the probe characteristics can be obtained using appropriate assumptions for the given operating conditions. In fusion devices, in addition to the above considerations, it must be determined how large the effect of the magnetic field

is, and if there are any other perturbing sources such as an RF-field or high energy charged beams.

For the typical ATF operating parameters in Table 4.1, $\lambda_D \sim 2 \times 10^{-3}$ cm and $\lambda \sim 100$ cm at the edge region and the radius of our probe is 7.9×10^{-2} cm. Therefore the ATF edge region lies on $K_n \gg 1$ and $\lambda \gg R \gg \lambda_D$ — so-called “conventional thin sheath” regime.

The magnitude of the magnetic field at the ATF edge was about 0.7 T when the central magnetic field was 0.95 T. In this case, with $T_i = 10$ eV and $T_e = 20$ eV, the electron Larmor radius was $\rho_e \simeq 1.5 \times 10^{-3}$ cm and the ion Larmor radius was $\rho_i \simeq 6.5 \times 10^{-2}$ cm. This meant that the effect of the magnetic field could not be ignored. Also high frequency (up to 30 MHz) RF-field effects on the probe characteristics had to be considered.

The probe was operated in the ion saturation current regime to avoid higher electron current influx to the probe from an unexpected plasma condition like disruption. When a probe is inserted into a plasma, there is a sheath region surrounding the probe, in which charge neutrality is violated and a strong electric sheath potential occurs. Therefore one has to solve the Poisson equation self-consistently with the equations of motion for the electrons and the ions. This problem is usually very complicated and impossible to handle analytically. Under the conditions given above, a thin sheath surrounding the probe is assumed and a planar approximation is then adequate.

If it is assumed that the probe is operating in the ion-saturation current regime where all electrons are repelled, one can make the approximation

$$n_e(x) \approx n_\infty \exp \frac{eV(x)}{T_e}, \quad (3.35)$$

where n_∞ is unperturbed plasma density.

The ion velocity can be written as

$$|v_i| = \left(\frac{-2eV}{m_i} \right)^{\frac{1}{2}}, \quad (3.36)$$

for $T_e \gg T_i$, assuming that the ions have zero energy at ∞ . The total ion particle current density is $A\Gamma_i = An_i v_i$ where A is the area of the surface through which the ion current flows and this should be constant in equilibrium, and is denoted by J_i :

$$J_i = An_i v_i = \text{constant}. \quad (3.37)$$

Therefore the Poisson equation becomes

$$\begin{aligned} \nabla^2 V &= \frac{-e}{\epsilon_0} (n_i - n_e) \\ &= \frac{-e}{\epsilon_0} \left[\frac{J_i}{A} \left(\frac{m_i}{-2eV} \right)^{1/2} - n_\infty \exp \frac{eV}{T_e} \right]. \end{aligned} \quad (3.38)$$

Next, this equation is applied to two distinct regions. First, at large distances from the probe there is a plasma region where quasi-neutrality is satisfied. In this region, the $\nabla^2 V$ term may be neglected and the equation becomes

$$\frac{J_i}{A \left(\frac{-2eV}{m_i} \right)^{1/2}} = n_\infty \exp \frac{eV}{T_e}. \quad (3.39)$$

For the sheath region, $\nabla^2 V$ cannot be ignored. Bohm et al.[18] first derived the condition that V at the plasma-sheath boundary equals $\frac{-T_e}{2e}$ by Taylor expansion about $V = V_s$, yielding the well-known Bohm current as

$$\begin{aligned} J_i &= A_s n_\infty \exp \frac{eV_s}{T_e} \left(-\frac{2eV_s}{m_i} \right)^{1/2} \\ &= 0.61 A_s n_\infty \left(\frac{T_e}{m_i} \right)^{1/2}, \end{aligned} \quad (3.40)$$

where A_s is the area of the sheath surface, which for a cylindrical probe is given by

$$A_s \simeq A_p \left(1 + \frac{\xi}{R} \right), \quad (3.41)$$

where A_p is the area of the probe surface, and ξ is approximately $4\lambda_D$ for hydrogen. This is generally applicable, provided the sheath is thin and $T_e \gg T_i$.

Several people have solved the full Poisson equation to get exact solutions numerically. The calculations of Laframboise[19] are sufficient for establishing the current-voltage characteristics of spherical and cylindrical probes over essentially the entire range of practical conditions of operation, in the collisionless limit. For practical purposes, the approximate fits to his results are quoted as given by Kiel[20] for ion collection by a cylindrical probe with $Z_i = 1$,

$$J_i = F(\epsilon) \left[1 + \frac{f(\epsilon)}{\xi_p^{3/4}} (-\chi_p^*)^{1/2} \right], \quad (3.42)$$

where,

$$\begin{aligned} F(\epsilon) &= \epsilon^{1/2} (e^{\chi_s} \text{erf}(\sqrt{\chi_s}) + 2\sqrt{\chi_s/\pi}), \\ \chi_s &= \frac{0.693}{\epsilon} \quad \text{for } \epsilon \leq 1, \\ f(\epsilon) &= 2.18(1 - 0.2\epsilon^{0.35})(1 + \epsilon)^{-1/8}, \\ \epsilon &= \frac{T_i}{T_e}, \\ \xi_p &= \frac{R}{\lambda_D}, \\ \chi_p^* &= \frac{eV_p}{T_e}. \end{aligned}$$

The error function $\text{erf}(t)$ is defined as,

$$\text{erf}(t) \equiv \frac{2}{\sqrt{\pi}} \int_0^t e^{-y^2} dy. \quad (3.43)$$

In the ATF plasma, as mentioned before, the effects of the magnetic field should be included. Although there have been no rigorous studies for magnetic field effects, Harrison and Thompson [21] obtained a simple result which was the same expression as for the field-free-case Bohm current presented in Eq.(3.40), with two

small modifications: The area was replaced by the projection area in the direction of the magnetic field, and the coefficient changed from 0.61 to 0.5. In the ion saturation regime,

$$J_i = 0.5en_\infty C_s, \quad (3.44)$$

where C_s is the sound speed defined as

$$C_s = \left[\frac{k(T_e + T_i)}{m_i} \right]^{\frac{1}{2}}. \quad (3.45)$$

From this equation, an unperturbed, distant density was obtained as

$$n_\infty \simeq \frac{2I_i}{A_\perp C_s e}, \quad (3.46)$$

where I_i was a measured ion saturation current and A_\perp was the projection area in the direction of the magnetic field.

For fusion plasmas with large magnetic fields, the following features were observed[22]: (a)The ion saturation portion is usually flat while in an unmagnetized plasma it was never saturated. This is presumably owing to the large value of R/λ_D , (b)The ratio of J_e/J_i was small compared to an unmagnetized plasma where this ratio was about $\sqrt{\frac{m_i}{m_e}} \sim 60$. This is due to the electric field increasing along the flux tube which repels ions in front of the probe. Figure 3.20 shows these features measured in the ATF plasma. In ATF the ratio of J_e/J_i was in the range of two to five.

Finally, the effect of the high frequency RF field must be considered. The ATF ICRH experiments used frequencies up to 30 MHz. The RF field moved the probe characteristic curve back and forth with the RF frequency. The frequency response of the Langmuir probe was less than 1 MHz. Even if the density increased, the frequency response won't exceed 10 MHz due to the stray capacitance. Therefore the probe could not follow the fast moving curve at all. What it measured was the time-averaged curve which might be distorted significantly from the original curve. Figure 3.21

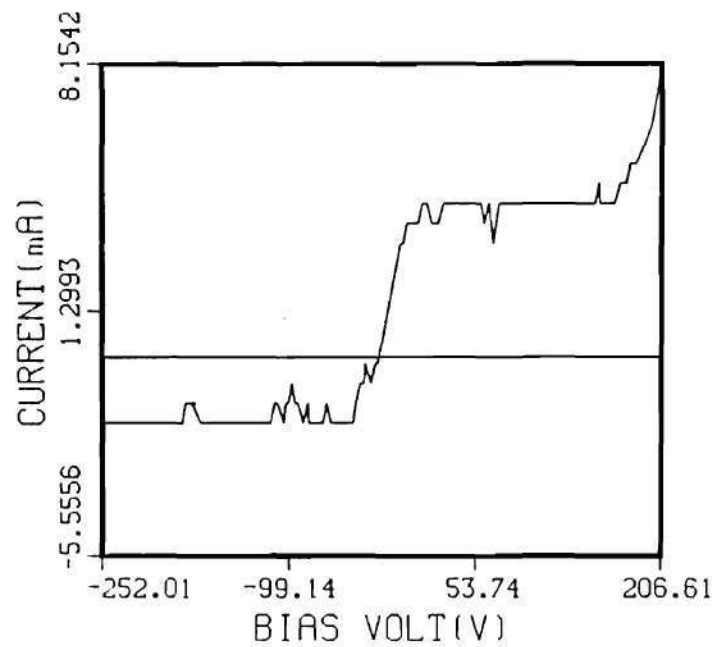


Figure 3.20: Typical I-V Characteristic Curve for an ATF Plasma Showing Features of Strong Magnetic Field Effects

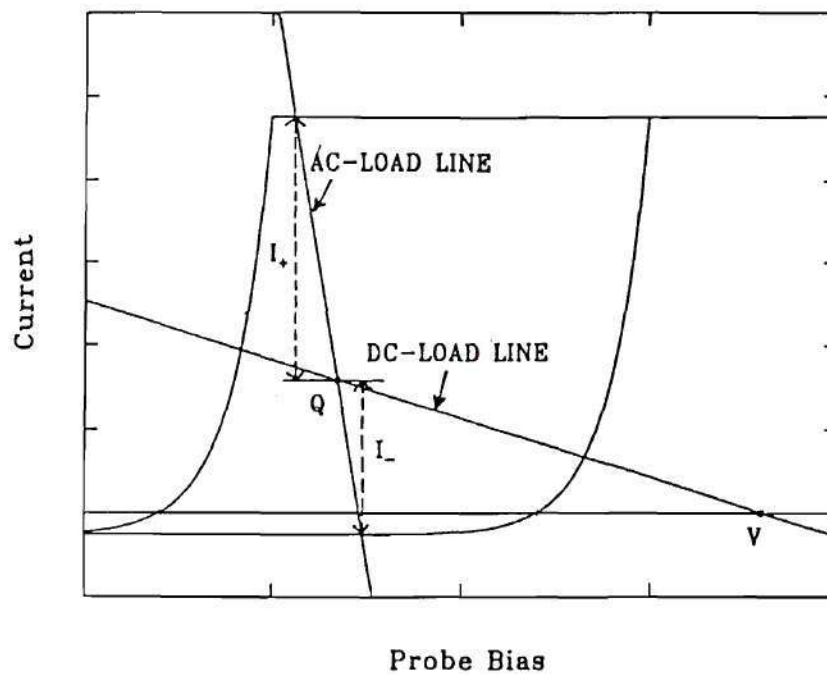


Figure 3.21: RF Effect on the Langmuir Probe Characteristic Curve

shows the effect of stray capacitance on the probe characteristic curve.[23] An AC impedance due to stray capacitance gives a load line with slope $|(1/R_L + j\omega C_s)|$, where $j \equiv \sqrt{-1}$, R_L is the load resistance and C_s is the stray capacitance. The DC load line normally has a slope $1/R_L$. The operating point of the probe is determined by the intersection of the two load lines. For floating potential measurements, the load line should be close to the horizontal axis because the intersection with the characteristic curve is at a point close to where $I = 0$. Therefore R_L should be large for this case, and C_s must be small for the higher-frequency case. The former requirement would be easy, while the latter could be difficult to achieve. The easiest way is to put the resistor as close to the end of the probe as possible. There also are various other techniques to overcome this problem[23].

For electron density and temperature measurements, a smaller resistor is required. But since the RF-fields distorted the curve substantially, care should be taken in analyzing data from the probe. Figure 3.22 shows a distorted time-averaged curve with two extreme possibilities for the corresponding instantaneous curve. The fatal change is the slope of the curve in the transition region, which is used to determine temperature and density. Also the floating potential of the time-averaged curve is different from the time-averaged floating potential.

Even in high-frequency RF environments, however, there is a region in the characteristic curve which is little changed — the ion saturation regime. Taking a slope from there and multiplying by two would restore the original curve as shown in Figure 3.22. The electron density is calculated according to Eq.(3.46). This was attempted by Caughman, et al.[10]. Another method, the so-called two probe method, was proposed by F.F. Chen[24].

Once the density is known, the temperature can be obtained from the slope at a point where the characteristic curve deviated from an exponential fit in the ion-saturation regime.

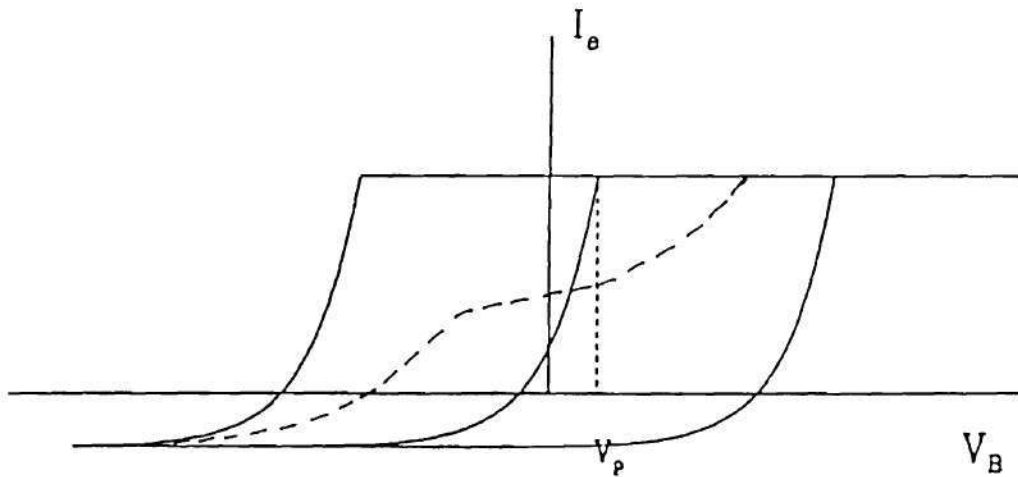


Figure 3.22: Time-Averaged Langmuir Probe Characteristic Curve (Dashed) with Two Extreme Cases

There is still not a good way to measure the floating potential in a high-frequency RF environment with this conventional floating Langmuir probe⁷.

Applications of Probe Measurements to ICRH Experiments on ATF

Three magnetic probes and a Langmuir probe were installed on ATF for the ICRH experiments. Figure 3.23 shows the locations of the probes. The big probe and a small probe were placed on the antenna port (TN-5) and another small probe was placed on adjacent bottom port (Bottom-4).

The big probe was equipped with a motor-driven translator and the two small probes were equipped with manual translators. Each translator had an 8-inches (20.5-

⁷Capacitive and emissive probes are widely used for this purpose.

Table 3.3: The Exact Probe Positions in (r, z, ϕ) Coordinates

		R (cm)	ϕ (Degree)	Z (cm)
Probe I (Big probe)	Max-In	226.06	9.72	10.29
	Max-Out	242.0	10.07	10.29
Probe II (Small 1)	Max-In	230.62	4.57	-25.25
	Max-Out	247.35	5.28	-25.25
Probe III (Small 2)	Max-In	210.25	-2.77	-47.62
	Max-Out	210.25	-2.77	-37.62

cm) stroke.

Under normal conditions, the maximum probe-in positions were 20.5-inches (52-cm) for the big probe and the small probe on the antenna port and 21-inches (53-cm) for the small probe on the adjacent bottom port. Each distance was measured from the inside of the port cover flange to the top of the probe head. The toroidal angles for these probes at the maximum probe-in position were $\sim 10^\circ$, $\sim 4^\circ$ and $\sim 2^\circ$, respectively. The exact positions in (r, z, ϕ) coordinates are tabulated in Table 3.3. Here r is major radius, z is vertical distance from the plasma center, and ϕ is toroidal angle.

The magnetic probes were used for monitoring the antenna near field, eigenmode detection, and field attenuation measurements during RF heating. With a fast digitizer, a frequency spectrum was obtained to examine the correlation of magnetic field fluctuation with other plasma performance characteristics.

The Langmuir probe was basically used for edge electron density and temperature measurements. Along with these data, FIR interferometer measurements gave the whole plasma column density profile with and without ICRH.

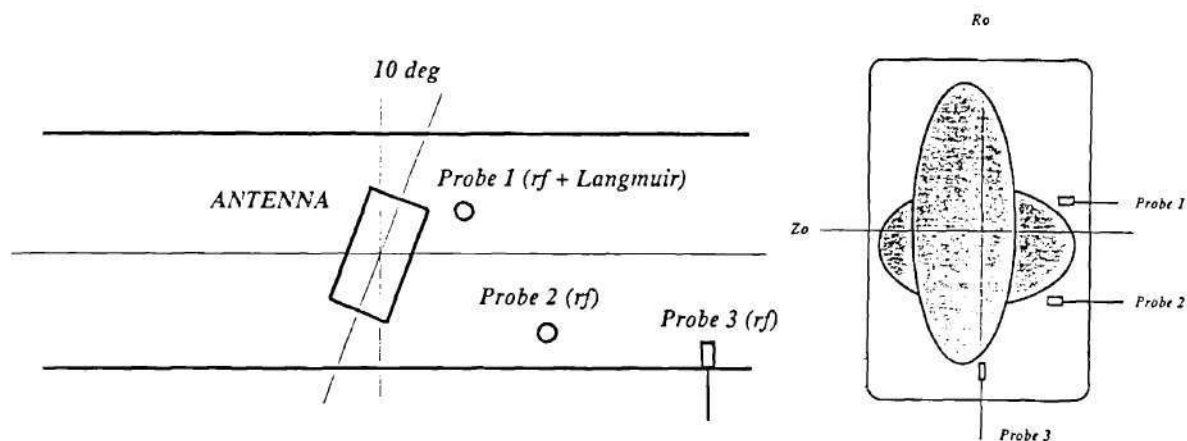


Figure 3.23: Relative Locations of the Three Edge Probes

A probe data analysis program, *PDA*, was written by which the magnetic probe and Langmuir probe data were read, analyzed and plotted.

Experimental Considerations

Probe Design The ATF environment was very harsh for probes even in the edge region. Every probe had to be protected from high heat flux. Graphite armour was adopted to protect the loops and to shield out electrostatic coupling for the magnetic probes as shown in Fig. 3.24. The probe shown in Fig. 3.24 was damaged by insertion too far into the plasma column for 3 days.

In the magnetic probes, for high frequency response, a single turn loop was used with a large area to improve the S/N ratio. A 0.141-inch (0.36-cm) stainless steel (SS) coax cable ran through the SS tube attached to the translator outside the vacuum vessel, and arrived at the SS base. From there, stripped cable ran through the graphite armours and ceramic spacers to the ring conductors in the top. As

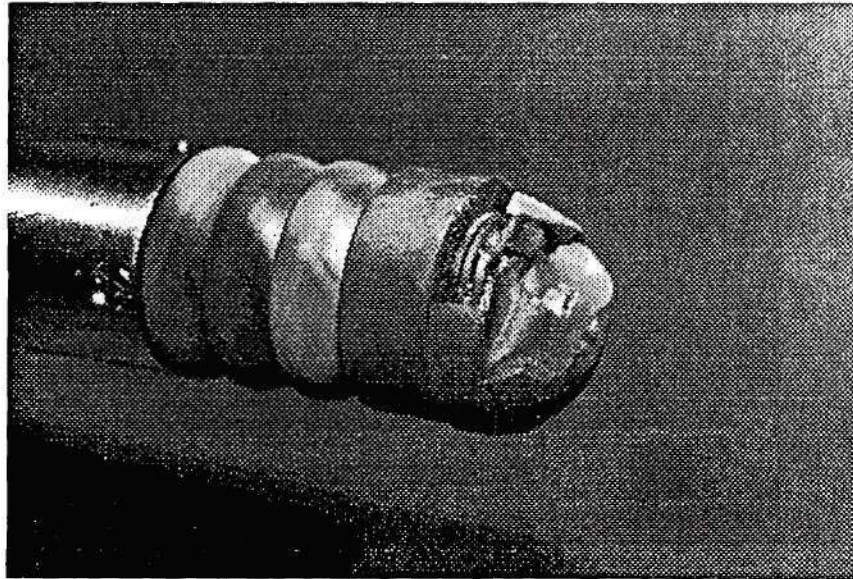


Figure 3.24: Graphite Shield and Inside of the Graphite Head Shown in the Damaged Magnetic Probe

four coax cables were connected in this way, each cable was separated exactly by 90 degrees around the ring conductor. The two separate ring conductors were used, each of which was connected to the two stripped cables, separated by 180 degrees, so that two separate, orthogonal loops were formed. To reduce the impedance by preventing the formation of other loops between coax cable legs, the four coax cables were tightened together without spaces in between them.

In the big probe which consists of two magnetic probe loops and two single Langmuir probe tips, two additional coax cables ran from the tips to the translator to form the double-tip Langmuir probe. The two graphite tips were 1.6 mm long, 0.63 mm in radius, and separated by 5.75 mm. To avoid particle accumulation between the graphite tip and the graphite armour, a ceramic insulator was added between them.

In summary, the main features of these probes were 1) graphite armour to

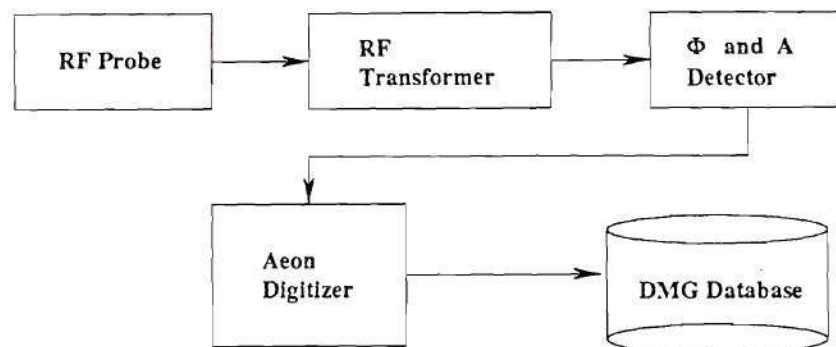


Figure 3.25: Diagram of the Electronics for RF Probe Measurements

reduce heat and particle flux to the loops and tips, 2) large loop area to compensate signal degradation due to graphite Faraday shields and single-turn design, 3) two orthogonal loops to determine two components of the B-field, 4) in the big probe, two single Langmuir probe tips were placed on top of the graphite probe head, and 5) all probes were position-controlled by translators.

Electronics The electronic system used for the magnetic probes in the ATF ICRH experiment is shown in Fig. 3.25. An RF transformer was used to couple the probe signal with the measurement electronics. The whole circuit was shielded from external magnetic fields. Two different ground paths were used for the loop and the electronics so that the measurement circuit was floating with respect to the vacuum vessel. The box which enclosed the transformer was placed near the probe to minimize the path length for the probe signal. The signals coupled through the transformers were transmitted directly to the phase and amplitude detection modules in which

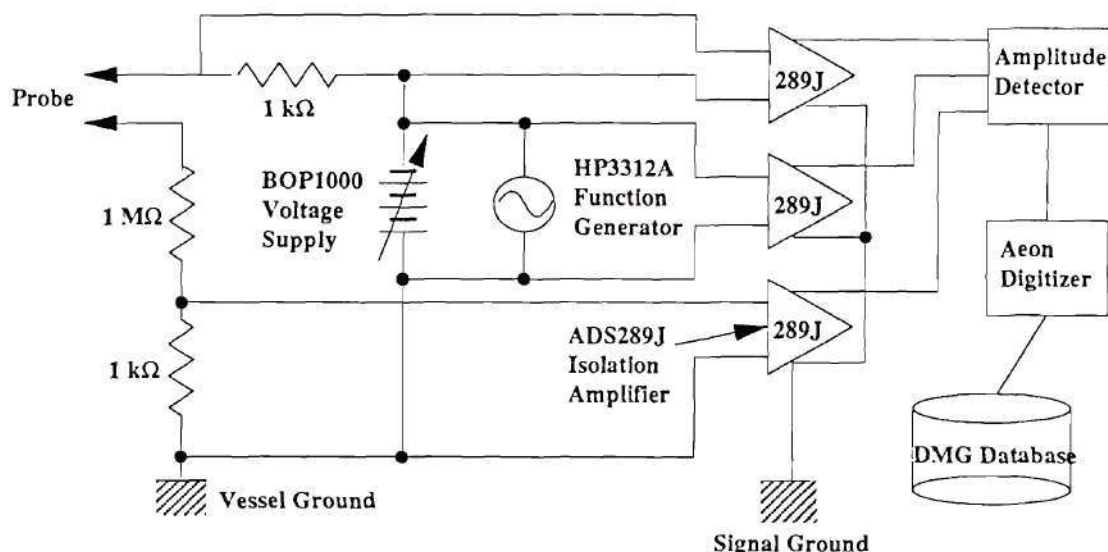


Figure 3.26: Diagram of the Electronics for Langmuir Probe Measurements

information about the phase with respect to a reference signal and the absolute amplitudes of the signal was obtained and sent out to a CAMAC data acquisition module.

Circuits for the Langmuir probe were more complicated and varied depending on the experimental conditions. The circuit used in ATF is shown in Fig. 3.26. The ATF timing clock signal triggered a waveform train from a Hewlett-Packard function generator (3312A), typically a sawtooth form amplified by a KEPCO bipolar operational amplifier (BOP1000M). This bias voltage set a potential difference between one of the tips and the plasma. One probe tip was used for current measurements, and the other tip was used for potential measurements. These two tips were connected to smaller and larger resistors, respectively, then the signals were transmitted through two differential amplifiers (ADS 289J) and finally recorded in an Aeon 3232 digitizer. As in the magnetic probe circuit, the probe ground path was different from the ground path of the electronics. The Langmuir probe was equipped with a motor-

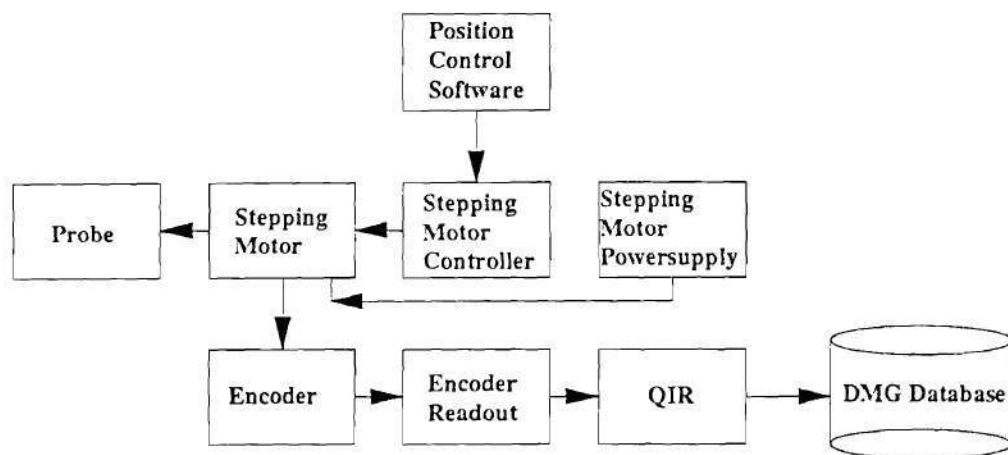


Figure 3.27: Diagram of Langmuir Probe Positioning Circuit

driven translator for remote position control. Figure 3.27 shows the CAMAC system for probe positioning. A Joerger stepping motor controller unit was used to control the motor, and an encoder provided the probe position through a digital read-out. The position data was registered in registers (QIR). The software used for stepping motor control for the Thomson scattering system was modified for probe position control⁸.

⁸The author is grateful to D. A. Rasmussen for providing the program and to D. C. Giles for helping him modify it.

The ATF Data Acquisition System

ATF Data System

The ATF data system[25,26] consists of a variety of hardware and software items. The hardware acquired all forms of data, generated all control waveforms and provided trending and logging services for the safety interlock and control systems.

The hardware consists of two VAX 8700 cpu's, two MicroVAX front ends and a set of PLCs. The VAX 8700 system manages overall data acquisitions and dynamic control. The CAMAC system is driven by this VAX 8700 system, which performs physics-related control including generation of waveforms. State control is done by four Modicon 584 PLCs and interfaced with the VAX 8700 system by a MicroVAX front end. There is an optical juke box which is a WORM disk used for back-up data and almost on-line storage. By using utility software the data are rapidly brought on-line for analysis.

The software supervises and monitors data flow and memory, manages the data and files, and provides interface to the PLC and CAMAC. The software consists of the following:

SAMS: supervising and monitoring system,

DMG: a signal-based data and file management package,

ORNL/FED: CAMAC driver package,

ONSPEC: commercial package to interface to the PLC,

IDL: commercial, general purpose data analysis package,

PLOTCH: a "quick look" package.

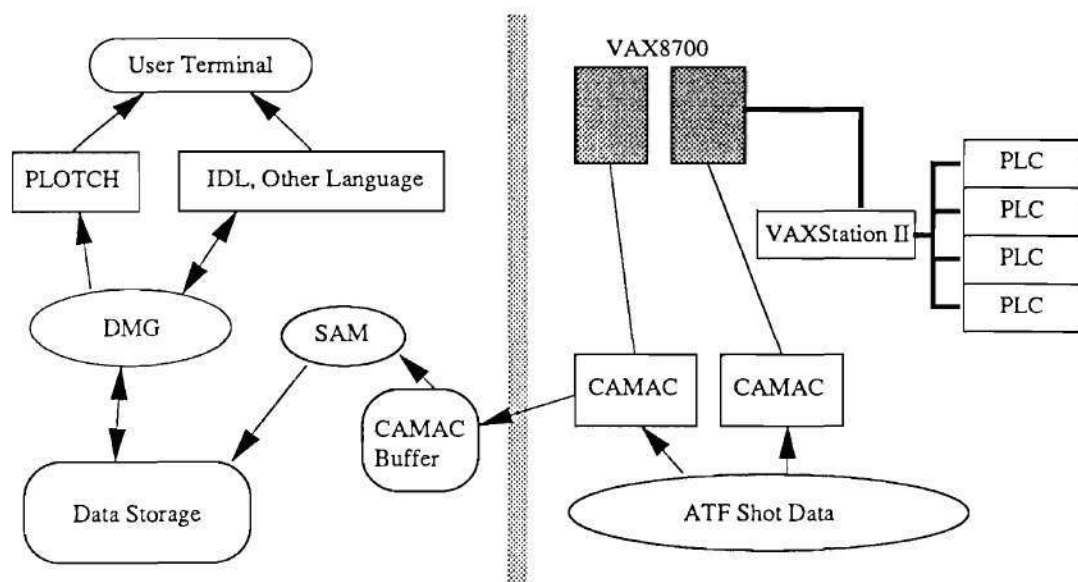


Figure 3.28: The ATF Data Acquisition System and Data Flow Diagram

Figure 3.28 shows the outline of the ATF data system and the data flow through this system.

ICRH Data System

The ATF ICRH project has two diagnostic names: ICRF and ICRFAUX. Most of the RF data are acquired under ICRF except for the two fast digitizer signals which are acquired under ICRFAUX. There are 30 signal names in ICRF and 2 signal names in ICRFAUX as listed in Table 3.4.

All analog signals for ICRF are digitized by an AEON 3232 digitizer unit which has 32 channels with a 5 kHz sampling rate. Other digital signals are directly stored in a Jorway QIR (Quad input register) before being read by a CAMAC controller. The two signals in ICRFAUX are digitized in two TRANSIAC digitizers each

Table 3.4: Signal Name and Description in ICRF and ICRFAUX

IC_AT1C1	Antenna Capacitor 1 Position
IC_AT1C2	Antenna Capacitor 2 Position
IC_AT1RI	Imaginary Part of Antenna Reflection Coefficient
IC_AT1RR	Real Part of Antenna Reflection Coefficient
IC_AT1RV	Antenna Reflected Voltage
IC_AT1TI	Imaginary Part of Antenna Transmission Coefficient
IC_AT1TR	Real Part of Antenna Transmission Coefficient
IC_AT1FV	Antenna Forward Voltage
IC_CPRB1	Current Probe Signal
IC_DPC	Langmuir Probe Current Signal
IC_DPPOS	Langmuir Probe Position
IC_DPSPW	Langmuir Probe Bias Sweep Voltage
IC_DPV	Langmuir Probe Floating Potential
IC_RF1BP	RF Probe 1, Loop 1 Signal
IC_RF1BT	RF Probe 1, Loop 2 Signal
IC_RF1PH	RF Probe 1 Phase
IC_RF1PK	RF Probe 1 Fast Digitizer Signal
IC_RF2BP	RF Probe 2, Loop 1 Signal
IC_RF2BT	RF Probe 2, Loop 2 Signal
IC_RF2PH	RF Probe 2 Phase
IC_RF2PK	RF Probe 2 Fast Digitizer Signal
IC_RF3BP	RF Probe 3, Loop 1 Signal
IC_RF3BT	RF Probe 3, Loop 2 Signal
IC_RF3PH	RF Probe Phase
IC_SETUP	Analyzer Setup Parameter
IC_TR1FV	Transmitter Forward Voltage
IC_TR1RV	Transmitter Reflected Voltage

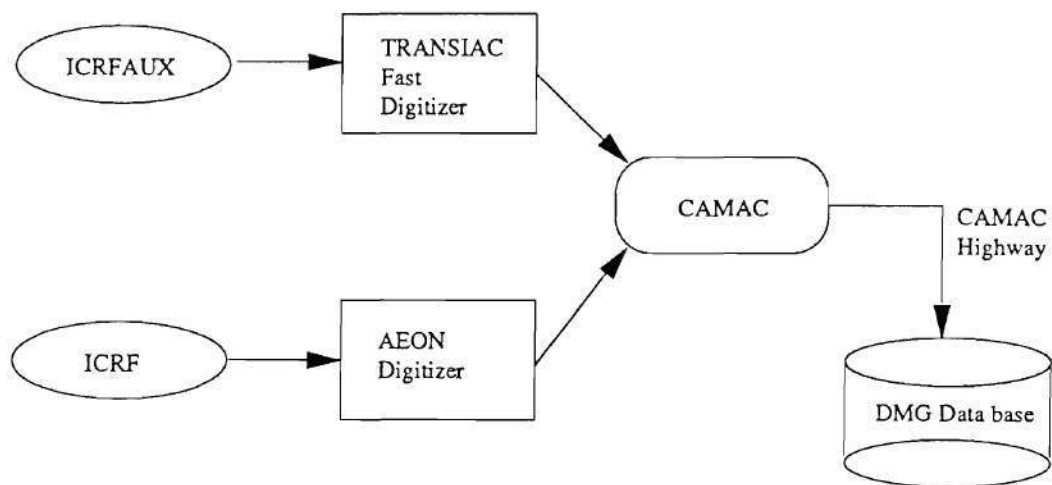


Figure 3.29: The ICRH Data Acquisition System and Data Flow Diagram

of which has 1 channel with a 100 MHz sampling rate. A block diagram of the ICRF and ICRFAUX data acquisition system and data flow is illustrated in Fig. 3.29.

REFERENCES

- [1] Lyon, J. F., et al., "The Advanced Toroidal Facility," *Fusion Technol.*, **10**, 179 (1986).
- [2] Saltmarsh, M. J., et al., "Initial Experimental Results from the ATF Torsatron," Proc. 12th Int. Conf. Plasma Physics and Controlled Nuclear Fusion Research, Nice, France, October 12-19, 1988, IAEA CN-50/C-1-2, International Atomic Energy Agency (1989).
- [3] Murakami, M., et al., "Overview of Recent Results from the Advanced Toroidal Facility," Report ORNL/TM-11453, Oak Ridge National Laboratory (1990).
- [4] Isler, R. C., et al., "Spectroscopic Studies of Plasma Collapse in the Advanced Toroidal Facility," *Nucl. Fusion*, **29**, 1384 (1989).
- [5] Colchin, R. J., et al., "Overview of Results from the ATF Torsatron," *Bull. Am. Phys. Soc.*, **34**, 1999 (1989).
- [6] Harris, J. H., et al., "Second Stability in the ATF Torsatron," *Phys. Rev. Lett.*, **63**, 1249 (1989).
- [7] Ramo, S., Whinnery, J. R., Van Duzer, T., *Fields and Waves in Communication Electronics*, (John Wiley and Sons, New York, 1984), Chapter 5.
- [8] There was a series of workshops on "RF/edge physics." The first one was held in Oct. 1987 at Oak Ridge, TN, the second one was in Apr. 1988 at Boulder, CO, and the third one was held in Oct. 1989 at Garching, Germany. The proceeding of the last workshop was published in *Fusion Engineering and Design*, **12**, 1-286 (1990).

- [9] Lehrman, I. S., "A Study of Coupling and Edge Processes for ICRF Antennas," Ph.D Thesis, University of Wisconsin at Madison (1988).
- [10] Caughman, J. B. O., "The Distribution of Ion Energy Incident on an ICRH Antenna Faraday Shield," Ph.D Thesis, University of Illinois at Urbana-Champaign (1989).
- [11] Greene, G. J., "ICRF Antenna Coupling and Wave Propagation in a Tokamak Plasma," Ph.D Thesis, California Institute of Technology (1984).
- [12] Segre, S. E., and Allen, J. E., "Magnetic Probes of High Frequency Response," *J. Sci. Instrum.*, **37**, 369 (1960).
- [13] Ashby, D. E., et al., "A Multi-Coil Magnetic Probe," *J. Sci. Instrum.*, **40**, 384 (1963).
- [14] Decker, G., and Honea, D. L., "Magnetic Probes with Nanosecond Response Time for Plasma Experiments," *J. Phys. E*, **5**, 481 (1972).
- [15] Chen, F. F., "Electric Probes" in Plasma Diagnostics Techniques, Huddleston, R. H., and Leonard, S. L. eds., (Academic Press, New York, 1965), Chapter 4.
- [16] Hutchinson, I. H., Principles of Plasma Diagnostics, (Cambridge University Press, Cambridge, England, 1988), Chapter 3.
- [17] Chung, P. M., Talbot, L., and Touryan, K. J., Electric Probes in Stationary and Flowing Plasmas: Theory and Application, (Springer-Verlag, New York, 1975) Chapters 1 and 2.

- [18] Bohm, D., Burhop, E. H. S., and Massey, H. S. W., "The use of Probes for Plasma Exploration in Strong Magnetic Fields" in *The Characteristics of Electrical Discharges in Magnetic Fields*, Guthrie, A. and Wakerling, R. K. eds., (Mcgraw-Hill, New York, 1949) Chapter 2.
- [19] LaFramboise, J., "Theory of Cylindrical and Spherical langmuir Probes in a Collisionless Plasma at Rest," in *Rarefield Gas Dynamics*, Vol. II, De Leeuw, J. H. eds., (Academic Press, New York, 1966) p.22.
- [20] Kiel, R. E., *AIAA J.*, **6**, 708 (1968).
- [21] Harrison, E. R., and Thompson, W. B., *Proc. Phys. Soc.*, **74**, 145 (1959).
- [22] Stangeby, P. C., "The interpretation of Plasma Probes for Fusion Experiments" in *Plasma Diagnostics*, Vol. I, Auciello, O., and Flamm, D. L. eds., (Academic Press, New York, 1989) Chapter 5.
- [23] Hershkowitz, N., "How Langmuir Probes Work" in *ibid.*, Chapter 3.
- [24] Chen, F. F., "Modern Uses of Langmuir Probes," Report IPPJ-750, Institute of Plasma Physics, Nagoya University, Nagoya, Japan (1985).
- [25] Wing, W., et al., "The ATF Data System," *Bull. Am. Phys. Soc.*, **33**, (1988).
- [26] Stewart, A., et al., "The Data Acquisition and Control Systems for ATF: An Overview," unpublished.

CHAPTER IV

EXPERIMENTAL OBSERVATIONS

In this chapter, the results of ICRH experiments performed on ATF are presented. Detailed analysis is presented in Chapter V. Wall and antenna conditioning are the first topic and a description of the target plasma and global changes due to ICRH follows. Some important diagnostic signal traces with ICRH are presented in detail. These are antenna loading, spectroscopy data, neutral particle analyzer data, and edge probe signals.

Wall Conditioning and ECH Target Plasma

Wall conditioning in ATF

Most of the experimental work on ATF (including ICRH) required clean walls and a good base vacuum. To obtain these conditions ATF used three different wall conditioning techniques: baking, glow discharge cleaning, and gettering.

Baking was accomplished by inductance coupling of ac power to the vacuum vessel with low-power excitation of the helical windings. The rate at which adsorbed gases are spontaneously desorbed from a metal surface in a vacuum can be described by the equation [1]:

$$\frac{dc}{dt} = \frac{c_0}{\tau_0} \exp\left(-\frac{E_d}{kT}\right), \quad (4.1)$$

where c is the surface concentration, c_0 is the initial concentration, τ_0 is the time constant when there is no binding energy, E_d is the binding energy and T is the surface temperature. Since the desorption rate depends on the baking temperature, it is possible to calculate the time for a specific gas to be desorbed at a given temperature.

For ATF, the maximum allowable temperature was 150 °C and a 6 minute baking cycle was used (2.5 minutes on and 3.5 minutes off). However, tightly adsorbed molecules or atoms still cannot be released in any realistic time, so even after baking the walls remained covered with adsorbed species. The consequence of this was that the wall released gas in large quantities when bombarded by plasma particles. This was the reason for using glow discharge cleaning (GDC) simultaneously with baking.

There were several excitation sources for GDC, they consisted of a DC power supply (600 - 1000 V), an RF power supply (13.6 MHz), and a microwave power supply (1-3 GHz). In some cases a parallel combination of dc and high frequency sources was used. In ATF, the 1 kV, 2.5 A DC power supply was used for H₂ and D₂ GDC. Initial breakdown occurred at about 15 mTorr for a "dirty" vessel and about 40 mTorr for a "clean" vessel. There was also electron cyclotron resonance discharge cleaning (ECR-DC) which consisted of 3 kW cw at 2.45 GHz, applied simultaneously with a small magnetic field. The resonant $|B|$ is 0.0875 T and it was used with 3×10^{-5} Torr H₂ gas. Induction heating (baking) and GDC have been performed simultaneously. This resulted in lengthening the time to radiative collapse in the early phase of ATF operation[2]. Since the magnetic field created when the helical field coils are used for baking significantly reduces the size of the glow discharge volume, GDC was much more effective after the induction coil was turned off which was for 3.5 minutes of the 6 minute cycle (58%).

The ICRH antenna was initially conditioned during baking and GDC cycles, and significant outgassing was observed. Outgassing was especially high when the antenna was operated in the multipactor breakdown regime, typically a very low RF

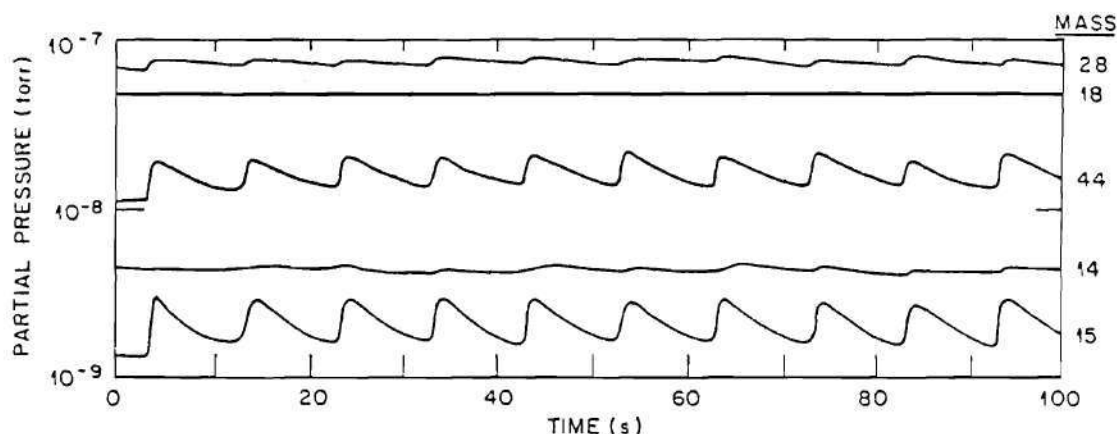


Figure 4.1: Partial Pressure of Five Dominant Mass Peaks vs Time during Antenna Conditioning (Taken during Multipactor Breakdown)

power as shown in Fig. 4.1. During later experimental periods after extensive antenna conditioning and gettering, this phenomenon was not observed and only a few hours of antenna conditioning was needed for launching full RF power (~ 200 kW).

In early ATF operation, a plasma stored energy collapse followed by a density collapse usually happened during NBI+ECH discharges even though the Z_{eff} was very low (≤ 2) and radiated power was only about 30% of the input power. Induction heating and GDC could not eliminate this problem. Neither did gettering with two Cr balls help. At the time, magnetic field errors were thought to be the primary cause of the problem. However, field error correction did not eliminate the collapse. As the number of getter balls was increased the time to the collapse was delayed significantly even though the problem was not completely solved. With six-ball Ti gettering, which covered $\sim 70\%$ of the wall area, NBI heating sustained the plasma as long as 300 ms without a collapse.

In a typical getter cycle, each source is heated to 1150°C and yields a sub-

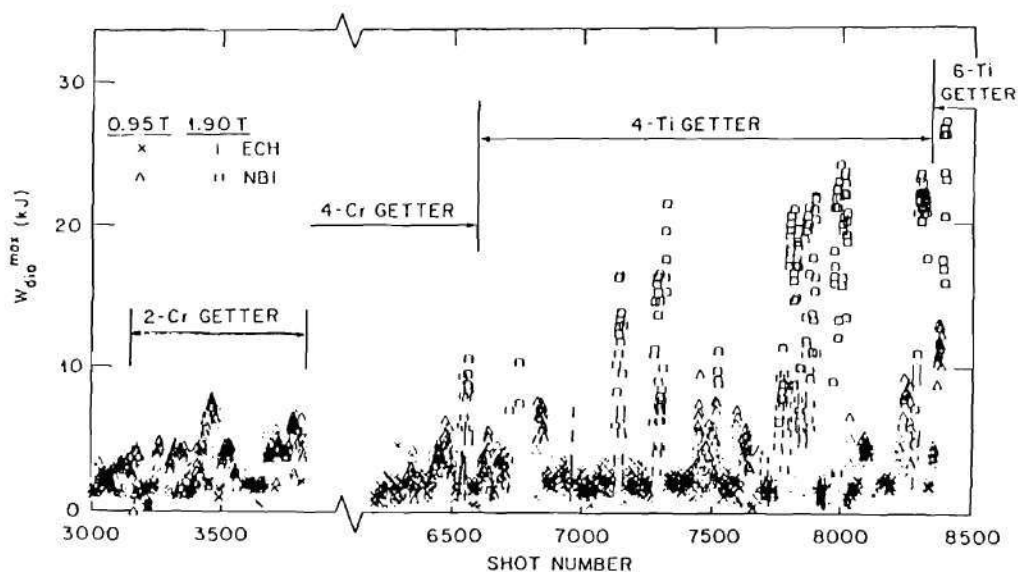


Figure 4.2: Maxima of the Stored Energy for Discharges with a Variety of Gettering Configurations[4]

limination rate of 0.1 g/h. The deposition process is continued for half an hour and deposits an average of 5 monolayers of titanium. The effect of gettering on plasma performance has been studied by R. Isler et al.[3], and Fig. 4.2 shows the effects on the stored energy. The radiation from low-Z impurities and the impurity content were lower than for pre-gettering periods according to spectroscopic measurements. However, high-Z impurity lines appeared as the edge temperature increased.

This evolution of the wall condition affected the ICRH also. Figure 4.3 is a chart showing the evolution of the ATF wall condition and antenna conditioning in terms of the duration necessary for vacuum conditioning of the antenna and the timing of major ATF vacuum openings. In 1988 when the first ICRF wave power experiments started, the maximum RF power level injected into the plasma without collapse was about 40 kW. In 1989 when 30 hours of antenna conditioning were done before attempting ICRH, 100 kW of RF power still collapsed a plasma pre-gettered

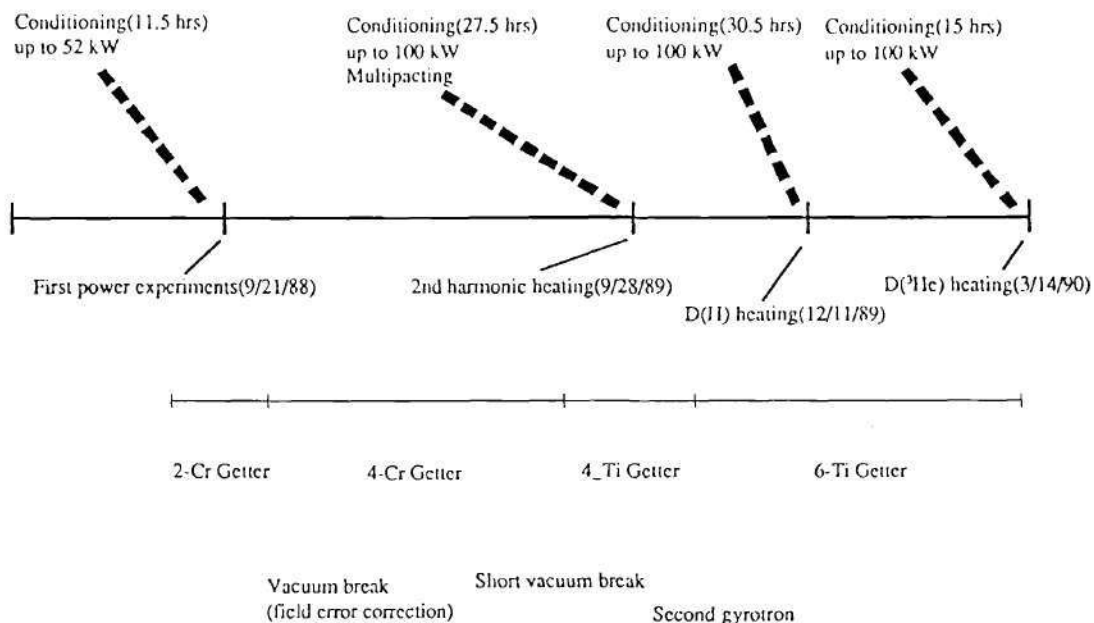


Figure 4.3: A Diagram Showing the Evolution of ATF Vessel and Antenna Conditioning

with four Ti balls. Three months later, after 30 hours of antenna conditioning and six Ti ball gettering, 200 kW of rf power could be launched into the plasma without causing a collapse.

ECH Target Plasmas and Changes During ICRH

Target plasmas for the ICRH experiments were generated by electron cyclotron heating (ECH) with a 53 GHz, 200 kW gyrotron. A second gyrotron with the same specifications was installed in October, 1989. As mentioned previously, wall conditioning evolved and magnetic field errors were fixed during the course of the ICRH experiments. This affected plasma performance, and so the basic parameters of the plasma were not the same during the whole experimental period. The effect of six-Ti gettering and the second gyrotron particularly changed the target plasma parameters (including density, stored energy and edge temperature). The field error

Table 4.1: ATF Parameters for ICRH Target Plasma

ECH Power	350-400	kW
Line Avg. Electron Density	$\sim 0.6 \times 10^{13}$	cm^{-3}
Central Electron Temperature	800-1000	eV
Central Ion Temperature	150-200	eV
Stored Energy	1.5-2	kJ
Z_{eff}	2	

correction produced broader profiles of electron temperature and density[5].

Since most of the data used in this dissertation were obtained after the second gyrotron installation, the plasma parameters described here will reflect those plasma conditions. Table 4.1 shows some important plasma parameters for the period after installation of the second gyrotron.

It should be noted that since these parameters were varying day by day, detailed comparisons must be made with care.

During ICRF most of the plasma parameters influenced by wave-plasma interactions were affected. Global changes occurred in density, temperature, stored energy, Z_{eff} , radiated power, edge parameters and particle distributions. The changes in these parameters are interconnected, and often have different time scales, so that there is an effective time scale for a discharge to transiently evolve to a new equilibrium. In the ATF ICRH experiments, with up to 200 kW of power, little change in the equilibrium was observed if the target plasma had constant density when ICRH was applied. The temporal behavior of a typical shot in this category is shown in Fig. 4.4.

Rising-density shots were another type of discharge into which RF waves were injected. During these shots the plasma density would rise uncontrollably, resulting

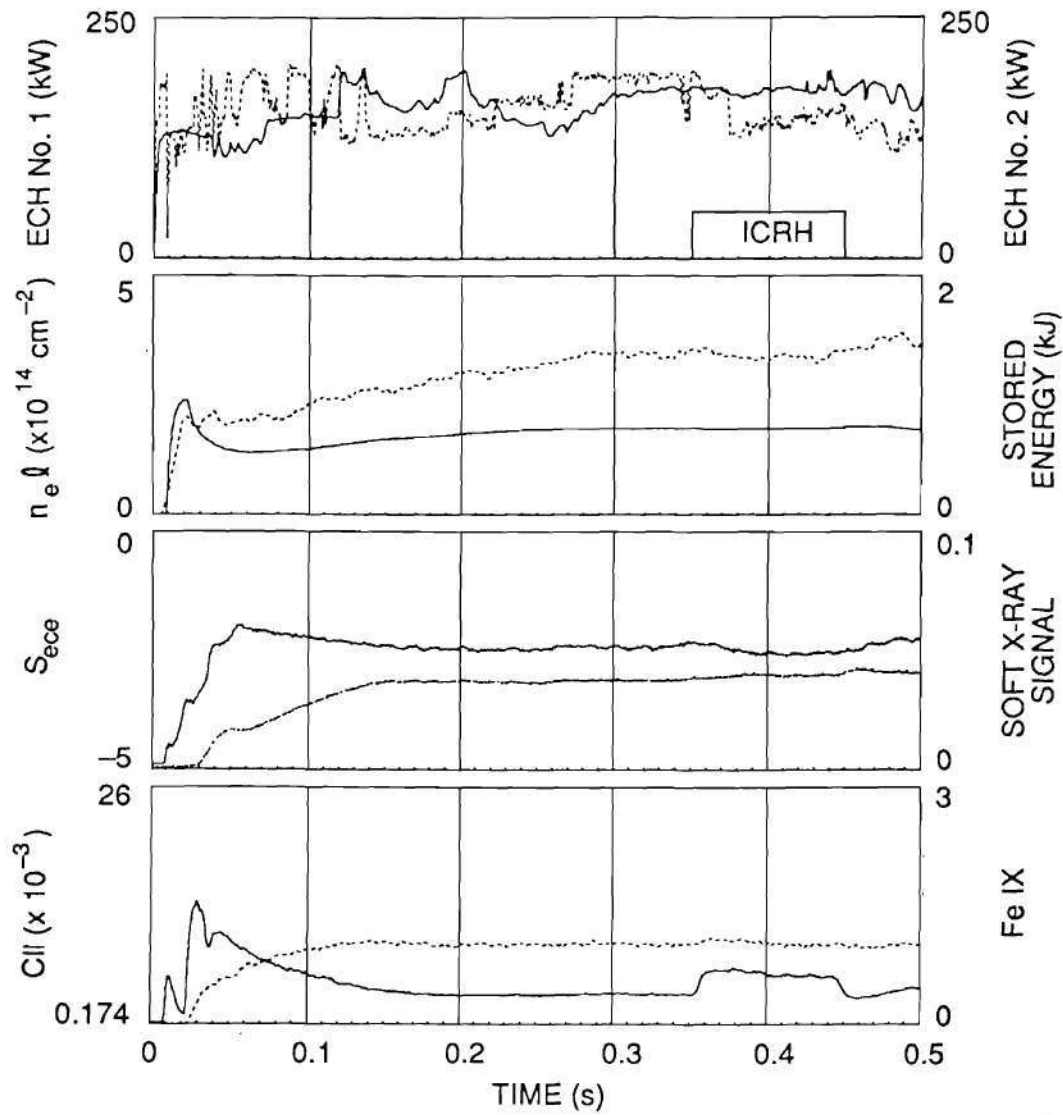


Figure 4.4: The Time Behavior of Various Signals for a Typical Constant-Density Shot

in collapse of the energy content of the plasma. This was not present without RF. The time behavior of various signals for this category of shot is shown in Fig. 4.5. Usually the density rise during ICRH was prevented by gettering and adjusting the gas puff, but occasionally uncontrollable density increases occurred. In a sequence of shots with uncontrolled density increase, typically the onset time of the density rise would move earlier and earlier in time, so that finally the density increase would begin immediately as the ICRH was turned on.

A common behavior was observed in both constant density shots and rising density shots. The density trace showed an immediate drop as soon as the RF wave was initiated, as illustrated in Fig. 4.6. This density drop is believed to have been caused by a fast ion loss since the orbits of edge heated fast ions become unconfined, as will be discussed in Chapter V.

In both cases, no measurable bulk ion or electron heating was observed from the Doppler broadening of the impurity line measurements and the Thomson scattering measurements even though the NPA measured a large minority ion (hydrogen) tail up to 50 keV and some (apparent) deuterium temperature increase. The stored energy was also constant or decreased slightly during ICRH. In later experiments the radiated power measured by a bolometer did not change during ICRH even though several impurity lines measured by spectroscopy increased. These data and other detailed observations are presented in following sections.

Loading Measurements

Loading measurements during ICRH experiments were performed by two different techniques. Low power loading measurements were performed with a Hewlett-Packard network analyzer (HP-8753A) and an antenna directional coupler. This

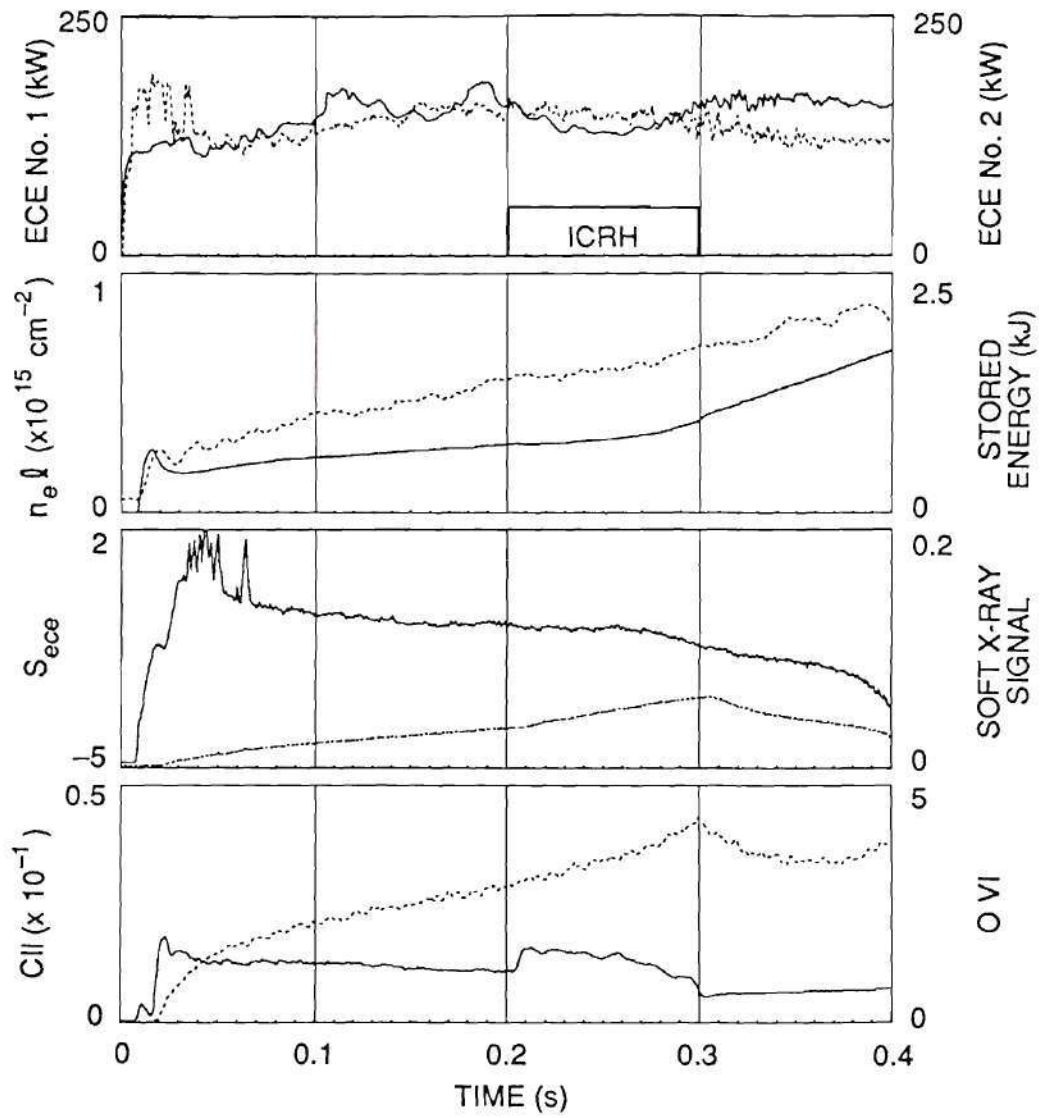


Figure 4.5: The Time Behavior of Various Signals for a Typical Rising Density Shot

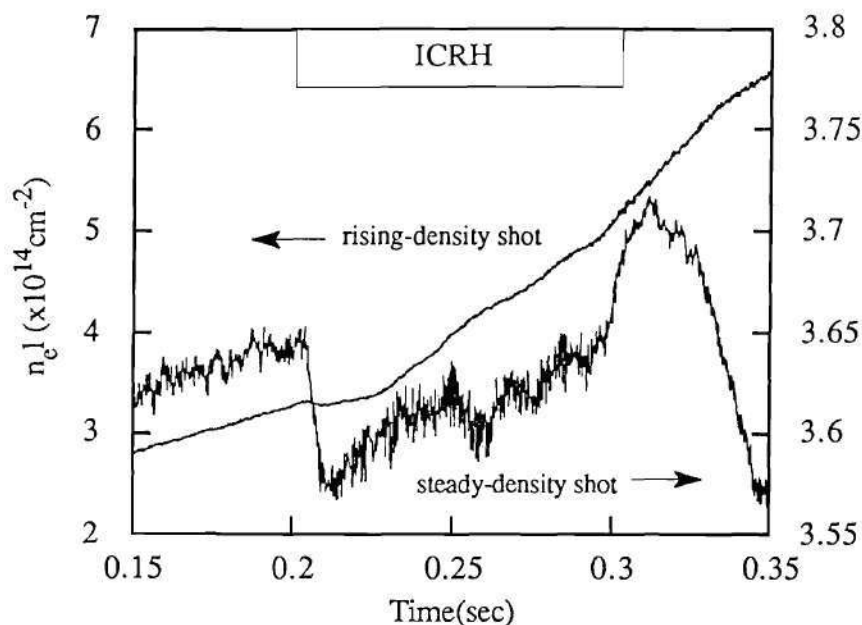


Figure 4.6: The Line-Integrated Density Trace Measured by a 2 mm Interferometer for a Steady Density and a Rising Density Shot

method was also used for high power experiments. The other technique involved using a current probe to measure the antenna strap current. With a knowledge of the vacuum loading and the equivalent probe signal, loading was calculated using the antenna current probe signal.

Low power loading measurements at 28.8 MHz were performed during the early period of ATF operation with ECH+NBI target plasmas. The 28.8 MHz frequency was equivalent to the second harmonic frequency of hydrogen for a magnetic field of 0.95 T on the plasma axis. The plasma condition was poor due to impurities and the field error problem and the antenna was not fully conditioned. The dependence of the loading on the density and the frequency is shown in Fig. 4.7 and Fig. 4.8. From these figures, it can be seen that the loading was very sensitive to both the plasma density and the frequency of the RF wave. The frequency dependence was verified by experiments with different frequencies and in different heating

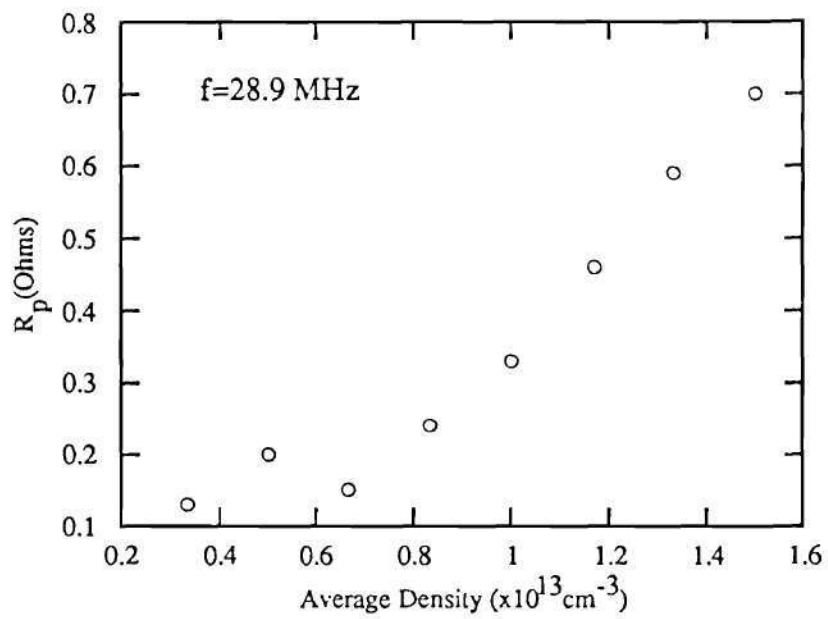


Figure 4.7: Loading Change as a Function of Density

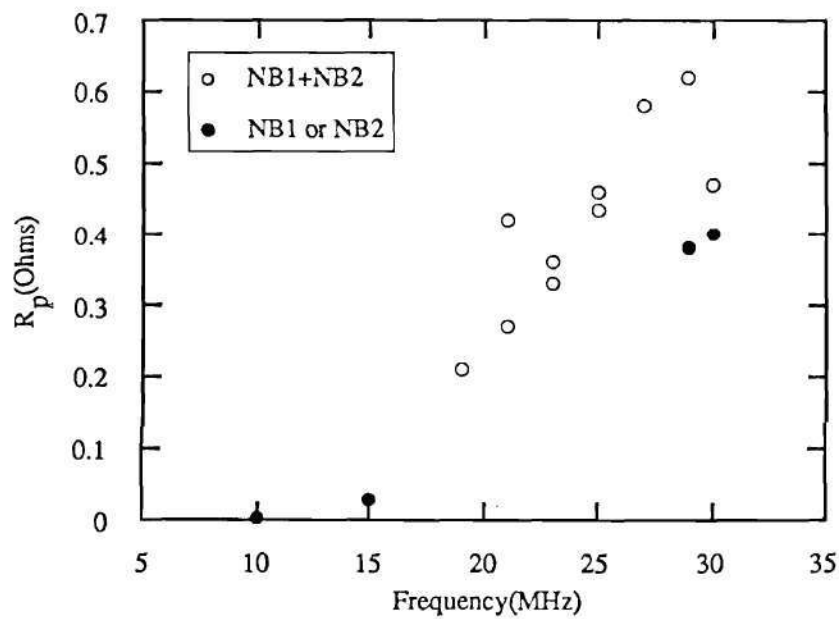


Figure 4.8: Loading Change as a Function of Frequency

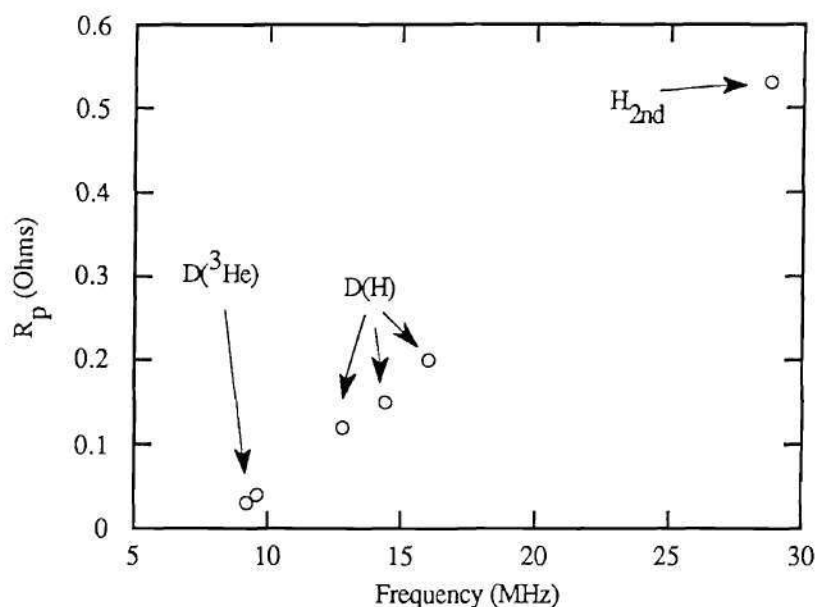


Figure 4.9: Loading Change as a Function of Frequency Determined by Various Heating Regimes (Low Density ECH Plasma)

regimes as shown in Fig. 4.9. In the hydrogen second harmonic regime (28.8 MHz), the measured loadings were highest. In the D(H) regime (14.4 MHz), plasma loading was less than the vacuum loading, which meant that half of the power was dissipated in the antenna structure. The D(^3He) regime (9.63 MHz) exhibited the lowest loading. This frequency sensitivity of the plasma loading was also observed during ICRH experiments in the Elmo Bumpy Torus (EBT)[6]. No high-Q eigenmodes, however, were observed during either of these experiments. Vacuum loading was also measured as a function of RF frequency. The vacuum loading was proportional to \sqrt{f} within $\pm 10\%$.

In the September, 1989, experiments, for most of the high power (~ 100 kW) shots, the loading was peaked in the very early phase of the RF pulse (20 to 30 msec), then decreased to $\sim 0.1 \Omega$ for the rest of the RF pulse. The loading also changed with the RF power level. For 5 and 10 kW of RF power, the loading stayed up around

0.5 Ω . Above about 20 kW of RF power, loading went down after the initial peak. These phenomena clearly showed that RF power above ~ 20 kW changed the edge plasma conditions in front of antenna within 20 to 30 msec after RF onset, which changed the antenna loading. This was consistent with the Langmuir probe results on that day which showed large changes in n_e and T_e around the antenna for power levels above 20 kW.

After gettering with six Ti balls and extensive antenna conditioning started (December 1989) plasma loading in the D(H) regime at 0.95 T, 14.4 MHz, 200 kW of RF, increased to 0.2 Ω , slightly higher than the vacuum loading. It was also observed that loading did not degrade during the shot due to edge plasma changes. However, as the experiments progressed, loading dropped to 0.1 Ω , probably because the wall gettering was wearing off during the day. Typically plasma conditions at the end of the day were not as good as at the beginning unless a break for gettering was taken during the middle of the day. The rising-density shots looked better in terms of loading than the constant density shots.

Another parameter on which loading depended sensitively was the gap between the plasma and the antenna. After pushing the antenna in as far as possible, the plasma was then shifted outward to change the gap by changing the inner and outer vertical-field coil currents. When this was done the plasma equilibrium was radically changed, producing a very low density plasma when the plasma was shifted out. Surprisingly, the loading almost tripled. Most of the loading change was probably contributed by edge plasma coupling, since the ICRF wave could not propagate into the low density central plasma region due to a thick evanescent layer. This will be demonstrated in Chapter V. The RF probes also showed evidence of edge propagation as shown in the edge probe measurements section of this chapter.

Increasing the density was clearly observed to be the best method of increasing the antenna loading. In ATF however, the ECH target plasmas were limited

in density by the cutoff density of the 53 GHz ECRF wave, which was at about $n_{el} = 5.0 \times 10^{14} \text{ cm}^{-2}$ ($\bar{n}_e \sim 0.8 \times 10^{13} \text{ cm}^{-3}$). Neutral beam injection was an alternative way to increase the loading. Unfortunately it was not possible to do more than make loading measurements with NBI. The beams were required to be hydrogen since D beams would have created an unacceptable neutron radiation hazard. With hydrogen neutral beams the H fraction was too high for D(H) experiments, and the H minority resonance at the edge would have prevented succesful D(^3He) experiments. Hydrogen second harmonic experiments with beam injection would have been possible but were never attempted after the field error was fixed. Another possibility for increasing the density was D pellet injection. Due to poor matching, no succesful shots were achieved, although this may be done in the future. The major problem in using pellets was that ECH plasmas could not be sustained during the pellet injection experiments. This might change in the future with the use of smaller pellets or increased ECH power/frequency.

Summarizing the loading measurements, with the ATF plasma and RF conditions described, the loading was very low due to poor propagation and low density. The loading was also sensitive to the wave frequency, increasing with the square root of frequency. Some experiments were done to change the loading without changing the target plasma. These experiments indicated that higher density, shifted-out plasmas would be better target plasmas as far as loading was concerned.

Spectroscopic Measurements

Even though ATF was equipped with good spectroscopic instruments, there were no systematic measurements with ICRF wave injection during the experiments for this thesis. However, in most of the ICRH experiments, a grazing incidence UV

spectrometer and a vacuum Czerny-Turner spectrometer were working, measuring a specific impurity line amplitude and/or ion temperature from Doppler broadening of the impurity line. There were also two impurity monitors tuned to 2838 Å and 3791 Å which were the CII and OIII line wavelengths, respectively.¹

After extensive six-element Ti gettering on ATF, most of the carbon lines disappeared, while CII measured from the impurity monitor still appeared in significant amounts. This is attributed to the fact that the impurity monitor has a relatively wide wavelength band so that other low charge state, high Z impurity lines made contributions rather than carbon[3].

In this section no conclusive statements are attempted due to the lack of dedicated operations and data, however, a clue about the effect of ICRH on the impurity behavior and some related topics are presented in a careful manner.

Typical impurity line signals with ICRH are shown in Fig. 4.10. An RF power threshold was observed around 40 kW after starting the six-element Ti gettering cycle. After 6-Ti gettering, (which increased the edge temperature) the signals from the two impurity monitors and H_{α} signal quickly increased initially, as before, but then slowly decreased. This is illustrated in Fig. 4.11. The initial increase was clearly due to energetic particle loss but the subsequent decrease is not understood; however, it is assumed to be the effect of edge cooling. These two signals were very well correlated with loading data and the neutral particle analyzer data which are shown later in this chapter.

Overall, six-element Ti gettering was good for ICRH. This can be seen by the fact that before 6-Ti gettering, ICRH always forced the plasma to collapse with ~ 100 kW power, however, after 6-Ti gettering accompanied with extensive antenna

¹The author is grateful to R. C. Isler, E. C. Crume, L. D. Horton, S. Hiroe and T. Uckan for providing data presented in this section and valuable comments

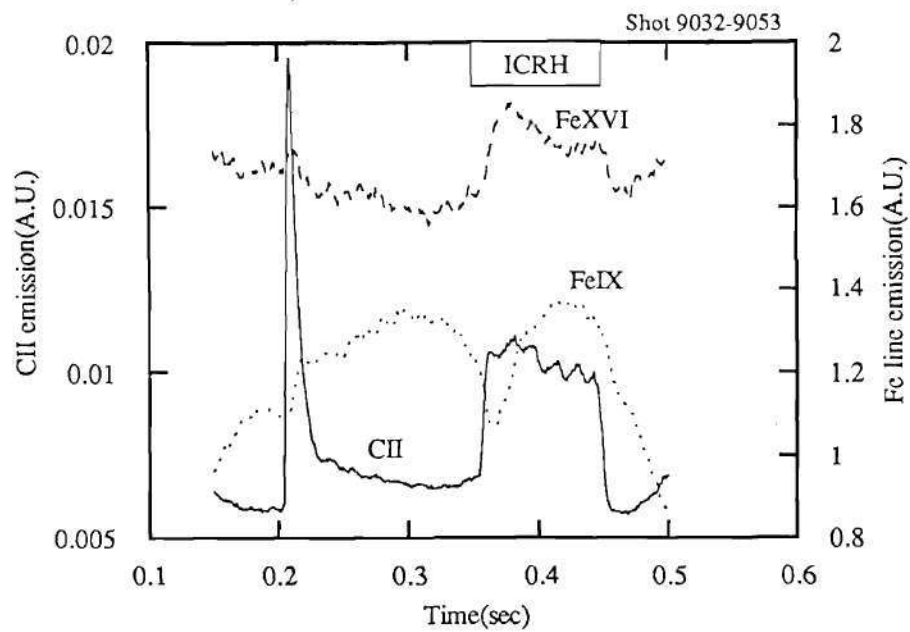


Figure 4.10: The Response of Various Impurity Lines to ICRF Wave Injection

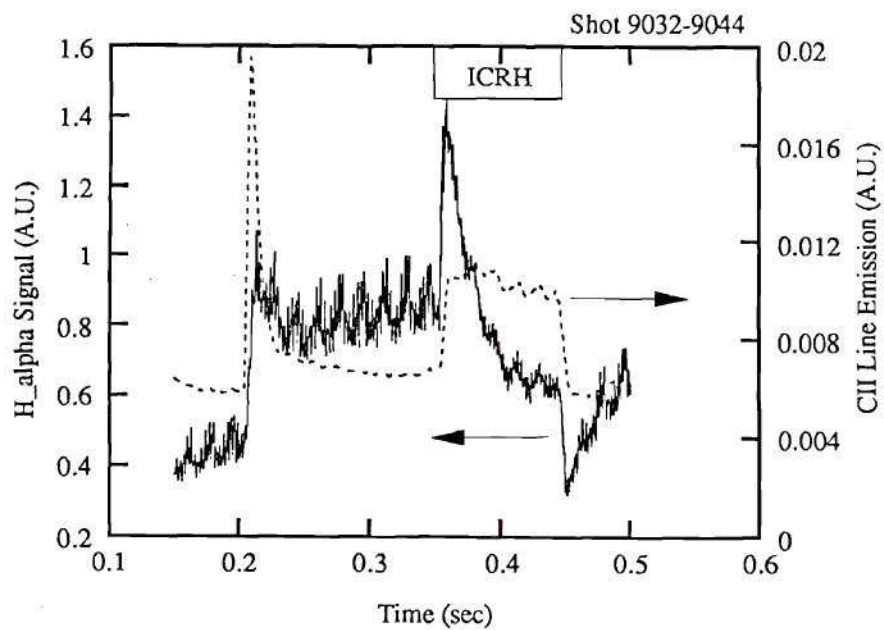


Figure 4.11: The Edge Cooling Shown in Impurity Monitor and H or D $_{\alpha}$ Signals

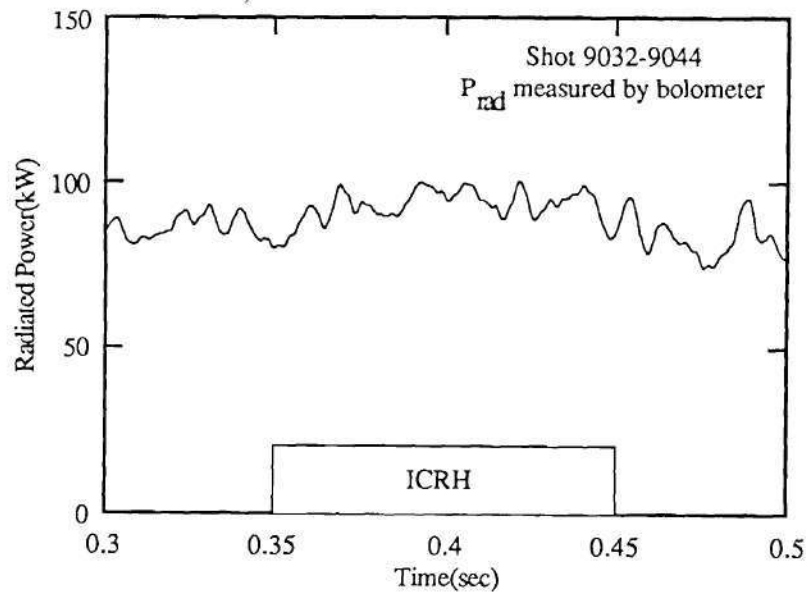


Figure 4.12: Radiated Power During ICRH After 6 Ti Gettering

conditioning, 200 kW of RF power could be launched without causing a collapse. This was in agreement with the radiated power during ICRH measured by the bolometer as shown in Fig. 4.12. Although the radiated power measured by the bolometer did not change during ICRH, this was contradicted by spectroscopic measurements, for which radiation emission from low Z and high Z impurities changed in time with ICRH. No data for the total radiated power inferred from spectroscopy with ICRH was available.

The grazing incidence UV spectrometer was used mostly for measuring single impurity lines in the UV during ICRF heating. Due to the lack of any systematic measurements, some observations were made by looking at the measured data and correlating with other signals or plasma and RF conditions.

A rapid density drop was observed at the very beginning of the ICRF phase in most shots, again indicating direct fast ion loss. Fig. 4.13 shows the shot average of the line integrated density and FeXVI emission signal during ICRH from shot

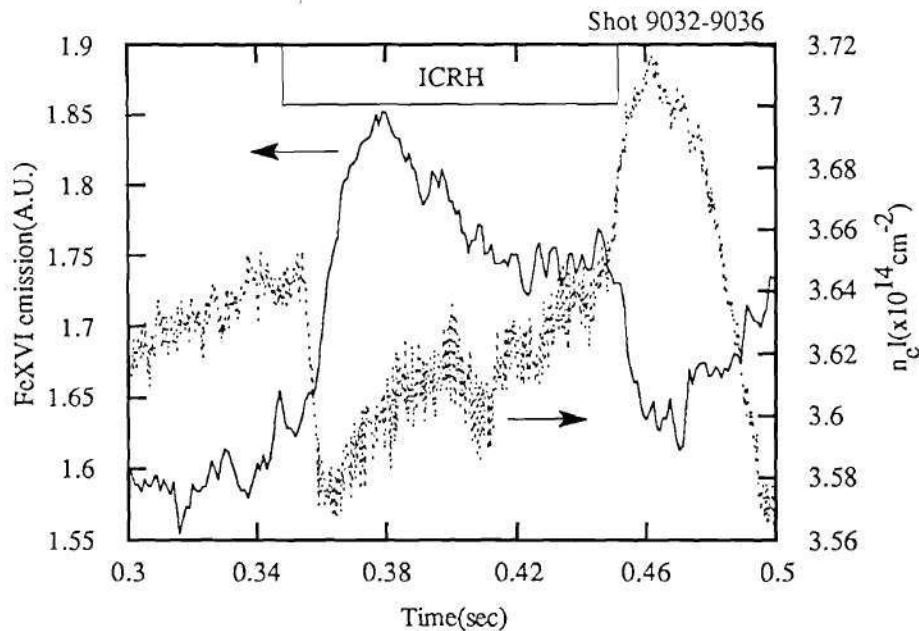


Figure 4.13: Fast Ion Loss and Induced Wall Sputtering

9004 to 9016. A correlation was found between these two signals, showing that the initial density drops were direct fast ion losses which increased the wall sputtering rate resulting in increased FeXVI line emission. The fast ion loss induced by ICRH seems only to have occurred in the early phase of the RF pulse as inferred from the FeXVI line in the sequential shots. To obtain a consistent picture, Fig. 4.14 shows the temporal changes in the fast minority ion distribution measured by a neutral particle analyzer (NPA), the OIII line emission measured by impurity monitor, stored energy measured by a saddle loop, and changes in the plasma loading measured by an antenna current probe. For some reason, RF heating was apparently only effective during the early phase of the pulse for ~ 30 msec on these shots. These data were taken during the second day of a dedicated week of ICRH experiments. The data on the first day, however, showed quite different results as shown in Fig. 4.15, but spectroscopic data was not available on that day. The highest energy fast ion spectrum stayed at a constant level throughout the RF pulse, and loading was higher

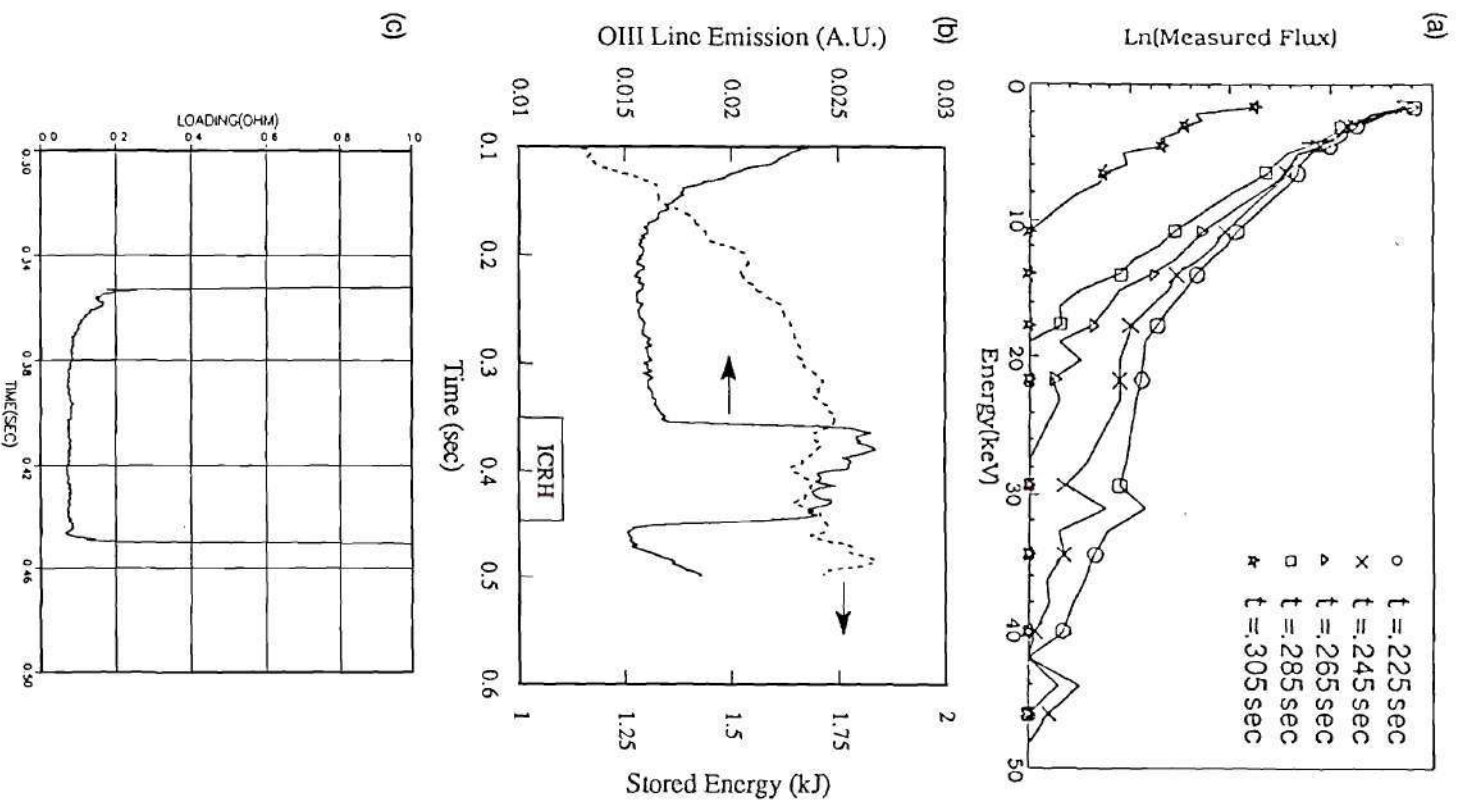


Figure 4.14: (a) Fast Ion Distribution vs. Time, (b) OIII Line Emission and Stored Energy, (c) Plasma loading during ICRH in Shot 9004 through 9018

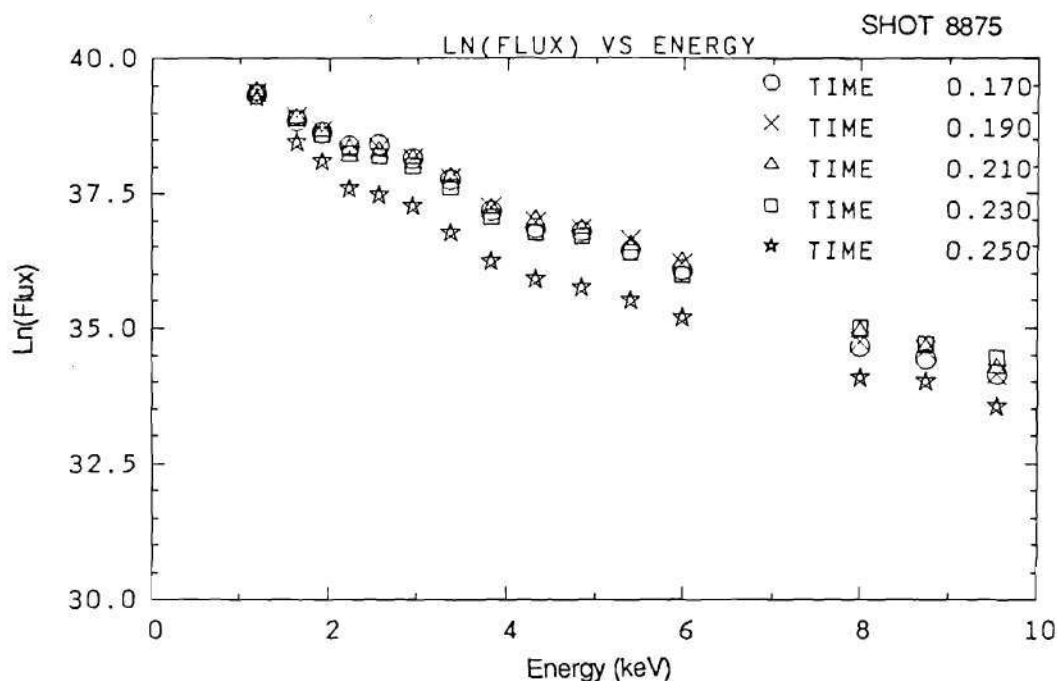


Figure 4.15: Temporal Changes in Fast Ion Distribution on the First Day of Operation in the Week of Dec. 11, 1989

than in the sequence of shots, 9004-9016.

The antenna served as an impurity source when it was pushed in. Since the Faraday shield was made of carbon, carbon radiation would be expected to increase due to enhanced sputtering even if Ti gettering covered the Faraday shield with several layers of titanium. Figure 4.16 shows the comparison between the impurity monitor signal (tuned to CII line) with the antenna in and with the antenna out. The limiter, also made of carbon, was usually located at its maximum-out position during the ICRH experiments in order to avoid RF leakage problems caused by the limiter contacting the plasma.

A vacuum Czerny-Turner spectrometer was used for measuring ion temperatures from Doppler broadened impurity lines. Usually the OVII line was used for central temperature measurements and the CV line for outer measurements. None of the shots showed any significant increase in central temperature with 200 kW of

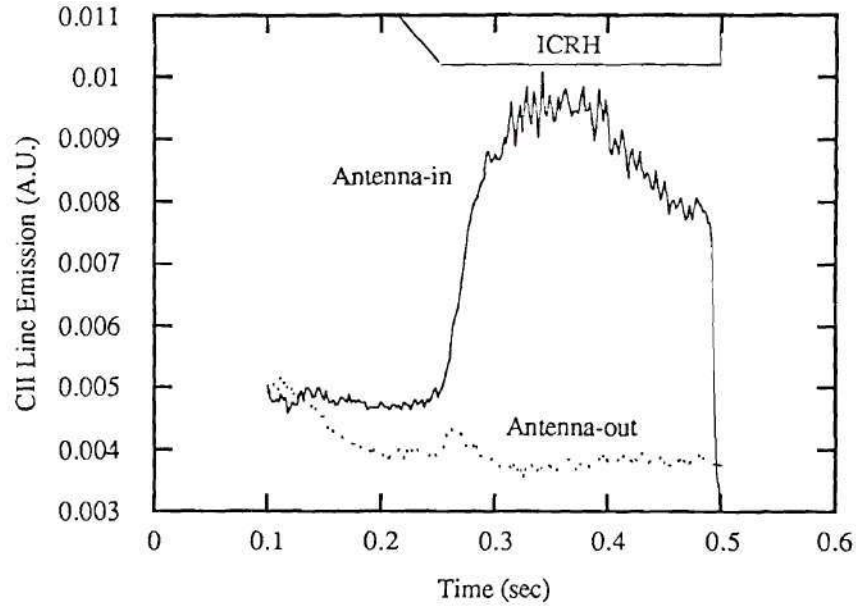


Figure 4.16: CII Line Emission for Antenna In and Out Radial Positions

RF power, while the edge temperature sometimes increased 10 to 30 eV. Figure 4.17 shows a comparison of the measured ion temperatures with RF and without RF for two different radial locations. The ion temperature measured by the spectrometer was quite different from that measured by NPA, which is presented in the next section.

The Doppler broadened ion temperature measurements show that the RF power was absorbed outside rather than at the plasma center. This will be analyzed in more detail in Chapter V.

Finally, Z_{eff} changes were calculated from bremsstrahlung emission measurements. The expression used for emission is [7],

$$Z_{eff} = \frac{CS(W_p(0.5 + \frac{0.7}{n_{el}} - \frac{0.2}{n_{el}^2}))^{0.35}}{n_{el}^{2.35}}, \quad (4.2)$$

where C is the calibration constant, S (mV) is the detected signal amplitude, W_p (kJ) is the stored energy, and $n_{el}(10^{14} \text{ cm}^{-2})$ is the line-integrated density. Figure 4.18 shows the result for the ICRH shots (11376-11389). The ICRH increased the Z_{eff}

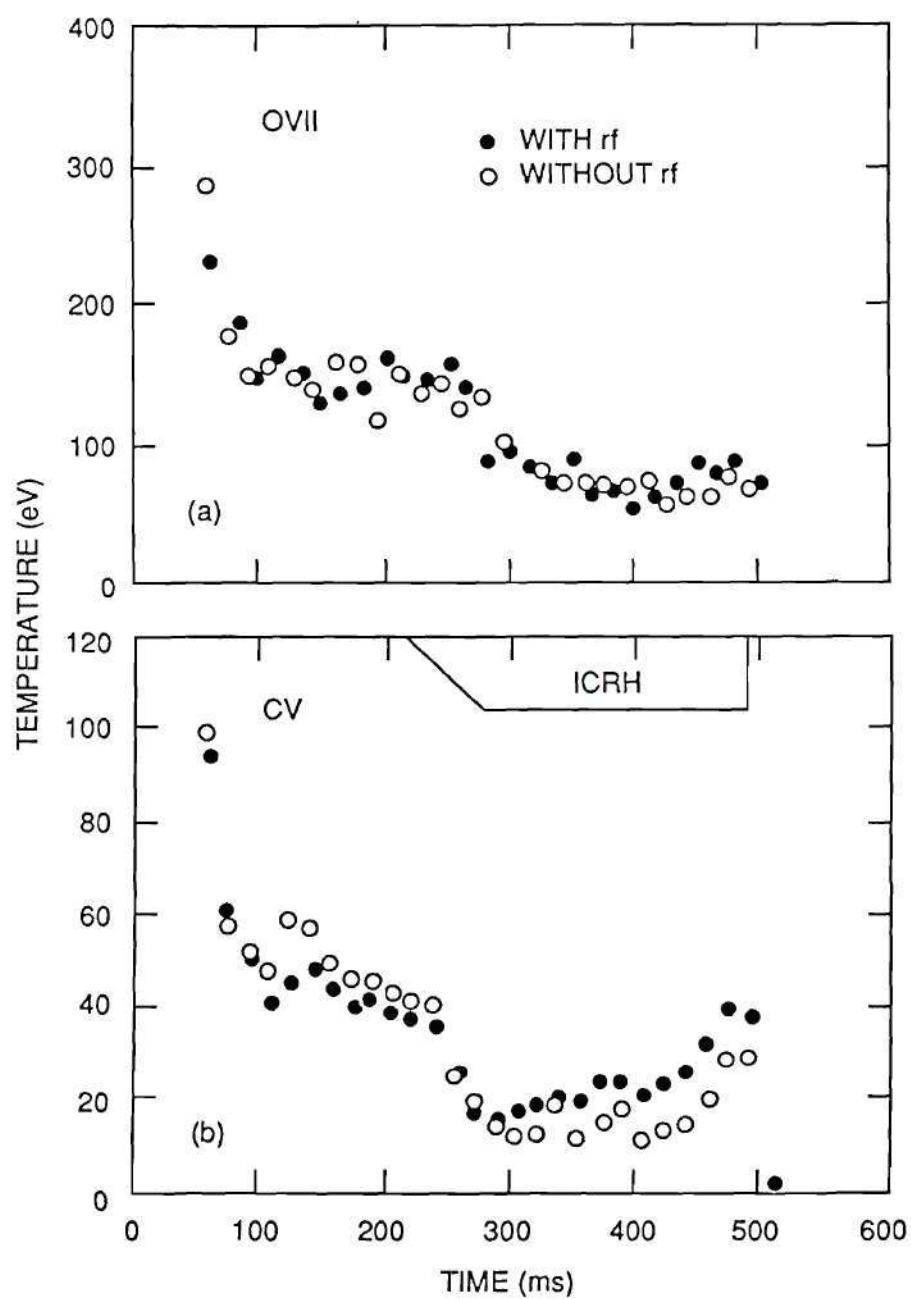


Figure 4.17: Ion Temperature Measured by Spectroscopy for Two Different Radial Locations During ICRH. The ICRH was on from 230 ms to 480 ms.

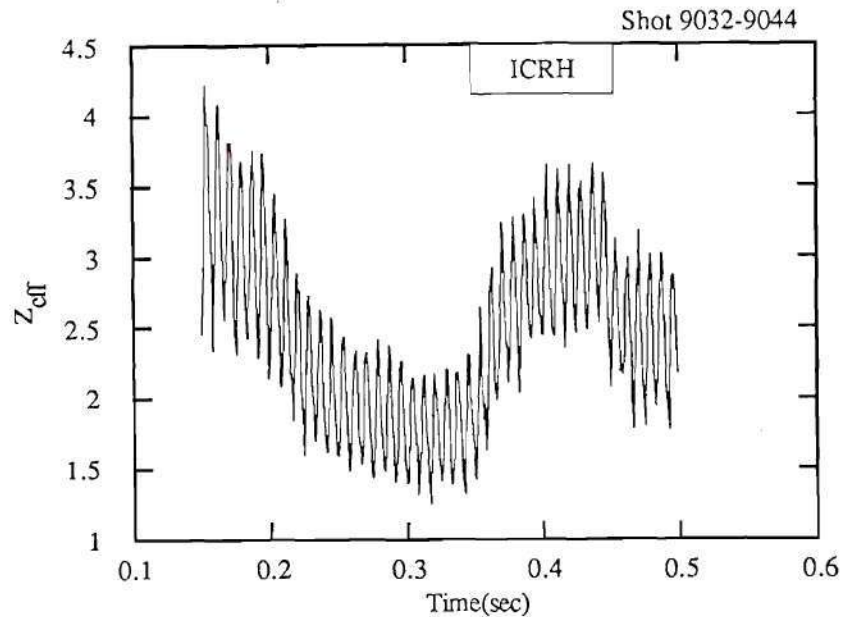


Figure 4.18: Z_{eff} Inferred from Bremsstrahlung Radiation Measurements

value by 50%. The increase in Z_{eff} is attributed to high-Z impurities sputtered by fast ions created by ICRH and to low-Z impurity influx caused by direct edge heating or other RF-induced plasma-wall interactions as seen in other ICRH experiments surveyed in the last section in Chapter II.

The Neutral Particle Analyzer Measurements

The horizontally and vertically scannable neutral particle analyzer (NPA) was installed on ATF² in the summer of 1989. Initial attempts to use the NPA during ICRF heating experiments on ATF failed due to an electromagnetic interference

²The author is grateful to M. R. Wade and R. J. Colchin for providing NPA data and valuable comments

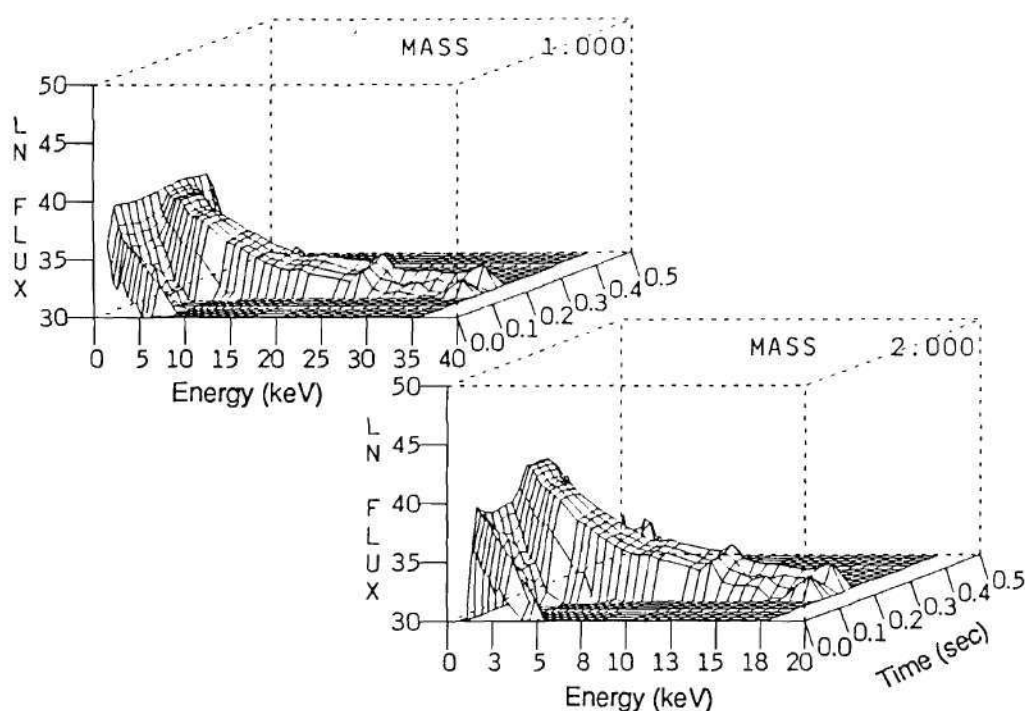


Figure 4.19: A 3-D Plot Showing the Fast Ion Tail in Both Hydrogen and Deuterium Channels

(EMI) between the RF system and the NPA. Several locations were found where RF signals leaked from the torus. After sealing the suspected areas, the NPA began to provide useful data. Unfortunately, there were no data for the second harmonic heating regime because of the EMI. Thus all the NPA data presented here were measured in the hydrogen or helium-3 minority heating regime. The main experimental result is that ICRF produces an energetic minority ion tail.

Figure 4.19 shows a typical minority ion tail distribution. This tail formation was clearly dependent on the RF power, plasma conditions, and the location of the resonance layer. Also, the tail was not constant with time during the RF pulse. Figure 4.20 shows the power dependence of the energetic hydrogen minority ion tail formation. In changing from 40 kW to 70 kW of RF power, the tail energy changed significantly.

The temporal behavior of the energetic tail is shown in a previous subsection

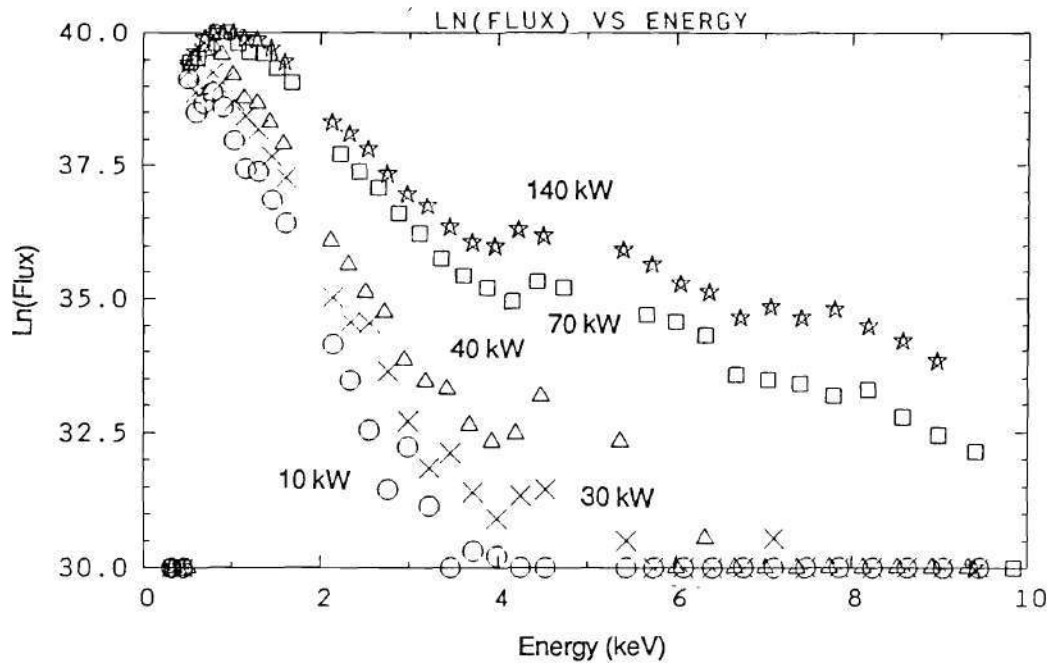


Figure 4.20: Fast Minority Ion Tail Formation as a Function of RF Power at a Fixed Time into the Discharge

in Fig. 4.14. During most of the minority ICRH experiments, the NPA data showed a big tail around 30 to 50 msec after RF wave injection began, then the tail energy was significantly degraded. This means that the RF efficiency or RF absorption was decreased, probably due to RF-induced plasma changes. Plasma degradation was seen in the stored energy trace and T_{ece} trace³. Low frequency edge magnetic fluctuations around 50 kHz were also observed at the time of energy degradation. As mentioned in the preceding section, there were differences in the NPA signal between shot 8875 during which the ion tail energy maintained a constant level throughout the RF pulse, and the shot 9004 series during which the ion tail energy degraded 50 msec after RF wave injection began.

The minority species concentration η_H also affected the tail formation. At a

³The stored energy data were provided by W. Wing and T_{ece} data were provided by G. L. Bell.

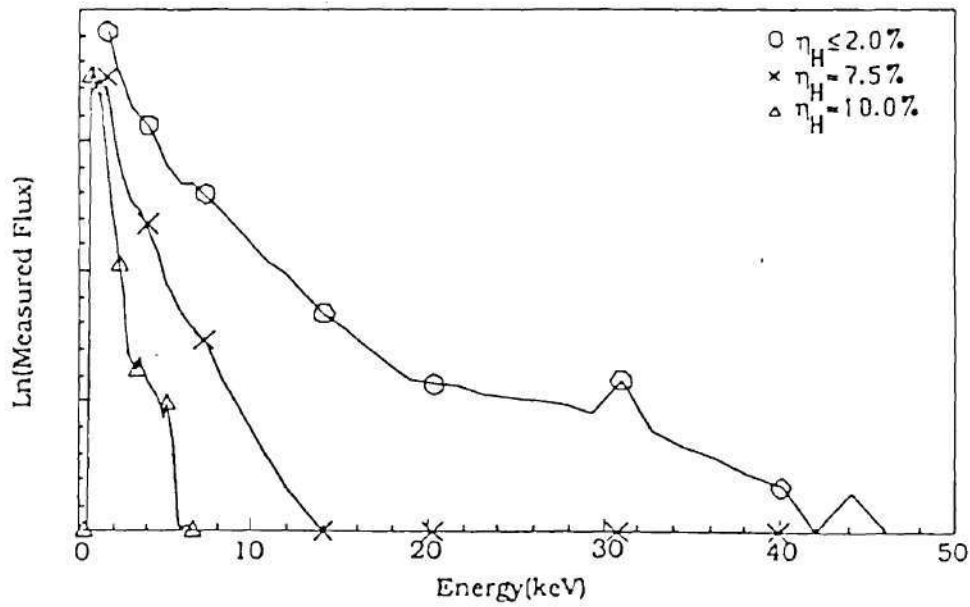


Figure 4.21: Minority Ion Tail Energy as a Function of Minority Species Concentration

fixed power level, a lower concentration produced a higher tail energy. Figure 4.21 demonstrates the η_H dependence of the tail formation.

Here, an important issue arises related to the minority concentration and its effect on location of the hybrid resonance layer. With a 14.4 MHz RF wave launched into a magnetic field of 0.95 Tesla on the plasma axis, a minority concentration of less than 2% would keep the hybrid resonance from being located beyond the saddle point. However with greater than 4% concentration, the hybrid resonance moved beyond the saddle point as illustrated in Fig. 4.22. These results were consistent with the results of the Magnetic field scan in Heliotron-E[8], where the most energetic ion tail was formed when the hybrid resonance layer was located at the plasma axis. The frequency scan data, to be presented later, also showed consistent results. This also agrees with 2-D code simulations. More detailed analysis will be given in the next chapter.

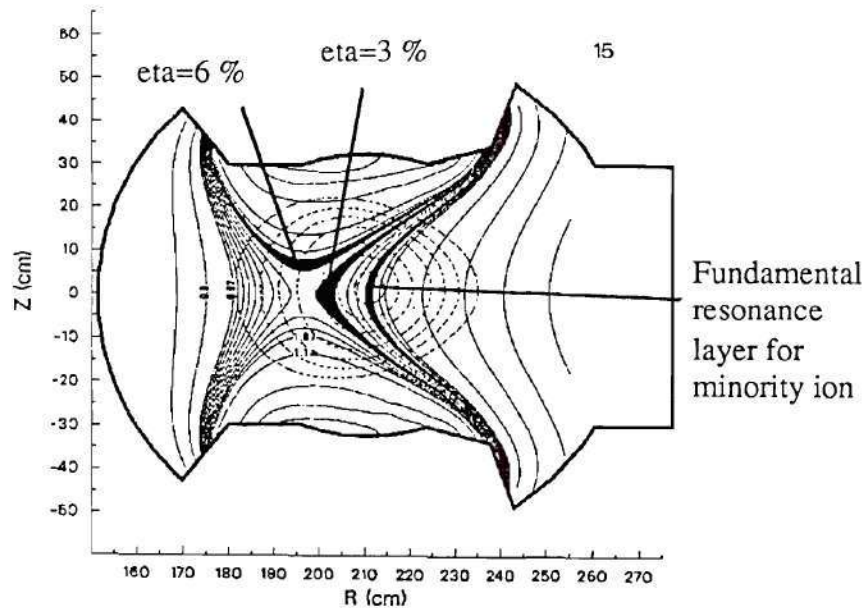


Figure 4.22: Location of the Hybrid Resonance Layers as a Function of Minority Ion Concentration

It should be noted that in ATF for ECH discharges, direct orbit loss was the only mechanism which had a faster time scale than charge exchange loss. Thus if a tail was truncated above a certain energy in the NPA spectrum, there were two possibilities. Either there was no high energy tail above that energy level or the fast ions were lost before they charge exchanged. Understanding which situation occurred is important because if the former is correct, then poor absorption of RF energy might be the cause while if the latter explanation is correct, then energetic particle loss might be an intrinsic problem for ICRH heating of low collisionality discharges (e.g., low density ECH) in ATF. There was some indirect evidence of direct high-energy particle loss. If there were no transport (CX) or slowing down (i.e., low collisionality), then direct particle loss might be related to "stripe" formation on the vacuum vessel wall. At one point when the vacuum vessel was opened to air, a picture of the antenna Faraday shield surface showed clear stripe traces in contrast

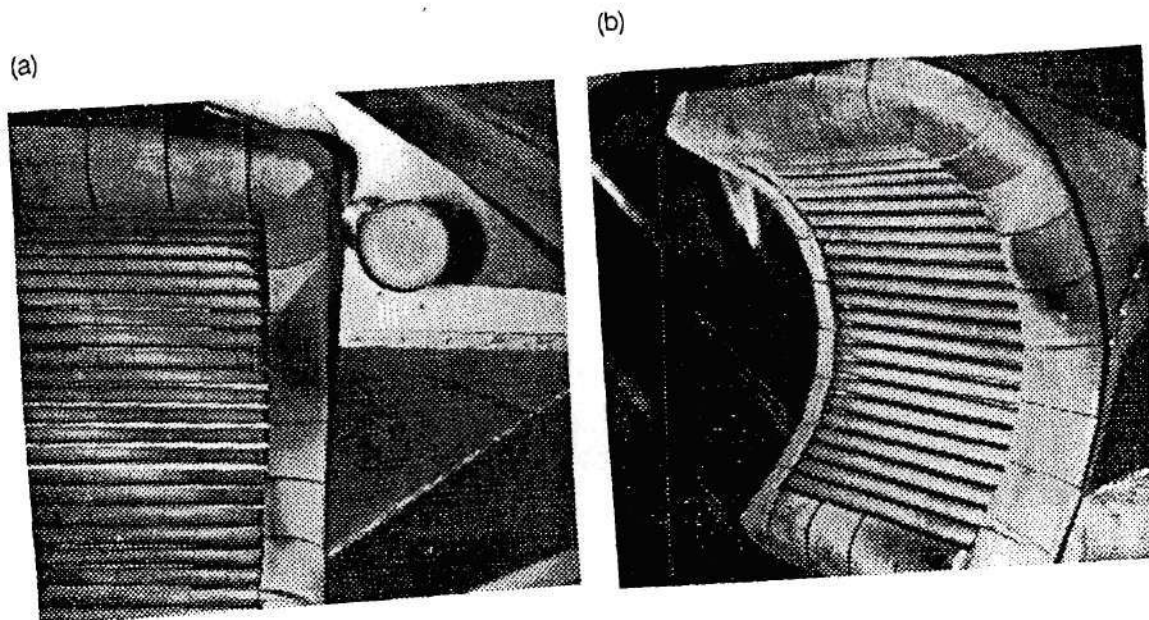


Figure 4.23: (a) Picture Showing Stripes due to Ion Orbit Loss (?), (b) Picture Does Not show any Trace of Stripes Formed

with the bright Ti-gettered vacuum vessel surface, as shown in Fig. 4.23. But it is not clear whether these stripes were caused by ICRH. A second picture taken the day after subsequent ICRH experiments showed no evidence of stripes. Figure 4.6 in the previous section shows, however, the immediate decrease in line averaged density after RF onset, although the gas puff signal cannot explain such a strong decrease. As previously discussed, the wall sputtering rate also increased during the density drop.

Other interesting NPA data were taken showing energetic tail formation during frequency and position scans. As the ICRH frequency was decreased, moving the resonance layer outward from the magnetic axis, the tail energy increased (Fig. 4.24). In addition, shifting the plasma center outward increased the antenna loading (even though the average density decreased) and generated a big tail (even though η_H probably increased), which is shown in Fig. 4.25.

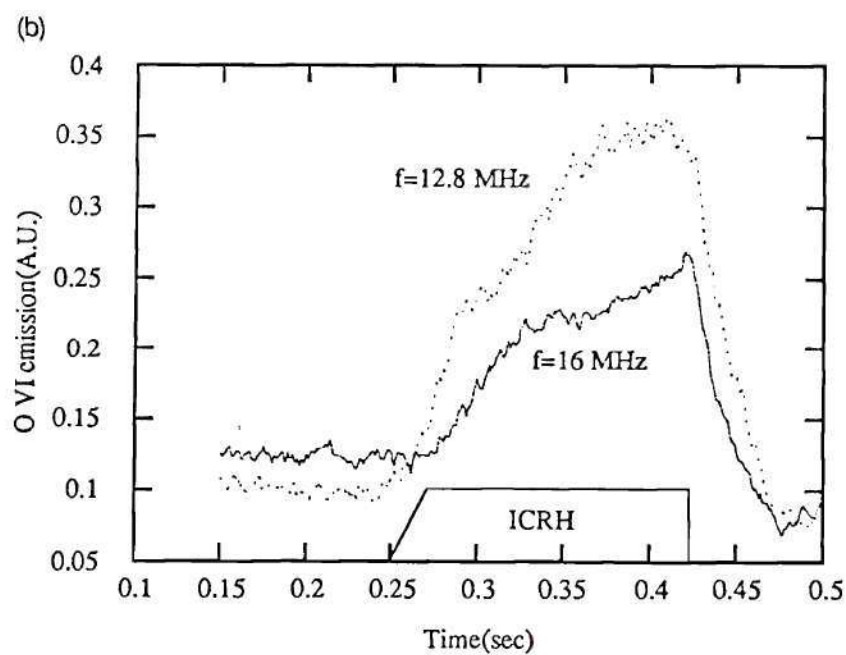
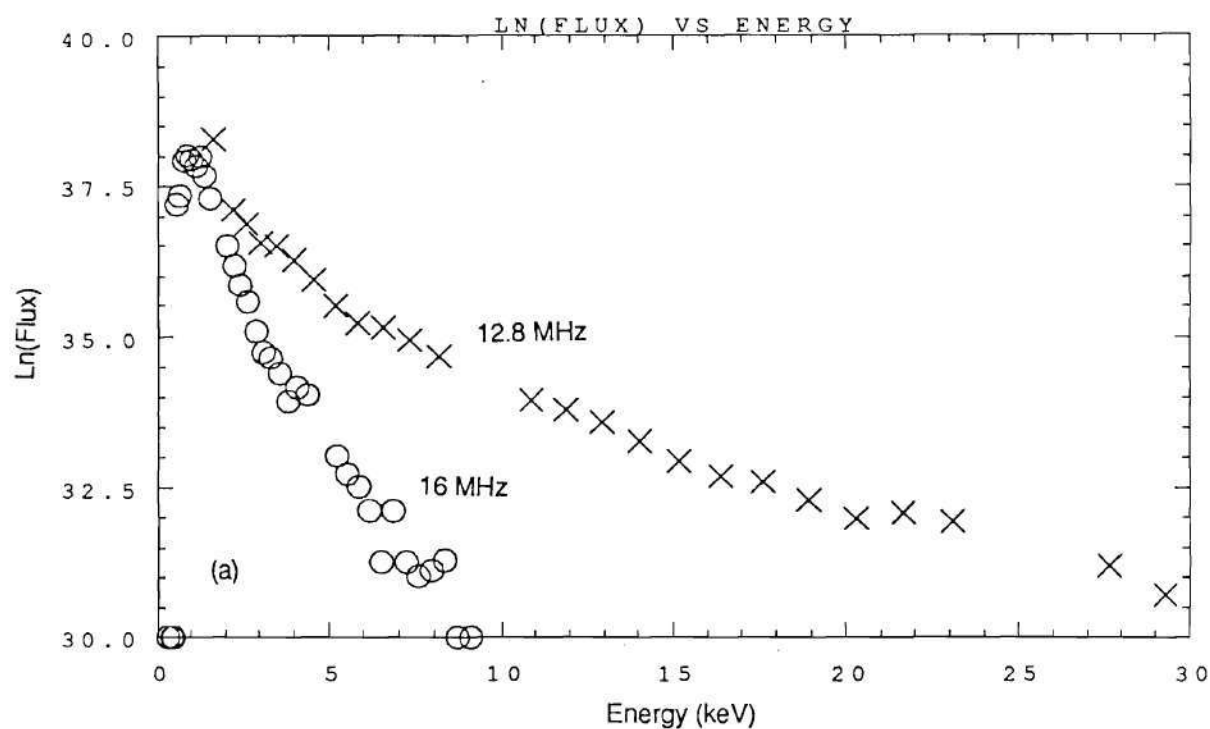


Figure 4.24: (a) Fast Minority Ion Nonthermal Tail for Two Different Frequencies
(b) The OVI Impurity Line for These Two Frequencies

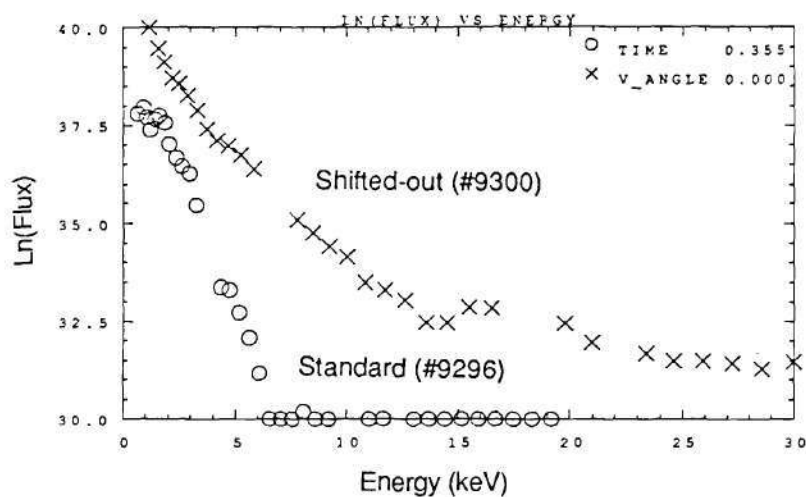


Figure 4.25: Fast Ion Tail in the NPA Spectrum for Standard Plasma and Shifted-out Plasma Configurations

The NPA also made horizontal and vertical scans with the RF applied (the NPA moved between reproducible shots). Interesting data during the RF pulse were obtained from these scans as shown in Fig. 4.26. The peak in the distribution occurred at an angle of the NPA away from the perpendicular to the magnetic field direction. At first thought, it would seem to be a banana orbit particle effect as in tokamaks[9, 10]. In an attempt to confirm this hypothesis, two more scans with different RF frequencies, equivalent to different resonance layer positions, were performed. These results [Fig. 4.26(b) and (c)] look different from the distribution with the resonance on axis shown in Fig. 4.26(a). It is certain that RF energy affects particle orbits in a consistent way, and to understand the data more theoretical analysis must be done on how RF energy affects various particle orbits in ATF.

In ATF, three methods were used to measure the ion temperature, namely impurity line Doppler broadening measurements as shown in the previous section,

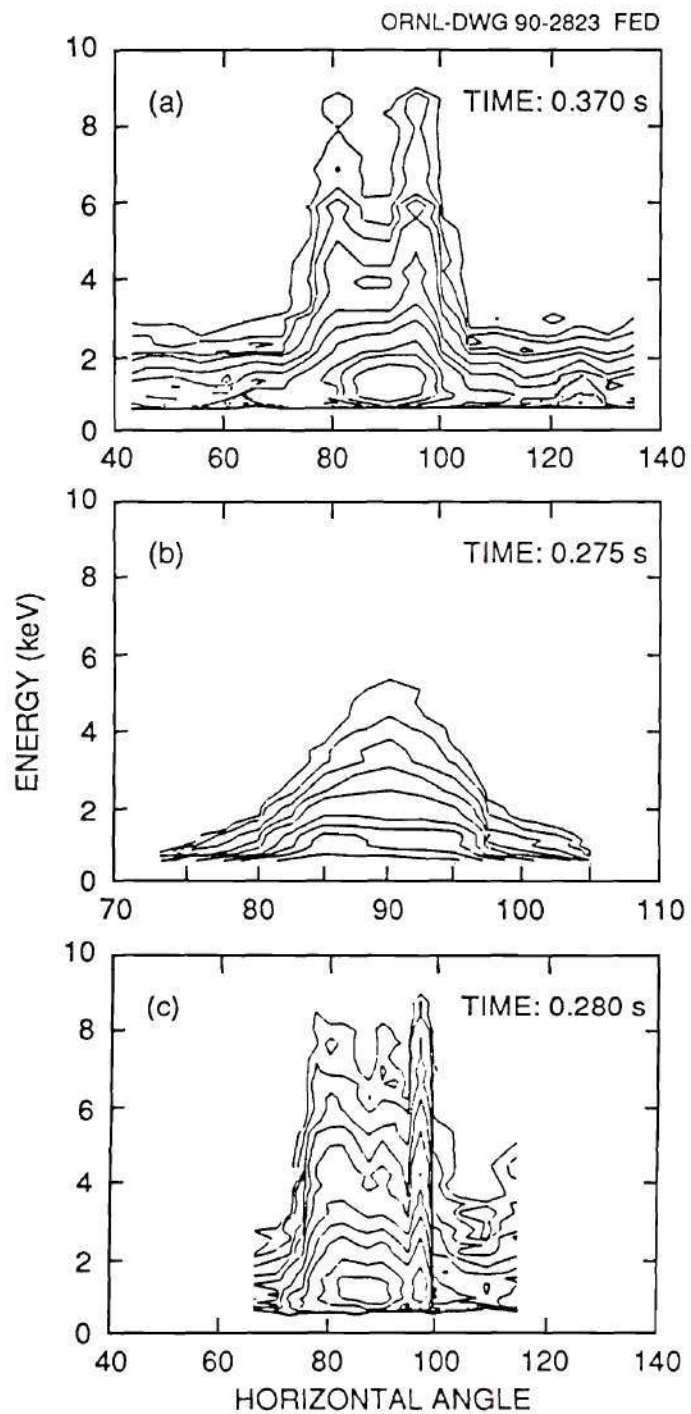


Figure 4.26: Minority Ion Distribution Measured by Scanned NPA at (a) 14.4 MHz, (b) 12.8 MHz and (c) 16 MHz

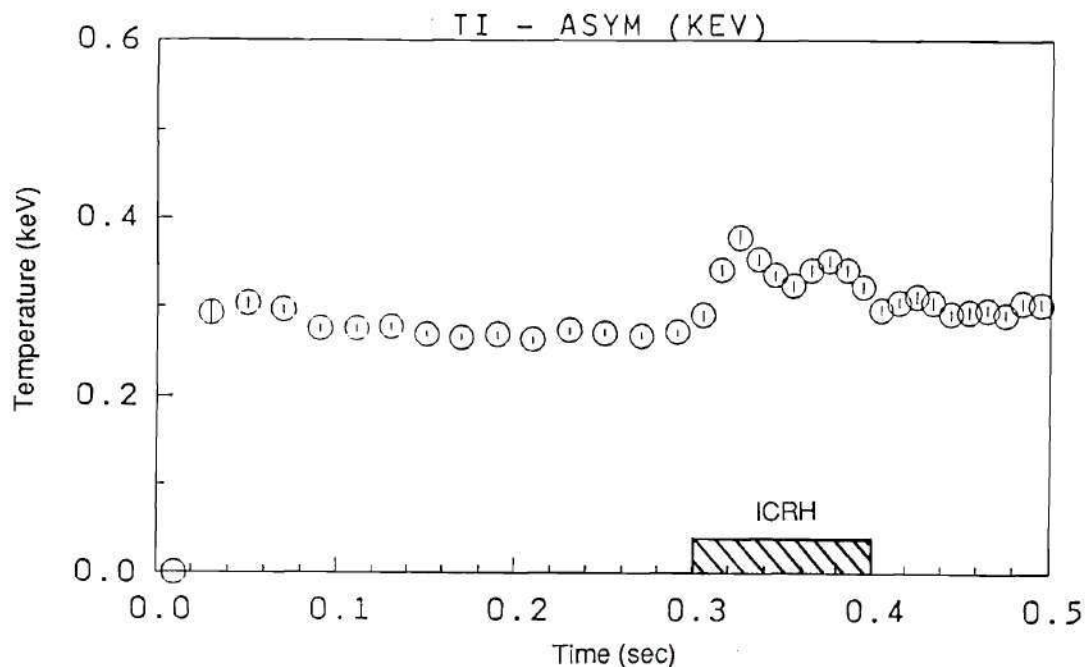


Figure 4.27: Deuterium temperature measured by NPA with ICRH in the D(H) regime a neutral particle analyzer, and neutron detectors⁴ for D-D reactions. In the preceding section, it was shown that in all of the low density ICRH experiments, the Doppler broadening measurements showed no measureable increase in the central ion temperature. However, in some cases the edge ion temperatures measured from the CV line were increased by 10 to 30 eV. The NPA measurements were strikingly different from the spectroscopic measurements. The inferred ion temperature increased substantially by several tens to as much as a couple of hundred eV (Fig. 4.27). This difference is attributed to the poor mass rejection of the NPA deuterium channel so that the big hydrogen tail could be seen in the deuterium channels.

Another concern about the ion temperature measurement made by the NPA in ATF was the location of the gas puff valves. One valve was located at a port on the wall opposite to the NPA port, in order to increase the flux to the NPA. This

⁴The author is grateful to A. C. England for providing neutron data.

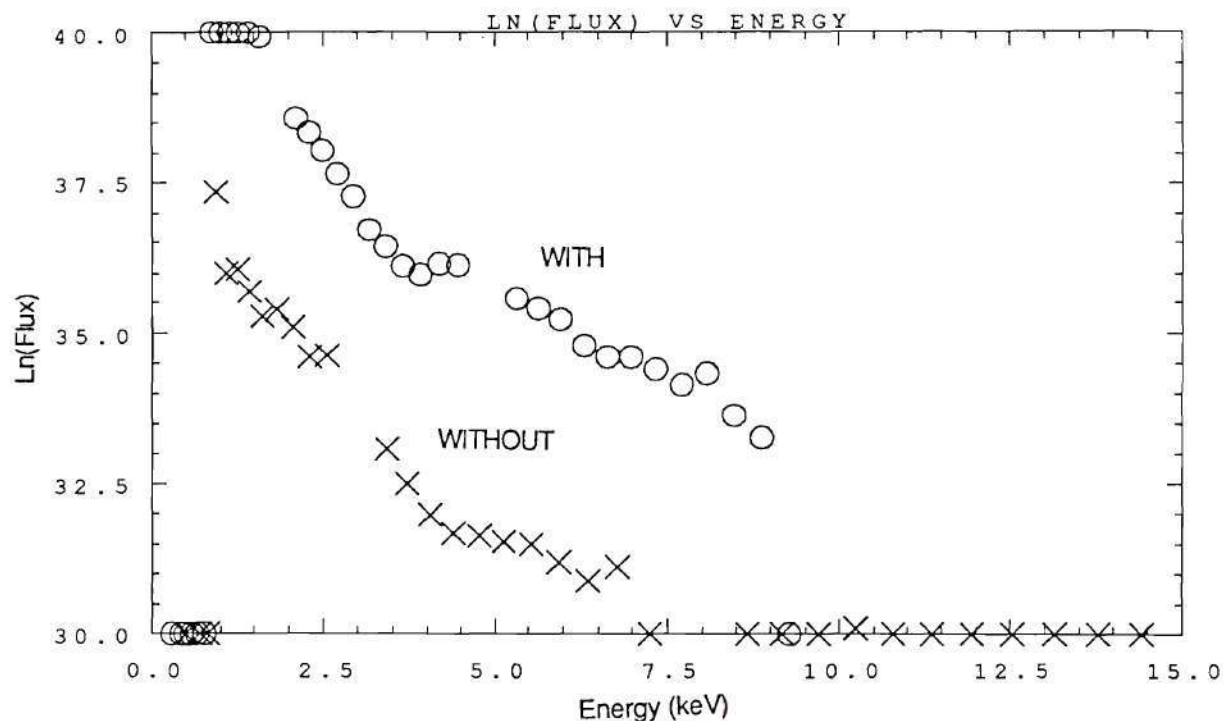


Figure 4.28: Energetic Tail Formation for Two Different Cases: With and Without Using the Inside Gas-puff Valve

nonlinearly increased the neutral density as a function of plasma radius (with the largest density increase at the edge) resulting in a higher charge exchange probability. It was found that the high energy tail formation was clearly related to the location of the gas-puff valve as shown in Fig. 4.28.

The neutron measurements were not useful for low ion temperatures. A simple calculation shows that the minimum ion temperature which could have been measured by the ATF neutron detectors was about 600 eV. Since no neutrons were detected above the noise level, it can be inferred that the ATF ion temperature was less than 600 eV, in agreement with the spectroscopic measurements.

Edge Probe Measurements

Three probes installed around the fast wave antenna were used to monitor changes in edge RF fields and to measure edge plasma parameters during the RF pulse. Due to the possible toroidal asymmetry and direct interaction of the plasma with the antenna, probe results near the antenna might not be consistent with data obtained in other toroidal sectors in ATF. However, edge plasmas usually responded very quickly to the RF wave no matter where measurements were made around the torus. The floating potential changed within a few msec after the RF wave injection began. The two impurity monitor signals and the line integrated density also responded very quickly, as mentioned before. This was probably due to the fact that in the low density (ECH) plasmas, toroidal damping was so weak that RF wave filled the torus uniformly in the toroidal direction.

Langmuir Probe Measurements

The ICRF Langmuir probe had double tips, one measuring the floating potential and the other measuring n_e and T_e by sweeping a bias voltage. The floating potential responded very quickly to the RF as mentioned before, however, the sweep frequency was limited to less than 10 Hz due to stray capacitance, therefore it was not possible to measure the time response of n_e and T_e to the RF. However, the current signal during a sweep clearly changed at the RF onset time. Figure 4.29 shows the response of the Langmuir probe signal to the ICRH. The most distinctive effects of RF injection on the Langmuir probe I-V characteristics were noisy fluctuations of the current signals, changes in the floating potential, higher signal amplitude and a different slope in the transition region. The electron saturation point was difficult to determine and even in the ion saturation region, the ion saturation current was always changing, indicating fluctuations in density and temperature. The ion satura-

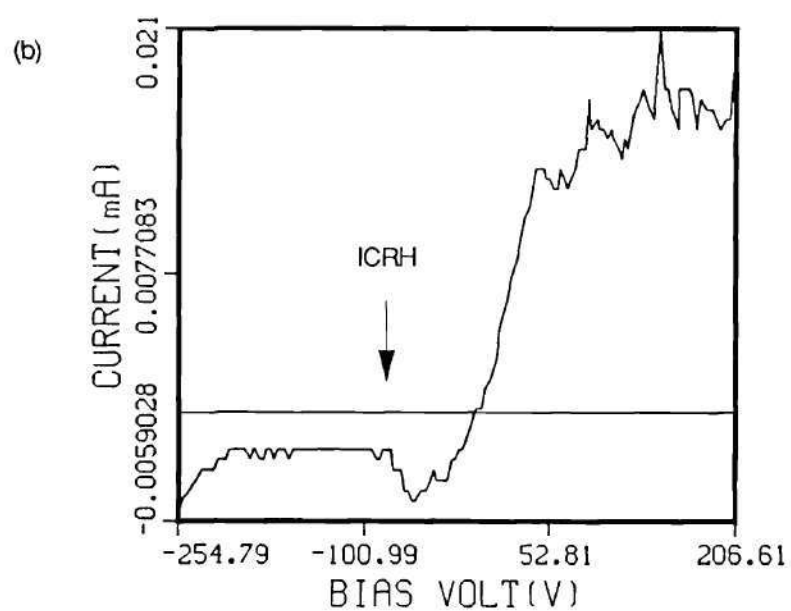
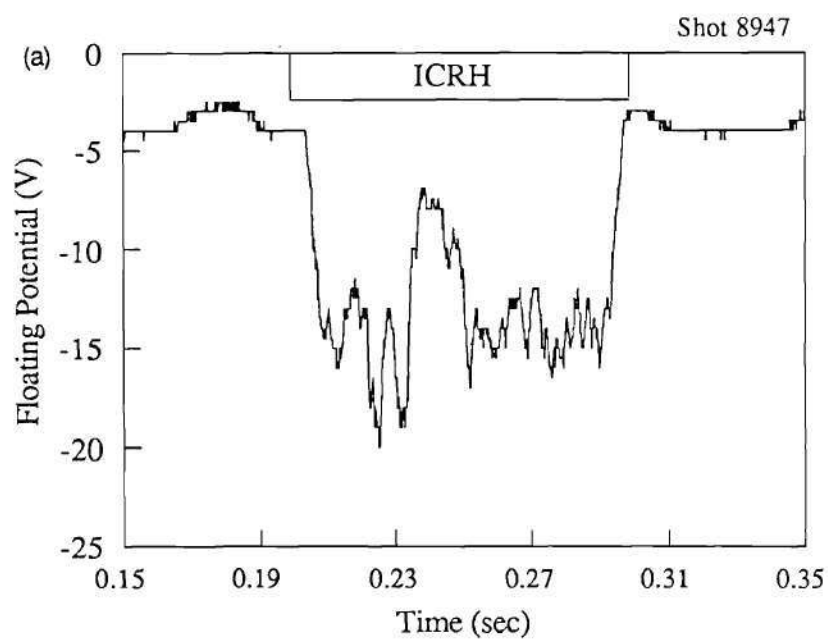


Figure 4.29: (a) Floating Potential, (b) Probe Current Signal During a Bias Voltage Sweep

tion current without RF injection was otherwise constant due to the strong magnetic field. Arc tracks over the 0.6 mm distance between the biased probe tip and the graphite head armour of the probe, which was always grounded, were occasionally observed, especially during high density discharges with high bias voltage.

Figure 4.30 shows the n_e and T_e edge measurements observed during D(H) minority regime ICRH. This direct edge measurement showed that ICRH increased the edge temperature and density, which could be interpreted as evidence of direct edge coupling of the RF wave.

During these low-density ECH plasma ICRH experiments in ATF, propagation was poor due to the low spectral density of low $k_{||}$ modes launched. According to the loading measurements, more than half of the injected power went to the antenna structure or vacuum vessel. In addition, fast ions generated by the RF which was absorbed, and direct edge heating by edge propagating modes, enhanced wall sputtering and reionization which changed the edge conditions very rapidly. Because of the small number of accessible modes, loading was very sensitive to changes in edge conditions. As shown in preceding sections, loading dropped quickly in the first few tens of msec of RF injection, during which edge conditions changed rapidly as indicated by the diagnostic signals discussed above.

The edge density also reflected the line average density changes observed during ICRH in the rising density shots. The edge density sharply increased in the first 10 to 20 ms of RF injection, then slightly decreased even if n_{el} was still increasing. The H_{α} and impurity monitor signals were consistent with the sharp increase in the plasma edge density seen at the same time. During these shots, the H_{α} and impurity monitor signal decreased in time after an initial peak. The plasma edge density remained at a higher level than during the pre-RF period.

During the constant-density shots, the density started increasing inside the radius corresponding to the current-strap position. Figure 4.31 shows the radial

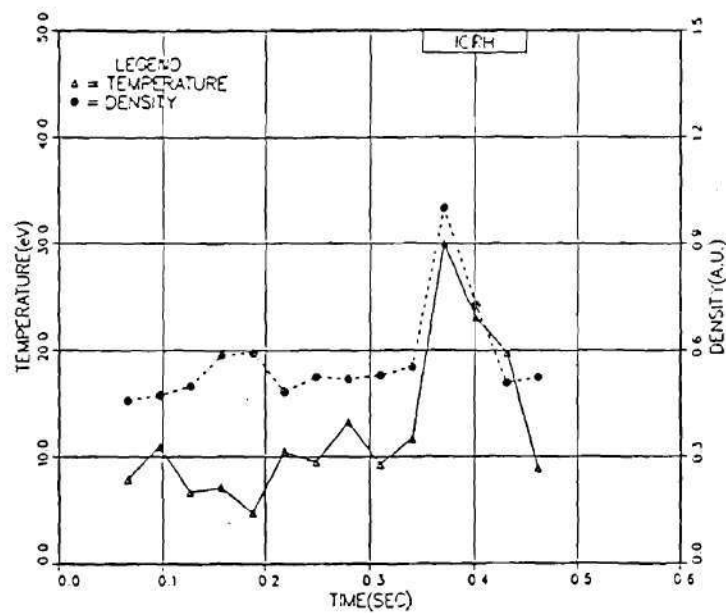


Figure 4.30: Edge Electron Density and Temperature Measured by Langmuir Probe for Hydrogen Minority Heating Regime

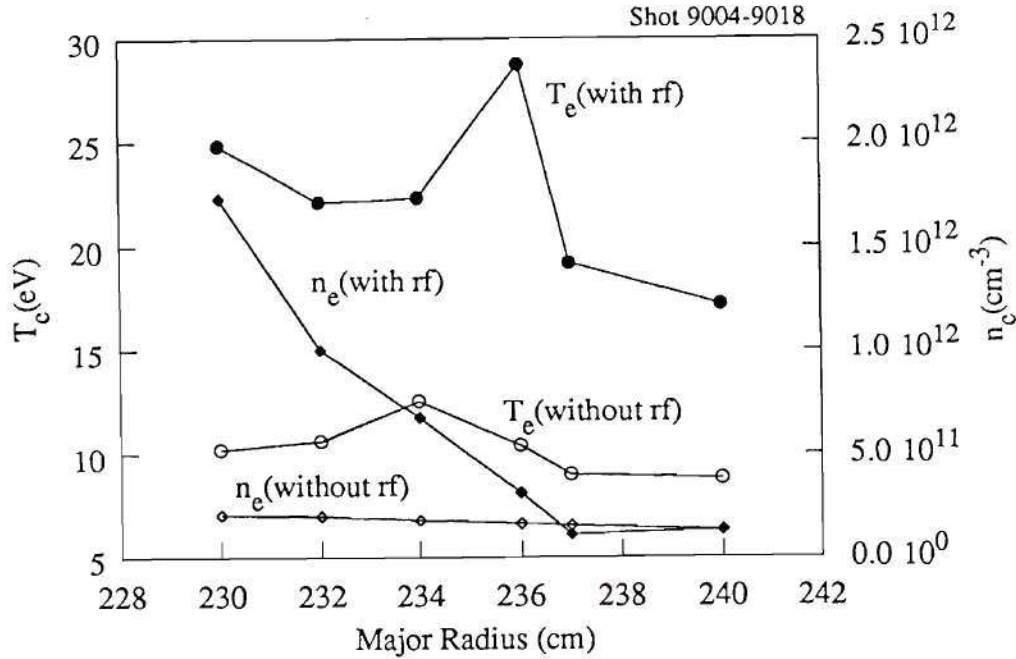


Figure 4.31: Radial Profile of the Edge Electron Temperature and Density

profile of n_e and T_e in the constant density shots at 50 msec after RF was injected. As the probe passed $R \simeq 232$ cm, particle flux from the face of the Faraday shield started reaching the probe tips. Density increased 4 to 10 times the values observed further out, and the temperature also increased. From this observation, it is obvious that the antenna itself divided the scrape-off-layer (SOL) and the two regions were quite different during the RF phase. No data are available without RF for this configuration.

RF Probe Measurements

The ICRF magnetic probes measured two orthogonal components of the magnetic field[11]. Since the magnetic field lines in ATF were very complicated and the shear in the field was largest at the edge region, alignment of the loops to the local magnetic field line was somewhat difficult (i.e., arbitrary). As the probe moved in and out radially, the angle between the perpendicular direction of the loop and the

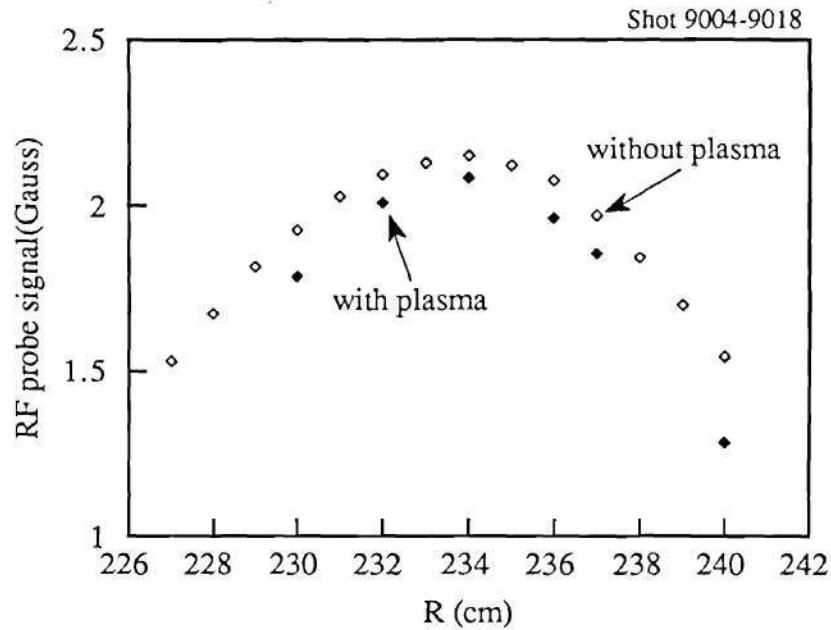


Figure 4.32: Radial Profile of the Near Field From ICRH with Plasma Compared to the Equivalent Profile ICRH into Vacuum

field line changed. Therefore the data were only meaningful when compared with a reference signal, such as the probe signals during vacuum only RF injection. Comparison of the probe signal from RF injection into plasma with RF injection into vacuum allowed determination of the wave propagation direction.

A typical vacuum signal from the big probe was peaked at the current strap position and then decreased. The other two probe signals showed the effect of the angle to the local magnetic field line on their signal amplitudes and radial profiles. Taking the sequence of shots from 9004-9018, which were in the D(H) regime, constant-density shots with no eigenmodes, a comparison with calibrated vacuum data is shown in Fig. 4.32. The angle between the local vacuum magnetic field line and the perpendicular direction of the probe loop surface varied about 17 degrees during the

full radial translation of the probe⁵. The radial positions of the probe, except the last one ($R=230$ cm) were located behind the Faraday shield.

In low density plasmas, the wave mode was likely to be an eigenmode. Even in the constant-density shots, the dominant mode was a single mode as will be shown in the next chapter. In the rising density shots, a few discrete eigenmodes were observed during the density rise. Figure 4.33 shows a typical RF probe signal with discrete eigenmodes. The amplitude of each mode was either higher or comparable to the equivalent vacuum value. This means that the observed eigenmodes were not penetrating modes but rather edge circulating modes. This characteristic can be seen by correlation with other edge diagnostic signals[11].

The RF probes were also used to measure high frequency magnetic fluctuations during D(H) RF heating experiments. A 100 MHz sampling rate Transiac digitizer was used for sampling data and an IDL (IDL is a proprietary data analysis software package) fast Fourier transform (FFT) routine⁶ was used to obtain the frequency spectrum. In a sequence of reproducible shots, a narrow band of low frequency fluctuations was found about 30 to 40 msec after RF injection. This time was also the effective RF coupling time after which loading decreased, T_{ece} and the stored energy were slightly reduced, and the NPA showed a less energetic tail formation. It is not clear whether the low frequency modes were correlated with these phenomena. These low frequency modes appeared regularly throughout a sequence of shots and a radial profile of its amplitude showed a kind of standing wave form as shown in Fig. 4.34. Note that the sensitivity of the probe to the low frequency signal is much lower than to the high frequency signal. In this figure the signals were not calibrated

⁵The author is grateful to D. K. Lee for providing a computer code to calculate this angle.

⁶The author is grateful to S. Hiroe and D. C. Giles for providing the hardware and software for fast digitizer measurements and to W. Wing for providing the FFT routine.

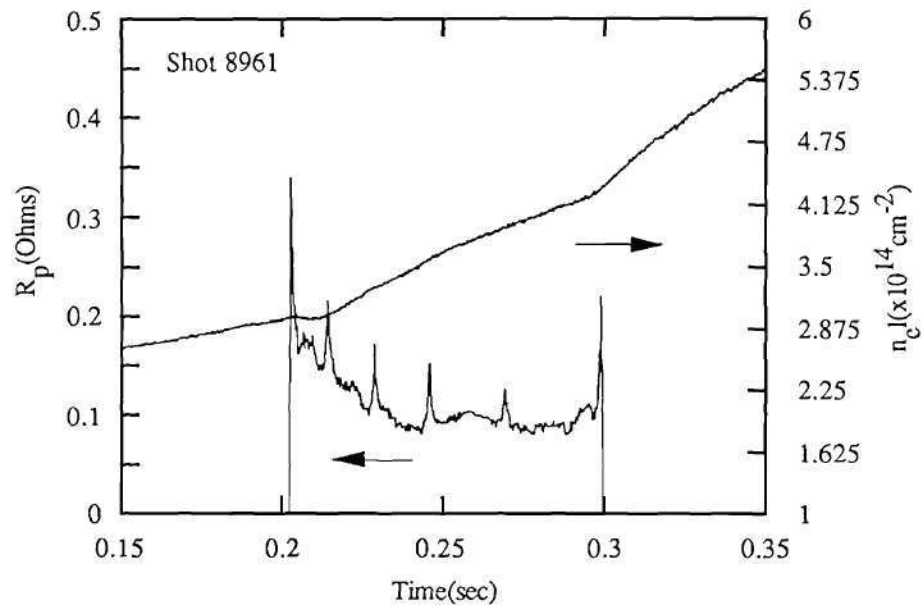


Figure 4.33: Discrete Eigenmodes Observed from an RF Probe Signal (Solid) During the Rising Density Shot (shot number 8958) Compared with Line Integrated Density (Dashed)

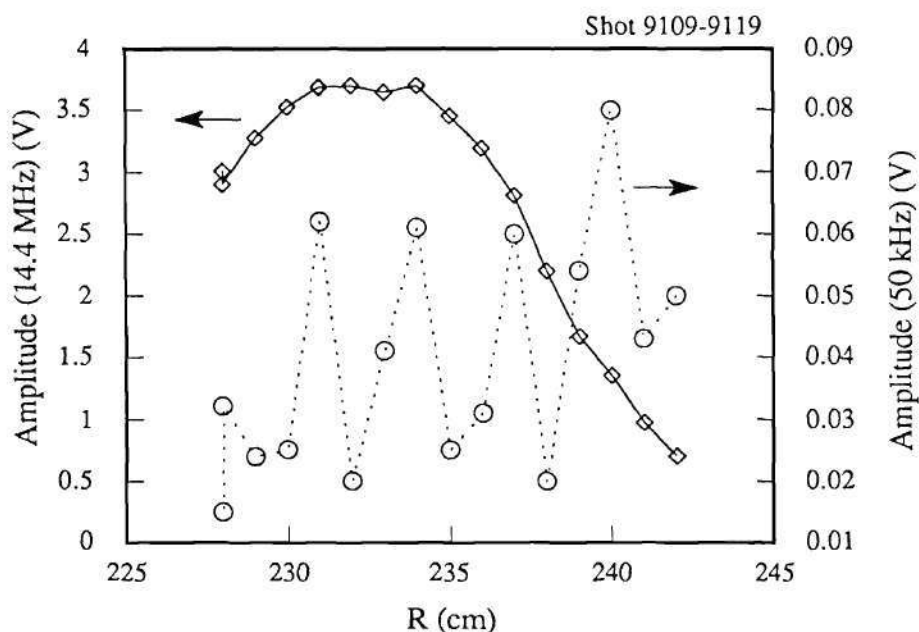


Figure 4.34: Radial Profile of the Amplitudes of Low (50 kHz) and High (14.4 MHz) Frequency Signal Measured from RF Probe

because sensitivity measurement was too erroneous in the low frequency region. Since the measured signal is proportional to the fluctuating magnetic field times angular frequency, the high frequency (14.4 MHz) signal is 288 times larger than the low frequency (50 kHz) signal for the same magnetic field fluctuation. In most of the shots, higher harmonics of the fundamental RF frequency also appeared on the RF probes, showing some non-linear coupling possibly due to RF sheath effects. No parametric decay instability of the RF was observed during these shots. The frequency spectrum measured by one of the RF probes is plotted in Figs 4.35 and 4.36.

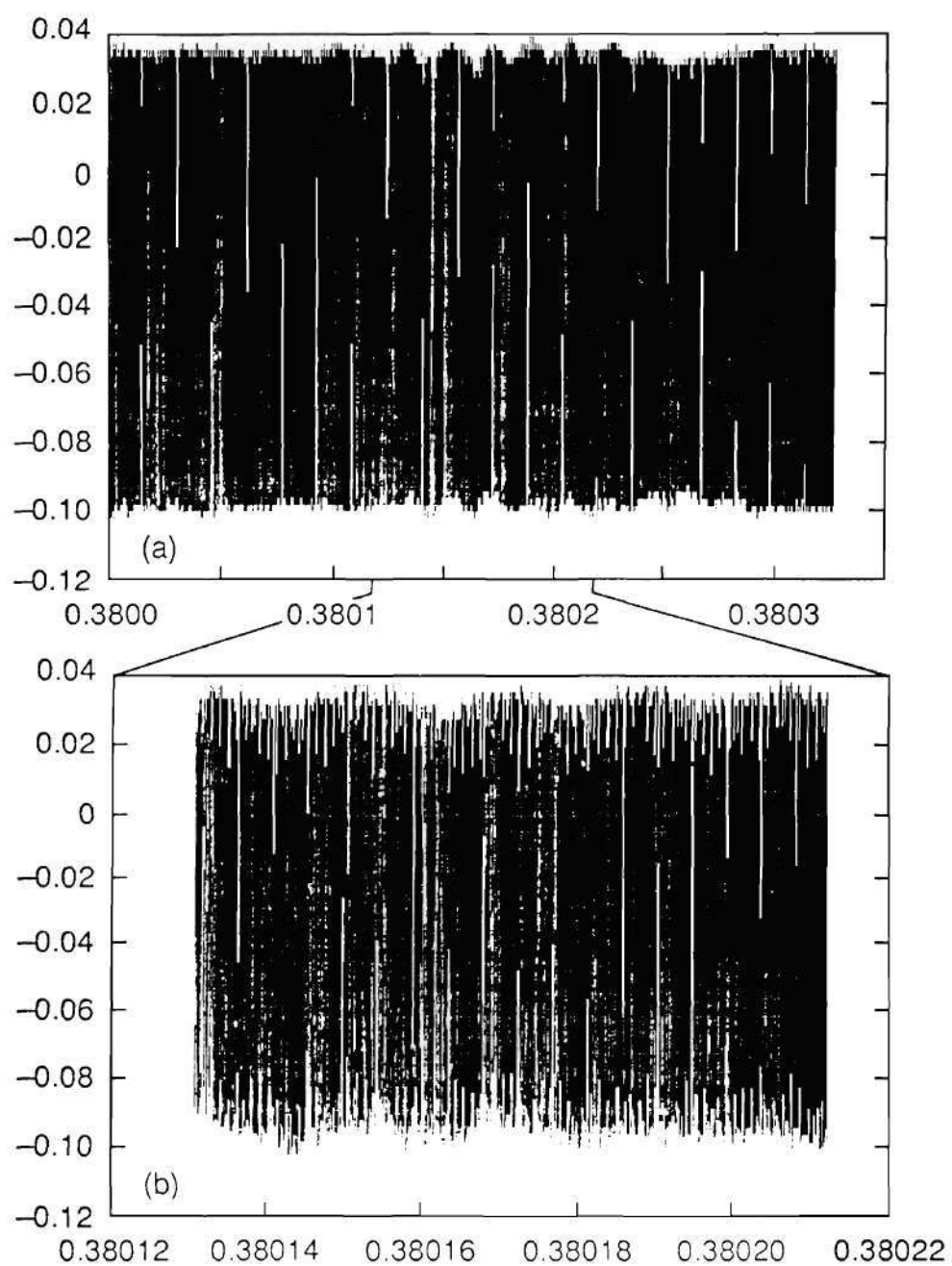


Figure 4.35: RF Frequency Spectrum: (a)Raw Data Measured by 100 MHz Digitizer
(b)Expanded Spectrum Showing a Low Frequency Fluctuation

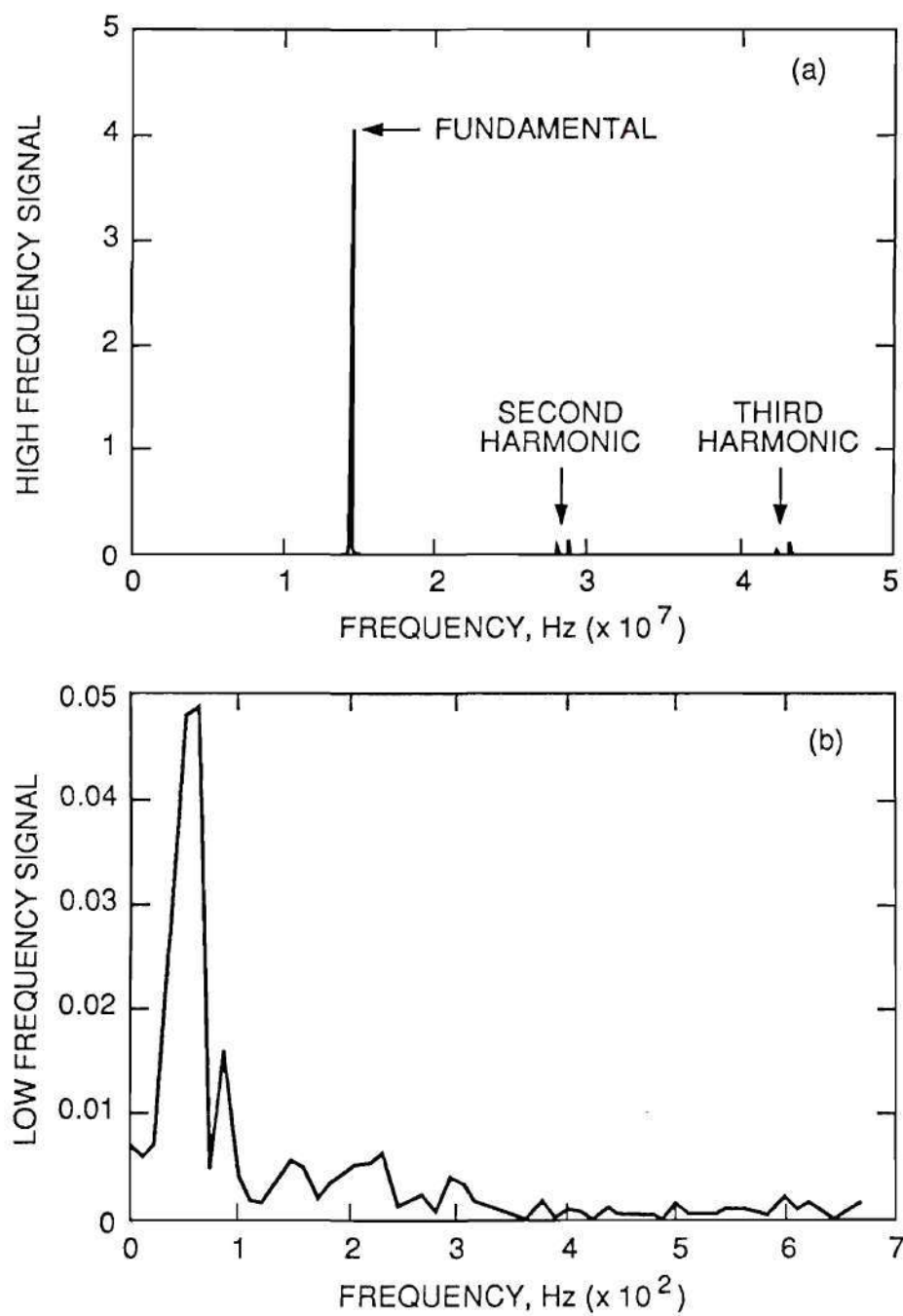


Figure 4.36: RF Frequency Spectrum: (a)High Frequency Spectrum (b)Low Frequency Spectrum

Summary

Extensive wall conditioning including induction heating, glow-discharge cleaning and six-element Ti gettering with antenna conditioning significantly improved the ICRH operational performance as well as general ATF performance. Even with these good operational conditions, (due to the low density plasma) the ICRH deposited most of its power to the edge region resulting in degraded heating performance. Loading measurements and spectroscopic measurements support this observation and also showed edge cooling due to RF-induced impurity influx or wall sputtering. The neutral particle analyzer showed a large nonthermal minority ion tail caused by unconfined orbit loss of edge heated particles, which will be explained in Chapter V. These results were consistent with the edge probe measurements indicating direct RF/edge interactions.

It was also observed that loading was sensitive to frequency, strap - plasma gap and density. An optimized ATF magnetic configuration was crucial for better performance. This was a function of RF frequency and minority concentration as well as plasma temperature and mod-B configuration. The frequency scan and minority concentration scan demonstrated the importance of these parameters.

Some physics including fast ion confinement, eigenmode study and magnetic fluctuations are discussed in the next chapter. The initial results showed that in stellarator geometry it requires more effort to understand these important issues rather than is required for tokamak geometry. Assumptions such as toroidal or poloidal symmetry must be avoided in the stellarator geometry.

REFERENCES

- [1] McCracken, G. M., and Stott, P. E., "Plasma-Surface Interactions in Tokamaks," *Nucl. Fusion*, **19**, 889 (1979).
- [2] Langley, R. A., et al., "Recent Results on Cleaning and Conditioning the ATF Vacuum System," unpublished.
- [3] Isler, R. C., et al., "The Effects of Chromium and Titanium Gettering on the Operation of the Advanced Toroidal Facility," presented in the 17th EPS Conference on the Controlled Fusion and Plasma Heating, Amsterdam, June, 1990.
- [4] Colchin, R. J., et al., "Overview of Results from the ATF Torsatron," *Bull. Am. Phys. Soc.*, **34**, 1999 (1989).
- [5] Rasmussen, D. A., et al., "Electron Temperature and Density Profile Analysis in ATF," *Bull. Am. Phys. Soc.*, **34**, 1947 (1989).
- [6] Owens, T. L., et al., "Heating Experiments in the Ion Cyclotron Range of Frequencies on EBT-S," *Nucl. Fusion*, **23**, 49 (1983).
- [7] Morita, S., "Some Results of Z_{eff} from Visible Bremsstrahlung," unpublished.
- [8] Mutoh, T., et al., "ICRF Experiment on the Heliotron-E," unpublished.
- [9] Kaita, R., et al., "Fast Ion Orbit Effects During Ion Cyclotron Range of Frequency Experiments on the Princeton Large Torus," Report PPPL-1993, Plasma Physics Laboratory, Princeton University, Princeton (1983).
- [10] Hammet, G. W., "Fast Ion Studies of Ion Cyclotron Heating in the PLT Tokamak," Ph.D Thesis, Princeton University, Princeton (1986).

- [11] Kwon. M, et al., "Edge Plasma and RF Field Measurements during Fast-Wave ICRH Experiments on ATF," *Bull. Am. Phys. Soc.*, **34**, 1950 (1989).

CHAPTER V

DATA ANALYSIS AND DISCUSSION

In this chapter, analytic and numerical modeling are employed in an effort to better understand the experimental data and to find future directions and expectations for the ATF ICRH experiments. In particular, missing links in the experimental data needed to build a whole, consistent picture of the ATF ICRH experiments are supplied from calculations. Some of the topics investigated are:

- Propagating modes and their characteristics,
- RF power absorption,
- RF/edge interaction,
- Fast ion confinement in ATF,
- RF power balance.

It is not possible to cover all of these topics exhaustively, but some of them will be examined in considerable detail.

Table 5.1: Input Parameters of ATF Plasma and Vacuum Vessel for Computer Simulations

$T_e(0)$	eV	800
$T_e(a)$	eV	20
$T_i(0)$	eV	150
$T_i(a)$	eV	15
$n_e(0)$	cm^{-3}	9×10^{12}
$n_e(a)$	cm^{-3}	2×10^{12}
λ_n	cm	5
R	m	2.1
\bar{a}	m	0.3
η_{minority}		0.05
Gap between strap and plasma	cm	6
Strap width	cm	10.8
Side wall width	cm	22.0

Simulation With a 2-D RF Heating Code

The 2-D RF heating code discussed in Chapter II was used for simulating the ICRH experiments performed on ATF. Experimental values were used for most of the required input parameters of the code, including density and temperature profiles. Table 5.1 shows typical input parameters used for simulation of the D(H) experiments.

For density and temperature profiles the following functional form was used:

$$f(\rho) = (f(0) - f(a))[1.0 - \rho^\alpha]^\beta + f(a), \quad (5.1)$$

where ρ is the radial flux coordinate, $f(0)$ and $f(a)$ are the values of f at the plasma

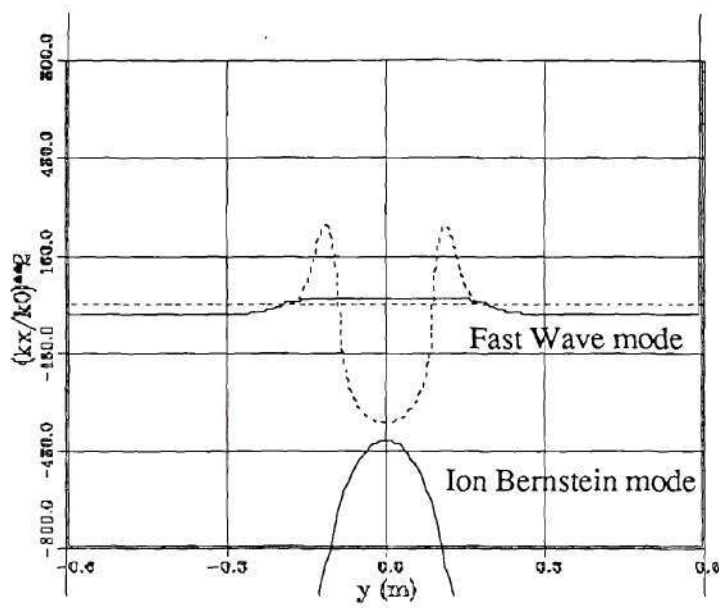


Figure 5.1: Warm Plasma Dispersion Relation for $k_z = 10 \text{ m}^{-1}$ and $\eta_H = 0.05$

center and last closed flux surface, respectively, and α and β are numeric constants which were determined from the experimental data.

Basic physical characteristics and global characteristics of RF waves in the ATF plasma are discussed first. A dominant propagating mode of the k_{\parallel} spectrum in terms of power absorption from the launched antenna spectrum appeared in these low density target plasmas. A detailed study of this mode follows, including polarization, region of propagation, absorption layer, and wave field profiles. The power deposition profile is discussed later with the 3-D calculation results (helical symmetry assumed) and compared with the experimental observations.

The simulation of the ATF magnetic field geometry used by the 2-D code was shown in Fig. 2.7. For the geometry shown in the figure, the warm plasma dispersion relation of the fast wave, launched from the low field side on a horizontal (vertical in the code geometry) chord is displayed in Fig. 5.1. The magnetic field saddle point in the 2-D code is the field of the minority species fundamental resonance (for which the

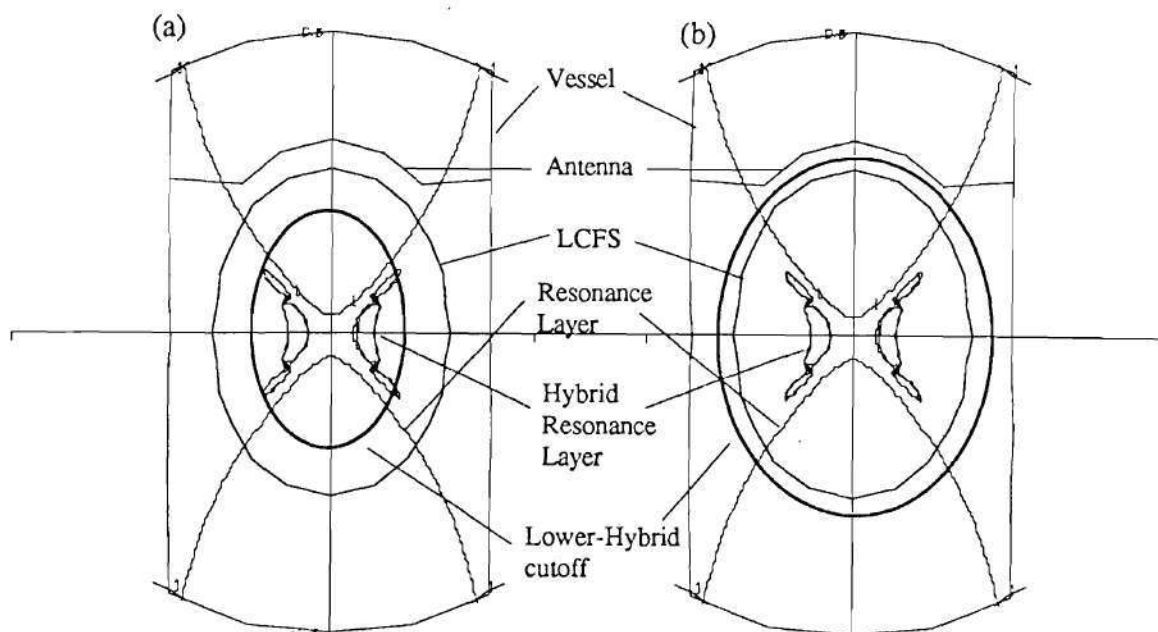


Figure 5.2: Two-Dimensional Plot Showing Fundamental Resonance Layer, a Pair of Cut-off and Hybrid Resonance Layers and the Lower Hybrid Cut-off for (a) $k_{\parallel} = 3.8 \text{ m}^{-1}$ and (b) $k_{\parallel} = 10 \text{ m}^{-1}$

ICRH is tuned). Therefore the hybrid resonance is located “sideways” (perpendicular to the chord) and does not appear in Fig. 5.1. Hence the ion Bernstein wave is cutoff. Figure 5.2 is a two dimensional plot which shows the locations of the resonance layer and cut-off layer for two different k_{\parallel} modes.

For smaller k_{\parallel} modes, the fast wave was able to propagate over most of the region in front of the antenna, while for larger k_{\parallel} modes, the lower hybrid cutoff layer was located in the plasma region. This made the evanescent layer very thick, which made it difficult for the ICRH wave to tunnel through it.

The RF field profiles were also different for these two k_{\parallel} modes. For the given plasma conditions, $k_{\parallel} = 10 \text{ m}^{-1}$ appeared as the dominant mode. With this in mind, the field profile for this mode showed an eigenmode structure with an odd m number but the $k_{\parallel} = 3.8 \text{ m}^{-1}$ did not. However, since the $k_{\parallel} = 10 \text{ m}^{-1}$ mode had a larger

edge evanescent layer, power deposition was limited to the edge region, while for the $k_{||} = 3.8 \text{ m}^{-1}$ mode, good penetration to the central plasma column was possible, where power would be deposited as shown in Fig. 5.3. In this figure, contours of constant field and power deposition are shown in the ATF geometry.

The antenna spectrum was primarily determined by the width of the strap and the gap between the side walls. For this low density plasma, the strap width ($\sim 10 \text{ cm}$) and gap between the side walls (22 cm) were too narrow to launch the narrow band of accessible modes (low $k_{||}$ modes). The side wall image currents affected the spectrum so that low $k_{||}$ modes were suppressed. Unfortunately, the suppressed modes were the ones which would have penetrated to the plasma center, and possibly performed useful heating. This situation would improve with the higher density plasmas for which this antenna was originally designed.

Figure 5.4 shows the $k_{||}$ power spectrum. The broken line is the spectrum for the strap without a toroidal current distribution and the solid line is for the strap with a toroidal current distribution, including image currents. Note that a dip appears around $k_{||} = 0$ when the toroidal distribution was included. There is also asymmetry around $k_{||} = 0$. This is caused by the helically symmetric configuration and poloidal field effects (the antenna strap is at an angle to the toroidal portion of the field). When the field is reversed, this asymmetry is also reversed. It is interesting to compare this spectrum with an antenna spectrum without plasma effects as shown in Fig. 5.5¹. The peak in B_z appears at $k_{||} \sim 20 \text{ m}^{-1}$, (note: k_z and $k_{||}$ denote the same quantity) but this mode has such a high $k_{||}$ number that it does not penetrate into the central plasma column at all, as was shown in Fig. 5.4. Therefore it is speculated that the higher $k_{||}$ modes (higher than $\sim 15 \text{ m}^{-1}$), did not contribute much

¹The author is grateful to P. M. Ryan for calculating the antenna spectrum for several different cases.

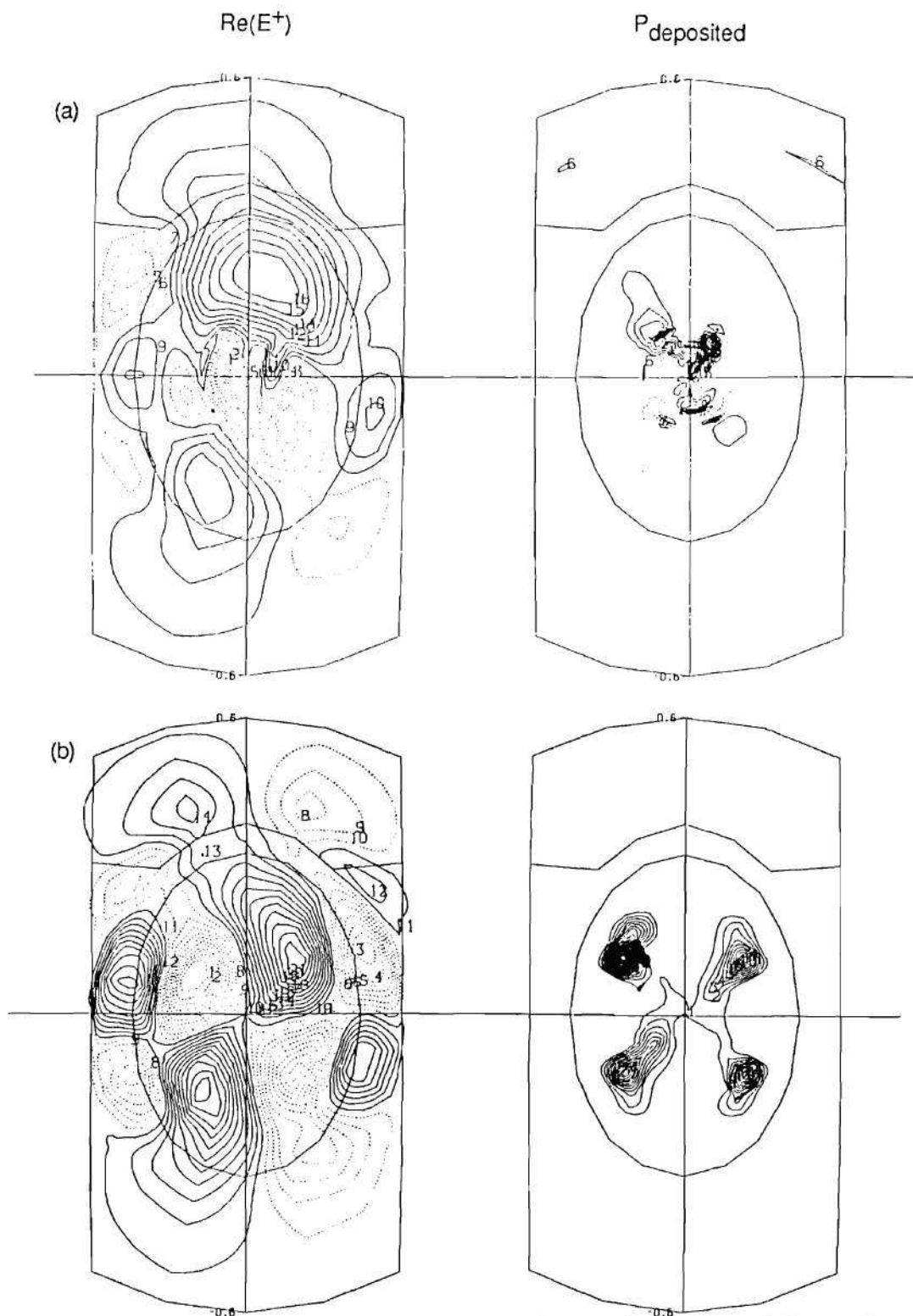


Figure 5.3: Two Dimensional Wave Electric Field ($\text{Re } E_+$) Profile and Power Deposition Profile for (a) $k_{\parallel} = 3.8 \text{ m}^{-1}$ and (b) $k_{\parallel} = 10 \text{ m}^{-1}$

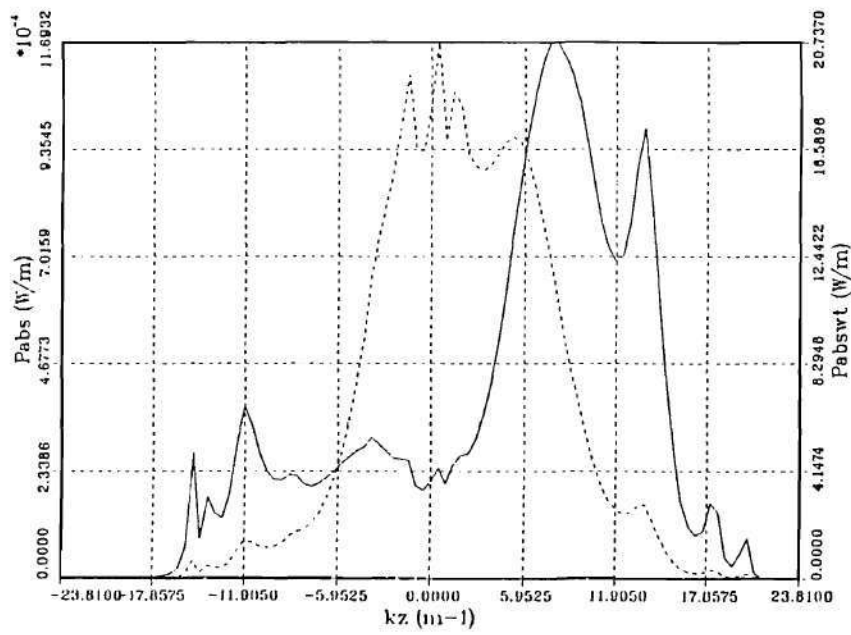


Figure 5.4: The Power Absorption Spectrum as a Function of $k_{||}$ with (Solid) and Without (Dashed) Taking the Effect of the Toroidal Current Distribution into Account

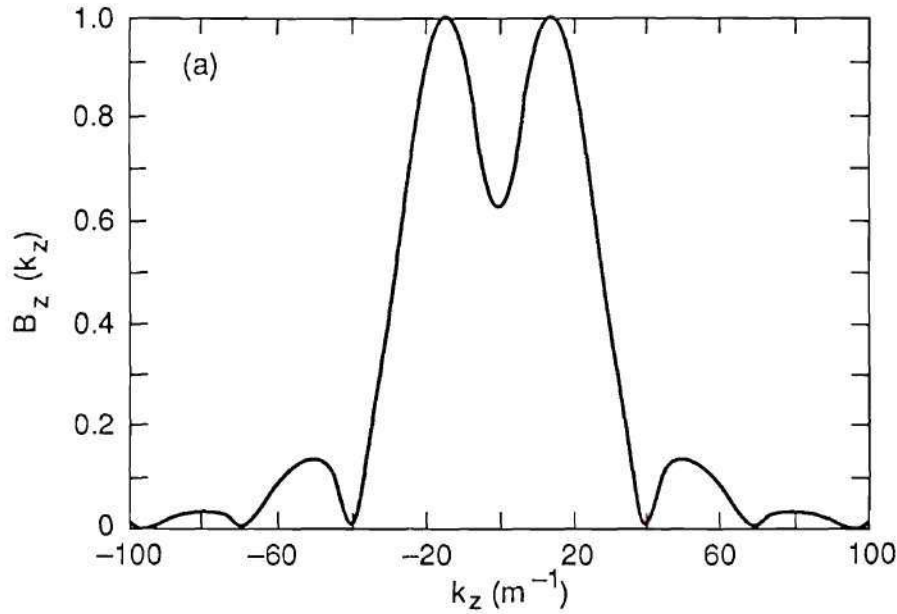


Figure 5.5: ATF Antenna Spectrum without Plasma Effects: B_z is Calculated at 3 cm from the Faraday Shield Surface.

to power absorption in the low density plasmas because reflection was too high. It should be noted that although high k_{\parallel} modes had poor penetrating capability in low density plasmas, they allow larger Doppler shifts of the resonance layer, which would increase cyclotron absorption by moving the resonance layer toward regions where the polarization is favorable to ion heating (the left-hand polarization is increased). This is why high-density plasmas, which permit propagation of high- k_{\parallel} modes, are more efficiently heated by ICRF.

The left-hand polarized electric field profile as plotted in Fig. 5.6 shows that $|E_+|$ was zero at the resonance layer within numerical error.

Loading is calculated from $\int P_{abs} dV / |I|_{ant}^2$ as given in Eq. 2.152. Although any plasma parameter can affect loading, the loading was experimentally found to be most sensitive to density and frequency. Here the effects of density included profile effects and the gap between the antenna and plasma. Overall, simulated loading

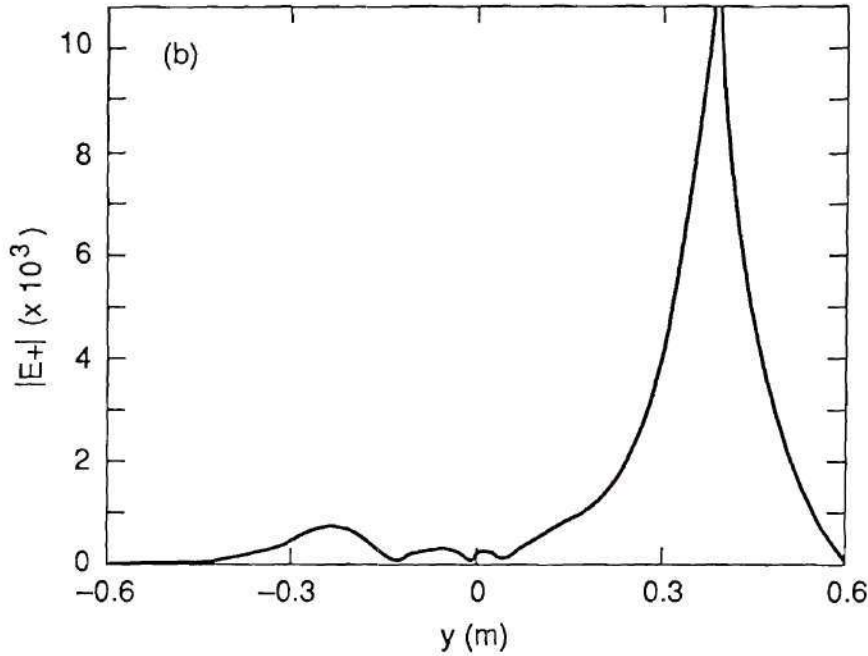


Figure 5.6: The Radial Profile of the Left-Hand Polarized Electric Field ($|E_+|$)

data matched the experimental data quite well. Figure 5.7 shows the calculated density dependence of the loading. Eigenmodes were observed but they appeared more often for the same density range in the experiments. Figure 5.8(a) shows the frequency dependence of loading for the D(H) regime in which the frequency of 14.4 MHz placed the fundamental resonance layer on the magnetic axis in the typical ATF ECH plasma. The simulated loading is higher with slightly lower frequencies than 14.4 MHz. This is believed to be due to the difference in topology of the resonance-cutoff layers. Figure 5.8(b) shows magnetic configurations for different frequencies. It can be seen that the highest loading occurs when the resonance layer and hybrid layer occur near the flat region around the saddle point. The same effect can be obtained by changing the magnetic field or minority concentration. However, increasing the minority ion concentration also increases the distance between the fundamental resonance layer and the hybrid resonance layer which would decrease the efficiency or require higher temperature (velocity) as indicated by Eq. (2.14).

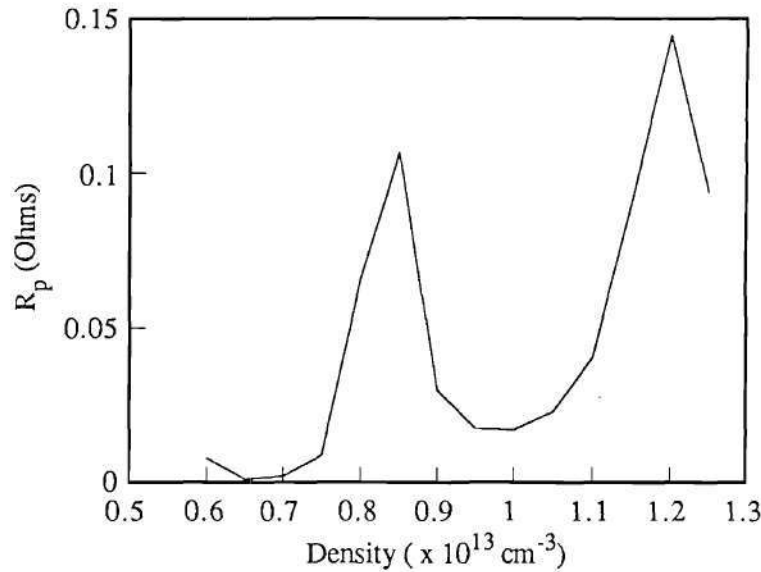


Figure 5.7: Loading vs Density for the Range of Typical ATF Plasma Densities

According to the simulation results, in ATF at 14.4 MHz in the D(H) regime, to keep the hybrid resonance near the saddle point, the minority concentration should be less than 5%, taking the fact that the saddle point is slightly inside the plasma magnetic axis into account.

Simulation of the RF power deposition profiles was the most important output of the 2-D code. Due to the lack of a kinetic model in the plasma response function (the warm plasma dielectric tensor), the power partitioning to each plasma species could not be calculated with the 2-D code. For higher $k_{||}$ modes, as expected, the calculation shows that power was deposited on the outside at these low densities. In Fig. 5.4, the k_z spectrum for power absorption shows that the dominant mode was a single $k_z = 10 \text{ m}^{-1}$ mode and the power of this mode was deposited in the outer half radius. This is reasonable because in the experiments the measured loading was very low, which shows that not much power was absorbed by the plasma and that edge heating occurred during ICRH. If the calculation is correct, in a low density plasma a

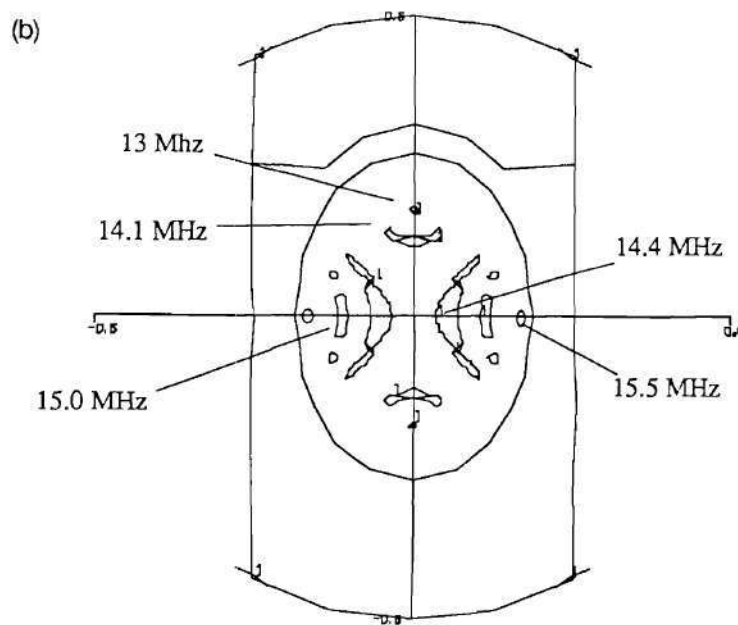
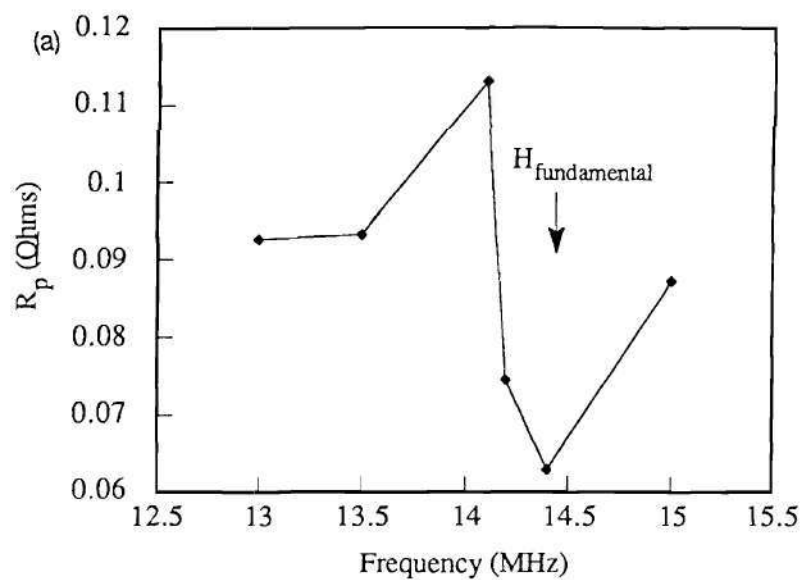


Figure 5.8: (a) Frequency Dependence of Loading and (b) Resonance Surface Geometry as a Function of Frequency at 0.95 T

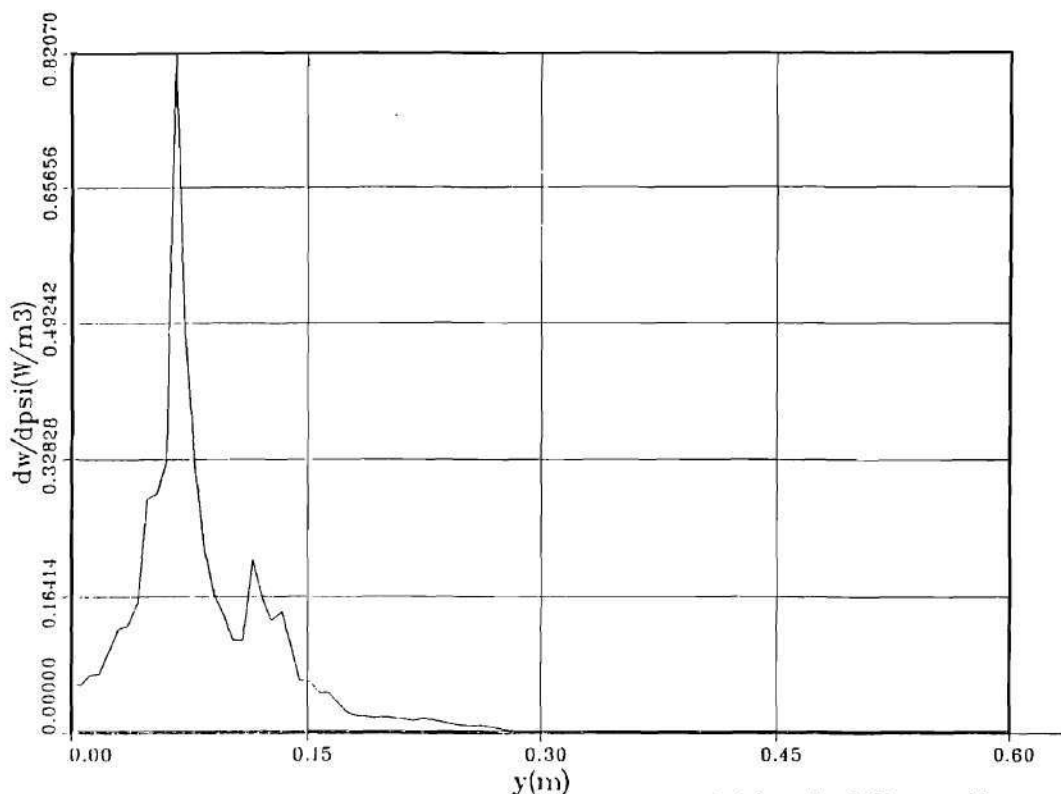


Figure 5.9: Radial Profile of the Flux Surface Averaged Absorbed Power Summed over All $k_{||}$

little power would go to the central column, large edge heating due to the evanescent wave would have occurred in the plasma edge, and toroidal damping would have been very weak. As discussed in Chapter IV, no central heating was observed, and the electron temperature in the plasma edge region increased dramatically. Experimental evidence of weak toroidal damping was also observed. Several diagnostic signals - impurity monitor signals, spectroscopy signals, H_{α} signals - measured on the far side of the torus from the antenna responded instantly to RF wave injection and the RF signal leaked through the limiter on the far side of the torus when there was plasma. Since the wave length of the dominant mode was comparable to the vacuum vessel radius, a standing wave was probably formed. All these conditions enhanced edge heating. Figure 5.9 shows the radial profile of the calculated flux-surface-averaged absorbed power for $k_{||}=10 \text{ m}^{-1}$. In this case 80% of the power was deposited in the outer half radius, including the effect of larger volume with increasing minor radius.

In calculating the power balance, it is useful to define a quality factor [1] Q as the ratio of the imaginary part of the absorbed power to the real part of the absorbed power. If Q is small, more of the RF wave is coupled resistively to the plasma and loading increases, while when Q is large, reactively coupled power is large and the loading decreases. Since the vacuum loading was measured as $\sim 0.18\Omega$ at 14.4 MHz and the calculated loading did not include vacuum loading, by comparing the calculated loading with the measured vacuum loading, the relation between the ratio of the absorbed power to the total input power in measurements and the equivalent Q value in calculations can be estimated. Here it was assumed that the calculated loading was equal to the total experimental loading after the vacuum loading was subtracted: $Z_m = Z_p + Z_v$, and $Z_c = Z_p$, where subscripts m, p, v and c stand for "measured", "plasma", "vacuum" and "calculated", respectively. For $Z_p = Z_v$, 50 % of the power is absorbed by the plasma and the other half would be lost by ohmic coupling to the structure. In this case ($Z_p = Z_v = Z_c$) the simulation showed the equivalent $Q \sim 50$. This quantity is useful in the next chapter where projections for future experiments are discussed.

In summary of this section, by using a 2-D RF heating code the power deposition spectrum of the antenna was studied as a function of the $k_{||}$ mode number for low-density ATF plasmas. It was found that the launched waves could not penetrate to the central plasma because of high- $k_{||}$ mode launching (low- $k_{||}$ modes were unfortunately suppressed by the antenna design). This caused most of the RF power to be deposited in the plasma edge region. The loading calculations from the code were in good agreement with the measured loading. Both the calculated and measured loading indicated that half of the RF power was lost to the antenna structure via ohmic loss. The density dependence of the loading showed an eigenmode characteristic. The frequency dependence of the loading indicated that the location of the Doppler-shifted resonance layer is very important.

RF/Edge Interaction

Though extensive edge diagnostics were not available for the ATF ICRH experiments, there was data from various diagnostics which were specially designed for edge studies, namely H_α detectors, spectrometers and probes. These diagnostics were used to examine the RF/edge interaction within the limits of their applicability.

$H_\alpha(D_\alpha)$ detectors have been widely used to assess particle confinement by measuring the interaction of electrons with edge neutral hydrogen (deuterium). The $H_\alpha(D_\alpha)$ signal is a function of the edge neutral density, electron density, and electron temperature. During the ICRH experiments in ATF, the H_α signal showed an initial peak then decreased as shown in Fig. 4.11. Since the edge density was increasing, as indicated by the Langmuir probe measurements, the source which caused the H_α signal to increase came from the plasma edge region. The decrease after an initial peak is believed to be caused by edge plasma cooling due to impurity flux from sputtering of the structure induced by unconfined fast-ions, and wall impurity influx enhanced by direct edge heating (the reader is reminded that edge [edge plasma] here means plasma outside the last closed flux surface and plasma edge means the plasma just inside the last closed flux surface). Note that the H_α detection filter installed in ATF had a wide enough wavelength bandwidth to detect the H_α and D_α lines simultaneously. Therefore the detector signal was the sum of collisional excitation of H atoms and/or D atoms produced by recycling and dissociation of H_2/D_2 molecules.

There was insufficient data to totally characterize the antenna-near field interaction except for the observation that the edge density and temperature increased during the RF even behind the antenna Faraday shield layer, observation of eigenmodes generation, and observation of harmonics of the generator frequency in RF probe signals, probably due to sheath rectification.

The radial profiles of the edge electron density and temperature as shown in

Fig. 4.31 were used for energy accounting during the RF. Assuming that the dominant loss was parallel heat flux to the antenna and that fast ion orbit loss might be ignored for the edge region, a simple analytic formula for the parallel energy flux is given by [2],

$$q_{\parallel}^{\text{total}} = (2\tau\mu_E + \gamma_e)kT_e n_e C_s f(\tau), \quad (5.2)$$

where,

$$\begin{aligned} \tau &= \frac{T_i}{T_e}, \\ \mu_E &\sim 1 \text{ for } \tau \geq 1, \\ \gamma_e &= \frac{2}{1 - \nu_e} + \frac{e|V_{\text{sheath}}|}{kT_e}, \\ eV_{\text{sheath}} &= \frac{kT_e}{2} \ln \frac{m_e T_i}{m_i T_e} \sim -3.8 \text{ for } \tau = 1, \end{aligned}$$

ν_e is the secondary electron emission coefficient, C_s is the sound speed defined as

$$C_s \equiv \sqrt{\frac{k(T_e + T_i)}{m_i}},$$

and $f(\tau)$ is a density reduction factor ranging from 0.487 for $\tau = 0$ to 0.798 for $\tau = \infty$. The total power deposited at this toroidal location was obtained by integrating $q_{\parallel}^{\text{total}}$ over the minor radius. Assuming that the effective region was just in front of the antenna, then the total power deposited in this area was obtained from

$$P_{\text{total}} = \int_{r_{\text{lim}}}^{\infty} dr \int_{\theta_1}^{\theta_2} r d\theta q_{\parallel}^{\text{total}} 2\pi r dr, \quad (5.3)$$

where θ_1 and θ_2 were the minimum and maximum poloidal angle of the antenna aperture. Figure 5.10 shows the result of a rough calculation of the $q_{\parallel}^{\text{total}}$ profile using Eq. (5.2) and the data of Fig. 4.31. The total power deposited in front of the antenna in this case was about 21 kW which was 10% of the total RF power. Because there was no data point inside $R \simeq 230$ cm and due to the small assumed effective area, this result might somewhat underestimate the RF power deposition in the edge region.

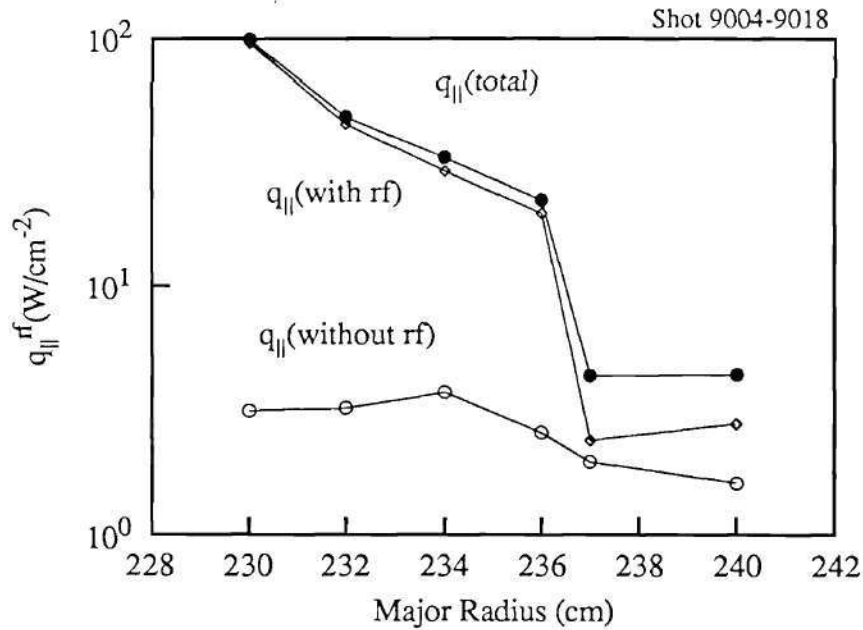


Figure 5.10: $q_{||}^{\text{total}}$ Profile with and without RF

Ohmic loss to the structure was also responsible for edge parameter changes and should be subtracted from the calculated value of the edge RF energy accounting to calculate only the ratio of RF/edge interaction to the total RF power. Obviously the value calculated above is too uncertain to use for a precise power-balance study. A comparison will be made between an indirectly calculated value and the above value in a later section in this chapter.

Discrete eigenmodes were observed in the rising-density shots as shown in Fig. 4.33. Identification of each eigenmode requires a systematic measurement from different toroidal and poloidal locations around the vacuum vessel. Since the ATF was not equipped with a sophisticated probe array, only a simple analysis was attempted using a radially moving probe to measure the phase difference between the RF signal and a reference signal. The phase difference between the current-strap current signal and one component of each probe was measured simultaneously. Since the two small probes tended to rotate as they were radially translated, only the results from the

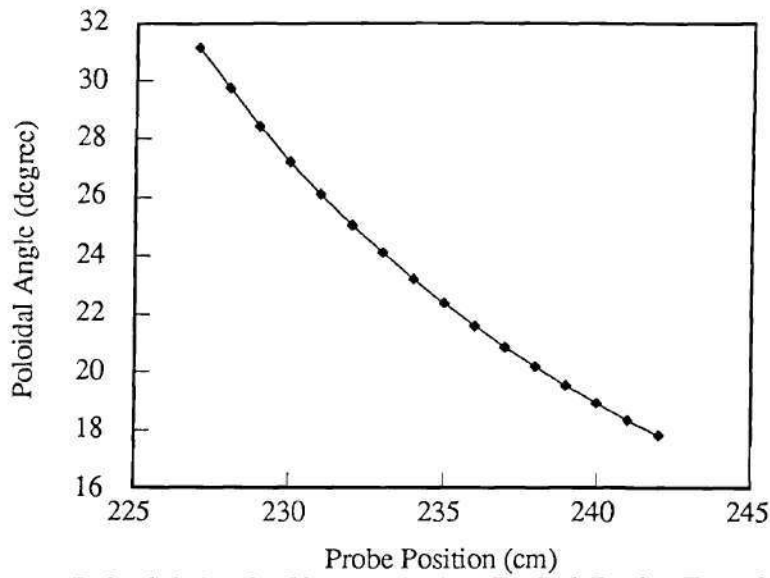


Figure 5.11: Poloidal Angle Change during Radial Probe Translation

big probe (moved remotely by a stepper motor drive) are shown here. As the probe moved radially, the toroidal probe location was little changed but the poloidal location was changed by $\sim 15^\circ$ as shown in Fig. 5.11. Using this information, phase angle versus poloidal angle is plotted as in Fig. 5.12. In this case, the measured changes in the phase angle came almost solely from the poloidal components because of the reasons described next. If an $e^{i(n\phi+m\theta)}$ dependence where ϕ and θ are the toroidal and poloidal angle is assumed, the shear effect is neglected and $\Delta\phi \simeq 0$ along the radial probe path, then $e^{im\theta}$ is the dominant term. Between successive eigenmodes, no change was observed in the toroidal component of the phase angle at the same probe position but the poloidal phase angle deduced from the radial profile measured as the probe moved was different. This indicates that successive eigenmodes had the same toroidal mode number. It is now possible to identify the modes with a simple calculation as shown below.

The fast wave dispersion relation, Eq. (2.59) can be adapted to a helical

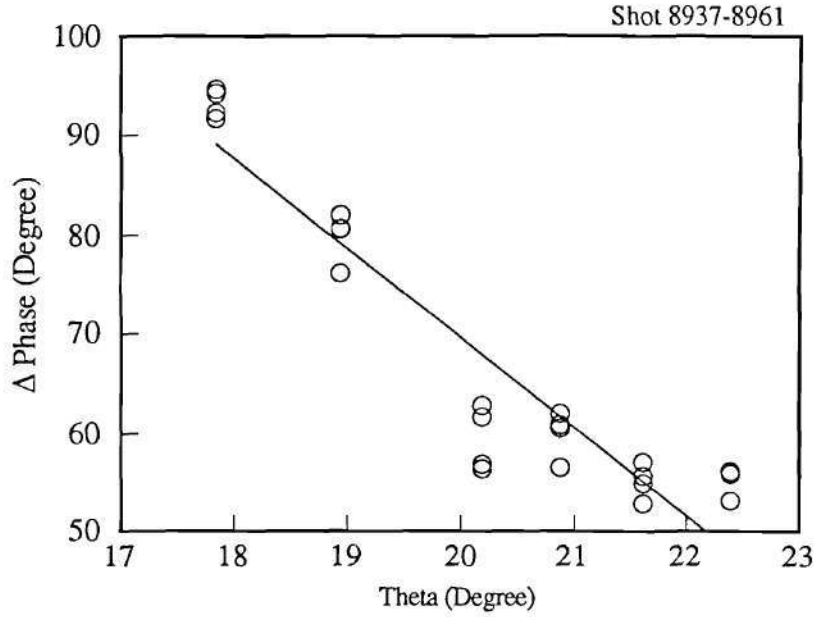


Figure 5.12: A Plot of Measured Phase Angle as a Function of the Angular Changes in Poloidal Location of the Probe

geometry as

$$(k_z - mh)^2 = \frac{1}{2} \left(\frac{\omega^2}{v_A^2} - k_\perp^2 \right), \quad (5.4)$$

where v_A is the Alfvén velocity, m is the poloidal mode number and h is the helical pitch. For an average radial mode number defined as [3]

$$k_r = \begin{cases} \frac{\pi}{2a} & \text{for } m = \pm 1, \\ \frac{\pi}{a} & \text{otherwise,} \end{cases}$$

$k_z = 10 \text{ m}^{-1}$, $v_A = 0.084\omega$ determined from Table 4.1, and with $f=14.4 \text{ MHz}$ for the D(H) heating regime at 0.95 T, the onset densities for $m = 0, 1, 2, 3, 4$ modes calculated from Eq. (5.4) are 0.81, 0.37, 0.5, 0.56, and $0.76 \times 10^{13} \text{ cm}^{-3}$, respectively. For the $m = -1$ mode, the onset density becomes $0.97 \times 10^{13} \text{ cm}^{-3}$. Comparing this with the measured density (Fig. 4.33) the possible poloidal mode numbers are $m = 0, 1, 2, 3$, and 4, as shown in Fig. 5.13.

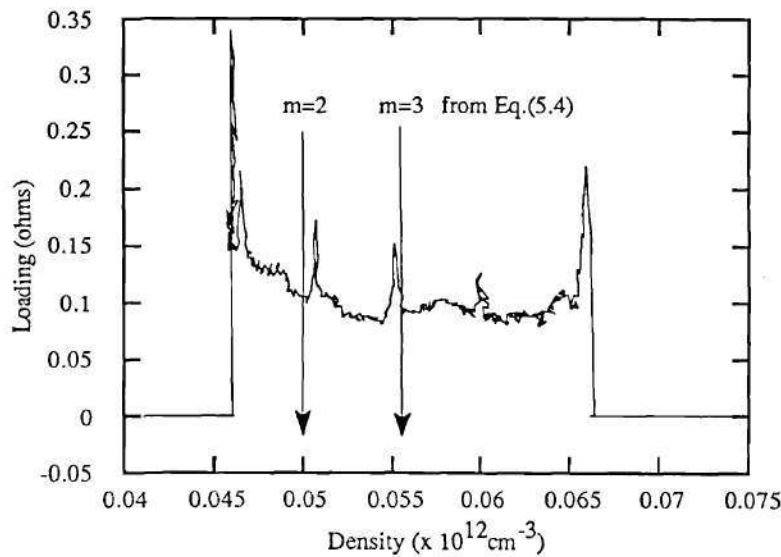


Figure 5.13: Comparison Between Calculated Eigenmodes and Measured ones

In stellarators/torsatrons, toroidally and poloidally resolved edge data are more important than in other machines because of the complex edge geometry. Even in the Alcator C tokamak [5] (the edge geometry of tokamaks is much less complicated particularly for circular plasmas), there sometimes existed a large poloidal asymmetry in particle flux. During the initial RF experiments, RF effects appeared everywhere around the torus, because (as demonstrated in Chapter IV and above), toroidal damping was very weak. However, it will be demonstrated in the next chapter that as density is increased in future experiments toroidal damping should become strong, and most of the nonlocal phenomena should disappear.

In summary of the RF/edge interaction section, the energy deposited to the edge plasma region directly by the RF was calculated using the data from a Langmuir probe. This calculation indicates that 10% of the total RF power was deposited in the edge region (the gentle reader is once again reminded that edge here means outside the last closed flux surface). The RF probe measurements demonstrated eigenmode

generation during a density ramp, which probably were poloidal modes, as shown in the calculation above. The importance of the generation and identification of the eigenmodes is that it reinforces our argument for the modes which were launched by the antenna, showing that they were basically edge dominated modes which did not penetrate to the plasma center. The observed eigenmodes agree reasonably well with those calculated from the launched antenna spectrum with the 2-D RF code.

Fast Ion Studies

Confinement of fast minority ions generated by ICRH is the key factor for success of the minority heating scheme with a low minority concentration. In this section, this topic is discussed by analyzing the measured NPA data shown in Chapter IV. Understanding of the fast ion behavior in the ATF plasma is necessary for this work. The time scales for possible fast ion loss channels in the low density ATF plasmas are discussed first. Then a study of the loss cone in ATF follows. The effects of RF on the particle orbit are also illustrated with a collisionless orbit following code. From this basic knowledge, an interpretation of the NPA data is performed.

First of all, some time scales for the competing energy transfer and loss mechanisms for fast ions are considered. The direct ion loss time is estimated [6] as

$$\tau_{\text{loss}} = \frac{1}{3} \frac{P_{\text{Stix}} W_{\text{loss}}}{P_{\text{loss}} T_{\text{Stix}}} \tau_s, \quad (5.5)$$

where $P_{\text{loss}}/P_{\text{Stix}}$ is the ratio of power lost due to unconfined orbits to the total absorbed power as calculated from the Stix formula, Eq. (2.111), W_{loss} is the energy above which particles are lost, T_{Stix} is temperature defined as

$$T_{\text{Stix}} = \frac{P_{\text{Stix}}}{3n_{\text{minority}}} \tau_s, \quad (5.6)$$

and τ_s is the fast ion slowing down time [7] given by

$$\tau_s = \frac{3 \times 10^{14} A(T_e/e)^{3/2}}{n_e Z^2 \ln \Lambda} \text{ (sec).} \quad (5.7)$$

In words, Eq. (5.6) states that in the case when unconfined orbit loss is dominant, the power which is lost is a function of the tail temperature only. Then from Eq. (5.7) and the equation

$$P_{\text{loss}} = \frac{W_{\text{loss}} n_{\text{minority}}}{\tau_{\text{loss}}}, \quad (5.8)$$

Eq. (5.6) was obtained. The tail temperature, T_{Stix} , is proportional to the RF energy absorbed by fast ions for the slowing down time, τ_s , during which electrons drag fast ions dynamically. The relation between $P_{\text{loss}}/P_{\text{Stix}}$ and $T_{\text{Stix}}/W_{\text{loss}}$ was calculated and is plotted in Fig. 5.14. For the outer edge of the standard ATF plasma where $P_{\text{loss}}/P_{\text{Stix}}$ was ~ 1 , τ_{loss} was about $0.033\tau_s$ or $\tau_{\text{loss}} \sim 1\text{-}2$ msec.

The charge-exchange-loss time scale is easily calculated from a basic knowledge of atomic physics and is given by:

$$\tau_{CX} = \frac{1}{n_{\text{neutral}} \langle \sigma v \rangle_{cx}}, \quad (5.9)$$

where n_{neutral} is the neutral density and $\langle \sigma v \rangle_{cx}$ is the charge exchange cross section, which is a function of energy. For the case where the fast ion velocity is large compared to the neutral velocity,

$$\langle \sigma v \rangle_{cx} = \sigma(E) v_{\text{fast ion}}, \quad (5.10)$$

where E is the fast ion energy. Spatially resolved (or even averaged) neutral density is apparently one of the most difficult quantities to measure in fusion experiments, since it has exponentially (or even more nonlinear) toroidal and poloidal variations (depending on gas sources and recycling points), which means that knowledge of it at any single position does not imply knowledge anywhere else [8]. No measurement of the neutral density was attempted in ATF. Based on measurements [9] of similar conditions in the Heliotron-E plasma, it is estimated that the central neutral density

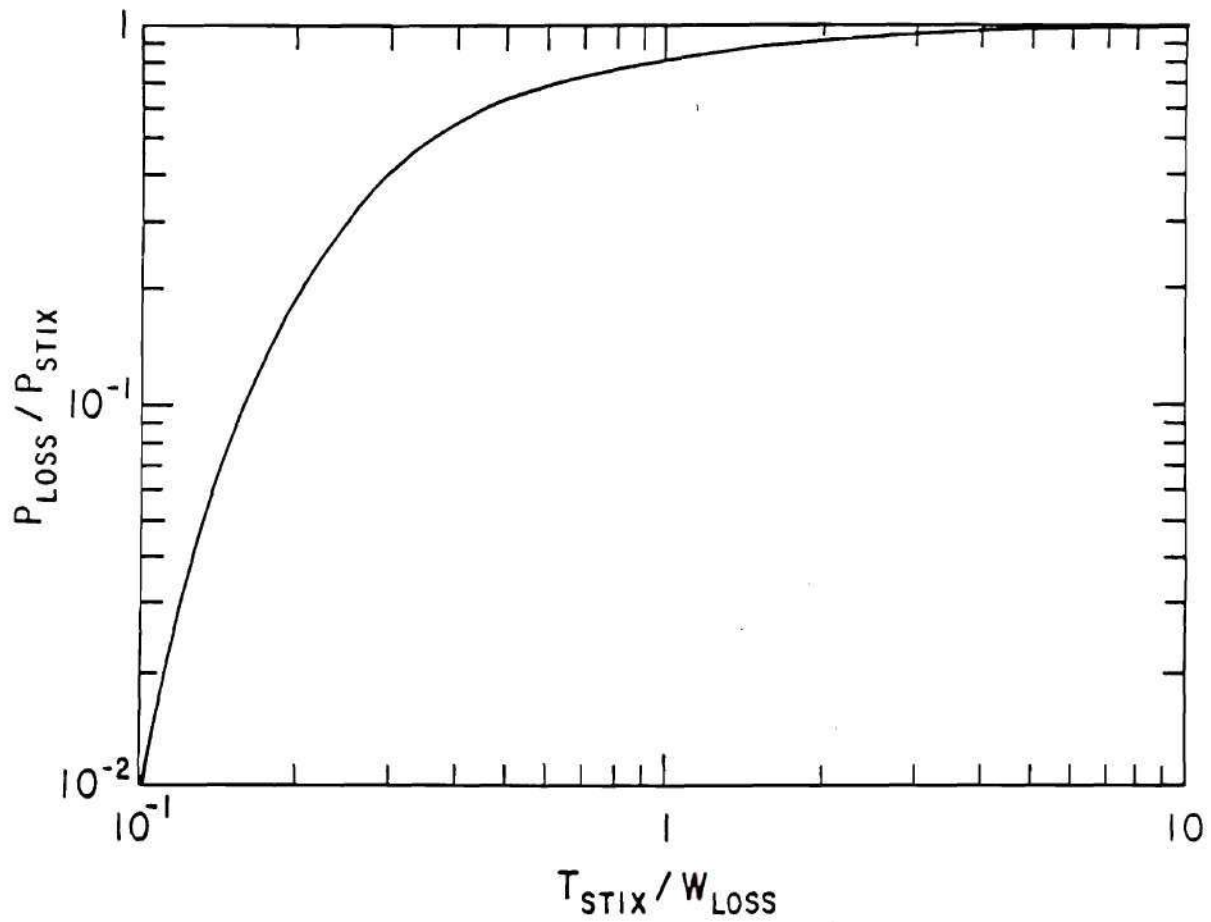


Figure 5.14: An Isotropic Model Calculation of the Fraction of RF Power Lost to Unconfined Orbits $P_{\text{loss}}/P_{\text{stix}}$, as a Function of the Tail Temperature T_{stix} Normalized to the Energy Loss W_{loss} [6]

was on the order of $0.5 \times 10^8 \text{ cm}^{-3}$ and the edge neutral density was $0.5 \times 10^9 \text{ cm}^{-3}$. For this case τ_{CX} is in the range between 5 and 50 msec for the plasma region where the ions of interest (10 to 100 keV) are believed to have been created. But this value is subject to change at the NPA position due to a gas-feed valve located at the IN-1 port.

The time scale for hydrogen fast ion energy transfer to electrons can be represented as the energy equilibration time for proton-electron collisions [10]:

$$\tau_{pe} = \left[1.8 \times 10^{-19} \frac{(m_p m_e)^{\frac{1}{2}} n_e \lambda_{pe}}{(m_p T_e + m_e T_p)^{\frac{3}{2}}} \right]^{-1}, \quad (5.11)$$

where λ_{pe} is the Coulomb logarithm for $p - e$ collisions. This time is calculated as about 50 msec for the typical ATF low density parameters shown in Table 5.1.

The time scale for hydrogen energy transfer to deuterium is much longer than τ_{pe} and is give by [10] as

$$\tau_{pd} = \left[1.8 \times 10^{-19} \frac{(m_p m_d)^{\frac{1}{2}} n_d \lambda_{pd}}{(m_p T_d + m_d T_p)^{\frac{3}{2}}} \right]^{-1}, \quad (5.12)$$

where λ_{pd} is the coulomb logarithm for $p - d$ collisions. With the same parameters from Table 5.1, τ_{pd} is calculated as about 200 msec. All the quantities in Eqs.(5.11) and (5.12) have the *cgs* units except the temperature which is in eV.

From the above scaling it can be seen that in the plasma edge region of ATF fast ions generated by RF were rapidly lost due to unconfined orbits, while in the central region, CX loss was competing with electron drag. Unfortunately, in the low density ATF plasmas, as discussed previously, the RF power flux to the central minority ions was very small. Thus, total energy transfer to the plasma via electron drag was negligible. It would be interesting to consider how this picture is improved for higher density plasmas, and this is discussed in the next chapter.

To understand energetic particle confinement in ATF better, a Monte-Carlo

orbit following code² which simulated the ATF magnetic geometry in Boozer coordinates was used to calculate the confined-particle fraction as a function of energy. The whole $v_{||}/v$ space was divided into eight cells and four particles were started in each cell with a random starting position in ρ , which is the radial coordinate in the Boozer coordinate system [11], where the radial coordinate is the gradient of the magnetic flux surface represented as a circle. For a set period of time, the code followed the orbit of each particle and determined if it remained confined. A particle was lost if the particle orbit hit the last closed magnetic flux surface. Figure 5.15 shows the results as a function of particle energy and position in ρ .

The confinement fraction was calculated as the sum of the confined time of each particle divided by the total given time in each cell. Clearly, the confinement fraction averaged over the whole pitch angle was degraded as ion energy increased and as ρ increased (Fig. 5.15(a)). The pitch-angle dependence showed that particles with smaller pitch were more poorly confined (Fig. 5.15(b)), as expected.

A comprehensive study of the loss cone in the ATF magnetic geometry has not been performed. However, an initial study [12] showed that when the effects of the equilibrium electric field are not included, most of the particles in the outside region are within the loss cone, even for a 1-keV particle. This study also showed that the presence of the radial electric field reduced the loss cone for particles of energy 1 keV. But this favorable effect of the electric field is not effective for particles with energy higher than seven to ten times the electron temperature ($T_e \sim 1$ keV in the ATF) [13].

Orbit studies in ATF have revealed that there is a factor which affects particle confinement significantly, the minimum-B contour [14,15]. In Boozer coordinates, these contours appear as shown in Fig. 5.16 for the ATF standard configuration,

²The author is grateful to S. Painter for allowing him to use this code and assisting with it.

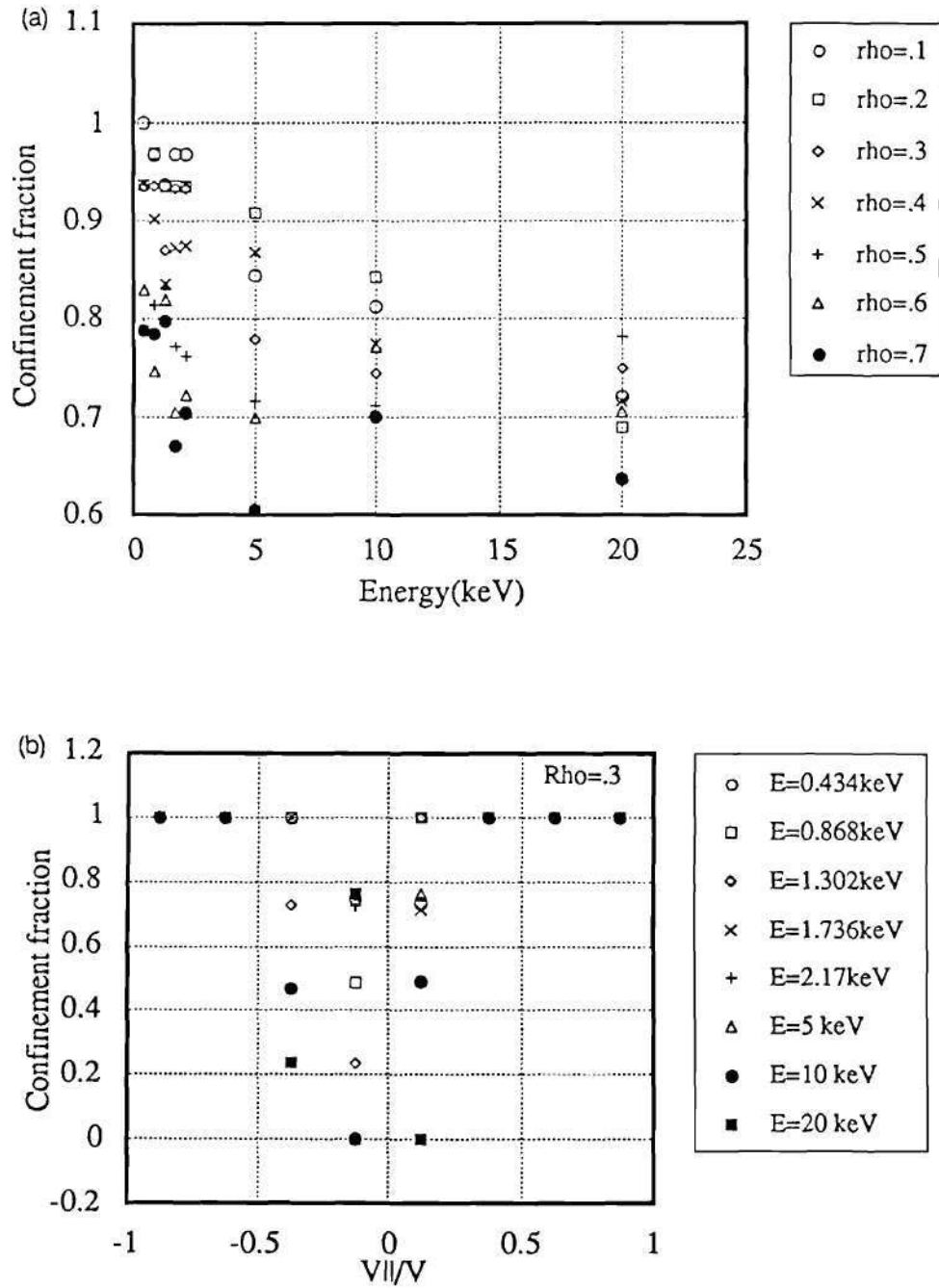


Figure 5.15: The Confinement Fraction of the ATF Standard Configuration as a Function of (a) Particle Energy and (b) Pitch Angle in Velocity Space

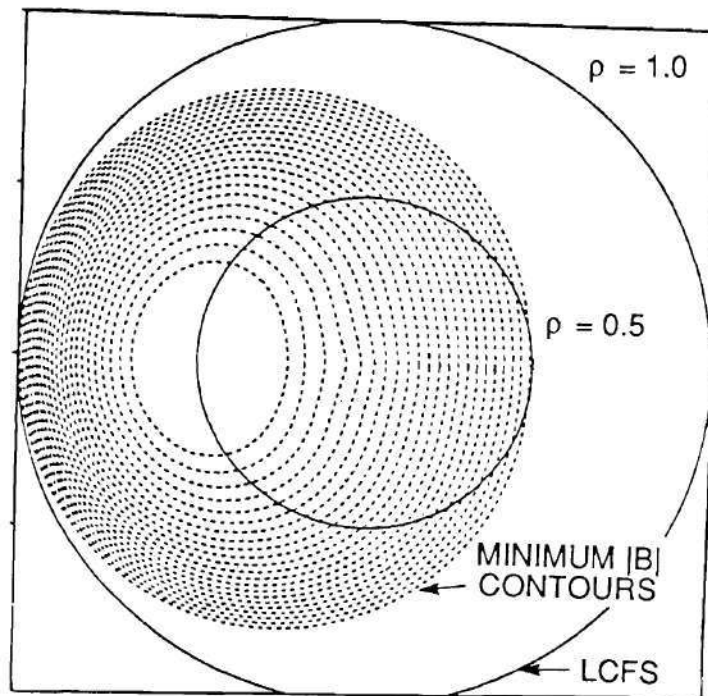


Figure 5.16: The Minimum-B Surface Plot in Boozer Coordinates for the Standard ATF Configuration

where it can be seen that the closed contour region occurs mainly inside the plasma magnetic axis. The location of the minimum-B contours in ATF can be varied by changing the mid-vertical field coil current. It was found [14] theoretically that as the area of the closed minimum-B contours increases, particle confinement is better. Particle confinement enhancement by controlling the configuration of the minimum- $|B|$ contours has been proposed for helical devices [14]. This enhancement occurs because the drift orbits of energetic trapped particles approximately follow the min-B contour according to both analytic (J-invariant) and numerical (guiding-center-orbit-following code) calculations [15]. If this is the case, particles heated in the inside region (see Fig. 5.16) where most of the minimum-B contours are closed, would be confined better.

Exact inclusion of RF effects in the orbit following code would have been quite difficult, even though the RF-induced electric fields can be calculated everywhere.

Exact calculation of particle orbits with RF would require the solution of the full equation of motion of the particle including the RF-particle interaction term which would be a function of gyrophase of both the particle and wave. This was attempted by other researchers for a mirror-based configuration and demonstrated a stochastic behavior of the wave-particle interactions [16,17,18]. Since such work would have taken significantly more manpower and time than was available, a simplified RF heating model was used to show how RF affects the particle orbit in the collisionless regime³. In ATF, fast-ion generation by ICRH could be treated as a collisionless phenomenon because the 90-degree scattering time was much longer than the loss time due to charge-exchange or particle drift orbits, as will be demonstrated in the following section. Therefore confinement of RF-created minority fast-ions could be studied by simply using an orbit following code without including collisional effects. For the simple model, it was assumed that every particle passing through the local resonance layer was heated by the RF wave electric field (which was pre-determined from the RF heating code) and the RF amplitude was assumed constant at the resonance layer everywhere in the torus. Phase mixing effects were ignored, and the energy and pitch were recalculated whenever a particle passed through the resonance layer. *The particle orbit was then followed with those new values.* For the RF perpendicular (to the magnetic field) kick to the particle energy, Eq. (2.111) was used. An example of this calculation is shown in Figs. 5.17 through 5.19. Even though this was not a precise simulation of RF effects on particle orbits, several interesting points can be seen. First, a trapped particle absorbs more energy from the RF wave than a passing particle. Particles are heated to high energies in a relatively short time, especially if the particle is helically trapped. The RF can also

³The author is grateful to R. H. Fowler for providing the orbit following code and to C. L. Hedrick, M. D. Carter and E. F. Jaeger for enlightening discussions about simulation of RF effects on particle orbits.

change the type of the particle orbit as the particle is heated. This can be seen in Fig. 5.17, where the passing particle orbit was not changed by the RF, while in Fig. 5.18, the passing particle orbit was changed to a banana particle orbit. For a helically trapped particle, as shown in the Fig. 5.19, resonance localization was evident, indicating that the turning point was localized towards the resonance layer as it was kicked by the RF. Actually these cases shows the maximum energy that a particle could obtain since the phase of the gyromotion of the particle was assumed in-phase with the wave electric field as the particle passed through the resonance layer.

In a tokamak, ICRH produces energetic, banana trapped ions whose banana tips lie near the resonance layer [19,20]. The banana width grows as they are accelerated to higher energies and are lost via charge exchange, or collisional scattering out of the resonant orbit. However, it is possible for the electron collisional drag to balance the acceleration by transferring energy from the fast ions to electrons. In stellarators, ICRH is assumed to produce helically trapped particles. The number of banana trapped particles is small in stellarators and the ripple in the magnetic field is larger than in tokamaks. Particles heated at major radii in the outer region beyond the plasma center ($R \geq R_0$) where the mirror ratio is large, are likely to be lost due to large $\nabla|B|$ orbit drifts. However, particles heated on the inside can follow a closed minimum- $|B|$ contour and be confined longer. Deeply helically trapped particles can absorb large amounts of RF energy since they stay longer in the resonance layer. In the central region of a stellarator, the number of helically trapped particles is so small that the contribution to heating from trapped ions is small. In the edge at large major radii ($R \geq R_0$, as before) a large fraction of the ions are trapped and easily absorb RF energy, but due to the large loss cone in this region these ions are likely to be lost before transferring energy to other particles. Therefore in ATF, for good fast ion confinement, RF power deposition should occur in the region where there are

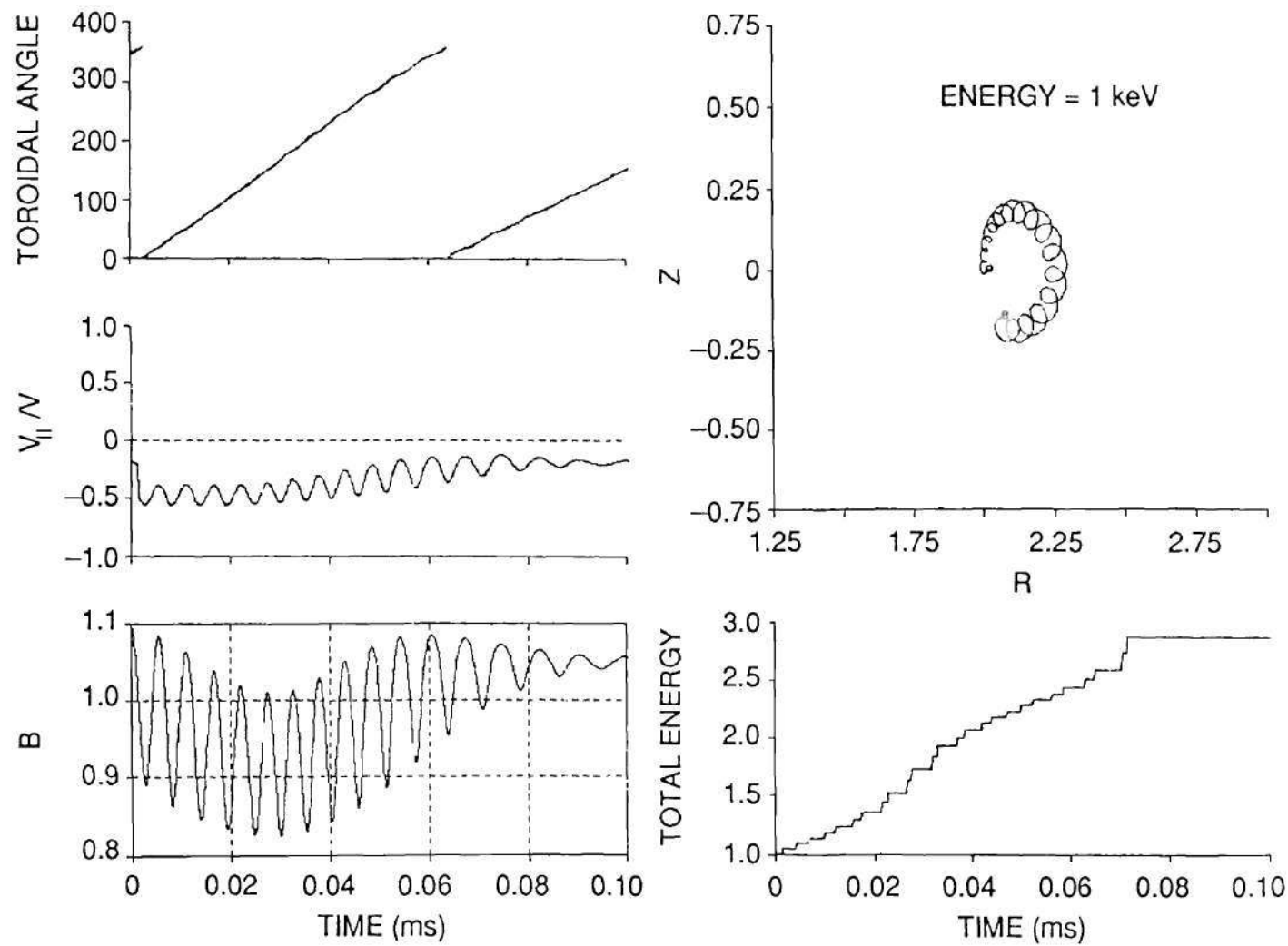


Figure 5.17: Passing Particle Orbit with RF Effects Showing Unchanged Particle Orbit

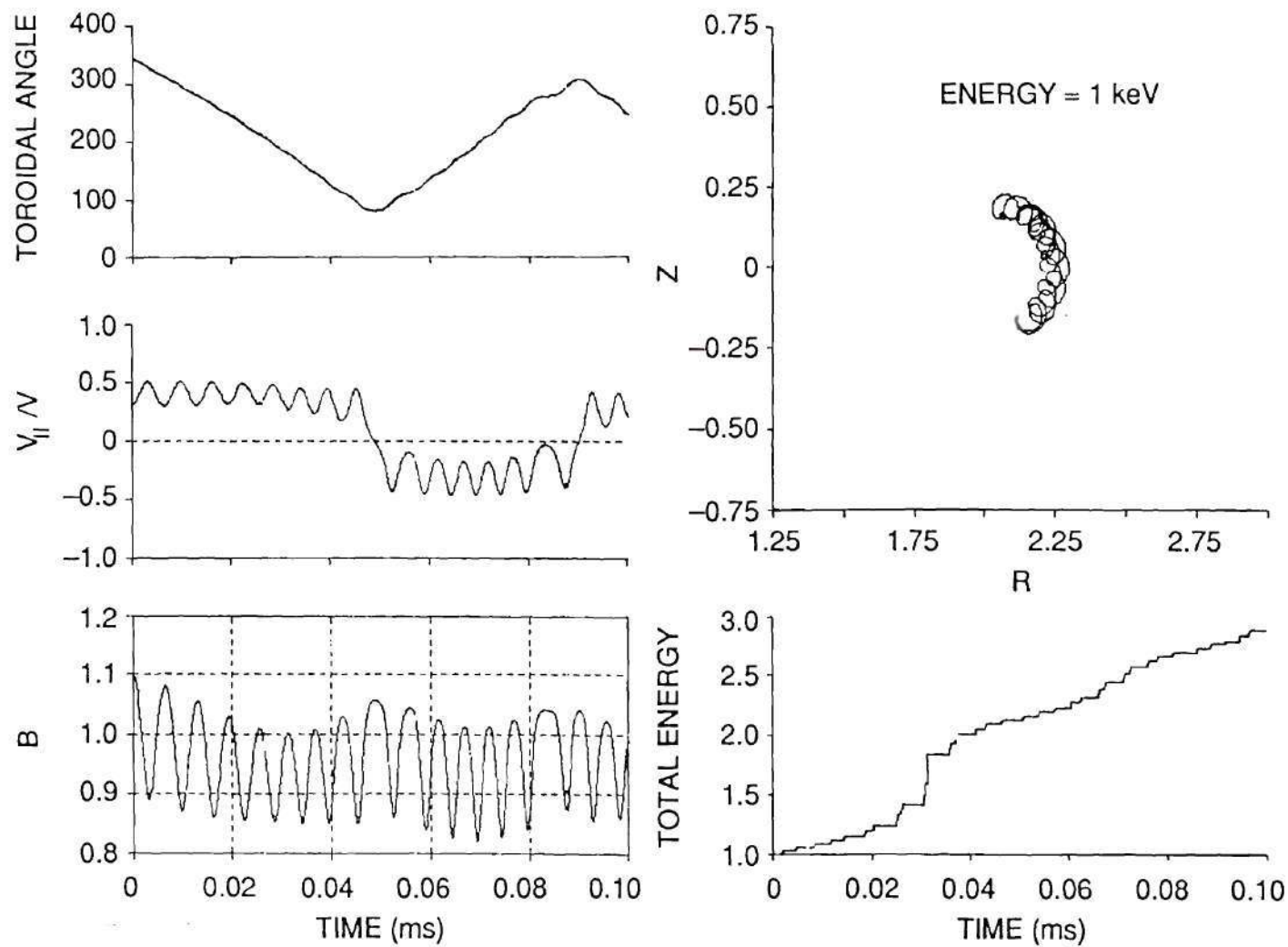


Figure 5.18: Passing Particle Orbit with RF Effects Showing Changed Particle Orbit to Banana Trapped Particle

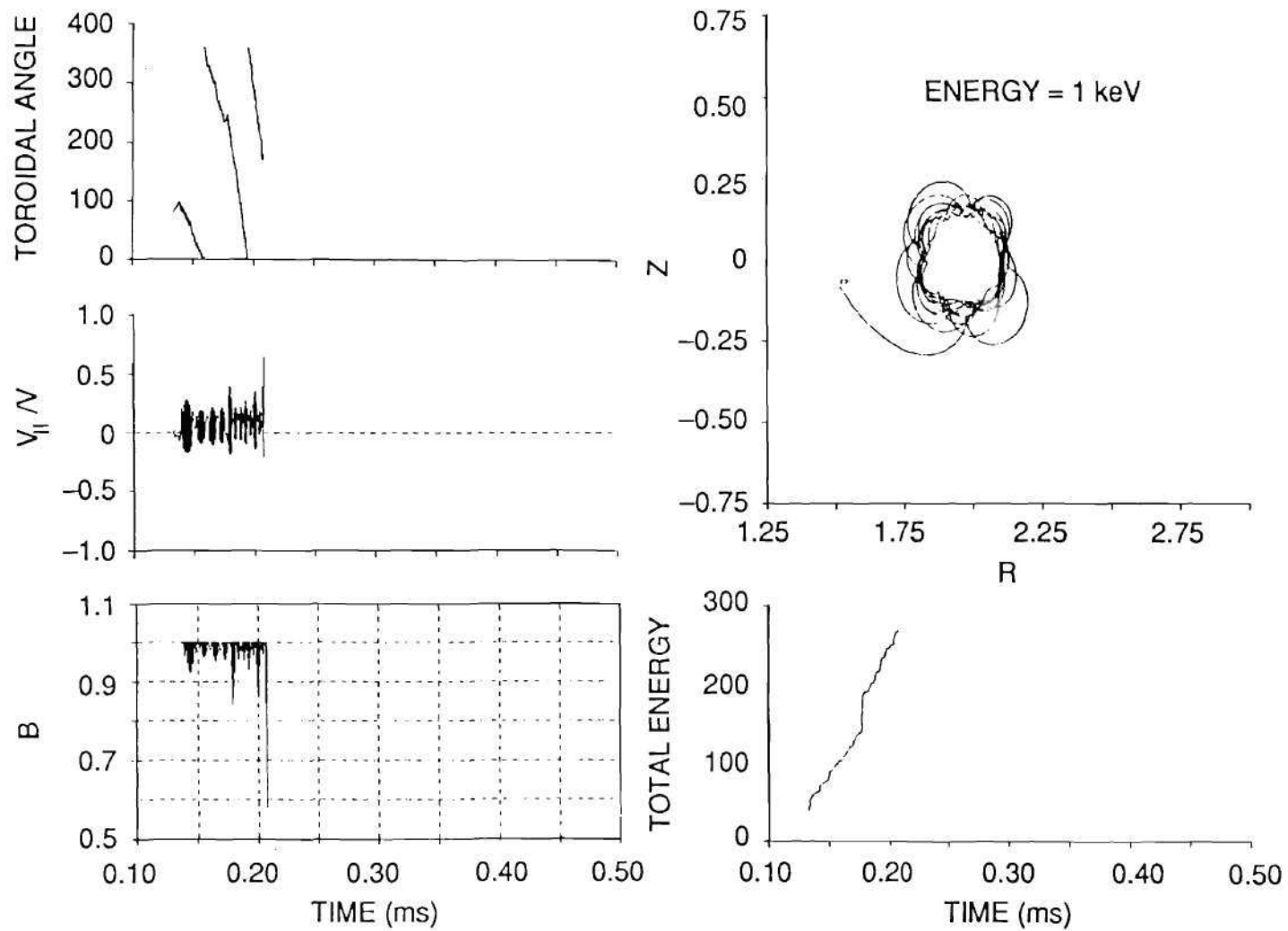


Figure 5.19: Helically Trapped Particle Orbit with RF Effects

closed minimum- $|B|$ contours and a larger number of untrapped particles.

In the ATF ICRH experiments, fast ion tails were observed during D(H) minority heating, while no energy transfer to the bulk plasma was measured. If unconfined fast-ion loss was dominant, high energy particles generated by ICRF would have been lost before they transferred their energy to the bulk plasma via collisions. With the knowledge of the power deposition profile in the low density ATF plasma discussed in the preceding section, it can be seen that plasma edge (now we use plasma edge, as opposed to edge plasma, to mean that portion of the plasma in the confined region just inside the last closed flux surface) heating led to enhanced fast ion loss because of the unconfined orbits in this region.

With the preceeding background of the response of the ATF plasma and magnetic geometry to the RF-generated fast ions, the NPA data measured during ICRH can now be analyzed. It was shown in the previous chapter that the NPA measured a large proton tail (up to 50 keV) during most of the D(H) experiments. In other words, there were particles accelerated to 50 keV energy, and confined at least for the charge exchange time scale. The most ambiguous parameter here is again τ_{CX} which is inversely proportional to the neutral density. In most of the ICRH experiments, a gas-puff valve located at the opposite port (IN-1) to the NPA aperture (TN-1) was used for gas feed to the experiment. Two separate experiments with this valve and with a different valve showed significant differences in the energetic tail energies as shown in Fig. 4.28 (remember that the y-axis has a log scale). When a different gas puff valve (located toroidally far away) was used it is probable that the particles heated in the outer region of the torus experienced direct orbit loss (as discussed above) before they were lost to charge exchange. Therefore the small tail observed was formed by particles confined for a significant time whose RF energy gain was balanced by electron drag. On the other hand, when the valve was used, τ_{CX} for the edge particles was small and was comparable to the orbit confinement

time of the edge heated particles, which was less than 2 ms. In this case, edge heated particles contributed significantly to the measured NPA signal.

The frequency scan in the D(H) regime at 0.95 T showed large differences in tail energy as a function of frequency, as shown in Chapter IV. One experiment was done at 16 MHz which placed the resonance layer inside of the magnetic axis, and another experiment was done at 12.8 MHz which placed the resonance layer farther outside, past the plasma magnetic axis. Here, a much larger tail was generated for the 12.8 MHz case. This caused a larger impurity influx as demonstrated in Fig. 4.24. Loading was higher in the higher frequency case. No evidence of bulk heating was observed in either case. The reason for a larger tail in the low frequency case is presumed to be the higher power density. A 2-D RF heating code simulation showed that toroidal damping at the low frequency was very strong, while it was very weak at the high frequency, which increased the deposited power density at the low frequency by about ten times. This increase was large enough to account for the measured loading discrepancy. The reason for higher loading at the higher frequency is probably just the already observed frequency dependence.

The NPA horizontal scan data for each of three different frequencies showed considerable change as the frequency changed. This was shown in Fig. 4.26. Resonance localization and banana-trapped particle orbits [6,20] which appear in tokamak geometry could not be used to explain these data. The primary reason for this is that there are not many banana trapped particles in the stellarator geometry. These banana trapped particles were used to explain the NPA spectra for the tokamak case. When the same analytic calculation was performed for the ATF⁴, it was found that the calculated peaks of the distribution at 14.4 MHz and 16 MHz should be different,

⁴M. R. Wade and the author did this calculation. The author is grateful to C. L. Hedrick for enlightening discussions about this calculation

but the measurements looked the same, as shown in Fig. 4.26. The effect of absorbed RF power on the particle orbits (helically trapped particles) in stellarator geometry must be considered to resolve this discrepancy.

Even without theoretical analysis of the orbits, simple consideration of the data provides some insight. Figure 4.26 shows that the minority fast ion tails were only present for certain ranges of the horizontal and vertical angle of the NPA to the magnetic field (recall that the NPA could be scanned in both vertical and horizontal angles). For this range of analyzer angles, the NPA could detect only particles which had small pitch ($v_{\perp} \gg v_{\parallel}$). Comparing the NPA data taken for 14.4 MHz RF injection with and without opening the gas-feed valve close to the analyzer, the scanning spectrum of flux vs. energy vs. angle looked similar for both cases, except that the amplitude was different. This means that edge heated particles (case for which the gas-feed valve close to the analyzer was open) and centrally heated particles (case for which a different gas-feed valve, toroidally far from the NPA, was open) contributed in the same way to the analyzer signal. Since toroidal damping was very weak, the effect of locally heated particles in the vicinity of the NPA port could have been dominant, especially for edge heated particles. With this thought in mind, for the 12.8 MHz case, at the perpendicular analyzer angle, in which the resonance layer was isolated near the outside and inside plasma surface (Fig. 5.20), where $n_{neutral}$ was high, locally trapped particles were likely to be charge-exchanged immediately, which would have increase the NPA measured signal at this angle (90-degree angle), as shown in Fig. 4.26(b).

In summary of the Fast Ion Studies section, an analytic estimation of the fast-ion loss time scale showed that in the plasma edge region the fast ion loss time and the fast ion charge exchange time were comparable to each other, but much faster than the time to transfer the fast ion energy to the background electrons or ions. In the central region, however, the energy transfer time was less than or equal

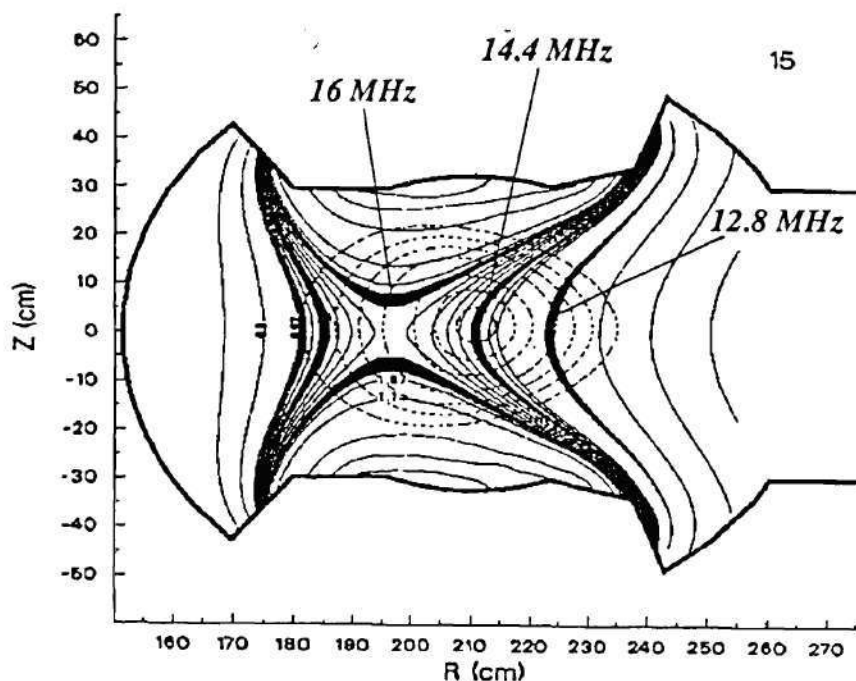


Figure 5.20: Fundamental Resonance Layer at 12.8 MHz with 0.95 T

to the charge exchange time, but certainly less than the time for fast-ions to be lost due to poorly confined orbits (i.e., the central fast-ion orbits were well confined). The particle orbits in the plasma edge region were in the loss cone according to the orbit studies, therefore plasma edge heated particles (either trapped or untrapped) were subject to rapid loss. Centrally heated particles were well confined (effect of the closed minimum-B contours). The effect of the RF on particle orbits was studied by using an orbit-following code with a simple RF model. This showed rather dramatic effects on the trapped particles. Edge heated trapped particles were rapidly lost due to unconfined drift orbits. The previous power deposition studies and these orbit studies mean that the RF power was deposited in the plasma edge, created fast ions, and was rapidly lost because of the loss cones in the plasma edge.

Power Balance Calculations

A very simple calculation of the RF power balance is presented below. The errors in this calculation were estimated (see below) and show that it is a very crude model. However, it remains relevant since the channels for RF power flow in ATF were so few, that the errors are smaller than the estimated power flow to each channel. In the cases that have been examined so far, the dominant loss channel was ohmic loss to the antenna structure as indicated by the low antenna loading. Over half of the input RF power was lost through this channel. The dominant loss channel for propagating power was demonstrated by the simulations discussed above to be fast ion loss and/or charge exchange loss. The NPA data were used as a tool to estimate this power loss, as discussed further below.

First, a simple analysis of the RF power balance is given to obtain some qualitative idea of where the RF power went. A simple expression for the RF power balance in ATF during ICRH is given by:

$$P_{\text{RF in}} = P_{\text{ohmic}} + P_{\text{edge}} + P_{\text{fast ion}}, \quad (5.13)$$

where P_{ohmic} is the power loss to the antenna structures, P_{edge} is the power coupled directly to the edge plasma (unconfined plasma outside the last closed flux surface) and $P_{\text{fast ion}}$ is the power absorbed by fast minority ions. The $P_{\text{fast ion}}$ power was assumed to be lost before transferring energy to the bulk plasma.

From loading measurements, P_{ohmic} was estimated by comparing the plasma loading with vacuum loading. Usually the ratio $P_{\text{ohmic}}/P_{\text{RF in}}$ was $\geq 50\%$ for low density plasma cases. For shots from 9004 to 9018, typical plasma loading was 0.15Ω which was slightly less than the vacuum loading, 0.18Ω (total loading on plasma shots was assumed to be equal to the vacuum loading plus the plasma loading, so the plasma loading was found by subtracting the vacuum loading from the total measured

loading). Therefore P_{ohmic} was ~ 110 kW out of ~ 200 kW RF power input. The Langmuir probe data and simple analytic formula given in Eq. (5.3) were used to estimate P_{edge} . As shown in the previous section, assuming most of the power was deposited in front of the antenna poloidally, $P_{\text{edge}} \sim 21$ kW. The term $P_{\text{fast ion}}$ was obtained from the equation:

$$P_{\text{fast ion}} = \frac{n_{\text{fast ion}} \bar{T}_{\text{fast ion}}}{\tau_{\text{fast ion}}}, \quad (5.14)$$

where $n_{\text{fast ion}}$ was the fast ion density which absorbed RF power, $\bar{T}_{\text{fast ion}}$ was the average energy of the fast ions and $\tau_{\text{fast ion}}$ was the energy confinement time of the fast ions. Since edge-heated fast ions were assumed to be lost immediately via direct orbit loss, and (as demonstrated previously in the simulations), τ_{CX} is assumed to be comparable to $\tau_{\text{fast ion}}$, $\bar{T}_{\text{fast ion}}$ can be calculated from the measured NPA ion distribution data since the measured NPA signal mostly consisted of contributions from orbit-lost fast ions. Here again the probability of charge exchange interaction is assumed to be the same for all ranges of the energy of lost fast ions as was done for Eq. (5.9). For this case $\bar{T}_{\text{fast ion}}$ was calculated from the data as about 1.5 keV (shot 9004-9018). Recalling $\tau_{\text{fast ion}} \sim \tau_{CX} \sim \tau_{\text{loss}}$, $\tau_{\text{fast ion}} \sim 2$ ms as calculated in Eq. (5.9), this looks reasonable. The density $n_{\text{fast ion}}$ was estimated from the n_{el} trace which showed an initial drop as shown in Fig. 4.6 which was assumed to be a result of fast ion loss. In this case, $n_{\text{fast ion}} \sim 6.7 \times 10^{11} \text{ cm}^{-3}$. Then $P_{\text{fast ion}}$ becomes 81 kW. From this simple analysis, the power ratios were calculated as $P_{\text{ohmic}} : P_{\text{edge}} : P_{\text{fast ion}} \simeq 5 : 1 : 4$.

Possible errors in this calculation are estimated by considering missing RF energy flow channels such as direct deuterium heating and by examining the validity of assumptions used for the above calculation. The fraction of direct deuterium absorption to the minority absorption was estimated in the D(H) regime as [21]

$$\frac{P_D}{P_H} = \frac{\beta_D n_D}{n_H}, \quad (5.15)$$

where $\beta_D = 2\mu_0 n_D T_D / B^2$ was the deuterium beta. From the data in Table 4.1, $\beta_D = 0.05\%$. For minority concentration of 5%, the fraction of direct deuterium absorption at the center is only 1% of the minority absorption. And toward the edge, this ratio is reduced more. Therefore P_D could be neglected as far as Eq. (5.15) is valid. Mode-conversion is another channel for RF power flow, however, as mentioned in Chapter II, for a low-field-side launch and low minority concentration (less than 10%) the fraction of mode converted wave should be negligible. But this fraction depends on the plasma conditions, too. Therefore more analysis is needed with accurate modeling to estimate this fraction correctly. However, the fraction of the RF power mode-converted is both small compared to the ECH power and ineffective at electron heating because it is in the edge. The assumption that all the energy absorbed by the minority ions was lost in $\tau_{CX} \sim 2$ ms may not be accurate. Since no evidence of bulk heating was observed, the possibility of power transfer to the background plasma is doubtful. However, it is also unknown whether the effects of 10 or 20 kW of RF power absorbed by electrons in comparison to 350 kW of ECH would be measurable. If $\tau_{\text{fast ion}} \ll \tau_{CX}$, the NPA would not see any directly-lost fast ions. As seen in Fig. 4.28, the case without using the inside gas-feed valve belongs to this category. Therefore for higher amplitude ion tails than this case, $\tau_{\text{fast ion}}$ must be closer to τ_{CX} . This remains to be seen in the following Fokker-Planck analysis (see below). More uncertainty came from the calculation of P_{edge} (power directly absorbed by the unconfined plasma outside the last closed flux surface in the antenna vicinity). Only the radial profile at a fixed toroidal and poloidal locations was used, which implies that the range of error could be very large. It was assumed that P_{edge} was deposited only in front of the antenna which covered one sixth of the total area of the poloidal edge region at a fixed toroidal location (antenna location). Therefore from Eq. (5.3) P_{edge} ranged from 21 kW to 126 kW out of 200 kW total RF power. Since the loading data were believed to be quite accurate, for the above case in which

the plasma loading was about the same as the vacuum loading, 100 kW would be the maximum power attainable for P_{edge} or $P_{\text{fast ion}}$. Due to a larger range of error and difficulties of modeling, direct determination of an accurate quantity for P_{edge} was almost impossible. Therefore after more precise estimation of $P_{\text{fast ion}}$ by analytic modeling and Fokker-Planck numerical calculations, the valid range of P_{edge} was determined.

Stix [19] performed analytic calculations to find the ion velocity distribution function during RF heating. He expressed the distribution in terms of an effective temperature given by Eq. (2.126). It seems irrelevant to compare Eq. (2.126) with the measured NPA data because Eq. (2.126) was derived with the Coulomb collision term as a single, dominant energy loss mechanism. For cases in ATF where drift orbit loss of fast ions constituted the major loss channel for the fast ion energy, comparison of the NPA data with Stix's equation would be unreasonable even if the drift loss term was included because the basic assumption of Coulomb collisional dominance would still be violated since the drift loss time is shorter than the electron drag time. All of the shots for which the gas-feed valve IN-1 (opposite the NPA) was used fall into this category. Fortunately, there were NPA data measured on shots when this valve was not used. These shots showed obviously smaller (less energetic) ion tails. In this case, since $\tau_{CX} \gg \tau_{\text{loss}}$, the contribution of drift loss particles was minimum (they were lost to the walls rather than charge-exchanging into the NPA) and the measured NPA ion distributions are believed to represent a quasi-steady-state collision dominated distribution in the plasma center.

For this case the charge exchange loss term and direct orbit loss term were included in the calculation. Following Stix, the kinetic equation for the ion velocity distribution function including these terms was found to be:

$$\frac{\partial f}{\partial t} = -\frac{f}{\tau_{CX}} - \frac{f}{\tau_{\text{loss}}} + C(f) + Q(F), \quad (5.16)$$

where the first term in the RHS is the charge exchange loss term, the second term is the unconfined orbit loss term and f is a function of $v_{\parallel}, v_{\perp}, \theta$ and t . Here, τ_{CX} and τ_{loss} are functions of temperature. The operators $C(f)$ and $Q(f)$ are the collision term and the RF contribution to the ion kinetics, respectively. The expressions for $C(f)$ and $Q(f)$ which Stix used are given by Eq. (2.124) and Eq. (2.123), respectively. Although τ_{CX} is a function of v , it seems to be reasonable to set it to a constant at any fixed radial position since the charge exchange cross section is a very slow function of energy between a few keV and 100 keV. Note that Eq. (2.126) is the analytic solution for the case where $\tau_{CX}, \tau_{loss} \rightarrow \infty$.

To solve this equation for the ATF ICRH experiments, the Fokker-Planck code, *RFTRANS*⁵ was used with a simple ATF plasma model. A description of the code *RFTRANS* is given in Ref. [22]. This code solves a 3-D, steady-state Fokker-Planck equation. The two velocity-space dimensions are speed v and pitch angle θ , with a real-space parameter, r . In Eq. (5.16), there are two loss terms, but in this version of the code, only the drift loss term was included. Since all the loss rates can be controlled by input parameters, ν_{CX} was implicitly included in ν_{loss} . To compare the calculations and NPA data for the ion distribution, the following assumptions must be made. First, since the calculation was done for a steady-state solution, the NPA data must be assumed to represent a quasi-steady-state. The NPA data at about 50 ms after the RF pulse began were taken as a steady-state distribution. Second, τ_{CX} must be much larger than τ_{loss} , otherwise the signal in the NPA is no longer representative of the confined particles but rather the lost ones, while f in Eq. (5.16) is the confined particle distribution function. Only for this case can an ion distribution measured by NPA be compared to the simulated ion distribution in

⁵The author is grateful to M. D. Carter for allowing him to use this code and for enlightening discussions about the results.

the loss cone, because the code only simulates the remaining particles, not the lost particles.

Even though the original code has a real space transport term, it was ignored in these calculations and the kinetic equation used for the steady-state condition was,

$$-\nu f(v, \theta) + S + C(f(v, \theta)) + Q(f(v, \theta)) = 0, \quad (5.17)$$

where ν is the loss rate modeled as discussed below, and S is a constant source rate (to compensate for drift orbit losses) which was needed for a steady state solution. Assuming that passing particles are diffusive and well-confined and only trapped particles are convective, the drift velocity consisting of the curvature and ∇B drift is calculated as

$$v_D \simeq \langle v_{R_c} + v_{\nabla B} \rangle \simeq \frac{v^2}{2R_c\Omega}, \quad (5.18)$$

where R_c is the radius of the curvature and Ω is the cyclotron frequency. The loss rate in this case becomes

$$\nu \simeq \frac{v_D}{a} \simeq \frac{v^2}{2aR_c\Omega}, \quad (5.19)$$

where a is the loss radius (which was taken to be the minor radius). This loss rate was compared to the 90° collision rate in order to compensate for any scattering back into the confined regime. The fast ion on slow ion and slow ion on electron 90° collision rates are given [10] by:

$$\nu_{\perp, fast}^{i/i'} \sim 1.8 \times 10^{-13} \frac{n_{i'}(zz')^2 \Lambda_{ii'}}{\mu^{1/2} \epsilon^{3/2}}, \quad (5.20)$$

$$\nu_{\perp, slow}^{i/e} \sim 3.2 \times 10^{-15} \frac{n_e z^2 \Lambda_{ie}}{\mu \epsilon T^{1/2}}, \quad (5.21)$$

where $\mu = m_i/m_p$, particle energy ϵ and temperature T are both in eV and Λ is the coulomb logarithm. The electron drag term, $C(f)$ is expressed as

$$C(f) = -\frac{1}{v^2} \frac{\partial}{\partial v} v^2 \left(D_{vv}^{cc} \frac{\partial f}{\partial v} + D_{v\theta}^{cc} \frac{1}{v} \frac{\partial f}{\partial \theta} - F_v^{cc} f \right) - \frac{1}{v \sin \theta} \frac{\partial}{\partial \theta} \sin \theta \left(D_{\theta v}^{cc} \frac{\partial f}{\partial v} + D_{\theta\theta}^{cc} \frac{1}{v} \frac{\partial f}{\partial \theta} - F_\theta^{cc} f \right), \quad (5.22)$$

where all coulomb collision coefficients are summed over plasma species. The simple RF operator given by Stix [19] was used,

$$Q(f) = \frac{P_{rf}}{2m_i n_i} \frac{1}{v_{\perp}} \frac{\partial}{\partial v_{\perp}} v_{\perp} \frac{\partial f}{\partial v_{\perp}}, \quad (5.23)$$

where the J_0 term in the original expression was approximated to be 1 and P_{rf} is the flux surface averaged power density.

To keep the model simple, the plasma region was divided into two separate regions (two-point model⁶). One region represents the central column of the plasma where fast ion confinement was relatively good, while the other region represents the plasma edge where the fast ions produced by the RF drifted out quickly, as discussed in the previous section. In this model there was no coupling between these two regions ("points"). The RF power deposited in each region, P_{rf} was estimated from the 2-D RF heating code.

To evaluate the validity of the model, a qualitative comparison to the NPA data was attempted. Table 5.2 shows the parameters used for calculations reflecting typical D(H) heating experiments. Based on the 2-D RF heating code results, it was assumed that the RF power was deposited uniformly in the toroidal direction and most of the power was absorbed in the outer edge region around the resonance layer.

There were several controllable free parameters. One was the RF power density which was much higher than for a uniform distribution model. Since most of the RF power was deposited along the resonance layer, a weighting factor was used to multiply the value for the uniform distribution case. In Table 5.2, P_{rf} is described as a constant multiplied by 0.027 kW/cm³, which was the power density with 100 kW of RF power uniformly distributed throughout the ATF plasma volume. The other

⁶This model was suggested by J. A. Rome.

Table 5.2: Input Parameters for Fokker-Planck Model of the ATF ICRH Experiment
Minority Fast Ion Distribution

$T_e(1)$	eV	830
$T_e(2)$	eV	600
$T_D(1)$	eV	200
$T_D(2)$	eV	150
$T_H(1)$	eV	200
$T_H(2)$	eV	150
$n_e(1)$	cm^{-3}	6.6×10^{12}
$n_e(2)$	cm^{-3}	5.4×10^{12}
$n_D(1)$	cm^{-3}	6.3×10^{12}
$n_D(2)$	cm^{-3}	5.1×10^{12}
$n_H(1)$	cm^{-3}	3.1×10^{12}
$n_H(2)$	cm^{-3}	2.6×10^{12}
$P_{rf}(1)$	$\times 0.027 \text{ kW}/\text{cm}^3$	0.17
$P_{rf}(2)$	$\times 0.027 \text{ kW}/\text{cm}^3$	2.0
R	m	2.1
\bar{a}	m	0.3
$R_m(1)$		1.05
$R_m(2)$		1.17

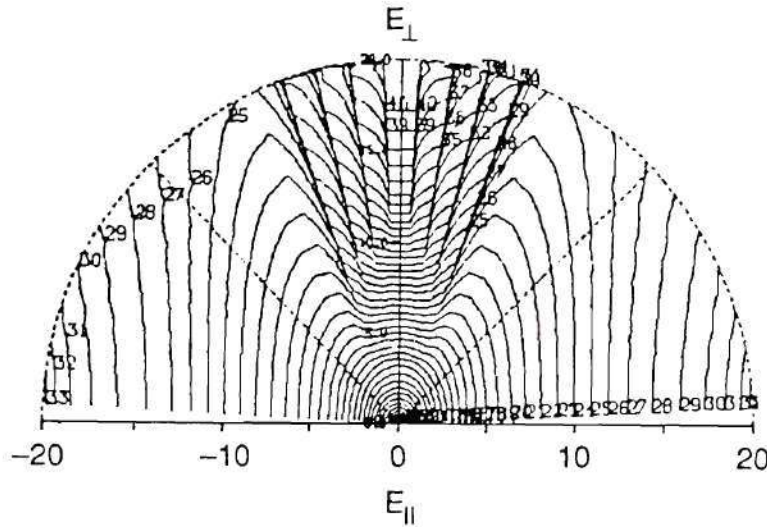


Figure 5.21: The Loss Cone Region in the Ion Velocity Distribution for $R_m=1.22$

important free parameter was the loss cone definition. Due to the lack of systematic studies of this topic for ATF, this adds another uncertainty to the results. The mirror ratio defined as $1/R_m = \sin^2 \theta$, was used to determine the loss cone angle, θ , from the $v_{\perp} = 0$ axis. For example, for $R_m = 1.22$, $\theta = 64.9^\circ$ which means that the loss cone was defined as shown in Fig. 5.21. The values $R_m=1.05$ and $R_m=1.17$ were used for the central and edge loss cone mirror ratios, corresponding to $\theta = 77.4^\circ$ and 67.6° , respectively.

The data shown in Table 5.2 show that 80 kW out of 200 kW was absorbed by the plasma and 80% of the absorbed power was absorbed in the outer edge region where the fast ions were only briefly confined. The rest of the power was absorbed in the central region where the fast ions were confined longer. The ion distribution calculated for this data agreed well with the measured NPA ion distribution and gave a reasonable number for the confinement time in each region.

The numerical calculations indicated that a moderate energy ion tail (up to 10 keV) was formed in the edge region as shown in Fig. 5.22 and Fig. 5.23. This value is comparable to the measured ion tail shown in Fig. 4.28 for cases without using the

IN-1 gas-feed valve. The calculated power transfer to the electrons was about 80 % for the central region and 10 % for the edge region. In the edge region it was calculated that 90 % of the power was lost through the drift orbit loss channel. The fast ion energy confinement times were calculated to be 32 ms and 1.7 ms and the thermal ion confinement times were 160 msec and 5 msec for the central and edge region, respectively. Even though there were free parameters controlled to match the calculation with the experimental data (namely RF power density and loss-cone angle), reasonable agreement was attained qualitatively in the ion tail formation between measured and calculated values. The calculated fast ion confinement time in the edge region is also in good agreement with the original experimental calculation, $\tau_{\text{fast ion}} \sim \tau_{CX} \sim 2$ ms. There was no possible way to experimentally confirm the fast-ion confinement times, due to a lack of knowledge of the neutral density profile, absolute calibration of the NPA, and absolute measurement of the creation rate of fast ions.

More precise power balance calculations would require better modeling of the fast ion orbits and loss cone distribution as well as a multi-region model with precise RF power density information for each region.

To summarize this power balance section, although a precise power balance analysis was not possible, the estimated ratio of the power loss channels from a simple calculation is $P_{\text{ohmic}} : P_{\text{edge}} : P_{\text{fast ion}} \simeq 5 : 1 : 4$. It is believed, considering all sources of error, that these calculations are correct within a factor of two. The largest uncertainty is the ratio of P_{edge} to $P_{\text{fast ion}}$. P_{ohmic} is believed accurate to the order of 5%. The end result of the power balance calculation is that about 100 kW out of 200 kW of the RF power went to the antenna and metal structure of ATF, 21 kW went to direct heating of the unconfined edge plasma, about 70 kW went to edge fast-ion orbit loss, and less than 10 kW out of the 200 kW was actually absorbed in the plasma center, and transferred to the thermalized plasma.

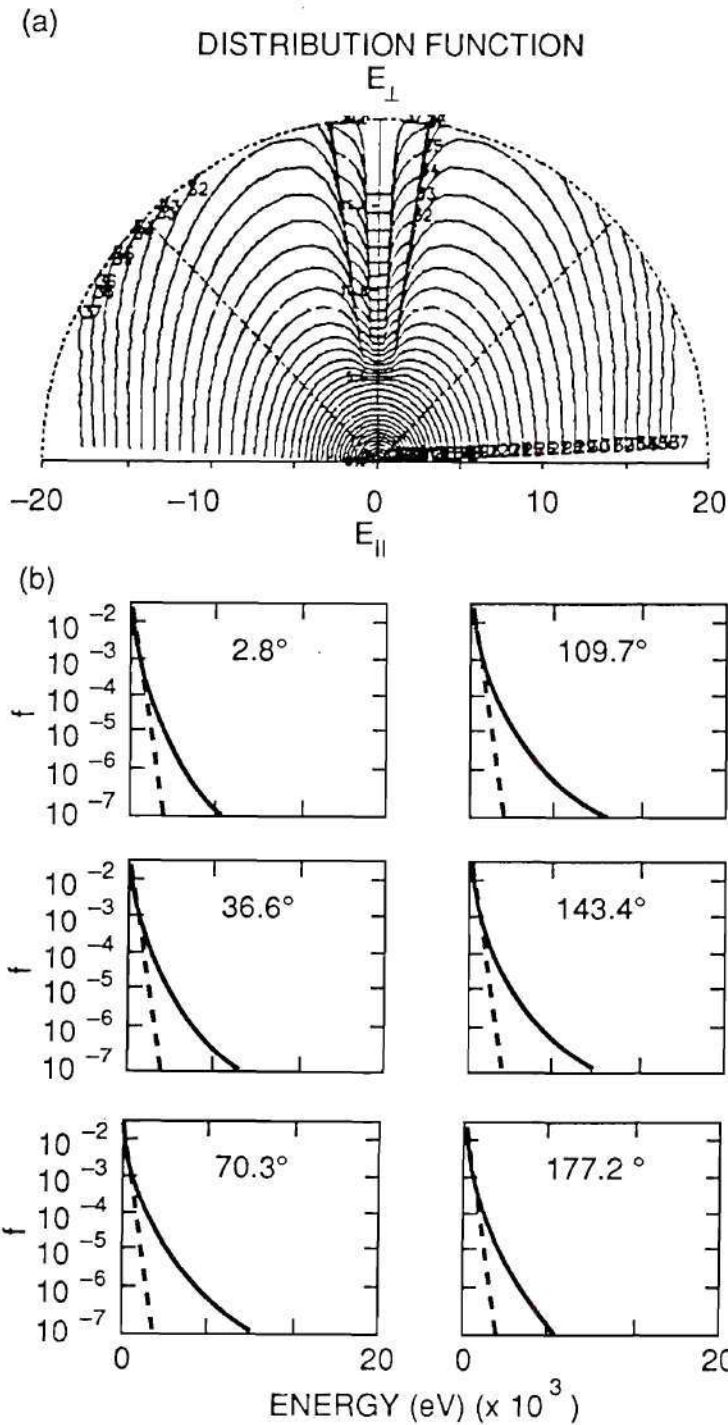


Figure 5.22: Results of the *RFTRANS* Fokker-Planck Calculation for ATF Low Density ICRH Case for Region 1 (Central Region): (a) Ion Distribution in Velocity Space (b) Ion Flux vs Energy at Different Pitch Angles in Velocity Space.

REFERENCES

- [1] Cattanei, G., et al., "ICRF Heating in the WVII-A Stellarator," IPP 2/290, Max-Planck Institut für Plasma Physik (1987).
- [2] Wan, A. S., "Ion and Electron Parameters in the Alcator C Tokamak Scrape-off Region," Ph.D thesis, MIT (1986).
- [3] Fukuyama, A., et al., "Propagation and Absorption of ICRF Waves in Helical Plasmas," *Nucl. Fusion*, **26**, 151 (1986).
- [4] Takahashi, I., "ICRF Heating in Tokamaks," Report PPPL-1374, Plasma Physics Laboratory, Princeton University, Princeton (1977).
- [5] Labombard, B., and Lipschultz, B., "Poloidal Asymmetries in the Scarape-Off Layer Plasma of the Alcator C Tokamak," M.I.T. Plasma Fusion Center Report PFC/JA-85-43 (1986).
- [6] Hammet, G. W., "Fast Ion Studies of Ion Cyclotron Heating in the PLT Tokamak," Ph.D Thesis, Princeton University (1986).
- [7] Chen, F. F., *Introduction to Plasma Physics and Controlled Fusion*, (Plenum Press, New York, 1984).
- [8] Neilson, G. H., Ph.D Thesis, University of Tennessee, and ORNL/TM-7333, Oak Ridge National Laboratory Technical Memorandum, December, 1980.
- [9] Nakashima, Y., et al., "Neutral Density Measurements by Charge Exchange Analysis on the Heliotron E Plasma," *J. Phys. Soc. Japan*, **52**, 4166 (1983).

- [10] Book, D. L., NRL Plasma Formulary, NRL Publication 0084-4040, Naval Research Laboratory (1987).
- [11] Boozer, A. H., *Phys. Fluids* **24**, 1999 (1981).
- [12] Morris, R. N., "Effect of Finite Drift Orbit Size on Interpretation of Neutral Particle Analyzer Spectra," *Bull. Am. Phys. Soc.* **34**, 1948 (1989).
- [13] Shaing, K., private communication.
- [14] Carreras, B. A., et al., "Low-Aspect-Ratio Torsatron Configuration," unpublished.
- [15] Hedrick, C. L., Cary, J. R., Tolliver, J. S., "Adiabatic and Full Guiding Center Motion in 3-D Toroidal Systems," unpublished (1989).
- [16] Jaeger, F., Lichtenberg, A. J., Lieberman, M. A., "Theory of Electron Cyclotron Resonance Heating - I. Short Time and Adiabatic Effects," *Plasma Phys.*, **14**, 1073 (1972).
- [17] Howard, J. E., "Effective Time and Resonance Width in Cyclotron Resonance Heating," *Plasma Phys.*, **23**, 597 (1981).
- [18] Carter, M. D., "Nonlinear Wave-Particle Interactions at Cyclotron harmonic Frequency," Ph.D Thesis, University of Wisconsin at Madison (1985).
- [19] Stix, T., "Fast-Wave Heating of a Two-Component Plasma," *Nucl. Fusion*, **15**, 737 (1975).
- [20] Kaita, R., et al., "Fast-Ion Orbit Effects During Ion Cyclotron Range of Frequency Experiments on the Princeton Large Torus," *Nucl. Fusion* **23**, 1089 (1983).

- [21] Perkins, F. W., "Heating Tokamaks via the Ion-Cyclotron and Ion-Ion Hybrid Resonances," *Nucl. Fusion* **17**, 1197 (1977).
- [22] Carter, M. D., Jaeger, E. F., Batchelor, D. B., "Non-Linear Core Plasma Response to ICRF Heating with Transport," *Nucl. Fusion*, **29**, 2141 (1989).

CHAPTER VI

CONCLUSIONS

Summary and Conclusions

Fast wave heating experiments were performed on low-density ECH target plasmas using 100-kW and 200-kW RF transmitters. Various heating regimes were investigated in the frequency range between 9.2 MHz and 28.8 MHz at magnetic fields of 0.95 T and 1.9 T.

For low-power loading measurements with NBI-heated plasmas in the second-harmonic hydrogen resonance heating regime, it was found that loading was proportional to density, antenna-plasma gap and RF frequency in low-density ATF plasmas.

Extensive wall conditioning including induction heating, glow-discharge cleaning and Ti gettering with antenna conditioning significantly improved the RF operational performance. For the final experiments, 200 kW of RF power (not accounting for antenna loss) could be launched into the ECH-produced, low-density target plasmas without severe impurity influx, radiation emission, or disruption.

With full-power experiments, loading was measured to be fairly low mainly due to the low density and large antenna-plasma gap. The low plasma loading led to higher ohmic loss to the antenna structure — more than half of the transmitter output power. Among various heating regimes, the second harmonic hydrogen resonance

heating regime showed the highest loading, about 0.6Ω for $\bar{n}_e \simeq 6.0 \times 10^{12} \text{ cm}^{-3}$. This was mainly due to the high RF frequency used for this regime (28.8 MHz).

During D(H) heating experiments, NPA signals showed suprathermal minority ion tails up to 60 keV. However, no measureable bulk ion and/or electron heating was observed. This was demonstrated to be due to the fact that RF-produced fast ions were on unconfined orbits, such that the energy transfer time to the bulk electrons/ions was much longer than the orbit loss time scale. A large part of the reason for heating of particles on loss orbits was the wave spectrum launched by the antenna, which consisted mostly of high k_{\parallel} modes. These high k_{\parallel} modes experienced a thick evanescent layer and deposited their energy in the edge plasma region (the antenna was originally designed for higher density plasmas). A Monte-Carlo type orbit calculation illustrated that the edge plasma region was dominated by a drift orbit loss-cone.

As both wall and antenna conditions were improved, RF effects on the edge region (unconfined region of the plasma between the last closed flux surface and the vacuum vessel wall) were much reduced. Langmuir probe measurements showed that n_e and T_e were increasing during ICRH near the antenna and peaked at the current strap position. The RF probes showed that the wave was not propagating well into the confined-plasma region, as indicated by comparison with the vacuum signals (for propagating waves the signals with plasma are much reduced from the vacuum level, but for these low density plasmas the signal levels were almost identical). During the density ramp, discrete eigenmodes were observed. Even though there were not enough probes for easy mode identification, the observed eigenmodes were likely poloidal modes, as shown by simple calculations and the phase measurements discussed in Chapter V. High-frequency spectrum measurements using a 100 MHz sample-rate digitizer showed some nonlinear coupling to higher harmonics around the edge plasma region, presumably due to antenna RF sheath effects. Low-frequency

spectra were also observed in the RF probe signal. These were correlated with a slight stored-energy degradation. Further systematic investigation is needed for thorough understanding of this possible instability.

A numerical simulation was performed with a 2-D RF heating code which simulated stellarator magnetic geometry by using helical symmetry. The image current of the ATF antenna was properly accounted for, yielding good agreement with experimental loading values. Simulations with ATF experimental parameters provided the power-absorption spectrum, wave-field profiles, RF power deposition, eigenmodes and polarization. A consistent picture with the experiment was obtained.

A simple RF power balance was performed with a relatively small number of RF power-flow channels. Since the collision time was longer than the charge exchange loss time, by replacing the electron drag term with a charge-exchange loss term, the kinetic equation for the ion velocity distribution function was numerically solved. This gave the estimated RF power flow to the suprathermal ion tail formation. The most dominant loss channel was parasitic loss to the antenna structure caused by the low loading. The other loss channel considered was RF/edge interaction. The RF/edge interaction energy was estimated from Langmuir probe radial profile measurements of n_e and T_e . This edge-deposited energy was in agreement with the power remaining after the power flows to the structure and fast ions were calculated. It was estimated that 50% of the RF power was lost to the antenna structure, 10% of the RF power was directly absorbed by the edge plasma, and 40% of the RF power was absorbed by fast ions, of which 75% was lost via drift orbit loss. Therefore at most only 10% of the total injected RF energy could be transferred to the bulk plasma, which made a negligible contribution to the bulk plasma power balance (i.e., no bulk heating was observed).

By including a fast-ion drift loss term in the ion kinetic equation, the *RF-TRANS* Fokker-Planck modeling code was used to understand fast ion confinement

and RF energy flow to the fast ion channel. A simple ATF plasma model (two point model) was adopted. Reasonable agreement was achieved in comparison with the experimental NPA data. The results indicated that about 25% of the total RF power absorbed by the plasma was transferred to the electrons and the rest of the power was lost through drift orbit loss. This loss was severe in the plasma edge region (confined plasma region just inside the last closed flux surface) where 90% of the absorbed power was lost to fast ions on unconfined drift orbits.

To illustrate the effect of RF on a single particle orbit, RF terms were included in the guiding center orbit following code. The result showed a dramatic RF effect on helically trapped particles which passed through a resonance layer. Particle energy increased a few hundred keVs in a tenth of a millisecond. The turning point moved closer to the resonance layer as particles were heated. More refinements to this model (code), including phase mixing in a simple form, are being undertaken.

A projection of the understanding gained in studying the low density experiments to the proposed high-power, high-density ICRH experiments was performed and showed much better results, including bulk heating due to a shorter fast ion energy transfer time, a broader power spectrum, a larger number of propagating $k_{||}$ modes, and higher loading. For even better results, slots in the antenna housing and more radial translation of the antenna system is proposed (see next section) to launch low $k_{||}$ modes and increase the plasma loading, especially for low density plasmas.

In general, the experimental observations were in good agreement with what was to be expected in the low density regime, as shown by the agreement of the numerical calculations of the theory with the experimental results. Projections to high density operation showed that ICRH would work quite well in ATF. To prove this, more power and higher density target plasmas are necessary and more operational time must be dedicated to ICRH experiments. A good summary of the low density ICRH heating experiments on ATF would be that no heating was obtained because

the launched spectrum of modes could only propagate in and be absorbed by the confined plasma edge, where high energy trapped particle orbits are unconfined, and any power absorbed has only a short distance to travel to leave the confined plasma region.

Prospects for Future Experiments on ATF

The experimental results shown in Chapter IV and the simulation results with the RF heating code revealed that the low density target plasma did not allow the RF wave to propagate to the plasma center, so that considerable energy was deposited in the edge region, plasma loading was reduced, and edge-heated fast-ion orbit loss resulted in little energy transfer to the bulk plasma. In this section, since there are plans to increase the target-plasma density, the effect of the higher density plasma on the ICRH is examined. To be realistic, the density level that can be achieved is surveyed first. The density limit in ATF ECH plasmas came from the cut-off density for propagation of the ECH wave. For ECH at 53 GHz, this limit was $\bar{n}_e \sim 0.8 \times 10^{13} \text{ cm}^{-3}$. There are plans to install a 106 GHz ECH source which would increase the density limit by four, since the critical density goes as the square of the frequency. Another possible method for obtaining a dense target plasma would be to use NBI-created plasmas as a target for the ICRH. Preliminary experiments along this line have already been performed. The data from these experiments was extremely preliminary, and not suitable for publication, but 100 kW of ICRH was launched into a target plasma driven with approximately 1 MW of NBI power, in a minority heating regime (helium neutral beams were injected into a deuterium target plasma with a hydrogen minority). The antenna loading increased by approximately a factor of 10 over the ECH driven target plasma case, and the stored energy of the plasma was observed to increase more than 10% for the case where the ICRH was injected

into the NBI plasma, as opposed to the case where only the NBI power sustained the plasma. These results, though modest, are nevertheless encouraging, considering the low RF power level. The experiments must be systematically reproduced with a full set of diagnostics, before they can be taken seriously.

The plasma density for the NBI target plasma mentioned above increased to $1.0 \times 10^{14} \text{ cm}^{-3}$ with a ~ 100 ms quasi-steady-state period. The biggest problem was the difficulty in controlling the hydrogen minority concentration because of considerable prior operation in hydrogen. Another concern was that the available RF power (~ 200 kW) seemed to be negligible compared to the NBI power (≥ 1 MW). At the time of this writing (July, 1990) a 1 MW RF source is being prepared for future experiments.

The simulation model discussed in Chapter V, which appears to be valid from comparisons with experimental data from the low-density ICRH experiments, was used to predict ICRH performance in higher density plasmas. The 2-D RF heating code was used for loading, the k_{\parallel} spectrum, propagation, and power-deposition calculations. The Fokker-Planck code, *RFTRANS* was used for calculating energy transfer to the bulk medium and for fast ion confinement studies.

The 2-D heating code results indicated that higher density plasmas ($\bar{n}_e \sim 1.5 \times 10^{13} \text{ cm}^{-3}$) would improve loading by a factor of 5, increase the lower k_{\parallel} portion of the spectrum, enhance wave propagation (as indicated by the RF-induced field profiles reaching into the central region), increase toroidal damping, and increase the fraction of RF power deposited in the central plasma region. The most likely scenario for future work with increased density target plasmas is to continue using helium neutral beam injection into deuterium plasmas with a hydrogen minority. The initial experiments mentioned above yielded high density ($\bar{n}_e \sim 1 \times 10^{14} \text{ cm}^{-3}$), non-collapsing plasmas up to 200 msec (limited by the NBI pulse length for the small amount of ICRH power available). The helium neutral beams were treated

in the numerical calculations discussed next as an impurity with high energy and concentration. The parameters for this case are listed in Table 6.1.

Figure 6.1 and Fig. 6.2 show the result from the simulation for the D(H) and D(³He) regimes. These simulations were performed at frequencies of 14.4 MHz and 9.63 MHz for a 0.95 T magnetic field, respectively. Loading was higher in the D(H) regime; however, in both cases the wave penetrated to the central column and power deposition was toroidally localized near the antenna. This means that good loading and heating results are to be expected for future high power experiments in these regimes. The Q defined in an earlier chapter is ~ 6 (compared to ~ 50 for the low density case) in both high density cases, which means that loading should be very high so that P_{ohmic} (the power to the metallic structures) should be negligible (i.e., the antenna launching efficiency to the plasma should be close to 100%).

The *RFTRANS* Fokker-Planck code simulation was also performed for these higher density cases with 200 kW power. This time, more power was assumed to be absorbed in the central column (as predicted by the 2-D code) and the power density was higher than for the lower density case owing to the higher loading. The results indicated that most of the power ($\geq 90\%$) would be transferred to the background plasmas and little high energy tail formation would be expected because slowing down was very fast, therefore most of the fast ion energy would be transferred to the background plasma (Fig. 6.3 and Fig. 6.4).

From this calculation it is observed that the fast-ion confinement time is approaching the preset diffusion time, indicating that RF energy thermalization would be limited by diffusive transport rather than by convective loss (fast ion orbit loss). Therefore a proper diffusion model becomes important.

Both of the simulations (Fokker-Planck and 2-D wave propagation) promise that ICRH will work well with higher-density target plasmas in ATF. The 2-D RF heating code showed that loading should be dramatically increased and RF power

Table 6.1: Input Parameters of ATF Plasma and Vacuum Vessel for Computer Simulation for Future High-Density Scenario

$T_e(0)$	eV	400
$T_e(a)$	eV	15
$T_{maj}(0)$	eV	250
$T_{maj}(a)$	eV	15
$T_{min}(0)$	eV	250
$T_{min}(a)$	eV	15
$T_{imp}(0)$	eV	850
$T_{imp}(a)$	eV	15
$n_e(0)$	cm^{-3}	1×10^{14}
$n_e(a)$	cm^{-3}	2×10^{13}
λ_n	cm	5
R	m	2.1
\bar{a}	m	0.3
$\eta_{minority}$		0.05
$\eta_{impurity}$		0.3
Gap between strap and plasma	cm	6
Strap width	cm	10.8
Side wall width	cm	22.0

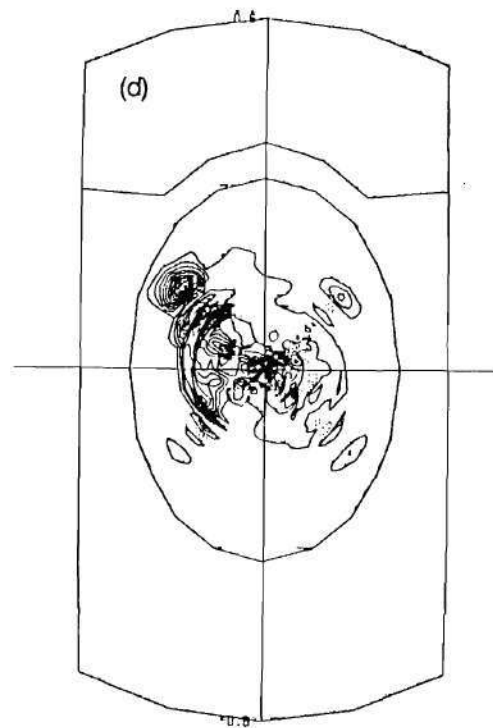
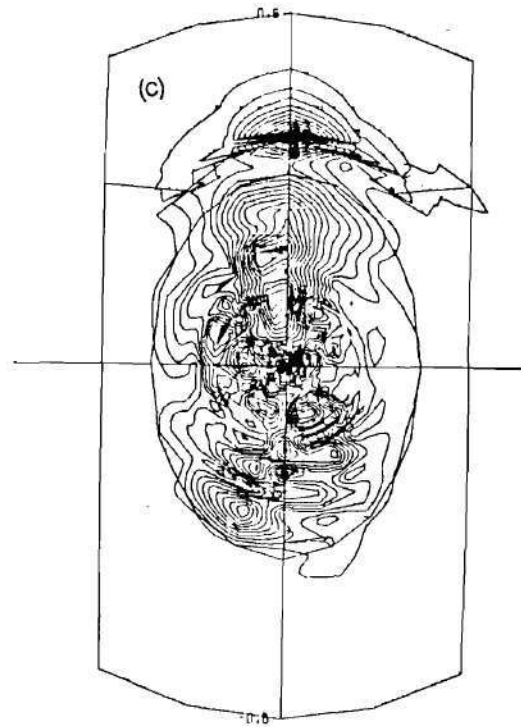
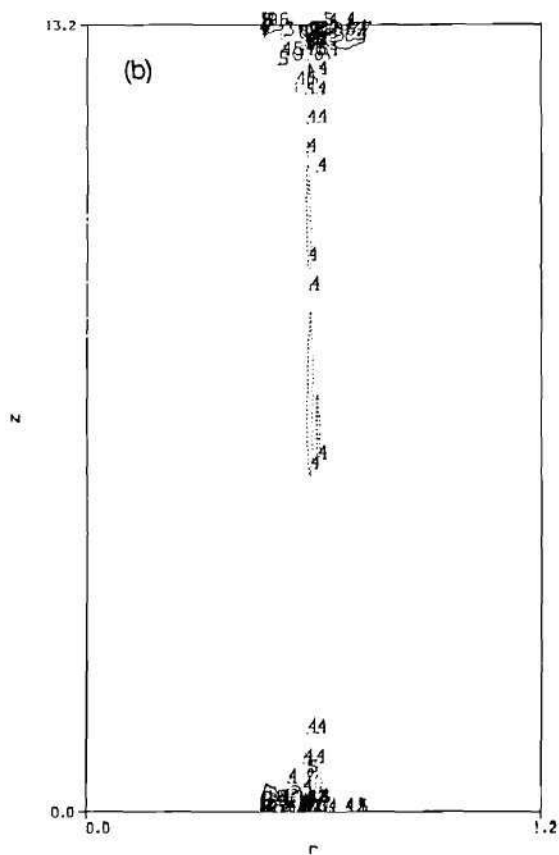
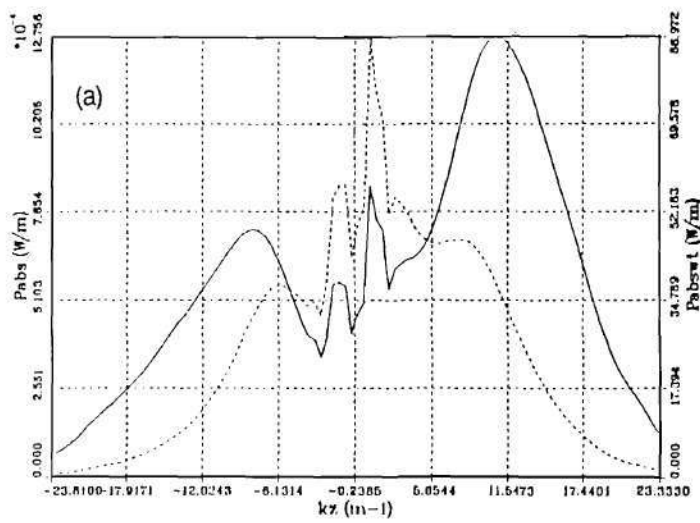


Figure 6.1: The 2-D RF Heating Code Results in D(H) Regime for a High Density Case ($\bar{n}_e \sim 7 \times 10^{13} \text{ cm}^{-3}$) (a) k_z Spectrum (b) Power Absorption Profile in Equatorial Plane (c) B_z Profile in $r - \theta$ Plane (d) Power Absorption Profile in $r - \theta$ Plane

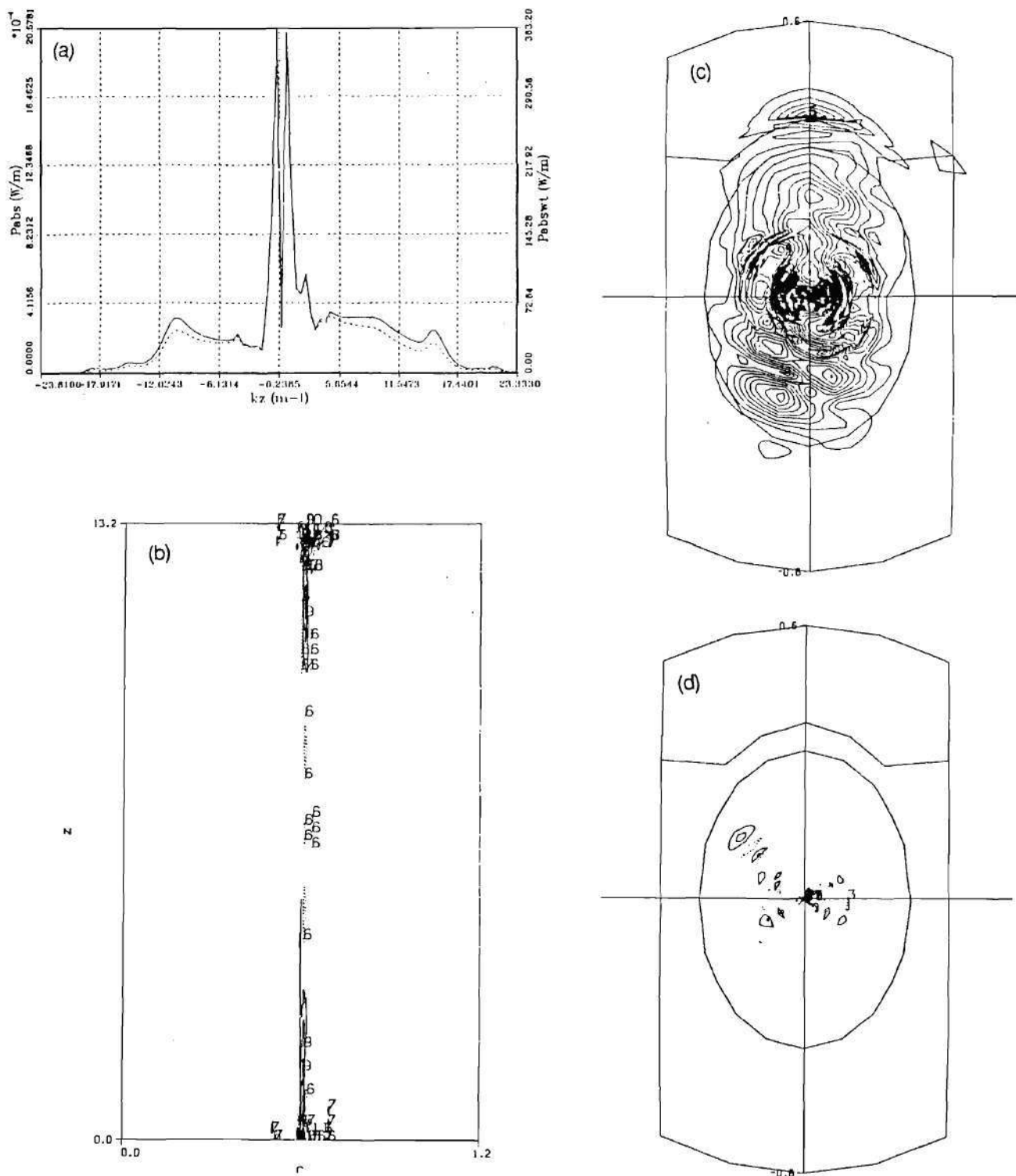


Figure 6.2: 2-D RF Heating Code Results in D(^3He) Regime for High Density Case ($\bar{n}_e \sim 7 \times 10^{13} \text{ cm}^{-3}$) (a) k_z Spectrum (b) Power Absorption Profile in Equatorial Plane (c) B_z Profile in $r - \theta$ Plane (d) Power Absorption Profile in $r - \theta$ Plane

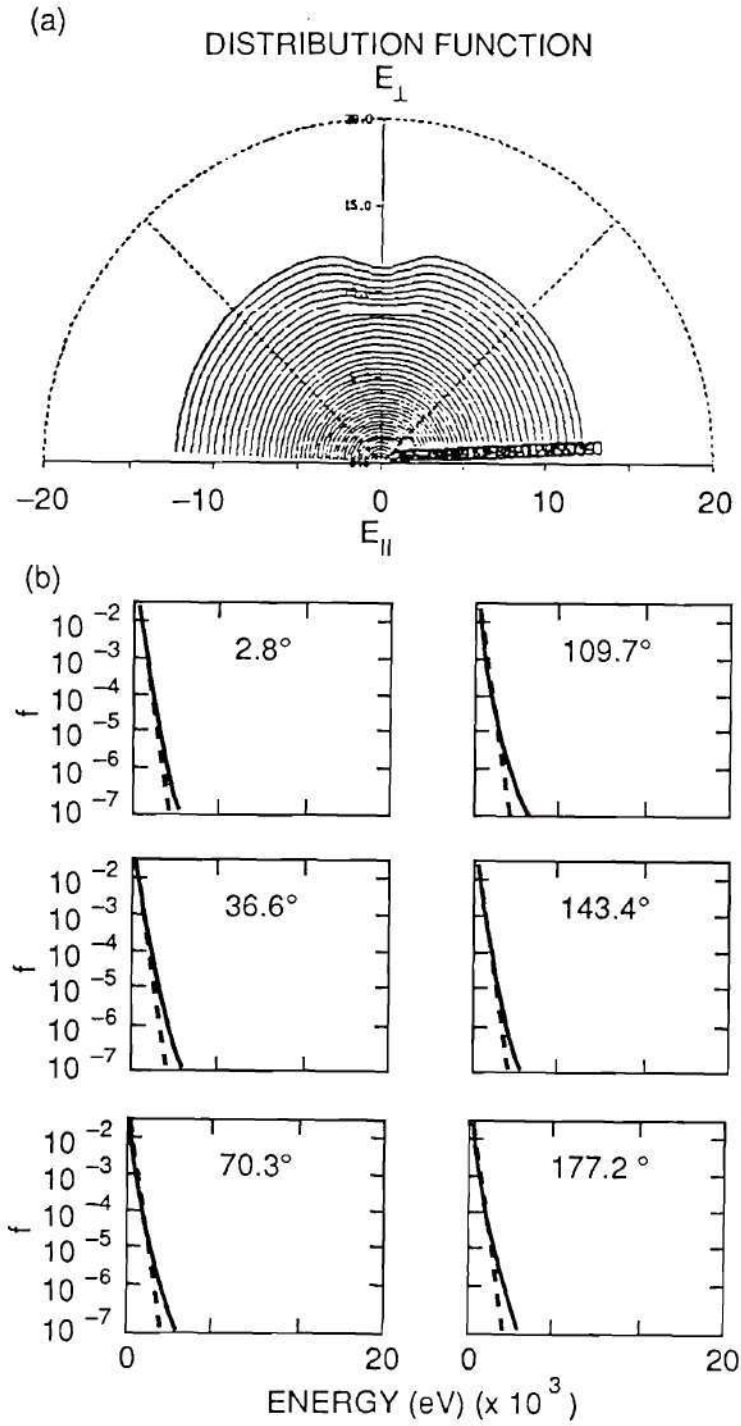


Figure 6.3: The Result of the *RFTRANS* Fokker-Planck Calculation for an ATF High Density ICRH Case for Region 1 (Central Region): (a) Ion Distribution in Velocity Space (b) Ion Flux vs Energy at Different Pitch Angles in Velocity Space

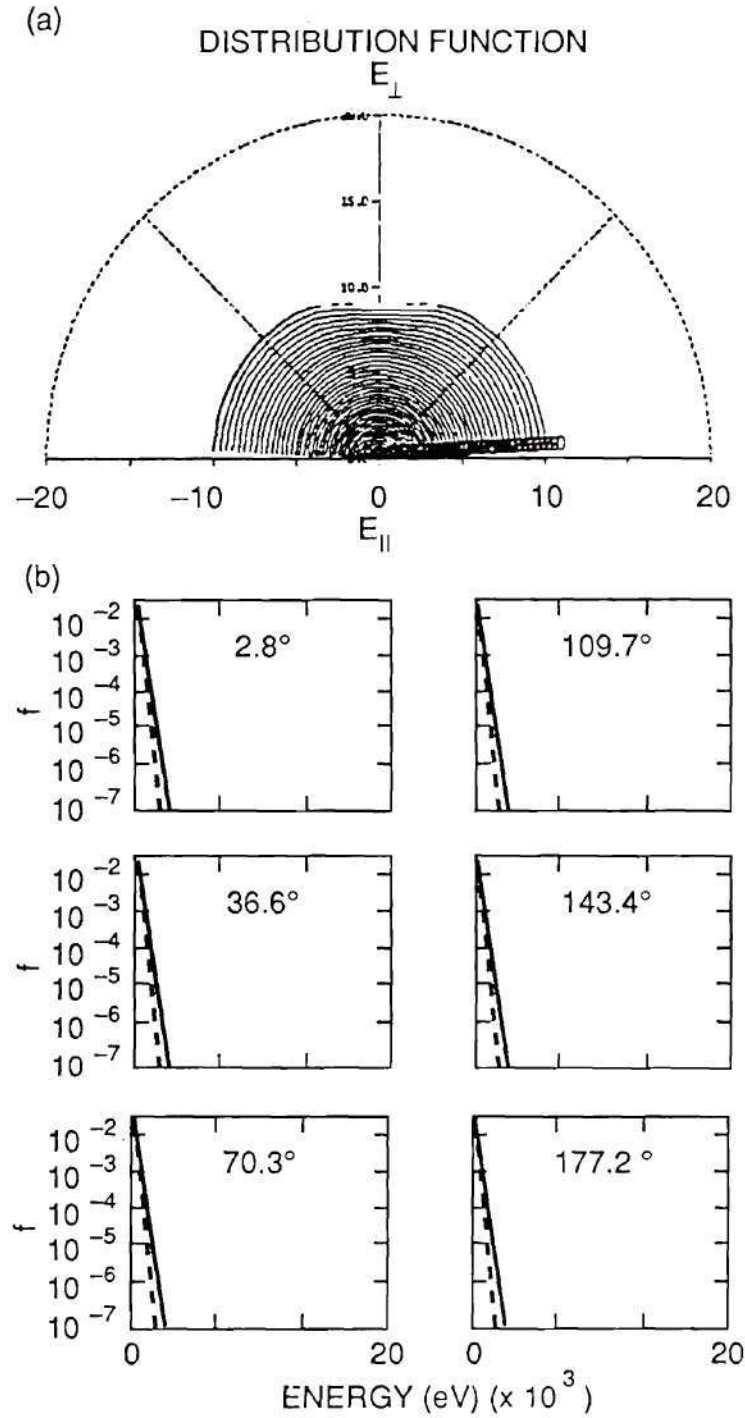


Figure 6.4: The Result of the *RFTRANS* Fokker-Planck Calculation for an ATF High Density ICRH Case for Region 2 (Edge Region): (a) Ion Distribution in Velocity Space (b) Ion Flux vs Energy at Different Pitch Angles in Velocity Space

absorption should be excellent. As far as fast ion confinement and RF power thermalization are concerned, the model (*RFTRANS* with two region model) predicts good bulk electron and ion heating through collisional drag, and good confinement of the fast ions for a diffusion time. Since this was only a two point (region) model however, better modeling of fast ion confinement and RF power thermalization in ATF must be performed in order to understand the planned future experiments.

Future Work

In the initial ICRH experiments, the $k_{||}$ spectrum of the antenna current appeared to be very broad, especially for low density plasmas. The effect of the side-wall current made the situation even worse by suppressing low $k_{||}$ modes (the only ones which could have propagated to the plasma center). To improve this situation with only minor hardware modifications, the current strap can be modified easily by changing the strap width and making slots in the strap housing (side walls). From a simulation, an increase in loading was observed with the latter modifications, as shown in Fig 6.5. The change in the strap width is not effective unless the width of the strap housing changes, which is technically difficult.

Several methods to increase the density of the target plasma were proposed. Simulations also indicate that good loading and heating data could be expected with higher density plasmas. Also optimizing the locations of the cyclotron and hybrid resonance layers, which are functions of frequency, η , and B_0 is important for maximizing efficiency. As suggested by simulations, a slightly lower frequency should be explored for which both resonance layers are moved slightly outward, and minority concentrations of less than 5% are necessary for good results (see Chapter V).

Fast ion confinement as a function of the area of the closed minimum-B con-

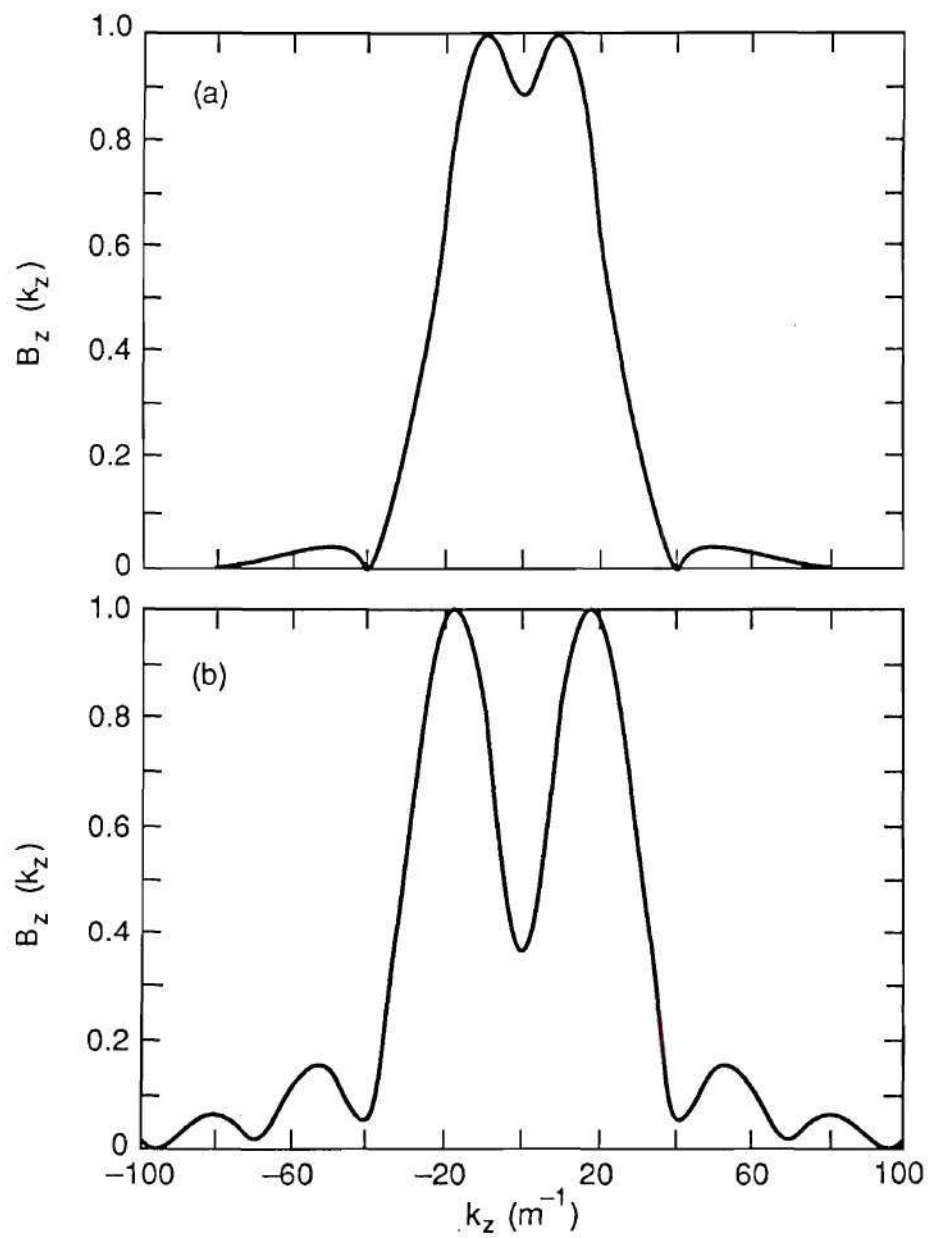


Figure 6.5: B_z Profile at 3 cm from the Faraday Shield (a) with and (b) without Side Wall Slots

tours can be tested. This experiment will test the theoretical proposal (see reference [14] and [15] in Chapter V) as well as help in optimizing ICRH. Fokker-Planck calculations are very useful to understand kinetic interactions between wave and particles. More precise modeling for stellarator geometry of the RF operator and loss cone should be undertaken. The validity of the model should be tested by comparing to experimental data. In higher density experiments, collision and diffusion in real-space become important. Proper modeling of these processes requires good understanding of the wave-particle interaction in stellarator geometry. Since the trapped ion portion is larger in a stellarator than in a tokamak with the same aspect ratio, the effect of the ICRF wave on these helically trapped particles should be pursued, as was done for tokamaks [1]. The concept of well-confined and barely-confined regions should be refined and fast ion confinement should be examined in both regions. The results of the present work suggest that in stellarators central heating is more important than in tokamaks as far as fast ion confinement is concerned. The hypothesis of the enhanced cyclotron absorption due to the helical geometry given in Chapter II stands on this assumption. The larger trapped ion population in the outer region of the plasma, which is caused by edge RF heating, could degrade ion confinement in this region. An orbit following code is a useful tool to examine these topics if it features a proper model of the RF effect on particle orbits. A simple RF-heating model was presented in this thesis, but a more precise model is necessary to obtain a good understanding of RF effects on the various orbits existing in stellarator geometry. This would also make it possible to simulate NPA scanning data and the physics behind it.

REFERENCES

- [1] Grekov, D. L., Carter, M. D., Pyatak, A. I., "Cyclotron Absorption of Fast Magnetosonic Waves by Trapped Ions in Tokamaks," *Sov. J. Plasma Phys.*, **15**, 661 (1989).

Appendix A

Fourier Representation of ICRH Antenna Current Including Side-Wall Image Currents

The antenna model in the 2-D RF heating code is the so-called "current sheet" model in which the antenna current was described as a jump condition in the RF magnetic field at a certain radial position. Since the RDL-type antenna has current-carrying side walls, Fourier expansion of the antenna spectrum should be changed to include these image currents. Figure A.1 shows the diagram of the current strap and side walls in this model. There are a main current strap and two side walls which can be treated as three-strap case with different current amplitudes and phases in each strap. Since even in a current strap, most of the current flows along the side edges, two current straps and two side walls (four-strap model) are also considered. Note that even though the side walls were stretched radially, this radial distribution is not considered in this calculation. Instead a weighting factor is used to compensate for this and typically it was assumed that 30% of the total image current flows through this radially localized side wall.

In the current sheet model, the antenna current is represented[1] as

$$J(r, \theta, z) = f(\theta)\hat{\theta}\delta(r - r_0)J(z), \quad (\text{A.1})$$

where, $f(\theta)$ is the poloidal current shape factor described in Ref.[1], $J(z) = I(z)/L$ is the toroidal current density distribution function and L is the toroidal strap width.

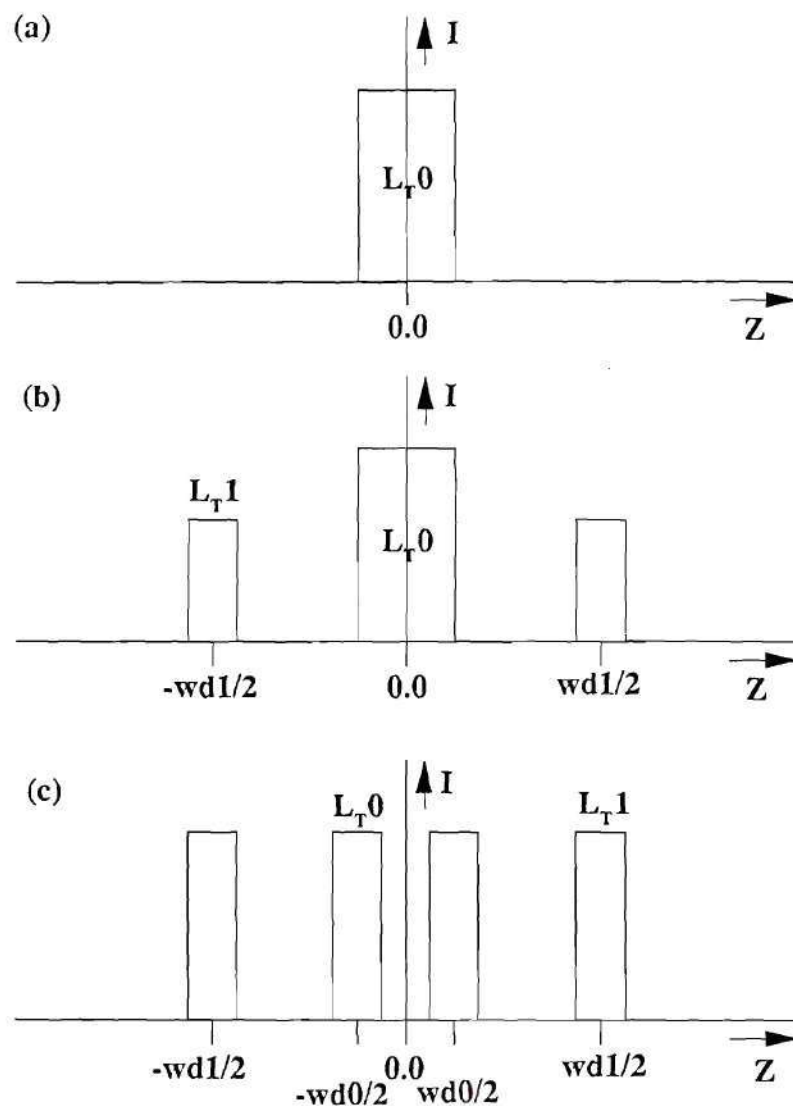


Figure A.1: Illustration of the Antenna Current Distribution Including Radially Localized Side Wall Image Current (a) Single-Strap without Side Wall Model (b) Three-Strap (One Current Strap and Two Side Wall Straps) Model (c) Four-Strap (Two Current Strap and Two Side Wall Straps) Model

Note that radially localized effect is represented as a delta function. It is assumed that the strap current and side wall currents are different in magnitude by the ratio $\gamma (= \frac{|I_1|}{|I_0|})$ and different in phase by $\delta\varphi$. $J(z)$ can be represented by Fourier sum as follow:

$$J(z) = \sum_{l=-\infty}^{\infty} J_{k_z} \exp(ik_z z), \quad (\text{A.2})$$

where, $k_z = \frac{l}{R_T}$ and R_T is the major radius. Taking the integral in both sides, then

$$J_{k_z} = \frac{1}{2\pi R_T} \int_0^{2\pi R_T} dz \exp\left(-i \frac{l}{R_T} z\right) J(z). \quad (\text{A.3})$$

For the three-strap case shown in Fig. A.1, the integral on the right-hand side in Eq.(A.3) is expressed as

$$J_{k_z} = \frac{1}{2\pi R_T} \left\{ J_0 \int_0^{\frac{L_T 0}{2}} dz e^{-i \frac{l}{R_T} z} + J_1 \int_{\frac{wd1}{2} - \frac{L_T 1}{2}}^{\frac{wd1}{2} + \frac{L_T 1}{2}} dz e^{-i \frac{l}{R_T} z} \right. \\ \left. + J_1 \int_{2\pi R_T - \frac{wd1}{2} - \frac{L_T 1}{2}}^{2\pi R_T - \frac{wd1}{2} + \frac{L_T 1}{2}} dz e^{-i \frac{l}{R_T} z} + J_0 \int_{2\pi R_T - \frac{L_T 0}{2}}^{2\pi R_T} dz e^{-i \frac{l}{R_T} z} \right\}, \quad (\text{A.4})$$

where all strap dimensions are shown in Fig. A.1. Some manipulations of Eq.(A.4) give

$$J_{k_z} = \frac{J_0}{\pi R_T k_z} \left\{ \sin \frac{L_T 0}{2} k_z + \gamma \exp(i\delta\varphi) \left[\sin \left(\frac{wd1 + L_T 1}{2} \right) k_z \right. \right. \\ \left. \left. - \sin \left(\frac{wd1 - L_T 1}{2} \right) k_z \right] \right\}, \quad (\text{A.5})$$

where, $\frac{I_1}{I_0} = \gamma \exp(i\delta\varphi)$. From Eq.(A.5), if $L_T 1$ is equal to zero (which means the single-strap case), the result reproduces Jaeger's original expression[1] for the single-strap model.

For the four-strap case, the integral on the right-hand side in Eq.(A.3) is expressed as

$$J_{k_z} = \frac{1}{2\pi R_T} \left\{ J_0 \int_{\frac{wd0}{2} - \frac{L_T 0}{2}}^{\frac{wd0}{2} + \frac{L_T 0}{2}} dz e^{-i \frac{l}{R_T} z} + J_1 \int_{\frac{wd1}{2} - \frac{L_T 1}{2}}^{\frac{wd1}{2} + \frac{L_T 1}{2}} dz e^{-i \frac{l}{R_T} z} \right. \\ \left. + J_1 \int_{2\pi R_T - \frac{wd1}{2} - \frac{L_T 1}{2}}^{2\pi R_T - \frac{wd1}{2} + \frac{L_T 1}{2}} dz e^{-i \frac{l}{R_T} z} + J_0 \int_{2\pi R_T - \frac{wd0}{2} - \frac{L_T 0}{2}}^{2\pi R_T - \frac{wd0}{2} + \frac{L_T 0}{2}} dz e^{-i \frac{l}{R_T} z} \right\}. \quad (\text{A.6})$$

This becomes

$$J_{k_z} = \frac{2J_0}{\pi R_T k_z} \left[\sin \frac{L_T 0}{2} k_z \cos \frac{wd0}{2} k_z + \gamma \exp(i\delta\varphi) \sin \frac{L_T 1}{2} k_z \cos \frac{wd1}{2} k_z \right] \quad (\text{A.7})$$

With Eq.(A.2) and Eq.(A.5) for the three-strap model and Eq.(A.2) and Eq.(A.7) for the four-strap model, Eq.(A.1) can be rewritten as

$$\vec{J}(r, \theta, z) = \vec{J}^A(r, \theta) J_0 \sum_{k_z} C_{k_z}(z), \quad (\text{A.8})$$

where,

$$\vec{J}^A(r, \theta) = f(\theta) \frac{\delta(r - r_0)}{2\pi R_T} \hat{\theta}. \quad (\text{A.9})$$

For three straps,

$$C_{k_z}(z) = \frac{2e^{ik_z z}}{k_z L_T 0} \left[\sin \frac{L_T 0}{2} k_z + 2\gamma \exp(i\delta\varphi) \frac{L_T 0}{L_T 1} \sin \frac{L_T 1}{2} k_z \cos \frac{wd1}{2} k_z \right], \quad (\text{A.10})$$

and for $k_z = 0$,

$$C_{k_z=0}(z) = 1 + 2\gamma e^{i\delta\varphi}. \quad (\text{A.11})$$

For four straps,

$$C_{k_z}(z) = \frac{4e^{ik_z z}}{k_z} \left[\frac{1}{L_T 0} \sin \frac{L_T 0}{2} k_z \cos \frac{wd0}{2} k_z + \gamma \exp(i\delta\varphi) \frac{1}{L_T 1} \sin \frac{L_T 1}{2} k_z \cos \frac{wd1}{2} k_z \right], \quad (\text{A.12})$$

and for $k_z = 0$,

$$C_{k_z=0}(z) = 2(1 + \gamma e^{i\delta\varphi}). \quad (\text{A.13})$$

Since it was assumed that the induced electric field $\vec{E}(r, \theta, z)$ and the plasma current $\vec{J}_p(r, \theta, z)$ were represented in the same way, then

$$\vec{E}(r, \theta, z) = I_0 \sum_{k'_z} \vec{E}_{k'_z}(r, \theta) C_{k'_z}(z), \quad (\text{A.14})$$

$$\vec{J}_p(r, \theta, z) = I_0 \sum_{k_z} \vec{J}_{k_z}^p(r, \theta) C_{k_z}(z). \quad (\text{A.15})$$

The total absorbed power can be represented as

$$\begin{aligned} P_{tot} &= \int \dot{W}(r, \theta, z) r dr d\theta dz, \\ &= \int r dr d\theta dz \frac{1}{2} \text{Re}[\vec{E}^*(r, \theta, z) \cdot \vec{J}_p(r, \theta, z)], \end{aligned} \quad (\text{A.16})$$

$$= 2\pi R_T I_0^2 \sum_{k_z} P_{abs}(k_z, \omega), \quad (\text{A.17})$$

where,

$$P_{abs}(k_z, \omega) = \int r dr d\theta \frac{1}{2} \text{Re}[\vec{E}_{k_z}^*(r, \theta) \cdot \vec{J}_{k_z}^p(r, \theta)] |C_{k_z}(z)|^2,$$

and

$$|C_{k_z}(z)|^2 = C_{k_z}^*(z) C_{k_z}(z).$$

Therefore, for three straps,

$$\begin{aligned} |C_{k_z}(z)|^2 &= \frac{4}{k_z^2} \left[\frac{1}{L_{T0}^2} \sin^2 \frac{L_{T0}}{2} k_z + 4\gamma^2 \frac{1}{L_{T1}^2} \sin^2 \frac{L_{T1}}{2} k_z \cos^2 \frac{wd1}{2} k_z \right. \\ &\quad \left. + 4\gamma \cos \delta\varphi \frac{1}{L_{T0} L_{T1}} \sin \frac{L_{T0}}{2} k_z \sin \frac{L_{T1}}{2} k_z \cos \frac{wd1}{2} k_z \right], \end{aligned} \quad (\text{A.18})$$

and for $k_z = 0$,

$$|C_{k_z}(z)|^2 = 1 + 4\gamma^2 + 4\gamma \cos \delta\varphi. \quad (\text{A.19})$$

For four straps,

$$\begin{aligned} |C_{k_z}(z)|^2 &= \frac{16}{k_z^2} \left[\frac{1}{L_{T0}^2} \sin^2 \frac{L_{T0}}{2} k_z \cos^2 \frac{wd0}{2} k_z + \gamma^2 \frac{1}{L_{T1}^2} \sin^2 \frac{L_{T1}}{2} k_z \cos^2 \frac{wd1}{2} k_z \right. \\ &\quad \left. + 2\gamma \cos \delta\varphi \frac{1}{L_{T0} L_{T1}} \sin \frac{L_{T0}}{2} k_z \cos \frac{wd0}{2} k_z \sin \frac{L_{T1}}{2} k_z \cos \frac{wd1}{2} k_z \right] \end{aligned} \quad (\text{A.20})$$

and for $k_z = 0$,

$$|C_{k_z}(z)|^2 = 4[1 + \gamma^2 + 2\gamma \cos \delta\varphi]. \quad (\text{A.21})$$

As shown in Eq.(A.18) through Eq.(A.21), $|C_{k_z}(z)|^2$ is no longer a function of z .

Since this code does not calculate the antenna current distribution self-consistently, it has to be given the optimized and realized current distribution. It should be noted that for the RDL-type antenna, the effect of the side-wall current

makes the average in the z -direction of the toroidal component of the induced magnetic field, and therefore the absorbed power at $k_z = 0$ zero.

For the purpose of illustration, to make the spectrum zero at $k_z = 0$, $|C_{k_z}(z)|^2$ should be eliminated at $k_z = 0$. For $\delta\varphi = \pi$ as usual, then From Eq.(A.19) and Eq.(A.21) γ should be 0.5 for the three-strap case and 1 for the four-strap case. Therefore if all the return current flows through two radially localized side wall, then $k_z = 0$ mode is completely suppressed. But in real geometry, the return current flows through the side wall with a certain radial distribution and also through the back plane. Therefore the amounts of the return current passing through the radially localized side walls as simulated in this code should be some fraction of the total return current. By comparing with a 2-D magnetostatic code calculating the vacuum antenna field as shown in Fig. 5.5, 30% of the total return current was assumed to flow through this localized side wall throughout the calculations in this thesis.

REFERENCES

- [1] Jaeger, E. F., Batchelor, D. B., Weitzner, H. and Whealton, J. H., "ICRF Wave Propagation and Absorption in Tokamak and Mirror Magnetic Fields- A Full-Wave Calculation", *Com. Phys. Commun.* **40**, 33 (1986)

VITA

Myeun Kwon was born on February 14, 1958 in Seoul, Korea. He attended the Seoul National University from 1976 to 1983 and received the B.S. degree in Nuclear Engineering. From 1978 to 1981, he served in the Korean Army for three years. He was awarded the An-Dong scholarship for the 1977, 1978 and 1982 academic years.

Upon graduation, he worked as a computer system engineer in the Korea Housing Bank. He entered graduate school in the Department of Nuclear Engineering and Health Physics at the Georgia Institute of Technology in 1984. He earned the M.S. degree in Nuclear Engineering in 1986. In 1987 he began his thesis research in the Fusion Energy Division of the Oak Ridge National Laboratory.

In April 1984, he was married to Mee Sun Kim. Their daughter, Yerin Heidi, was born on December 22, 1987.